Quasi-Majorana states in Majorana devices

Vuik, A.

DOI
10.4233/uuid:b61039b3-7014-425d-8803-eeb34f12ee1d

Publication date
2018

Document Version
Final published version

Citation (APA)
Vuik, A. (2018). *Quasi-Majorana states in Majorana devices*. [Dissertation (TU Delft), Delft University of Technology]. https://doi.org/10.4233/uuid:b61039b3-7014-425d-8803-eeb34f12ee1d

Quasi-Majorana states in Majorana devices

Quasi-Majorana states in Majorana devices

Proefschrift

ter verkrijging van de graad van doctor
aan de Technische Universiteit Delft,
op gezag van de Rector Magnificus prof. dr. ir. T.H.J.J. van der Hagen.
voorzitter van het College voor Promoties,
in het openbaar te verdedigen op woensdag 19 december 2018 om 15:00 uur

door

Adrianus Vuik

Natuurkundig ingenieur, Technische Universiteit Delft, Nederland,
geboren te Capelle aan den IJssel, Nederland.

Dit proefschrift is goedgekeurd door de

promotor: Dr. A. R. Akhmerov
copromotor: Dr. M. Wimmer

Samenstelling promotiecommissie:

Rector Magnificus,	voorzitter
Dr. A. R. Akhmerov,	Technische Universiteit Delft, promotor
Dr. M. Wimmer,	Technische Universiteit Delft, copromotor
Onafhankelijke leden:	
Prof. dr. ir. L. P. Kouwenhoven	Technische Universiteit Delft
Prof. dr. P. Brouwer	Freie Universität Berlin
Prof. dr. C. W. J. Beenakker	Universiteit Leiden
Dr. L. Fritz	Universiteit Utrecht
Dr. A. Caviglia	Technische Universiteit Delft
Prof. dr. Y. V. Nazarov	Technische Universiteit Delft, reservelid

This research was supported by the Netherlands Organization for Scientific Research (NWO/OCW), as part of the Frontiers of Nanoscience program, and an ERC Starting Grant.

Printed by: Gildeprint

Cover: Copyright © 2018 by Ilse Modder (www.ilsemodder.nl)

Casimir PhD Series Delft-Leiden 2018-49

ISBN 978-90-8593-378-6

Een elektronische versie van dit proefschrift is beschikbaar via
`http://repository.tudelft.nl/`.

CONTENTS

SUMMARY

Nowadays, quantum computers, a promising direction of computer hardware development, suffer too much from errors caused by disturbance of qubits to compete with the state-of-the-art classical computers. Topological phases in condensed matter physics offer a solution: the topological edge states emerging in such a phase are spatially separated by an insulating bulk, which makes a qubit constructed from such topological states much more resilient to local perturbations. Majorana states are examples of topological edge states, and form the main focus of research on topological quantum computing due to indications of successful creation and detection of Majorana states in one-dimensional superconductor-semiconductor hybrid devices.

Quasi-Majorana states share most characteristics of Majorana states, but appear in the topologically trivial phase and appear at the same position, in contrast to topological, spatially separated Majorana states. For this reason, quasi-Majorana states are not protected from noise, and hence appear to be not useful for quantum computing. For a long while, quasi-Majorana states were considered a nuisance, because they mimic the local signatures of topological Majorana states, and therefore can make a false positive signature in the search for Majorana states.

In trying to understand how Majorana devices work, I started this thesis with an investigation of electrostatics in Majorana devices. An applied gate voltage sets the chemical potential in a Majorana nanowire, relevant for the creation of Majorana states, but this is influenced by other electrostatic components in the environment. I found that these electrostatic effects introduce non-universal, geometry-dependent behaviour of two Majorana characteristics: the shape of the topological phase boundary and the oscillations of the Majorana splitting energy. In addition to controlling the band structure, gate electrodes alter the transport properties of electrons by creating a tunnel barrier or a constriction in the potential. Studying such constrictions, I have demonstrated that the confinement potential barriers are smooth, allowing to measure the helical gap in the band structure, which agrees with experimental observations.

Since quasi-Majorana states appear at the slope of a smooth confinement potential, the results of my simulations of the electrostatics motivated to continue with an investigation of these states. I showed that quasi-Majorana states not only have an exponentially suppressed energy as a function of magnetic field, but also have an exponentially different tunnel coupling across the barrier where they are located. This realization allowed me to strengthen the recent observations of similarity between Majorona states and quasi-Majorana states, and conclude that tunneling measurements can not distinguish Majorana states from quasi-Majorana states as a matter of principle.

Because of this extreme similarity, I turned to study a possible alternative strategy to distinguish topological Majorana states from quasi-Majorana states. This strategy

focusses on rectifying behaviour in the nonlocal conductance through a Majorana wire connected to two normal leads. This phenomenon measures a global topological phase transition, rather than a local measure of the density of states, and therefore it is not influenced by the presence of quasi-Majorana states.

The similarity of quasi-Majorana and topological Majorana states also leads to an unexpected consequence. Braiding (an exchange of two Majorana states), a building block of a topological quantum computer, can also be done with quasi-Majorana states. Although quasi-Majorana states appear next to each other, their couplings are exponentially different, which allows to control them individually. Braiding quasi-Majorana states can even be advantageous, because it requires less precise control over system parameters. I therefore conclude that braiding of quasi-Majorana states is within experimental reach, and opens an alternative route on realizing a quantum computer.

SAMENVATTING

Kwantumcomputers, een veelbelovende richting in de ontwikkeling van computerhardware, hebben op dit moment teveel last van fouten veroorzaakt door de verstoring van qubits om te kunnen concurreren met de state-of-the-art klassieke computers. Topologische fases in de vaste-stoffysica bieden een oplossing: de topologische randtoestanden die in zo'n fase ontstaan zijn ruimtelijk gescheiden van elkaar door een niet-geleidende bulk, waardoor een qubit gevormd door zulke topologische toestanden veel beter bestand is tegen lokale verstoringen. Majorana-toestanden zijn voorbeelden van topologische randtoestanden, en vormen de belangrijkste focus van het onderzoek naar topologische kwantumberekeningen vanwege aanwijzingen van de succesvolle creatie en detectie van Majorana-toestanden in ééndimensionale hybride supergeleider-halfgeleiderapparaten.

Quasi-Majorana-toestanden delen de meeste kenmerken van Majorana-toestanden, maar verschijnen in de topologisch triviale fase en verschijnen op dezelfde positie, in tegenstelling tot de topologische, ruimtelijk van elkaar gescheiden Majorana-toestanden. Hierdoor zijn quasi-Majorana-toestanden niet beschermt tegen ruis, en daarom lijken ze ongeschikt voor kwantumberekeningen. Lange tijd werden quasi-Majorana-toestanden als hinderlijk beschouwt, omdat ze de lokale signalen van topologische Majorana-toestanden imiteren, waardoor ze in de zoektocht naar Majorana-toestanden een vals positief signaal kunnen veroorzaken.

Om te begrijpen hoe Majorana-apparaten werken, startte ik deze thesis met een onderzoek naar de electrostatica in Majorana-apparaten. Een aangebrachte gatespanning reguleert de chemische potentiaal in een Majorana-nanodraad, relevant voor de creatie van Majorana-toestanden, maar dit wordt beïnvloed door andere electrostatische componenten in de omgeving. Ik ontdekte dat deze electrostatische effecten niet-universeel, geometrie-afhankelijk gedrag introduceren voor twee Majorana-kenmerken: de vorm van de topologische fasegrens en de oscillaties van de Majorana-splitsingenergie. Naast de controle over de bandenstructuur veranderen gate-electroden ook de transporteigenschappen van electronen door de creatie van een tunnelbarrière of een vernauwing in de potentiaal. Door het bestuderen van zulke vernauwingen heb ik aangetoond dat begrenzende potentiaalbarrières een flauwe helling hebben, wat de meting van helische kloof in de bandenstructuur mogelijk maakt, overeenkomend met experimentele observaties.

Omdat quasi-Majorana-toestanden ontstaan langs een flauw hellende begrenzingspotentiaal, vormden de uitkomsten van mijn simulaties van de electrostatica de motivatie om te vervolgen met een onderzoek naar deze toestanden. Ik heb aangetoond dat quasi-Majorana-toestanden niet alleen een exponentieel onderdrukte energie hebben als een functie van het magnetisch veld, maar ook exponentieel verschillende tunnelkoppelingen over de barrière waar ze zich bevinden. Deze bevinding zorgde ervoor dat ik de recente observaties van de similariteit van Majorana-

toestanden en quasi-Majorana-toestanden kon versterken, en kon concluderen dat tunnelmetingen principieel Majorana-toestanden niet kunnen onderscheiden van quasi-Majorana-toestanden.

Vanwege deze extreme similariteit begon ik met een onderzoek naar een mogelijke alternatieve strategie om topologische Majorana-toestanden te onderscheiden van quasi-Majorana-toestanden. Deze strategie focust op gelijkrichtingsgedrag in de niet-lokale geleiding door een Majorana-draad die verbonden is met twee normale contacten. Dit fenomeen signaleert een globale topologische fasetransitie in plaats van een lokale meting van de toestandsdichtheid, en daarom wordt het niet beïnvloed door de aanwezigheid van quasi-Majorana-toestanden.

De similariteit tussen quasi-Majorana- en topologische Majorana-toestanden leidt ook to een onverwachte consequentie. Braiding (de omwisseling van twee Majorana-toestanden), een bouwsteen van een topologische kwantumcomputer, kan ook gedaan worden met quasi-Majorana-toestanden. Hoewel quasi-Majorana-toestanden naast elkaar verschijnen, zijn hun koppelingen exponentieel verschillend, waardoor controle over de individuele toestanden mogelijk is. De braiding van quasi-Majorana-toestanden kan zelfs voordelig zijn, omdat het minder precieze controle over de systeemparameters vereist. Daarom concludeer ik dat braiding van quasi-Majorana-toestanden binnen bereik van de experimenten ligt, en dat dit een alternatieve route opent voor de realisatie van een kwantumcomputer.

1

INTRODUCTION

1.1. PREFACE

Physical research often starts from combining well-known fundamental concepts, which then results in surprising physical consequences. An example of this is the combination of topology, the study of quantities that cannot change continuously, and condensed matter physics. This combination results in new phases of matter, characterized by an insulating bulk and conducting states at the boundary of the material. Majorana states are examples of such edge states, appearing in one-dimensional nanowires. Besides the fundamental interest in Majorana states as an example of topology in condensed matter physics, Majorana states have potential applications in topological quantum computation.

Quantum computers use quantum mechanical concepts such as superposition and entanglement in quantum bits (or qubits) to manipulate many input parameters in parallel. Therefore, for specific problems a quantum computer provides exponential speedup compared to a classical computer [1–4]. However, decoherence of the qubit state due to interaction with the environment destroys the stored information, making long quantum computations impossible. Hence, achieving fault-tolerant quantum computation [5, 6] is a major goal of modern condensed matter research.

Topological quantum computation [7–9] is an approach to fault-tolerant quantum computation, where the fault-tolerance does not arise from error correcting schemes, but from an intrinsic protection of a topological quantum state against decoherence. The properties of a topological quantum state are protected by the symmetry and the spectral gap of the material, such that local perturbations do not affect such state.

The Majorana state is such a topological quantum state, and hence it has an intrinsic error protection which makes the state a promising candidate for a topological qubit. Shortly after theoretical work on creating Majorana states in solid state devices [10–12], first experimental signatures of Majorana states were reported [13–15]. However, the high complexity of the experiments due to the combination of many different physical concepts makes it challenging to reliably distinguish Majorana states from alternative explanations.

Like often happens with physics research, also in my thesis I combine well-studied concepts to study their interplay and the new physics resulting from this combination. I start from the combination of electrostatics and Majorana physics, in order to obtain more realistic physical modelling of Majorana devices. I find that the resulting potential profiles are often smooth, and hence I turn to the study of quasi-Majorana states that arise for such smooth potentials and reproduce Majorana properties in a non-topological regime. Finally, I investigate nonlocal conductance in Majorana devices in order to reliably distinguish quasi-Majorana states from topological Majorana states.

1.2. TOPOLOGY AND SYMMETRY IN QUANTUM SYSTEMS

Symmetry plays a crucial role in physics, because it describes phase transitions between different phases of matter. The Landau theory of phase transitions interprets them as the breaking of some underlying symmetry [16]. For example, the transition from a non-magnetic material to a ferromagnet breaks the spin rotation symmetry, since it forces all spins to point in a specific direction as opposed to keeping all directions equally likely. Until a few decades ago, symmetry breaking was considered the only mechanism underlying a phase transition. However, the theory following the experimental discovery of the quantum Hall effect [17] demonstrated that certain phase transitions are described by a change in topology rather than symmetry, or a *topological* phase transition [18, 19].

Topology studies quantities that cannot change continuously. An example from mathematics is the classification of surfaces based on the genus, which is the number of holes through the surface [20]. The genus is a global property of the surface topology, and is invariant under small perturbations of the surface: surfaces of the same genus can be continuously transformed into each other. Only a drastic change which creates or annihilates a hole in the surface can change the genus, and hence the genus is a *topological invariant*.

In condensed matter physics, the concept of topology is applicable to Hamiltonians of gapped quantum systems rather than to surfaces. Hamiltonians with a band gap that can be continuously transformed into each other without closing the gap are topologically equivalent, and have the same topological invariant. However, when the band gap of such Hamiltonian closes and reopens, the topological invariant changes and edge states appear, with an energy in the middle of the reopened band gap. Hence, a topological material surrounded by trivial matter has a bulk-boundary correspondence: the nontrivial topological invariant of the bulk is directly linked to the appearance of a finite number of boundary states.

Although symmetry breaking is not responsible for a topological phase transition, symmetry still plays an important role: it defines the type and the presence of a topological invariant. The relevant symmetries for topology in condensed matter systems are chiral (or sublattice) symmetry, particle-hole symmetry and time-reversal symmetry. The presence or absence of either of these symmetries classifies a system into one of the ten distinct symmetry classes as specified by Altland and Zirnbauer [21], and together with the dimension of the system, it determines the topological invariant [22, 23]. For example, the quantum Hall effect has dimension two and has none

of the three symmetries. This classifies the quantum Hall effect in symmetry class A, and it has a $\mathbb{Z}$ topological invariant: the invariant $\mathcal{Q}$ can only take integer values $\mathcal{Q} = 0, \pm 1, \pm 2, \ldots$. This topological invariant is directly connected to the presence of edge states at the boundary of a quantum Hall material: the invariant equals the number of edge states, and hence conductance through a quantum Hall system is quantized in integer units of the conductance quantum G_0.

Another, more recent example of topological phases of matter are Majorana wires. Majorana wires are one-dimensional wires with particle-hole symmetry, and no time-reversal or chiral symmetry (class D). The Majorana wire has a $\mathbb{Z}_2$ invariant: it can only assume the values $\mathcal{Q} = \pm 1$. Hence, the Majorana wire is either topologically trivial ($\mathcal{Q} = 1$), or non-trivial ($\mathcal{Q} = -1$), with, in the latter case, a single pair of Majorana edge states present at the endpoints of the wire. These Majorana states have two properties that make them an attractive qubit candidate in quantum computing. First, Majorana states store quantum information (the occupation of a pair of Majorana states that forms one fermionic mode) nonlocally, making the quantum state less sensitive to errors. Second, Majorana states obey non-Abelian statistics (interchanging two Majorana states has a nontrivial effect on their wave functions), allowing to perform quantum operations by braiding two Majorana states. Since the appearance of Majorana states is directly linked to the topology of the host material, quantum computations with Majorana states are an example of topological quantum computation.

1.3. MAJORANA STATES

Historically, Majorana states were known as elementary particles, not as a consequence of bulk topology in solid state materials. In 1930, Dirac stated with his Dirac equation that every elementary particle with positive energy must have an anti-particle with the same, but negative energy [24]. Seven years later, Majorana published a solution to the Dirac equation for which particle and anti-particle are the same, and consequently have zero energy [25]. These Majorana fermions never were observed as elementary particles, but in the 1990s Moore and Read [26] and Volovik [27] discovered that Majorana states can appear as quasi-particles in condensed matter. However, the physical systems they proposed to create these Majorana quasi-particle states are hard to construct and control experimentally. Therefore, creation and observation of Majorana states remained challenging.

1.3.1. KITAEV CHAIN

This situation changed with the introduction of Kitaev's model in 2001 [10], the simplest fermionic system that can host Majorana states. It consists of a one-dimensional tight-binding chain of spinless electrons with p-wave superconducting pairing, described by a Hamiltonian

$$H = -\mu \sum_{i=1}^{N} \left(a_i^\dagger a_i - \frac{1}{2} \right) + \sum_{i=1}^{N-1} -t \left(a_i^\dagger a_{i+1} + a_{i+1}^\dagger a_i \right) + \Delta a_i a_{i+1} + \Delta^* a_{i+1}^\dagger a_i^\dagger, \quad (1.1)$$

where the chain has N sites, a chemical potential μ, a hopping amplitude t, a p-wave superconducting pairing $\Delta = |\Delta|e^{i\varphi}$ (with φ the superconducting phase), and $a^\dagger, a$ are fermion creation and annihilation operators respectively. The fermionic creation and annihilation operators are written in terms of Majorana operators by the transformation

$$\gamma_{2i-1} = e^{i\varphi/2}a_i + e^{-i\varphi/2}a_i^\dagger, \tag{1.2}$$

$$\gamma_{2i} = -ie^{i\varphi/2}a_i + ie^{-i\varphi/2}a_i^\dagger, \tag{1.3}$$

with $j = 1, ..., N$. Majorana operators differ from conventional creation and annihilation operators as they satisfy $\gamma_{2i-1}^\dagger = \gamma_{2i-1}$, $\gamma_{2i}^\dagger = \gamma_{2i}$. Now, we write down the Hamiltonian (1.1) in terms of the Majorana operators (1.2) and (1.3):

$$H = \frac{i}{2}\sum_{i=1}^{N} -\mu\gamma_{2i-1}\gamma_{2i} + (t + |\Delta|)\gamma_{2i}\gamma_{2i+1} + (-t + |\Delta|)\gamma_{2i-1}\gamma_{2i+2}. \tag{1.4}$$

We consider two special parameter choices for this Hamiltonian. When $|\Delta| = t = 0$ and $\mu < 0$, Eq. (1.4) simplifies to

$$H = \frac{i}{2}(-\mu)\sum_{i=1}^{N}\gamma_{2i-1}\gamma_{2i} = -\mu\sum_{i=1}^{N}\left(a_i^\dagger a_i - \frac{1}{2}\right). \tag{1.5}$$

In this case, two Majorana operators from the same site i are paired together to form one normal fermion, as depicted in Fig. 1.1(a). However, if we instead choose $|\Delta| = t > 0$ and $\mu = 0$, Eq. (1.4) reduces to

$$H = it\sum_{i=1}^{N-1}\gamma_{2i}\gamma_{2i+1}. \tag{1.6}$$

This choice of parameters couples two Majorana operators from *different* fermionic sites, i.e. a Majorana operator at site i is coupled to a Majorana operator at site $i+1$. This situation leaves the first and the last Majorana operator of the chain γ_1 and γ_{2N} unpaired, see Fig. 1.1(b). Since these two operators are absent from Eq. (1.6), the corresponding fermionic state, constructed from both Majorana operators at both edges, has zero energy. Thus, choosing parameters $|\Delta| = t > 0$, $\mu = 0$ results in a Kitaev chain with two uncoupled, zero-energy Majorana states at the edges.

1.3.2. SYMMETRY AND TOPOLOGY IN THE KITAEV CHAIN

The example of the Kitaev chain demonstrates that Majorana states can appear as decoupled quasi-particles at the endpoints of a chain of normal fermions. But the parameter choice $|\Delta| = t > 0, \mu = 0$ is highly specific, raising the concern that uncoupled Majorana states only appear in precisely tuned systems. However, this is not the case: Majorana states persist for all μ as long as $|\mu| \lesssim 2t$, and will disappear only when $|\mu| > 2t$, or when the bulk superconducting gap Δ is closed. This observation can be understood from the viewpoint of symmetry: since the Kitaev chain is superconducting, it has a particle-hole symmetry, meaning that the exchange

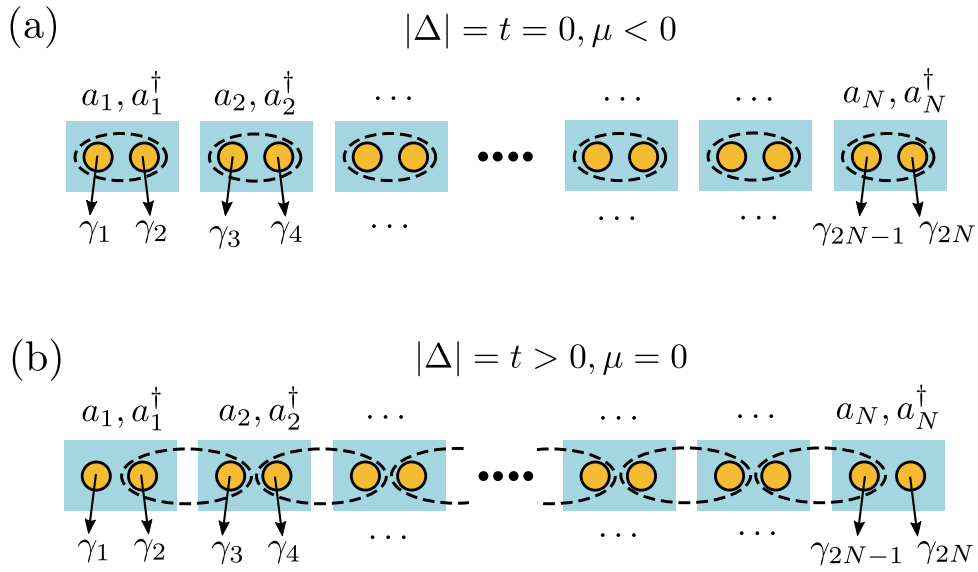

Figure 1.1: The Kitaev chain, consisting of fermionic sites (blue boxes) with creation and annihilation operators $a_i^\dagger, a_i$ for site i ($i = 1, \ldots, N$), each of which is decomposed into two Majorana operators $\gamma_{2i-1}, \gamma_{2i}$ (yellow dots). The dashed ovals denote the coupling between pairs of Majorana operators. (a): For $|\Delta| = t = 0, \mu < 0$, two Majorana operators of *the same* fermionic site couple. (b): For $|\Delta| = t > 0, \mu = 0$, Majorana operators of *different, adjacent* sites couple, leaving two Majorana operators at the chain edges γ_1, γ_{2N} uncoupled.

of particle states and hole states leaves the Kitaev Hamiltonian unchanged. Since a particle-hole symmetric energy spectrum must be symmetric around $E = 0$, a Majorana state at zero energy can not split off to higher energies, because this breaks the system's particle-hole symmetry. Hence, as long as the system obeys particle-hole symmetry, or equivalently, has a finite bulk superconducting gap, Majorana states are persistently bound to zero energy.

Alternatively, the appearance of Majorana states at the edges of the Kitaev chain can be understood from the topology of the chain. When $|\mu| > 2t$, the system is gapped and topologically trivial, so no edge states appear. For $\mu = 2t$, the bulk gap of the chain is closed, and the system goes through a topological phase transition, changing the bulk topological invariant. As a consequence, Majorana states appear at the edges of the chain, at the boundary of the topological system and the trivial surroundings.

To quantify this, we compute the topological invariant of an infinite Kitaev chain with a translationally invariant Hamiltonian in momentum space representation, $H = H(k)$, with k the momentum. Because of the particle-hole symmetry of H, we can write it in an antisymmetric form, $H^T = -H$. In this form, we can compute the Pfaffian of the Hamiltonian $\mathrm{Pf}[H]$. The Pfaffian is a mathematical expression defined for any antisymmetric matrix. Using the Pfaffian, we compute the topological

invariant $\mathcal{Q}$ as: [28]

$$\mathcal{Q} = \text{sign}\left(\text{Pf}[iH(k=0)]\text{Pf}[iH(k=\pi)]\right), \tag{1.7}$$

with $k = 0$ the center of the Brillouin zone, and $k = \pi$ the edge of the Brillouin zone. Writing the Hamiltonian Eq. (1.4) in momentum space representation, and computing the topological invariant using Eq. (1.7) results in

$$\mathcal{Q} = \begin{cases} +1, & \text{for } |\mu| > 2t \\ -1, & \text{for } |\mu| < 2t. \end{cases} \tag{1.8}$$

In other words, the Kitaev chain is topologically trivial for $|\mu| > 2t$, and topologically nontrivial for $|\mu| < 2t$. The topology argumentation agrees with our observation from the symmetry perspective, but it considers band structure properties rather than symmetry constraints on individual Majorana states. Hence, the topological description is more powerful, since it computes topological properties and the corresponding appearance of edge states systematically from the bulk Hamiltonian instead of relying on fine-tuning parameters of the Kiteav chain.

1.3.3. CREATING MAJORANA STATES IN SOLID STATE DEVICES

The Kitaev chain of Ref. [10] demonstrates how to create Majorana states with normal fermions, but it offers no path to experimental realization. The Kitaev model requires spinless electrons, while in practice electrons carry a spin. Furthermore, the model requires special p-wave superconductivity, forming Cooper pairs of electrons of the same spin, such that the spin degree of freedom can be ignored. However, p-wave superconductors are exotic and not reliable to work with in experiments. In the years after Kitaev's proposal, several other proposals were made to realize Majorana states in experimentally feasible systems, such as using the $\nu = 5/2$ fractional quantum Hall state [26] as topological qubits [9], the combination of a topological insulator with a conventional s-wave superconductor [29], or a two-dimensional topological insulator in combination with a conventional superconductor and ferromagnetic leads [30]. However, all these proposals are still challenging to realize in experiments.

A theoretical breakthrough came in 2010, when a model was developed that combined the necessary ingredients to create effective p-wave superconductivity with experimentally accessible components [11, 12]. The setup of this system is sketched in Fig. 1.2. A semiconducting nanowire is deposed on a superconducting layer, which induces superconductivity in the nanowire, and a magnetic field is applied parallel to the wire. This leads to an effective Hamiltonian

$$H = \left(\frac{\hbar^2 k^2}{2m} - \mu\right)\sigma_0\tau_z - \alpha k \sigma_y \tau_z + E_{\text{Z}}\sigma_x\tau_0 + \Delta\sigma_0\tau_x. \tag{1.9}$$

Here, k is the momentum along the wire in the x-direction, m the effective electron mass in the semiconductor, μ the chemical potential, α the spin-orbit interaction (SOI) strength, $E_{\text{Z}} = \frac{1}{2}g\mu_{\text{B}}B$ the Zeeman energy with g the Landé g-factor, μ_{B} the Bohr magneton, B the magnetic field, and finally, Δ is the superconducting gap. The

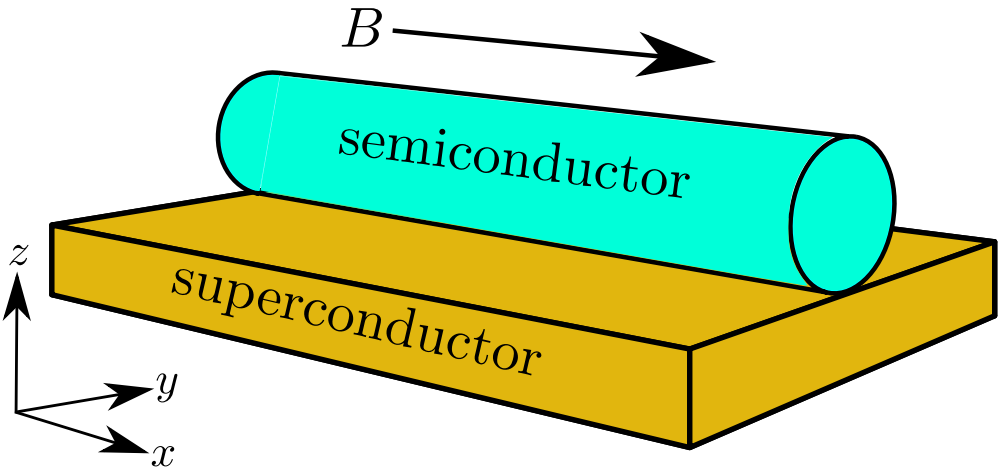

Figure 1.2: Setup of the system proposed by Refs. [11, 12] to create Majorana states with experimentally accesible components. It consists of a semiconducting nanowire with spin-orbit interaction on top of a superconducting layer, which proximitizes the nanowire. A magnetic field B is applied parallel to the nanowire.

matrices σ_i and τ_i, with $i = 0, x, y, z$, denote the identity/Pauli matrices that act in spin space and particle-hole space respectively.

The first term of Eq. (1.9), $(\hbar k)^2/2m - \mu$, describes a semiconducting wire with chemical potential μ. A semiconducting material is favourable, since it has a chemical potential close to the band bottom, a large level spacing, and hence a low electron density, which makes a semiconductor highly tunable. The dispersion of this term for $\mu > 0$ is sketched in Fig. 5.10(a): two spin-degenerate parabolic bands of opposite sign for electrons and holes, crossing at $E = 0$.

The second term, $-\alpha k \sigma_y$, describes Rashba SOI, the coupling of an electron's motion in an external electric field to the electron spin [31]. The motion of an electron in an electric field $\vec{E}$ generates a magnetic field perpendicular to both the direction of motion and the field: $\vec{B}_{\text{SO}} \propto \vec{k} \times \vec{E}$. The effective magnetic field $\vec{B}_{\text{SO}}$ couples to the electron spin and introduces a momentum-dependent term to the Hamiltonian, $H_{\text{SO}} \propto \vec{\sigma} \cdot \vec{B}_{\text{SO}} \propto \vec{\sigma} \cdot (\vec{k} \times \vec{E})$, with $\vec{\sigma}$ a vector with Pauli matrices. Since $\vec{k} = (k, 0, 0)$ in a one-dimensional wire and we assume an electric field in the z-direction, $\vec{E} = (0, 0, |E|)$, we rewrite the SOI Hamiltonian H_{SO} as $H_{\text{SO}} = -\alpha k \sigma_y$. The Rashba parameter α depends both on the electric field strength $|E|$ and on material parameters. The effect of Rashba SOI is sketched in Fig. 5.10(b). The spin bands shift in opposite directions, since both spins experience an opposite spin-orbit field B_{SO}.

SOI splits the spin bands, but it is not sufficient to create effective p-wave superconductivity. The system is time-reversal symmetric, $E_\uparrow(k) = E_\downarrow(-k)$, hence it has a Kramer's degeneracy: at every energy E there are two states present with opposite spin and opposite momentum. If the system is time-reversal symmetric, it is impossible to create a single local Majorana state, since states always come in pairs

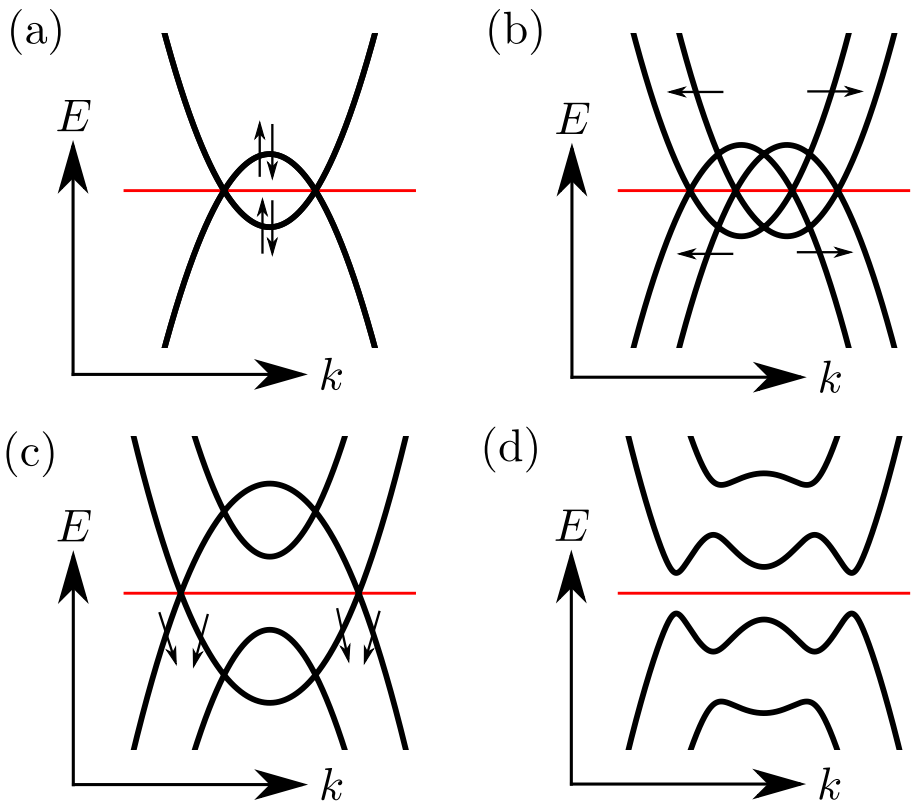

Figure 1.3: Dispersions of energy levels E as a function of momentum k of a semiconductor with various additional terms in the Hamiltonian. In all plots, the horizontal red line indicates the Fermi energy. Arrows indicate the spin direction of the corresponding energy band. (a): Dispersion of a semiconductor with $\mu > 0$, resulting in electron and hole states of both spin types at $E = 0$. (b) Same as in (a), but with added SOI ($\alpha > 0$): the dispersions of electrons and holes are split in k-space according to their spins. Spins rotate proportional to corresponding momentum k. (c): Same as in (b), but with an applied magnetic field along the wire E_Z. Spins align or anti-align to the Zeeman field. One spin band increases in energy, the other spin band decreases. This results in a single spin type at Fermi energy. (d): Same as in (c), but with a superconducting gap $\Delta > 0$. The Cooper pairs formed around the Fermi energy have the same spin, hence the superconducting pairing is effectively p-wave.

due to Kramer's degeneracy. To break time-reversal symmetry, the next ingredient of Eq. (1.9) is a parallel magnetic field B, resulting in the Zeeman term E_Z, which splits both spin bands. Since B and B_{SO} are perpendicular, spin conservation is broken, and hence eigenstates of the corresponding Hamiltonian do not have a definite spin, which is crucial to create effectively spinless Majorana states. For sufficiently strong magnetic fields, $E_Z > \mu$, the chemical potential is tuned into an effectively spin-polarized regime, see Fig. 5.10(c).

Finally, the superconducting term $\Delta\tau_x$ couples the electron- and hole bands and introduces particle-hole symmetry: for every particle-like excitation state in the spec-

trum, there is a hole-like excitation state at opposite energy. The superconductivity is of p-wave type, since Cooper pairs at $E = 0$ are formed from the same spin bands. Hence, this Hamiltonian combines all necessary ingredients for Majorana states: a highly tunable semiconducting nanowire, SOI that breaks spin conservation, a magnetic field that breaks Kramer's degeneracy and superconductivity that makes the spectrum particle-hole symmetric.

The Hamiltonian Eq. (1.9) realizes an effective p-wave superconductor, and its topological phase depends on the choice of the parameters μ, α, B, Δ, similar to the Kitaev chain parameters μ, Δ, t. Again, the topological phase can be determined from the Pfaffian Pf$(H(k))$, but a physically more insightful way is to study how the parameters affect the band gap at $k = 0$. For $E_{\mathrm{Z}} = 0$, the Hamiltonian has a gap Δ and is topologically trivial, since it is time-reversal symmetric. For $E_{\mathrm{Z}} > 0$, the Hamiltonian will stay gapped at $k > 0$ due to the finite SOI term. For $k = 0$, Eq. (1.9) reduces to

$$H(k = 0) = -\mu\sigma_0\tau_z + E_{\mathrm{Z}}\sigma_x\tau_0 + \Delta\sigma_0\tau_x, \tag{1.10}$$

which is diagonalized as

$$E(k = 0) = \pm E_{\mathrm{Z}} \pm \sqrt{\mu^2 + \Delta^2}. \tag{1.11}$$

The gap closes for $E_{\mathrm{Z}} = \sqrt{\mu^2 + \Delta^2}$, which marks the topological phase transition. For $E_{\mathrm{Z}} > \sqrt{\mu^2 + \Delta^2}$, the gap reopens because of the SOI, which prevents any spin band to cross at $k > 0$. Since the size of the topological gap increases for increasing SOI strength α, having a semiconductor with strong SOI is crucial to create well-protected Majorana states.

1.3.4. EXPERIMENTS ON MAJORANA DEVICES

Experiments to demonstrate the presence of Majorana states first have been performed in hybrid semiconductor-superconductor nanowire devices, but in recent years various other experimental platforms have been fabricated and measured. Examples of these alternative devices are chains of magnetic atoms deposited on a superconducting substrate [32, 33], quantum wires made of topological insulators [34], and two-dimensional heterostructures of topological insulators and superconductors [35, 36].

However, semiconducting nanowires with induced superconductivity are the most used Majorana platforms, because these devices are relatively easy to fabricate and control. The first experiments on Majorana states were performed in a slightly modified version of the setup as shown in Fig. 1.2. Since a superconducting layer underneath the wire causes screening effects, electrostatic control of the wire is difficult. Therefore, in these experiments the superconductor has been attached from the sides, and electrostatic gates, separated from the nanowire by a dielectric layer, control the chemical potential in the wire, see Fig. 1.4. The electrostatic back gates create tunnel barriers and allow, in combination with a connection to normal metallic leads, to perform tunnelling spectroscopy on the Majorana wire. This setup probes the density of states in the nanowire, which is a superconducting density of states with a gap of 2Δ centered at $E = 0$ in absence of Majorana states. In presence of

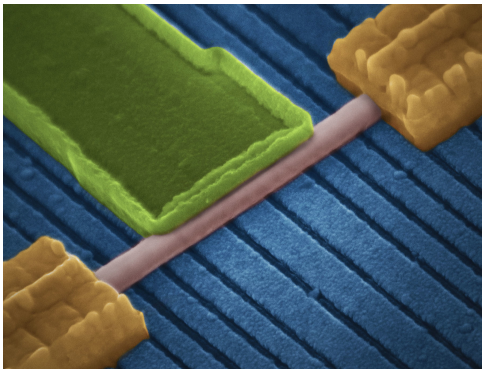

Figure 1.4: Colored scanning electron microscope image of a hybrid semiconductor-superconductor device as used in the first Majorana experiments. The InSb nanowire, pink, is connected from one side to a NbTiN superconductor (green) which proximitizes the nanowire. The metallic contacts on both sides of the wire (yellow) are used to perform tunnelling spectroscopy. Tunnel barriers and the chemical potential in the nanowire are adjusted with back gates (blue). Image courtesy of V. Mourik and K. Zuo.

Majorana states, the density of states shows a zero bias conductance peak, ideally with a quantized value of $2e^2/h$.

In 2012, several experimental groups reported zero-bias conductance peaks in these devices [13–15]. These experiments provided evidence of Majorana states, but several issues remained: the zero-bias conductance peak does not have a robust quantized value of $2e^2/h$ as theory predicts [37, 38], but is an order of magnitude smaller. Also, the induced superconducting gap is weak: the density of states inside the induced gap is reduced by less than one order of magnitude compared to the density outside the gap. This results in dissipation of the Majorana states, which, together with disorder in the nanowire, strongly reduces the topological protection of these states. Disorder and dissipation also leave room for alternative explanations of zero-bias conductance peaks, such as Kondo physics [39] or weak anti-localization [40]. In recent years, the experiments have seen progress mostly in material development and experimental fabrication techniques. This has resulted in clean, ballistic nanowire with a minimum of disorder-induced subgap states [41, 42], and strong induced superconductivity due to epitaxially-grown superconducting shells [43–46]. Subsequently, measurements of a quantized zero-bias conductance peak have been reported [47].

These developments in reducing disorder and dissipation make many explanations alternative to the presence of Majorana states unlikely. However, an alternative which is still indistinguishable from Majorana states by current experimental techniques, quasi-Majorana states trapped by smooth potential barriers [48, 49], is the focus of recent theoretical research [50–56]. Hence, distinguishing Majorana states with tunnelling spectroscopy remains challenging. Additionally, probing a zero-bias conductance peak is only a necessary condition for Majorana states, not a sufficient condition. Therefore, current experimental and theoretical work is also directed in providing sufficient proof for the existence of Majorana states. Such sufficient proof

is the measurement of a bulk topological phase transition, rather than individual Majorana states [57–60], or non-trivial braiding properties of Majorana states, proving their non-Abelian braiding characteristics [61–68]. Experimental efforts to perform braiding operations are directed to networks of one-dimensional nanowires [45], or patterned networks in two-dimensional electron gasses [44, 69–71].

1.4. ELECTROSTATICS IN MAJORANA DEVICES

The combination of electrostatics and Majorana physics has a surprising effect: smooth electrostatic potentials give rise to non-trivial quasi-Majorana states. However, the Hamiltonian Eq. (1.9) does not contain a potential term and assumes a constant chemical potential. In a realistic experimental device, see Fig. 1.4, the effective chemical potential is controlled by metallic back gates, which set the electrostatic potential. Besides the gates, other components of the device such as the dielectric layer and the superconducting contact further influence the exact shape of the potential, see Fig. 1.5. Also, charges in the nanowire lead to screening effects, which reduces the control of the back gates over the potential shape. Hence, the directly controllable, constant chemical potential of Eq. 1.9 is not realistic. In this section, we discuss the Schrödinger-Poisson equation, which describes electrostatics of a Majorana wire, and the Thomas-Fermi approach to Majorana electrostatics.

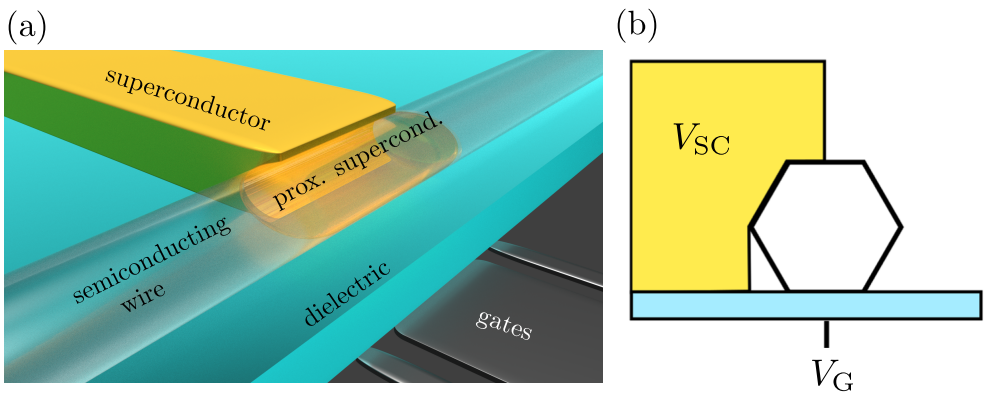

Figure 1.5: (a): Setup of a realistic Majorana device. A superconductor proximitizes part of a semiconducting wire from the side. Electrostatic back gates control the chemical potential in the nanowire. A dielectric layer separates the wire from the gates to avoid a short circuit. (b): Schematic of a 2D cross-section of the Majorana device. The setup has two electrostatic boundary conditions: a voltage V_G is applied to the lower edge of the dielectric layer simulating a back gate, and a voltage V_{SC} is applied to the superconducting lead.

1.4.1. THE SCHRÖDINGER-POISSON PROBLEM

The electrostatics of a Majorana device is governed by the Schrödinger-Poisson equation [72, 73]. This equation describes the electrostatic potential of a quantum system by the Poisson's equation, where the charge density term of the equation is

constructed from the wave functions and energies of the quantum system. The wave functions and energies are computed by solving the Schrödinger equation, where the Hamiltonian contains an electrostatic potential term. Hence, the Schrödinger-Poisson equation is a coupling between the Schrödinger and the Poisson equation, where the coupling terms generally are nonlinear.

To solve the Schrödinger equation including electrostatics, we assume an infinite, translationally invariant Majorana wire, such that the Hamiltonian is separable in a longitudinal and a tranverse part. We start from a slightly modified version of the Hamiltonian of Eq. (1.9):

$$H = \left(-\frac{\hbar^2}{2m}\nabla^2 - e\phi(y,z) + \frac{1}{2}E_{\text{gap}}\right)\sigma_0 - i\alpha\frac{\partial}{\partial x}\sigma_y + E_{\text{Z}}\sigma_x, \tag{1.12}$$

with e the electron charge, E_{gap} the semiconducting band gap and $\phi(y,z)$ the electrostatic potential, which only varies in the $y-$ and $z-$direction, since it describes a translationally invariant system. We neglect the superconducting term Δ, since it is only a small perturbation to the Hamiltonian and will have a negligible effect on the charge density. We split the Hamiltonian into a transverse Hamiltonian in the y,z-direction

$$H_{\text{T}} = -\frac{\hbar^2}{2m}\left(\frac{\partial^2}{\partial y^2} + \frac{\partial^2}{\partial z^2}\right) - e\phi(y,z) + \frac{1}{2}E_{\text{gap}}, \tag{1.13}$$

and a longitudinal Hamiltonian in the x-direction

$$H_{\text{L}} = -\frac{\hbar^2}{2m}\left(\frac{\partial^2}{\partial x^2}\right) - i\alpha\frac{\partial}{\partial x}\sigma_y + E_{\text{Z}}\sigma_x. \tag{1.14}$$

Here, we assume that the SOI strength α does not depend on the electrostatic potential ϕ. The separation of the Hamiltonian allows to separately solve the transverse Hamiltonian H_{T} for its discrete energy levels E_i with $i = 0, 1, 2, \ldots$, and wave functions ψ_i.

With the separable Hamiltonian (1.12), the charge density is

$$\rho(y,z) = -e\sum_{E_i<E_{\text{F}}} |\psi_i(y,z)|^2 n(E_i, E_{\text{Z}}, \alpha), \tag{1.15}$$

which sums the transverse probability density $|\psi_i|^2$ of the i-th mode, multiplied by the electron density of the mode $n(E_i, E_{\text{Z}}, \alpha)$, over all occupied electron levels below the Fermi level E_{F}. The electron density $n(E_i, E_{\text{Z}}, \alpha)$ follows from integrating the 1D density of states $g(E, E_i, E_textZ, \alpha)$ up to the Fermi energy:

$$n(E_i, E_{\text{Z}}, \alpha) = \int_{-\infty}^{E_{\text{F}}} g(E, E_i, E_{\text{Z}}, \alpha)dE, \tag{1.16}$$

where $g(E, E_i, E_{\text{Z}}, \alpha)$ is given by

$$g(E, E_i, E_{\text{Z}}, \alpha) = \frac{1}{\pi}\frac{dk(E, E_i, E_{\text{Z}}, \alpha)}{dE}. \tag{1.17}$$

The momentum k is obtained from writing the Hamiltonian (1.12) in a momentum space representation, where the transverse part of the Hamiltonian, Eq. (1.14), only enters via the discrete energies E_i. Inverting the momentum-dependent energy $E(k, E_i, E_Z, \alpha)$ corresponding to this Hamiltonian to an expression for momentum $k(E, E_i, E_Z, \alpha)$ and inserting this in Eq. (2.26), results in an analytical expression for $g(E, E_i, E_Z, \alpha)$.

The Poisson equation, describing the electrostatic potential $\phi(y, z)$, is given by

$$\nabla^2 \phi(y, z) = -\frac{\rho(y, z)}{\epsilon}, \tag{1.18}$$

with ϵ the dielectric permittivity. Equation (3.1) contains the charge density function $\rho(y, z)$, given by Eq. (1.16). As boundary conditions, we put a fixed potential V_G on the lower boundary of the dielectric layer where the back gate is situated, see Fig. 1.5(b)), and a fixed potential V_{SC} in the superconducting region.

Since solving Eq. (1.16) requires the diagonalization of the Hamiltonian Eq. (1.14), and this Hamiltonian in turn depends on the electrostatic potential ϕ, the Schrödinger equation (1.14) and the Poisson equation (3.1) are coupled nonlinearly. We arrive at the coupled nonlinear Schrödinger-Poisson equation for electrostatics in quantum systems:

$$\begin{cases} \nabla^2 \phi(y, z) = -\rho(\psi(y, z), E)/\epsilon, \\ \\ H[\phi(y, z)]\psi(y, z) = E\psi(y, z) \end{cases} . \tag{1.19}$$

Because of the nonlinear coupling between the Schrödinger and Poisson equation, an analytical solution can only be obtained for very simple Hamiltonians and geometries. Solving Eq. 1.19 for the geometry of Fig. 1.5(b) requires numerical methods. This implies discretizing the Hamiltonian (1.14) and solving the resulting linear system of equations. In this work, we use the tight-binding (or Finite Difference) approach to discretize and solve the Hamiltonian, for which we use the Kwant package for Python [74]. We discretize and solve the Poisson equation in the 2d cross-section of Fig. 1.5(b) using a Finite Element Method [75].

The solution of the Schrödinger equation (1.14), together with Eq. (1.16), form a functional $\bar{\rho}[\phi]$, while the Poisson equation defines a functional $\bar{\phi}[\rho]$. The Schrödinger-Poisson problem is solved self-consistently if

$$\bar{\phi}[\bar{\rho}[\phi]] - \phi = 0. \tag{1.20}$$

The numerical approach to solve Eq. (1.20) is drawn schematically in Fig. 1.6. Starting from an initial guess of the electrostatic potential, ϕ_{init}, both numerical Schrödinger solver and Poisson solver are called iteratively, until the norm of the difference between to subsequent iteration steps $|F|$ is smaller than some tolerance τ. In the simplest approach of this iteration scheme, the outcome of the previous iteration step ϕ_i is directly used as an input to the next iteration step in order to compute ϕ_{i+1}. However, various algorithms construct a more optimal input potential from one or more previous iteration steps in order to speed up the process [76].

The nonlinear coupling and singularities in the density of states function $g(E)$ for 1D systems make the Schrödinger-Poisson problem complicated to solve. An

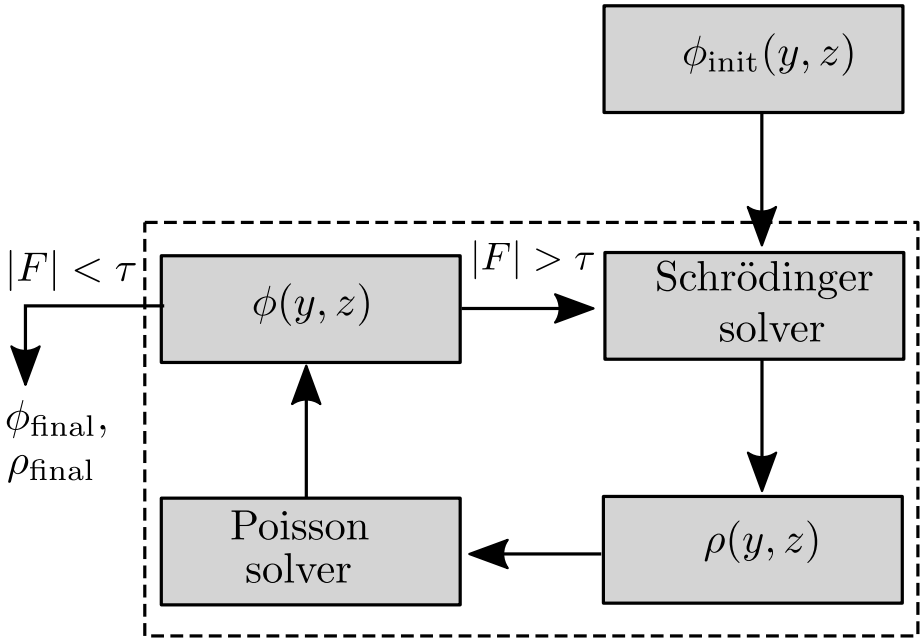

Figure 1.6: Nonlinear optimization scheme for the Schrödinger-Poisson problem. An initial guess, ϕ_{init}, is feed to the Schrödinger solver, which constructs the charge density ρ from the wave functions and energies of the diagonalized Hamiltonian. With this charge density, the Poisson equation is solved, resulting in a new estimate of the potential ϕ. This process is continued until the error between two subsequent steps, $|F|$, is smaller than some tolerance τ.

alternative is the Thomas-Fermi approach, a simpler, semiclassical approach to solve electrostatics in quantum systems [77, 78]. The Thomas-Fermi method constructs ρ from the 3D density of states, instead of solving the Schrödinger equation, thus disregarding wave functions and quantized energy levels. Quantum effects only enter via Fermi statistics: only two electrons of opposite spin can occupy a certain momentum state, and electron levels are filled up to the Fermi level.

The Thomas-Fermi method starts from the 3D electron density

$$n = 2 \times \frac{\frac{4}{3}\pi k_{\text{F}}^3}{(2\pi)^3} = \frac{\pi k_{\text{F}}^3}{3\pi^3}, \tag{1.21}$$

where k_{F} is the Fermi momentum and the factor of 2 counts the spin degeneracy of the momentum states. To find k_{F}, we consider the classical energy for an electron of momentum k_{F}, consisting of a kinetic term and a potential term:

$$E_{\text{F}} = \frac{\hbar^2 k_{\text{F}}^2}{2m} - e\phi(\vec{x}), \tag{1.22}$$

which we can invert to find the Fermi momentum:

$$k_{\text{F}} = \left(\frac{2m}{\hbar^2}\left(E_{\text{F}} + e\phi(\vec{x})\right)\right)^{1/2}. \tag{1.23}$$

Inserting Eq. (1.23) into Eq. (1.21) and writing the charge density $\rho(\vec{x}) = -en$, we find

$$\rho(\vec{x}) = -\frac{e}{3\pi^2}\left(\frac{2m}{\hbar^2}\left(E_{\mathrm{F}} + e\phi(\vec{x})\right)\right)^{3/2}. \tag{1.24}$$

This is the Thomas-Fermi approximation to the charge density in quantum systems. Taking E_{F} is zero, and inserting Eq. (1.24) into the Poisson equation Eq. (3.1), the equation that is solved in the Thomas-Fermi method for the translationally invariant 1D wire reads

$$\nabla^2\phi(y,z) = \frac{e}{3\pi^2\epsilon}\left(\frac{2me\phi(y,z)}{\hbar^2}\right)^{3/2}. \tag{1.25}$$

Equation (1.25) is a nonlinear partial differential equation, but it is continuous and not coupled to a second equation as in the Schrödinger-Poisson problem, and therefore it is generally much easier to solve numerically. Also, obtaining the charge density of Eq. 1.15 requires integration, which is a numerically demanding operation in particular for 3D systems or for complicated Hamiltonians. As a disadvantage, the Thomas-Fermi method does not capture quantum effects such as a Zeeman splitting of energy levels or spin-orbit interaction, or effects related to the 1D density of states, such as Van Hove singularities.

In Chapter 2, we specifically investigate the effects of Van Hove singularities and Hamiltonian terms such as SOI and Zeeman energy. Therefore, we apply the Schrödinger-Poisson method to a translationally invariant Majorana wire. In Chapter 3, we compute conductance through a finite 3D Majorana wire. Hence, we apply the Thomas-Fermi method to avoid the numerical complexity of solving Schrödinger-Poisson in 3D systems. In Chapters 4 and 5, we do not focus on detailed modelling of the electrostatics, and therefore we use analytic potential functions in the simulations of these chapters.

1.5. QUASI-MAJORANA STATES

Shortly after the first Majorana experiments, Ref. [48] demonstrated that smooth confinement potentials can create near-zero energy Andreev bound states or quasi-Majorana states in the topologically trivial state of the Majorana device. The initial focus of Majorana experiments was to improve on problems with disorder and dissipation, and the improvements in this direction have ruled out most alternative explanations to the Majorana description of the measured conductance characteristics. However, in the resulting clean and ballistic nanowires, the presence of smooth potentials with quasi-Majorana states has become more likely. Hence, recent theoretical research is focused on quasi-Majorana states [50–56]. Our modelling of electrostatics in 3D devices confirms that smooth confinement potentials on the length scale of the SOI length $l_{\mathrm{SO}} = \hbar^2/m\alpha$ are commonly appearing in Majorana devices.

To investigate properties of quasi-Majorana states, we calculate the low-energy spectrum of a 1D Majorana wire in presence of a smooth confinement potential. We

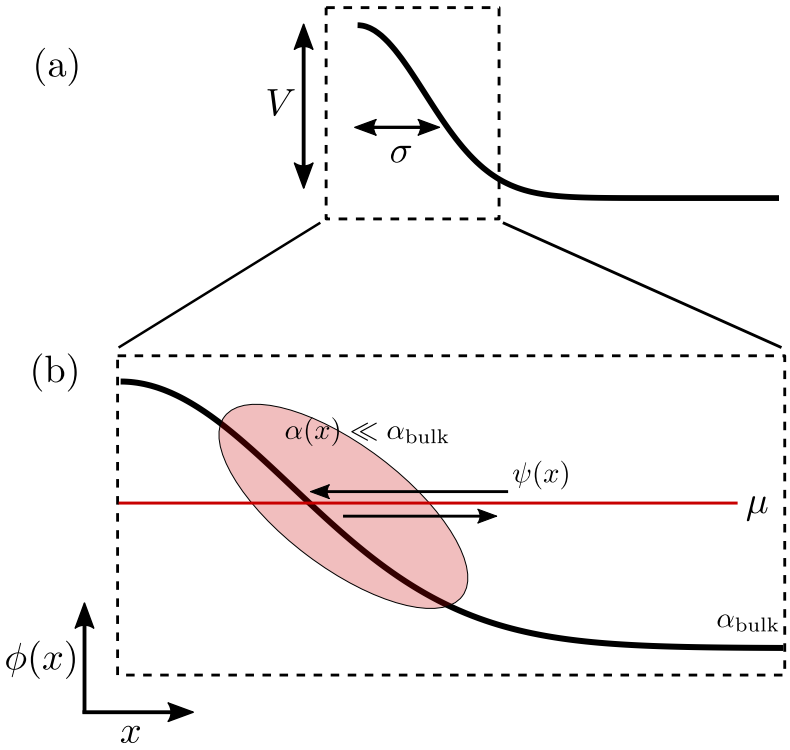

Figure 1.7: (a): Profile of a 1D potential barrier $\phi(x)$, modelled as a Gaussian of smoothness σ and height V. (b): Effect of the barrier on a wave function $\psi(x)$ with a chemical potential $\mu < V$. In a semiclassical approach, the wave function has a classical turning point at $\phi(x) = \mu$ (red line), where the momentum, and hence the space-dependent SOI $\alpha(x)$, becomes negligible compared to the bulk momentum and bulk SOI strength α_{bulk}. A smooth slope creates a large region of negligible SOI, as indicated by the red area.

start from a Hamiltonian similar to Eq. (1.9):

$$H = \left(\frac{\hbar^2 k^2}{2m} - \mu + \phi(x) \right) \sigma_0 \tau_z - \alpha k \sigma_y \tau_z + E_{\text{Z}} \sigma_x \tau_0 + \Delta \sigma_0 \tau_x, \tag{1.26}$$

where the potential $\phi(x)$ is modelled as a Gaussian barrier,

$$\phi(x) = V e^{-(x-x_0)^2/2\sigma^2}, \tag{1.27}$$

with V the barrier height, σ the barrier smoothness and x_0 the center of the barrier. Figure 1.7(a) shows the barrier, with its center at the left edge of a Majorana wire.

We consider a topologically trivial regime where the chemical potential is the largest energy scale, $\mu \gg E_{\text{Z}}, \Delta, \cdots$. Accordingly, the Fermi wavelength λ_{F} is the shortest length scale, and we can treat the problem quasi-classically. In a quasi-classical approach, the quasi-particle wave functions have classical turning points at the slope of the confinement potential for $\mu = \phi(x)$, see Fig. 1.7(b). At this point, the momentum, and hence the SOI strength α, vanish. For a steep confinement potential,

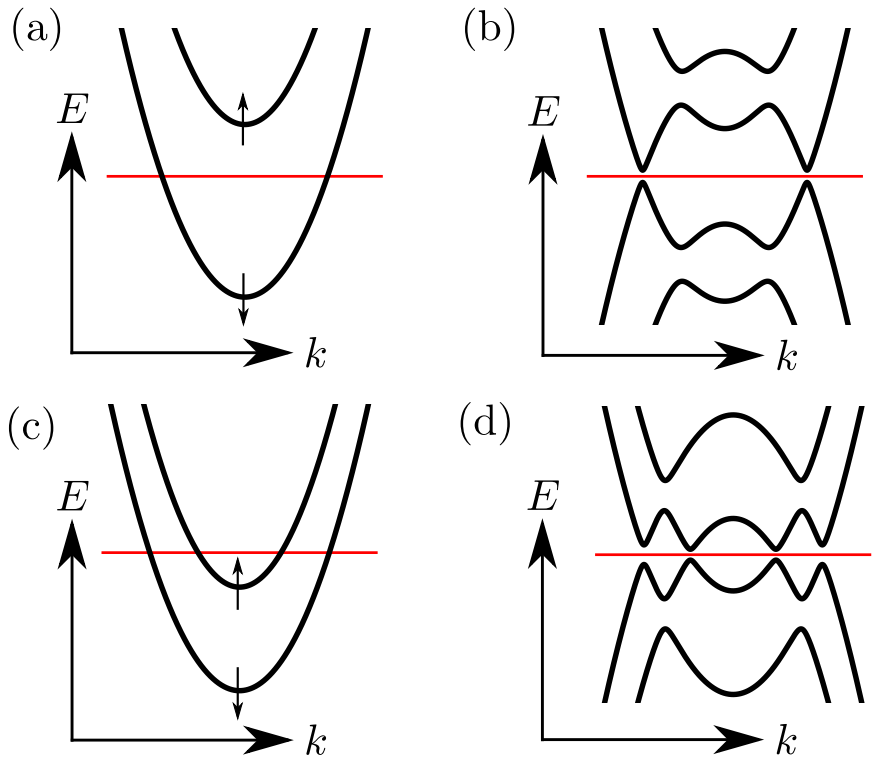

Figure 1.8: Disperions for strongly reduced SOI strength α in a topological wire with Majorana states, (a) and (b), and in a trivial wire with quasi-Majorana states, (c) and (d). (a): For $E_Z > \mu$ and $\Delta = 0$, only one spin band is below the Fermi energy (red line). (b) For nonzero Δ, a superconducting gap opens up around $E = E_F$, Cooper pairs and Majorana states are formed from the same spin band. (c): For $E_Z < \mu$ and $\Delta = 0$, two opposite spin bands are below the Fermi energy with a very weak coupling because of the small SOI. (d): For nonzero Δ, a superconducting gap opens up around $E = E_F$, Cooper pairs are formed from electrons of the same spin, but both spin species are present. The quasi-Majorana states are formed from two Majorana states from opposite spin bands, and hence have opposite spin.

the length of the region of strongly reduced SOI is small compared to the SOI length l_{SO}, and the effect on the wave functions given by the Hamiltonian of Eq. 1.26 is negligible. However, for a smooth potential, a large region of strongly suppressed SOI emerges at the slope of the confinement potential, see Fig. 1.7(b).

To investigate the effect of a suppressed SOI strength, we consider in Fig. 1.8 the dispersions in the topological regime and in the trivial regime. In absence of induced superconductivity and for $E_Z > \mu$, a single electron spin band is occupied, see Fig. 1.8(a). Turning on superconductivity, the system turns topological with two Majorana states from the same spin band, Fig. 1.8(b), where the topological gap is small because of the small SOI strength. However, for $E_Z < \mu$, both spin bands are occupied (Fig. 1.8(c)), and have a negligible coupling between the spin bands because of the small SOI strength. When turning on superconductivity, Fig. 1.8(d),

both uncoupled spin bands produce a pair of Majorana states of opposite spin at the endpoints of the 1D system. Hence, a smooth potential creates a large region of negligible SOI strength, and for $E_Z < \mu$, pairs of quasi-Majorana states of opposite spin appear at the smooth potential slope in the topologically trivial phase.

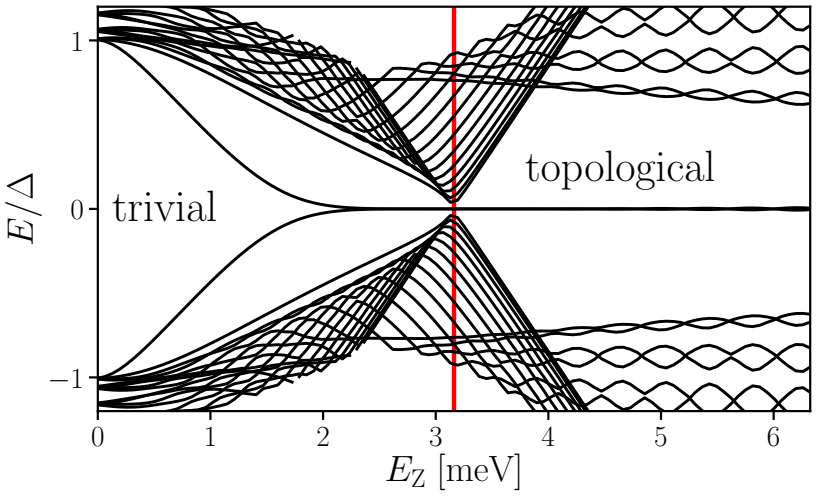

Figure 1.9: Spectrum of a Majorana wire with a smooth confinement potential. The red line indicates the topological phase transition, where the bulk gap is closed and spatially separated topological Majorana states are formed. For a range of Zeeman energies before the phase transition in the trivial phase, quasi-Majorana states are formed at zero energy.

We show the energy spectrum of a finite Majorana wire with a smooth potential slope on one side in Fig. 1.9. The figure shows the eigenenergies of the Hamiltonian (1.26) for a barrier with a smoothness of $\sigma = 200$ nm. Assuming an InSb nanowire, this is smooth on the length scale of the spin-orbit length, since we have $l_{SO} \approx 80$ nm for estimated InSb parameters $m = 0.014m_0$ and $\alpha = 70$ meVnm. The spectrum shows, as a function of Zeeman energy, a bulk gap closing and reopening at $E_Z^2 = \Delta^2 + \mu^2$, which marks the topological phase transition (red line in Fig. 1.9). In the topological phase, two Majorana states of zero energy emerge. However, a pair of quasi-Majorana states, located at the smooth potential barrier, is formed at zero energy already in the trivial phase. Because both quasi-Majorana and topological Majorana states form zero-energy bound states in the spectrum of a Majorana wire with a smooth potential, it is complicated to distinguish them in the conductance characteristics of Majorana experiments. This motivates the recent theoretical attention to quasi-Majorana states in Majorana devices.

1.6. STRUCTURE OF THIS THESIS

Chapter 2: Effects of the electrostatic environment on the Majorana nanowire devices. One of the promising platforms for creating Majorana bound states is a hybrid nanos-

tructure consisting of a semiconducting nanowire covered by a superconductor. We analyze the previously disregarded role of electrostatic interaction in these devices. Our main result is that Coulomb interaction causes the chemical potential to respond to an applied magnetic field, while spin-orbit interaction and screening by the superconducting lead suppress this response. Consequently, the electrostatic environment influences two properties of Majorana devices: the shape of the topological phase boundary and the oscillations of the Majorana splitting energy. We demonstrate that both properties show a non-universal behavior, and depend on the details of the electrostatic environment. We show that when the wire only contains a single electron mode, the experimentally accessible inverse self-capacitance of this mode fully captures the interplay between electrostatics and Zeeman field. This offers a way to compare theoretical predictions with experiments.

Chapter 3: Conductance through a helical state in an Indium antimonide nanowire.

The motion of an electron and its spin are generally not coupled. However in a one-dimensional material with strong SOI a helical state may emerge at finite magnetic fields, where electrons of opposite spin will have opposite momentum. The existence of this helical state has applications for spin filtering and Cooper pair splitter devices and is an essential ingredient for realizing topologically protected quantum computing using Majorana zero modes. Here we report electrical conductance measurements of a quantum point contact formed in an indium antimonide nanowire as a function of magnetic field. At magnetic fields exceeding 3 T, the $2e^2/h$ plateau shows a reentrant conductance feature towards $1e^2/h$ which increases linearly in width with magnetic field before enveloping the $1e^2/h$ plateau. Rotating the external magnetic field either parallel or perpendicular to the spin orbit field clearly connect this experimental signature to SOI. We compare our observations with a model of a QPC incorporating SOI and extract a spin orbit energy of ~ 6.5 meV, which is significantly stronger than the SOI energy obtained by other methods.

Chapter 4: Reproducing topological properties with quasi-Majorana states.

Andreev bound states in hybrid superconductor-semiconductor devices can have near-zero energy in the topologically trivial regime as long as the confinement potential is sufficiently smooth. These quasi-Majorana states show zero-bias conductance features in a topologically trivial phase, thereby mimicking spatially separated topological Majorana states. We show that in addition to the suppressed coupling between the quasi-Majorana states, also the coupling of these states across a tunnel barrier to the outside is exponentially different for increasing magnetic field. As a consequence, quasi-Majorana states mimic most of the proposed Majorana signatures: quantized zero-bias peaks, the 4π Josephson effect, and the tunnelling spectrum in presence of a normal quantum dot. We identify a quantized conductance dip instead of a peak in the open regime as a distinguishing feature of true Majorana states in addition to having a bulk topological transition. Because braiding schemes rely only on the ability to couple to individual Majorana states, the exponential control over coupling strengths allows to also use quasi-Majorana states for braiding. Therefore, while the appearance of quasi-Majorana states complicates the observation of topological Majorana states, it opens an alternative route towards braiding of non-Abelian anyons and topological quantum computation.

Chapter 5: Andreev rectifier: a nonlocal conductance signature of topological phase transitions.

The proximity effect in hybrid superconductor-semiconductor structures, crucial for realizing Majorana edge modes, is complicated to control due to its dependence on many unknown microscopic parameters. In addition, defects can spoil the induced superconductivity locally in the proximitised system which complicates measuring global properties with a local probe. We show how to use the nonlocal conductance between two spatially separated leads to probe three global properties of a proximitised system: the bulk superconducting gap, the induced gap, and the induced coherence length. Unlike local conductance spectroscopy, nonlocal conductance measurements distinguish between non-topological zero-energy modes localized around potential inhomogeneities, and true Majorana edge modes that emerge in the topological phase. In addition, we find that the nonlocal conductance is an odd function of bias at the topological phase transition, acting as a current rectifier in the low-bias limit. More generally, we identify conditions for crossed Andreev reflection to dominate the nonlocal conductance and show how to design a Cooper pair splitter in the open regime.

REFERENCES

[1] A. Ekert and R. Jozsa, *Quantum computation and Shor's factoring algorithm,* Rev. Mod. Phys. **68**, 733 (1996).

[2] L. K. Grover, *A fast quantum mechanical algorithm for database search,* Proceedings of the 28th Annual ACM Symposium on the Theory of Computing , 212 (1996).

[3] P. W. Shor, *Polynomial-Time Algorithms for Prime Factorization and Discrete Logarithms on a Quantum Computer,* SIAM J.Sci.Statist.Comput. **26**, 1484–1509 (1997).

[4] A. Steane, *Quantum Computing,* Rept. Prog. Phys. **61**, 117 (1998).

[5] P. W. Shor, *Fault tolerant quantum computation,* Proceedings of the 37th Symposium on the Foundations of Computer Science (FOCS) , 56 (1996).

[6] D. Aharonov and M. Ben-Or, *Fault-Tolerant Quantum Computation with Constant Error,* Proceedings of the 29th Annual ACM Symposium on Theory of Computing (STOC) (1997).

[7] A. Yu. Kitaev, *Fault-tolerant quantum computation by anyons,* Ann. Phys. **303**, 2 (2003).

[8] M. H. Freedman, *P/NP, and the quantum field computer,* PNAS **95**, 98 (1998).

[9] S. Das Sarma, M. Freedman, and C. Nayak, *Topologically Protected Qubits from a Possible Non-Abelian Fractional Quantum Hall State,* Phys. Rev. Lett. **94**, 166802 (2005).

[10] A. Yu. Kitaev, *Unpaired Majorana fermions in quantum wires,* Phys.-Usp. **44**, 131 (2001).

[11] R. M. Lutchyn, J. D. Sau, and S. Das Sarma, *Majorana Fermions and a Topological Phase Transition in Semiconductor-Superconductor Heterostructures,* Phys. Rev. Lett. **105**, 077001 (2010).

[12] Y. Oreg, G. Refael, and F. von Oppen, *Helical Liquids and Majorana Bound States in Quantum Wires,* Phys. Rev. Lett. **105**, 177002 (2010).

[13] V. Mourik, K. Zuo, S. M. Frolov, S. R. Plissard, E. P. A. M. Bakkers, and L. P. Kouwenhoven, *Signatures of Majorana Fermions in Hybrid Superconductor-Semiconductor Nanowire Devices,* Science **336**, 1003 (2012).

[14] A. Das, Y. Ronen, Y. Most, Y. Oreg, M. Heiblum, and H. Shtrikman, *Zero-bias peaks and splitting in an Al-InAs nanowire topological superconductor as a signature of Majorana fermions,* Nat. Phys. **8**, 887 (2012).

[15] M. T. Deng, C. L. Yu, G. Y. Huang, M. Larsson, P. Caroff, and H. Q. Xu, *Anomalous Zero-Bias Conductance Peak in a Nb–InSb Nanowire–Nb Hybrid Device,* Nano Lett. **12**, 6414 (2012).

[16] L. Landau, *On the theory of phase transitions,* Zh. Eksp. Teor. Fiz. **7**, 19–32 (1937).

[17] K. v. Klitzing, G. Dorda, and M. Pepper, *New method for high-accuracy determination of the fine-structure constant based on quantized hall resistance,* Phys. Rev. Lett. **45**, 494 (1980).

[18] R. B. Laughlin, *Quantized hall conductivity in two dimensions,* Phys. Rev. B **23**, 5632 (1981).

[19] D. J. Thouless, M. Kohmoto, M. P. Nightingale, and M. den Nijs, *Quantized hall conductance in a two-dimensional periodic potential,* Phys. Rev. Lett. **49**, 405 (1982).

[20] M. Nakahara, *Geometry, Topology, and Physics* (A. Hilger, London, 1990).

[21] A. Altland and M. R. Zirnbauer, *Nonstandard symmetry classes in mesoscopic normal-superconducting hybrid structures,* Phys. Rev. B **55**, 1142 (1997).

[22] A. P. Schnyder, S. Ryu, A. Furusaki, and A. W. W. Ludwig, *Classification of topological insulators and superconductors in three spatial dimensions,* Phys. Rev. B **78**, 195125 (2008).

[23] A. Kitaev, *Periodic table for topological insulators and superconductors,* in *American Institute of Physics Conference Series*, American Institute of Physics Conference Series, Vol. 1134, edited by V. Lebedev and M. Feigel'Man (2009) pp. 22–30, arXiv:0901.2686 [cond-mat.mes-hall] .

[24] P. A. M. Dirac, *A theory of electrons and protons,* Proc. R. Soc. Lond. A **126**, 360 (1930).

[25] E. Majorana, *Teoria simmetrica dell'elettrone e del positrone,* Nuovo Cimento **14**, 171 (1937).

[26] G. Moore and N. Read, *Nonabelions in the fractional quantum hall effect,* Nucl. Phys. B **360**, 362 (1991).

[27] G. E. Volovik, *Fermion zero modes on vortices in chiral superconductors,* Soviet Journal of Experimental and Theoretical Physics Letters **70**, 609 (1999).

[28] L. Fu and C. L. Kane, *Time reversal polarization and a Z_2 adiabatic spin pump,* Phys. Rev. B **74**, 195312 (2006).

[29] L. Fu and C. L. Kane, *Superconducting Proximity Effect and Majorana Fermions at the Surface of a Topological Insulator,* Phys. Rev. Lett. **100**, 096407 (2008).

[30] J. Nilsson, A. R. Akhmerov, and C. W. J. Beenakker, *Splitting of a Cooper Pair by a Pair of Majorana Bound States,* Phys. Rev. Lett. **101**, 120403 (2008).

[31] E. I. Rashba, *Properties of semiconductors with an extremum loop. 1. Cyclotron and combinational resonance in a magnetic field perpendicular to the plane of the loop,* Sov. Phys. Solid State **2**, 1109 (1960).

[32] S. Nadj-Perge, I. K. Drozdov, B. A. Bernevig, and A. Yazdani, *Proposal for realizing majorana fermions in chains of magnetic atoms on a superconductor,* Phys. Rev. B **88**, 020407 (2013).

[33] S. Nadj-Perge, I. K. Drozdov, J. Li, H. Chen, S. Jeon, J. Seo, A. H. MacDonald, B. A. Bernevig, and A. Yazdani, *Observation of Majorana fermions in ferromagnetic atomic chains on a superconductor,* Science **346**, 602 (2014).

[34] H. Peng, K. Lai, D. Kong, S. Meister, Y. Chen, X.-L. Qi, S.-C. Zhang, Z.-X. Shen, and Y. Cui, *Aharonov-Bohm interference in topological insulator nanoribbons,* Nature Materials **9**, 225 (2010).

[35] C.-K. Chiu, M. J. Gilbert, and T. L. Hughes, *Vortex lines in topological insulator-superconductor heterostructures,* Phys. Rev. B **84**, 144507 (2011).

[36] J.-P. Xu, C. Liu, M.-X. Wang, J. Ge, Z.-L. Liu, X. Yang, Y. Chen, Y. Liu, Z.-A. Xu, C.-L. Gao, D. Qian, F.-C. Zhang, and J.-F. Jia, *Artificial topological superconductor by the proximity effect,* Phys. Rev. Lett. **112**, 217001 (2014).

[37] K. T. Law, P. A. Lee, and T. K. Ng, *Majorana Fermion Induced Resonant Andreev Reflection,* Phys. Rev. Lett. **103**, 237001 (2009).

[38] K. Flensberg, *Tunneling characteristics of a chain of Majorana bound states,* Phys. Rev. B **82**, 180516 (2010).

[39] D. Bagrets and A. Altland, *Class D Spectral Peak in Majorana Quantum Wires,* Phys. Rev. Lett. **109**, 227005 (2012).

[40] D. I. Pikulin, J. P. Dahlhaus, M. Wimmer, H. Schomerus, and C. W. J. Beenakker, *A zero-voltage conductance peak from weak antilocalization in a Majorana nanowire,* New J. Phys. **14**, 125011 (2012).

[41] H. Zhang, O. Gül, S. Conesa-Boj, M. P. Nowak, M. Wimmer, K. Zuo, V. Mourik, F. K. de Vries, J. van Veen, M. W. A. de Moor, J. D. S. Bommer, D. J. van Woerkom, D. Car, S. R. Plissard, E. P. A. M. Bakkers, M. Quintero-Pérez, M. C. Cassidy, S. Koelling, S. Goswami, K. Watanabe, T. Taniguchi, and L. P. Kouwenhoven, *Ballistic superconductivity in semiconductor nanowires,* Nat. Comm. **8**, 16025 (2017).

[42] O. Gül, H. Zhang, J. D. S. Bommer, M. W. A. de Moor, D. Car, S. R. Plissard, E. P. A. M. Bakkers, A. Geresdi, K. Watanabe, T. Taniguchi, and L. P. Kouwenhoven, *Ballistic Majorana nanowire devices,* Nature Nanotechnology **13**, 192 (2018).

[43] W. Chang, S. M. Albrecht, T. S. Jespersen, F. Kuemmeth, P. Krogstrup, J. Nygård, and C. M. Marcus, *Hard gap in epitaxial semiconductor–superconductor nanowires,* Nature Nanotechnology **10**, 232 (2015).

[44] J. Shabani, M. Kjaergaard, H. J. Suominen, Y. Kim, F. Nichele, K. Pakrouski, T. Stankevic, R. M. Lutchyn, P. Krogstrup, R. Feidenhans'l, S. Kraemer, C. Nayak, M. Troyer, C. M. Marcus, and C. J. Palmstrøm, *Two-dimensional epitaxial superconductor-semiconductor heterostructures: A platform for topological superconducting networks,* Phys. Rev. B **93**, 155402 (2016).

[45] S. Gazibegovic, D. Car, H. Zhang, S. C. Balk, J. A. Logan, M. W. A. de Moor, M. C. Cassidy, R. Schmits, D. Xu, G. Wang, P. Krogstrup, R. L. M. Op het Veld, K. Zuo, Y. Vos, J. Shen, D. Bouman, B. Shojaei, D. Pennachio, J. S. Lee, P. J. van Veldhoven, S. Koelling, M. A. Verheijen, L. P. Kouwenhoven, C. J. Palmstrøm, and E. P. A. M. Bakkers, *Epitaxy of advanced nanowire quantum devices,* Nature **548**, 434 (2017).

[46] A. C. C. Drachmann, H. J. Suominen, M. Kjaergaard, B. Shojaei, C. J. Palmstrøm, C. M. Marcus, and F. Nichele, *Proximity Effect Transfer from NbTi into a Semiconductor Heterostructure via Epitaxial Aluminum,* Nano Letters **0**, null (0), pMID: 28072541, http://dx.doi.org/10.1021/acs.nanolett.6b04964 .

[47] H. Zhang, C.-X. Liu, S. Gazibegovic, D. Xu, J. A. Logan, G. Wang, N. van Loo, J. D. S. Bommer, M. W. A. de Moor, D. Car, R. L. M. Op het Veld, P. J. van Veldhoven, S. Koelling, M. A. Verheijen, M. Pendharkar, D. J. Pennachio, B. Shojaei, J. S. Lee, C. J. Palmstrøm, E. P. A. M. Bakkers, S. D. Sarma, and L. P. Kouwenhoven, *Quantized Majorana conductance,* Nature **556**, 74–79 (2018).

[48] G. Kells, D. Meidan, and P. W. Brouwer, *Near-zero-energy end states in topologically trivial spin-orbit coupled superconducting nanowires with a smooth confinement,* Phys. Rev. B **86**, 100503 (2012).

[49] E. Prada, P. San-Jose, and R. Aguado, *Transport spectroscopy of NS nanowire junctions with Majorana fermions,* Phys. Rev. B **86**, 180503 (2012).

[50] C.-X. Liu, J. D. Sau, T. D. Stanescu, and S. Das Sarma, *Andreev bound states versus Majorana bound states in quantum dot-nanowire-superconductor hybrid structures: Trivial versus topological zero-bias conductance peaks,* Phys. Rev. B **96**, 075161 (2017).

[51] C. Moore, T. D. Stanescu, and S. Tewari, *Two terminal charge tunneling: Disentangling Majorana zero modes from partially separated Andreev bound states in semiconductor-superconductor heterostructures,* arXiv:1711.06256 (2017).

[52] F. Setiawan, C.-X. Liu, J. D. Sau, and S. Das Sarma, *Electron temperature and tunnel coupling dependence of zero-bias and almost-zero-bias conductance peaks in Majorana nanowires,* Phys. Rev. B **96**, 184520 (2017).

[53] C. Moore, C. Zeng, T. D. Stanescu, and S. Tewari, *Quantized zero bias conductance plateau in semiconductor-superconductor heterostructures without non-Abelian Majorana zero modes,* arXiv:1804.03164 (2018).

[54] C.-X. Liu, J. D. Sau, and S. Das Sarma, *Distinguishing topological Majorana bound states from trivial Andreev bound states: Proposed tests through differential tunneling conductance spectroscopy,* arXiv:1803.05423 (2018).

[55] C.-K. Chiu and S. Das Sarma, *Fractional Josephson Effect with and without Majorana Zero Modes,* arXiv:1806.02224 (2018).

[56] A. Vuik, B. Nijholt, A. R. Akhmerov, and M. Wimmer, *Reproducing topological properties with quasi-Majorana states,* arXiv:1806.02801 (2018).

[57] A. R. Akhmerov, J. P. Dahlhaus, F. Hassler, M. Wimmer, and C. W. J. Beenakker, *Quantized Conductance at the Majorana Phase Transition in a Disordered Superconducting Wire,* Phys. Rev. Lett. **106**, 057001 (2011).

[58] B. Fregoso, A. Lobos, and S. Das Sarma, *Electrical detection of topological quantum phase transitions in disordered Majorana nanowires,* Phys. Rev. B **88**, 180507(R) (2013).

[59] P. Szumniak, D. Chevallier, D. Loss, and J. Klinovaja, *Spin and charge signatures of topological superconductivity in Rashba nanowires,* Phys. Rev. B **96**, 041401 (2017).

[60] T. O. Rosdahl, A. Vuik, M. Kjaergaard, and A. R. Akhmerov, *Andreev rectifier: A nonlocal conductance signature of topological phase transitions,* Phys. Rev. B **97**, 045421 (2018).

[61] P. Bonderson, M. Freedman, and C. Nayak, *Measurement-Only Topological Quantum Computation,* Phys. Rev. Lett. **101**, 010501 (2008).

[62] J. Alicea, Y. Oreg, G. Refael, F. von Oppen, and M. P. A. Fisher, *Non-Abelian statistics and topological quantum information processing in 1D wire networks,* Nat. Phys. (2011).

[63] J. D. Sau, D. J. Clarke, and S. Tewari, *Controlling non-Abelian statistics of Majorana fermions in semiconductor nanowires,* Phys. Rev. B **84**, 094505 (2011).

[64] B. van Heck, A. R. Akhmerov, F. Hassler, M. Burrello, and C. W. J. Beenakker, *Coulomb-assisted braiding of Majorana fermions in a Josephson junction array,* New Journal of Physics **14**, 035019 (2012).

[65] T. Hyart, B. van Heck, I. C. Fulga, M. Burrello, A. R. Akhmerov, and C. W. J. Beenakker, *Flux-controlled quantum computation with Majorana fermions,* Phys. Rev. B **88**, 035121 (2013).

[66] D. Aasen, M. Hell, R. V. Mishmash, A. Higginbotham, J. Danon, M. Leijnse, T. S. Jespersen, J. A. Folk, C. M. Marcus, K. Flensberg, and J. Alicea, *Milestones Toward Majorana-Based Quantum Computing,* Phys. Rev. X **6**, 031016 (2016).

[67] S. Plugge, A. Rasmussen, R. Egger, and K. Flensberg, *Majorana box qubits,* New Journal of Physics **19**, 012001 (2017).

[68] T. Karzig, C. Knapp, R. M. Lutchyn, P. Bonderson, M. B. Hastings, C. Nayak, J. Alicea, K. Flensberg, S. Plugge, Y. Oreg, C. M. Marcus, and M. H. Freedman, *Scalable designs for quasiparticle-poisoning-protected topological quantum computation with Majorana zero modes,* Phys. Rev. B **95**, 235305 (2017).

[69] M. Hell, M. Leijnse, and K. Flensberg, *Two-Dimensional Platform for Networks of Majorana Bound States,* Phys. Rev. Lett. **118**, 107701 (2017).

[70] M. Kjaergaard, F. Nichele, H. J. Suominen, M. P. Nowak, M. Wimmer, A. R. Akhmerov, J. A. Folk, K. Flensberg, J. Shabani, C. J. Palmstrøm, and C. M. Marcus, *Quantized conductance doubling and hard gap in a two-dimensional semiconductor–superconductor heterostructure,* Nature Communications **7**, 12841 EP (2016).

[71] J. S. Lee, B. Shojaei, M. Pendharkar, A. P. McFadden, Y. Kim, H. J. Suominen, M. Kjaergaard, F. Nichele, C. M. Marcus, and C. J. Palmstrøm, *Transport studies of epi-Al/InAs 2DEG systems for required building-blocks in topological superconductor networks,* arXiv:1705.05049 (2017).

[72] A. Trellakis, A. Galick, A. Pacelli, and U. Ravaioli, *Iteration schema for the solution of the two-dimensional Schrödinger-Poisson equations in quantum structures,* J. Appl. Phys. **81**, 7880 (1997), cited By 177.

[73] H. Wang, G. Wang, S. Chang, and Q. Huang, *Accelerated solution of Poisson-Schrödinger equations in nanoscale devices by Anderson mixing scheme,* Micro Nano Lett. **4**, 122 (2009).

[74] C. Groth, M. Wimmer, A. Akhmerov, and X. Waintal, *Kwant: a software package for quantum transport,* New J. Phys. **16**, 063065 (2014).

[75] A. Logg, K. Mardal, and G. Wells, *Automated Solution of Differential Equations by the Finite Element Method* (Springer, 2012).

[76] V. Eyert, *A Comparative Study on Methods for Convergence Acceleration of Iterative Vector Sequences,* J. Comp. Phys. **124**, 271 (1996).

[77] N. March, *The Thomas-Fermi approximation in quantum mechanics,* Advances in Physics **6**, 1 (1957).

[78] L. Spruch, *Pedagogic notes on Thomas-Fermi theory (and on some improvements): atoms, stars, and the stability of bulk matter,* Rev. Mod. Phys. **63**, 151 (1991).

2

Effects of the electrostatic environment on the Majorana nanowire devices

This chapter has been previously published as A. Vuik, D. Eeltink, A. R. Akhmerov, M. Wimmer, *Effects of the electrostatic environment on the Majorana nanowire devices*, New J. Phys. **18**, 033013 (2016)

2.1. INTRODUCTION

Majorana zero modes are non-Abelian anyons that emerge in condensed-matter systems as zero-energy excitations in superconductors [1–3]. They exhibit non-Abelian braiding statistics [4] and form a building block for topological quantum computation [5]. Following theoretical proposals [6, 7], experiments in semiconducting nanowires with proximitized superconductivity report appearance of Majorana zero modes signatures [8–12]. These "Majorana devices" are expected to switch from a trivial to a topological state when a magnetic field closes the induced superconducting gap. A further increase of the magnetic field reopens the bulk gap again with Majorana zero modes remaining at the edges of the topological phase.

Inducing superconductivity requires close proximity of the nanowire to a superconductor, which screens the electric field created by gate voltages. Another source of screening is the charge in the nanowire itself that counteracts the applied electric field. Therefore, a natural concern in device design is whether these screening effects prevent effective gating of the device. Besides this, screening effects and work function differences between the superconductor and the nanowire affect the spatial distribution of the electron density in the wire. The magnitude of the induced superconducting gap reduces when charge localizes far away from the superconductor. This restricts the parameter range for the observation of Majorana modes.

To quantitatively assess these phenomena, we study the influence of the electrostatic environment on the properties of Majorana devices. We investigate the effect of screening by the superconductor as a function of the work function difference between the superconductor and the nanowire, and we study screening effects due to charge. We focus on the influence of screening on the behavior of the chemical potential. In particular, we consider the response of the chemical potential to a magnetic field, because this directly impacts the Majorana signatures.

The zero-bias peak, measured experimentally in Refs. [8–12], is a non-specific signature of Majoranas, since similar features arise due to Kondo physics or weak anti-localization [13, 14]. To help distinguishing Majorana signatures from these alternatives, we focus on the parametric dependence of two Majorana properties: the shape of the topological phase boundary [15, 16] and the oscillations in the coupling energy of two Majorana modes [17–21].

Both phenomena depend on the response of the chemical potential to a magnetic field, and hence on electrostatic effects. Majorana oscillations were analyzed theoretically in two extreme limits for the electrostatic effects: constant chemical potential [19–21] and constant density [20] (see App. 2.7.1 for a summary of these two limits). In particular, Ref. [20] found different behavior of Majorana oscillations in these two extreme limits. We show that the actual behavior of the nanowire is somewhere in between, and depends strongly on the electrostatics.

2.2. SETUP AND METHODS

2.2.1. THE SCHRÖDINGER-POISSON PROBLEM

We discuss electrostatic effects in a device design as used by Mourik et al [8], however our methods are straightforward to adapt to similar layouts (see App. 2.7.2 for a

calculation using a different geometry). Since we are interested in the bulk properties, we require that the potential and the Hamiltonian terms are translationally invariant along the wire axis and we consider a 2D cross section, shown in Fig. 2.1. The device consists of a nanowire with a hexagonal cross section of diameter $W = 100\,\mathrm{nm}$ on a dielectric layer with thickness $d_{\mathrm{dielectric}} = 30\,\mathrm{nm}$. A superconductor with thickness $d_{\mathrm{SC}} = 187\,\mathrm{nm}$ covers half of the wire. The nanowire has a dielectric constant $\epsilon_{\mathrm{r}} = 17.7$ (InSb), the dielectric layer has a dielectric constant $\epsilon_{\mathrm{r}} = 8$ (Si_3N_4). The device has two electrostatic boundary conditions: a fixed gate potential V_{G} set by the gate electrode along the lower edge of the dielectric layer and a fixed potential V_{SC} in the superconductor, which we model as a grounded metallic gate. We set this potential to either $V_{\mathrm{SC}} = 0\,\mathrm{V}$, disregarding a work function difference between the NbTiN superconductor and the nanowire, or we assume a small work function difference [22, 23] resulting in $V_{\mathrm{SC}} = 0.2\,\mathrm{V}$.

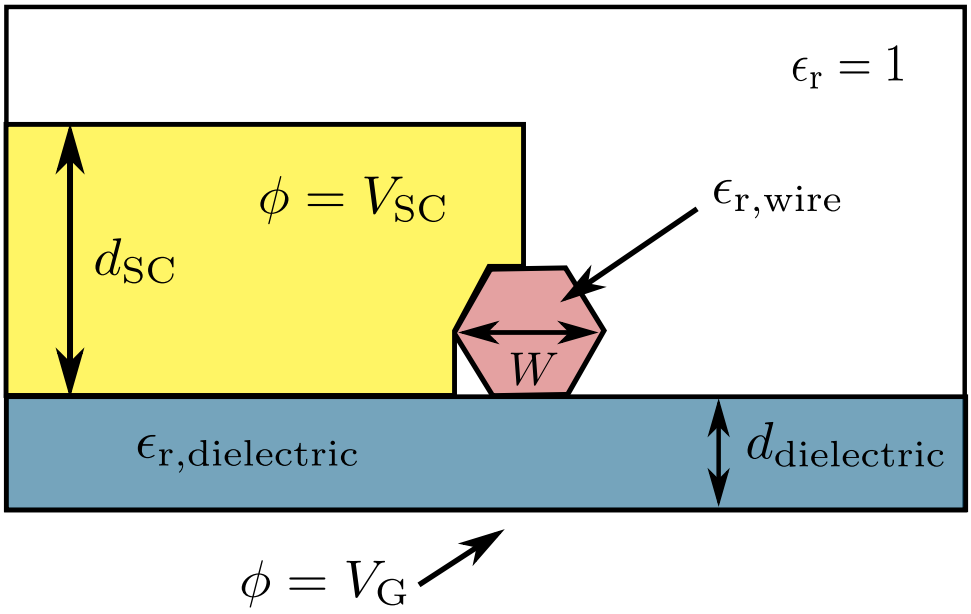

Figure 2.1: Schematic cross section of the Majorana device. It consists of a nanowire (red hexagon) lying on a dielectric layer (blue rectangle) which covers a global back gate. A superconducting lead (yellow region) covers half of the nanowire.

We model the electrostatics of this setup using the Schrödinger-Poisson equation. We split the Hamiltonian into transverse and longitudinal parts. The transverse Hamiltonian $\mathcal{H}_{\mathrm{T}}$ reads

$$\mathcal{H}_{\mathrm{T}} = -\frac{\hbar^2}{2m^*}\left(\frac{\partial^2}{\partial x^2} + \frac{\partial^2}{\partial y^2}\right) - e\phi(x,y) + \frac{E_{\mathrm{gap}}}{2}, \tag{2.1}$$

with x, y the transverse directions, $m^* = 0.014 m_e$ the effective electron mass in InSb (with m_e the electron mass), $-e$ the electron charge, and ϕ the electrostatic potential.

We assume that in the absence of electric field the Fermi level $E_{\rm F}$ in the nanowire is in the middle of the semiconducting gap $E_{\rm gap}$, with $E_{\rm gap} = 0.2\,{\rm eV}$ for InSb (see Fig. 2.2(a). We choose the Fermi level $E_{\rm F}$ as the reference energy such that $E_{\rm F} \equiv 0$.

The longitudinal Hamiltonian $\mathcal{H}_{\rm L}$ reads

$$\mathcal{H}_{\rm L} = -\frac{\hbar^2}{2m^*}\frac{\partial^2}{\partial z^2} - i\alpha\frac{\partial}{\partial z}\sigma_y + E_{\rm Z}\sigma_z, \tag{2.2}$$

with z the direction along the wire axis, α the spin-orbit coupling strength, $E_{\rm Z}$ the Zeeman energy and $\boldsymbol{\sigma}$ the Pauli matrices. The orientation of the magnetic field is along the wire in the z direction. In this separation, we have assumed that the spin-orbit length $l_{\rm SO} = \hbar^2/(m^*\alpha)$ is larger or comparable to the wire diameter, $l_{\rm SO} \gtrsim W$ [24, 25]. Furthermore, we neglect the explicit dependence of the spin-orbit strength α on the electric field. We ignore orbital effects of the magnetic field [26], since the effective area of the transverse wave functions is much smaller than the wire cross section due to screening by the superconductor, as we show in Sec. 2.3.

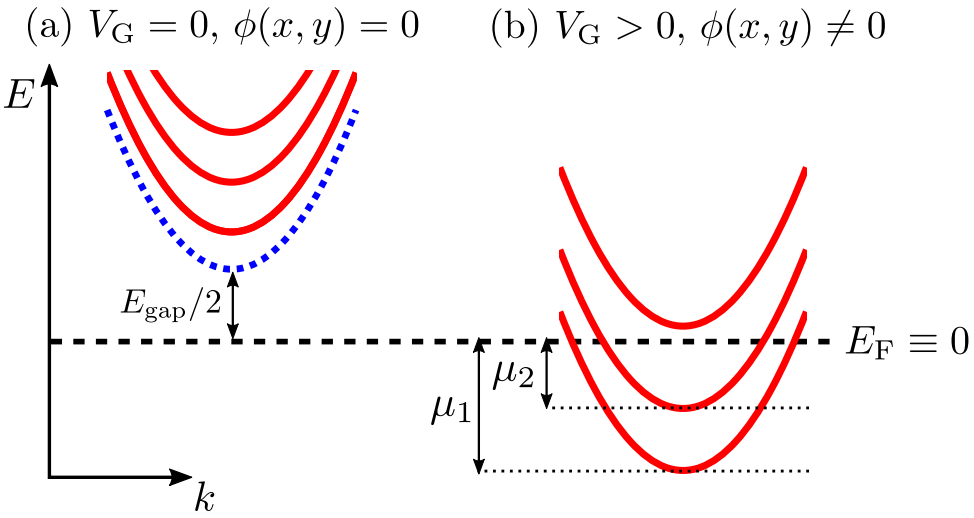

Figure 2.2: Band alignment and the Fermi level, shown schematically for $V_{\rm SC} = 0$. (a) In the absence of an electrostatic potential (gate voltage $V_{\rm G} = 0$) the Fermi level $E_{\rm F}$ is assumed to be aligned to the middle of the semiconducting gap (of size $E_{\rm gap}$, semiconductor conduction band shown as dashed blue line). Confinement in the nanowire leads to discrete subbands (red solid lines). (b) A positive gate voltage gives rise to an electrostatic potential landscape lowering the energy of all subbands. Subbands below the Fermi level $E_{\rm F}$ are occupied. For these bands, we define effective chemical potentials μ_i. (Note that the subband spacings depend on $\phi(x,y)$ and are typically different for different $V_{\rm G}$.) For simplicity, we set the spin-orbit interaction to zero in these dispersions. For nonzero spin-orbit strength, the chemical potentials μ_i are defined with respect to the crossing point of the spin bands rather than at the band edge.

Since the Hamiltonian is separable in the limit we are using, the charge density in the transverse direction $\rho(x,y)$ is:

$$\rho(x,y) = -e\sum_i |\psi_i(x,y)|^2\, n(E_i, E_{\rm Z}, \alpha), \tag{2.3}$$

with ψ_i the transverse wave function and E_i the subband energy of the i-th electron mode defined by $\mathcal{H}_\mathrm{T}\psi_i = E_i\psi_i$. Further, $n(E_i, E_\mathrm{Z}, \alpha)$ is the 1D electron density, which we calculate in closed form from the Fermi momenta of different bands in App. 2.7.3. The subband energies E_i depend on the electrostatic potential $\phi(x, y)$, and individual subbands are occupied by "lowering" subbands below E_F (shown schematically in Fig. 2.2(b)). [1]

The Poisson equation that determines the electrostatic potential $\phi(x, y)$ has the general form:

$$\nabla^2\phi(x, y) = -\frac{\rho(x, y)}{\epsilon}, \tag{2.4}$$

with ϵ the dielectric permittivity. Since the charge density of Eq. (2.3) depends on the eigenstates of Eq. (2.1), the Schrödinger and the Poisson equations have a nonlinear coupling.

We calculate the eigenstates and eigenenergies of the Hamiltonian of Eq. (2.1) in tight-binding approximation on a rectangular grid using the Kwant package [27]. We then discretize the geometry of Fig. 2.1 using a finite element mesh, and solve Eq. (2.4) numerically using the FEniCS package [28].

Eqs. (2.1) and (2.3) together define a functional $\bar{\rho}[\phi]$, yielding a charge density from a given electrostatic potential ϕ. Additionally, Eq. (2.4) defines a functional $\bar{\phi}[\rho]$, giving the electrostatic potential produced by a charge density ρ. The Schrödinger-Poisson equation is self-consistent when

$$\bar{\phi}[\bar{\rho}[\phi]] - \phi = 0. \tag{2.5}$$

We solve Eq. (2.5) using an iterative nonlinear Anderson mixing method [29]. We find that this method prevents the iteration process from oscillations and leads to a significant speedup in computation times compared to other nonlinear solver methods (see App. 2.7.5). We search for the root of Eq. (2.5) rather than for the root of

$$\bar{\rho}[\bar{\phi}[\rho]] - \rho = 0, \tag{2.6}$$

since we found Eq. (2.5) to be better conditioned than Eq. (2.6). The scripts with the source code as well as resulting data are available online as ancillary files for this manuscript.

2.2.2. MAJORANA ZERO MODES IN SUPERCONDUCTING NANOWIRES

Having solved the electrostatic problem for the normal system, i.e. taking into account only the electrostatic effects of the superconductor, we then use the electrostatic potential $\phi(x, y)$ in the superconducting problem. To this end, we obtain the Bogoliubov-de Gennes Hamiltonian $\mathcal{H}_\mathrm{BdG}$ by summing $\mathcal{H}_\mathrm{T}$ and $\mathcal{H}_\mathrm{L}$ and adding an induced superconducting pairing term:

[1] Note that E_i agrees with the subband bottom only if $\alpha = 0$ and E_Z=0. See App. 2.7.3 for details on the subband occupation in the general case.

$$\mathcal{H}_{\text{BdG}} = \left[\left(-\frac{\hbar^2}{2m^*}\nabla^2 - e\phi(x,y) + \frac{E_{gap}}{2}\right)\sigma_0 - i\alpha\frac{\partial}{\partial z}\sigma_y\right]\otimes\tau_z + E_{\text{Z}}\sigma_z\otimes\tau_0 + \Delta\sigma_0\otimes\tau_x, \tag{2.7}$$

with $\boldsymbol{\tau}$ the Pauli matrices in electron-hole space and Δ the superconducting gap.

The three-dimensional BdG equation (2.7) is still separable and reduces for every subband with transverse wave function ψ_i to an effective one-dimensional BdG Hamiltonian:

$$\mathcal{H}_{\text{BdG},i} = \left[\left(\frac{p^2}{2m^*} - \mu_i\right)\sigma_0 + \frac{\alpha}{\hbar}p\sigma_y\right]\otimes\tau_z + E_{\text{Z}}\sigma_z\otimes\tau_0 + \Delta\sigma_0\otimes\tau_x, \tag{2.8}$$

where $p = -i\hbar\partial/\partial z$ and we defined $\mu_i = -E_i$ (see Fig. 2.2(b)). Since the different subbands are independent, μ_i can be interpreted as the chemical potential determining the occupation of the i-th subband.

While the Fermi level is kept constant by the metallic contacts, the chemical potential μ_i of each subband does depend on the system parameters: $\mu_i = \mu_i(V_{\text{G}}, E_{\text{Z}})$. Most of the model Hamiltonians for Majorana nanowires used in the literature are of the form of Eq. (2.8) (or a two-dimensional generalization) using one chemical potential μ. To make the connection to our work, μ should be identified with μ_i, and not be confused with the constant Fermi level E_{F}. For example, the constant chemical potential limit of Ref. [20] refers to the special case that μ_i is independent of E_{Z}, and it is not related to E_{F} being always constant. [2]

Properties of Majorana modes formed in the i-th subband only depend on the value of μ_i (or equivalently E_i). In the following we thus determine the effect of the electrostatics on μ_i before we finally turn to Majorana bound states.

2.3. SCREENING EFFECTS ON CHARGE DENSITY AND ENERGY LEVELS

We begin by investigating the electrostatic effects in absence of Zeeman field and a spin-orbit strength with $l_{\text{SO}} = 233\,\text{nm}$, negligible for the electrostatic effects. We solve the Schrödinger-Poisson equation for a superconductor with $V_{\text{SC}} = 0\,\text{V}$ and a superconductor with $V_{\text{SC}} = 0.2\,\text{V}$, and compare the solutions to two benchmarks: a nanowire without a superconducting lead, and a nanowire in which we ignore screening by charge. Specifically, we compute the influence of screening by the superconductor and by charge on the field effect on the lowest energy levels and charge densities. To evaluate the role of screening by charges in the wire, we compare the full solution of the Poisson equation (2.4) to its solution with the right-hand side set to zero. Our results are summarized in Fig. 2.3 showing the dispersion of μ_i and Fig. 2.4 showing the charge density for the same situations and the values of V_{G} marked in Fig. 2.3.

The approximate rotational symmetry of the wire leads to almost doubly degenerate bands with opposite angular momenta when electric field is negligible—a

[2] Using the notion of a variable chemical potential μ is natural when energies are measured with respect to a fixed band bottom, i.e. in a single-band situation. In our case, different subbands react differently on changes in $\phi(x,y)$ and it is more practical to keep the Fermi level E_{F} fixed.

situation realized either in absence of the superconductor [Fig. 2.3(a)] or when $V_G = V_{SC}$ [Fig. 2.3(b), (c), (d)]. However in most cases, presence of the superconductor leads to a large V_G required to induce a finite charge density in the wire, and the degeneracy is strongly lifted.

The lever arm of the gate voltage on the energies E_i, reduces from the optimal value of 1, at $V_G < 0$ by approximately a factor of 4 due to charge screening alone [Fig. 2.3(a)]. Screening by the superconductor leads to an additional comparable suppression of the lever arm, however its effect is nonlinear in V_G due to the transverse wave functions being pulled closer to the gate at positive V_G. Comparing panels (b) and (c) of Fig. 2.3 we see that screening by the superconductor does not lead to a strong suppression of screening by charge when $V_{SC} = 0$: the field effect strongly reduces as soon as charge enters the wire when we take charge screening into account. This lack of interplay between the screening by superconductor and by charge can be understood by looking at the charge density distribution in the nanowire [Fig. 2.4(b), (c)]. Since a positive gate voltage is required to induce a finite charge density, the charges are pulled away from the superconductor, and the corresponding mirror charges in the superconductor area are located at a distance comparable to twice the wire thickness. On the contrary, a positive V_{SC} requires a compensating negative V_G to induce comparable charge density in the wire, pushing the charges closer to the superconductor [Fig. 2.4(d)]. In this case, the proximity of the electron density to the superconductor leads to the largest suppression of the lever arm, and proximity of image charges almost completely compensates the screening by charge.

The Van Hove singularity in the density of states leads to an observable kink in μ_i each time an extra band crosses the Fermi level [inset in Fig. 2.3(a)]. However, we observe that the effect is weak on the scale of level spacing and cannot guarantee strong pinning of the Fermi level to a band bottom.

2.4. ELECTROSTATIC RESPONSE TO THE ZEEMAN FIELD

2.4.1. LIMIT OF LARGE LEVEL SPACING

The full self-consistent solution of the Schrödinger-Poisson equation is computationally expensive and also hard to interpret due to a high dimensionality of the space of unknown variables. We find a simpler form of the solution at a finite Zeeman field relying on the large level spacing $\sim 10\,\mathrm{meV}$ in typical nanowires. It ensures that the transverse wave functions stay approximately constant, i.e. $|\langle\psi(E_Z)|\psi(0)\rangle| \approx 1$ up to magnetic fields of $\sim 7\,\mathrm{T}$. In this limit we may apply perturbation theory to compute corrections to the chemical potential for varying E_Z.

We write the potential distribution for a given E_z in the form

$$\phi(x, y, E_Z) = \phi_{\text{b.c.}}(x, y) + \sum_{i=0}^{N} \phi_i(x, y, E_z), \tag{2.9}$$

where $\phi_{\text{b.c.}}$ is the potential obeying the boundary conditions set by the gate and the superconducting lead, and solves the Laplace equation

$$\nabla^2 \phi_{\text{b.c.}}(x, y) = 0. \tag{2.10}$$

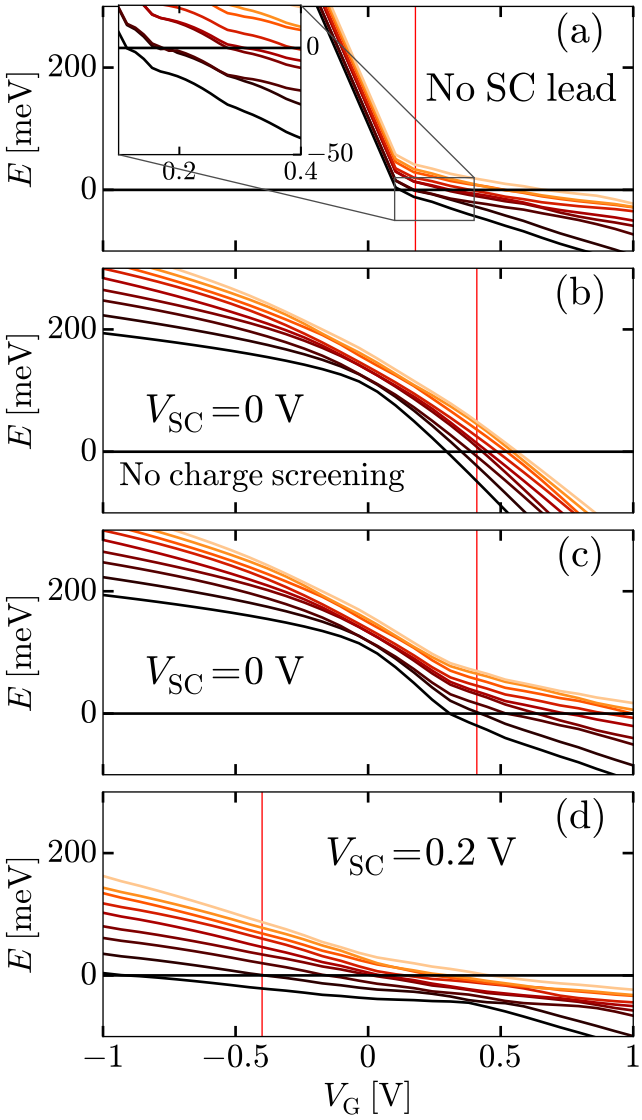

Figure 2.3: The nine lowest subband energies μ_i as a function of gate voltage. (a): Wire without a superconducting lead, (b): wire with a superconducting lead at $V_{SC} = 0\,V$, neglecting charge screening effects, (c): the same problem including charge screening effects, and (d): a superconducting lead with $V_{SC} = 0.2\,V$ including charge screening. The Fermi level $E_F = 0$ is indicated as a solid horizontal line. The red lines indicate the gate voltages used in the calculation of charge density and electric field of the corresponding panels in Fig. 2.4. In all plots, we take weak spin-orbit interaction (a spin-orbit length of 233 nm). The inset of the top panel shows a zoom, revealing Fermi level pinning every time a new band crosses the Fermi level.

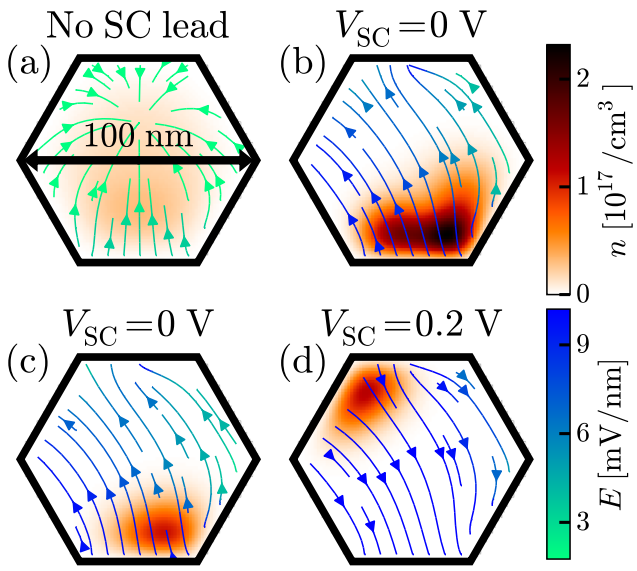

Figure 2.4: Charge density distribution and electric field in the wire cross section, at the gate voltage indicated by the red line in the corresponding panel of Fig. 2.3. (a): Self-consistent solution when no superconducting lead is attached. (b): Superconducting lead at $V_{SC} = 0\,\mathrm{V}$, neglecting screening by charge. (c): Same problem, but including screening by charge (self-consistent). (d): Self-consistent solution for a superconducting lead at $V_{SC} = 0.2\,\mathrm{V}$. The total density is $\approx 5.5 \times 10^5\,\mathrm{cm}^{-1}$ for plots (a), (c), and (d). Plot (b) has a total density of $\approx 1.6 \times 10^6\,\mathrm{cm}^{-1}$.

The corrections ϕ_i to this potential due to the charge contributed by the i-th mode out of the N modes below the Fermi level then obeys a Poisson equation with Dirichlet boundary conditions (zero voltage on the gates):

$$\nabla^2 \phi_i(x, y, E_Z) = \frac{e}{\epsilon} |\psi_i(x, y)|^2 \, n(-\mu_i - \delta\mu_i, E_Z, \alpha) \tag{2.11}$$

where we write the chemical potential at a finite value of E_Z as $\mu_i(E_Z) = \mu_i + \delta\mu_i$ where μ_i is the chemical potential in the absence of a field.

We now define a magnetic field-independent reciprocal capacitance as

$$P_i(x, y) = \frac{\phi_i(x, y, E_Z)}{-e\, n(-\mu_i - \delta\mu_i, E_Z, \alpha)} \tag{2.12}$$

which solves the Poisson equation

$$\nabla^2 P_i(x, y) = -\frac{1}{\epsilon} |\psi_i(x, y)|^2 \,. \tag{2.13}$$

Having solved the Schrödinger-Poisson problem numerically for $E_Z = 0$, we define $\delta\phi_i = \phi_i(x, y, E_Z) - \phi_i(x, y, 0)$ and $\delta n = n(-\mu_i - \delta\mu_i, E_Z, \alpha) - n(-\mu_i, 0, \alpha)$.

The correction δE_i to the subband energy E_i is then given in first order perturbation as

$$\delta E_i = -e\langle\psi_i| \sum_{j=0}^{N} \delta\phi_j |\psi_i\rangle \,. \tag{2.14}$$

Using Eqs. (2.12), (2.14) and $\delta\mu_i = -\delta E_i$ we then arrive at:

$$\delta\mu_i = -e^2 \sum_{j=0}^{N} P_{ij}\delta n_j \,, \tag{2.15}$$

with the elements of the reciprocal capacitance matrix P given by

$$P_{ij} = \langle\psi_i|P_j|\psi_i\rangle. \tag{2.16}$$

Solving the Eq. (2.15) self-consistently, we compute corrections to the initial chemical potentials μ_i. The Eq. (2.15) has a much lower dimensionality than Eq. (2.5) and is much cheaper to solve numerically. Further, all the electrostatic phenomena enter Eq. (2.15) only through the reciprocal capacitance matrix Eq. (2.16).

2.4.2. SINGLE- AND MULTIBAND RESPONSE TO THE MAGNETIC FIELD

We start by computing the electrostatic response to changes in the magnetic field when the Fermi level is close to the band bottom for a single band ($N = 1$, and we write the index $\mu_1 \equiv \mu$ for brevity). We study the influence of the electrostatic environment and assess whether the device is closer to a constant charge density or constant chemical potential situation (using the nomenclature of Ref. [20] explained in App. 2.7.1).

The top panel of Fig. 2.5 shows the chemical potential response to Zeeman field. Without a superconducting contact, the electron-electron interactions in the nanowire are screened the least, and the Coulomb effects are the strongest, counteracting density changes in the wire. In agreement with this observation, we find the change in chemical potential μ comparable to the change in E_Z. Hence, in this case the system is close to a constant-density regime.

A superconducting contact close to the nanowire screens the electron-electron interaction in the wire due to image charges. The chemical potential is then less sensitive to changes in magnetic field. We find that this effect is most pronounced for a positive work function difference with the superconductor $V_{SC} = 0.2\,\mathrm{V}$, when most of the electrons are pulled close to the superconducting contact. Then, the image charges are close to the electrons and strongly reduce the Coulomb interactions. In this case the system is close to a constant chemical potential regime. For $V_{SC} = 0\,\mathrm{V}$ screening from the superconducting contact is less effective, since electric charges are further away from the interface with the superconductor. Therefore in this case, we find a behavior intermediate between constant density and constant chemical potential.

Besides the dependence on the electrostatic surrounding, the magnetic field response of the chemical potential depends on the spin-orbit strength. Specifically, the chemical potential stays constant over a longer field range when the spin-orbit

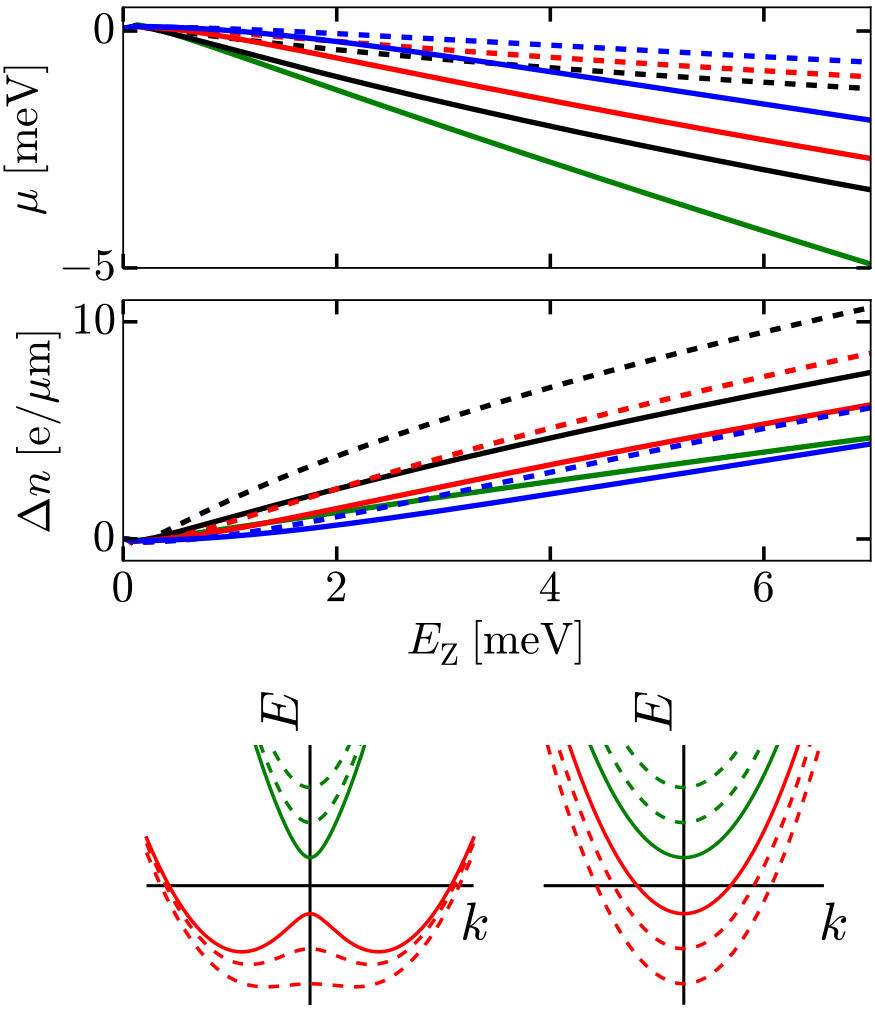

Figure 2.5: Top and middle panel: Variation in chemical potential (top panel) and in electron density (middle panel) as a function of magnetic field. The green solid line corresponds to the case without a superconductor. Other solid lines correspond to $V_{\mathrm{SC}} = 0\,\mathrm{V}$, dashed lines to $V_{\mathrm{SC}} = 0.2\,\mathrm{V}$. Black, red and blue indicate spin-orbit lengths of 233, 100, and $60\,\mathrm{nm}$ respectively. Bottom panel: Dispersion relation $E(k)$ for $E_{\mathrm{SO}} \gg E_{\mathrm{Z}}$ (left) and $E_{\mathrm{SO}} \ll E_{\mathrm{Z}}$ (right). Dashed lines indicate the evolution of the dispersion for the increasing magnetic field.

interaction is stronger. [3] The bottom panel of Fig. 2.5 explains this: when the spin-orbit energy $E_{\mathrm{SO}} \gg E_{\mathrm{Z}}$, the lower band has a W-shape (bottom left). A magnetic-field increase initially transforms the lower band back from a W-shape to a parabolic band,

[3] Although we decrease the spin-orbit length to $l_{\mathrm{SO}} = 60\,\mathrm{nm}$, which is smaller than the wire diameter of $100\,\mathrm{nm}$, we assume separable wave functions. Screening by the superconductor strongly localizes the wave functions, such that the confinement is still smaller than the spin-orbit length.

as indicated by the dashed red lines. During this transition, the Fermi wavelength is almost constant. Since the electron density is proportional to the Fermi wavelength, this means that both the density and the chemical potential change very little in this regime. We thus identify the spin-orbit interaction as another phenomenon driving the system closer to the constant chemical potential regime, similar to the screening of the Coulomb interaction by the superconductor. At large Zeeman energies $E_Z \gtrsim E_{SO}$, the spin-down band becomes parabolic (bottom right of Fig. 2.5). This results in the slope of $\mu(E_Z)$ becoming independent of the spin-orbit coupling strength, as seen in the top panel of Fig. 2.5 at large values of E_Z.

Close to the band bottom and when spin-orbit interaction is negligible, we study the asymptotic behavior of μ and n by combining the appropriate density expression Eq. (2.28) with the corrections in the chemical potential Eq. (2.15). In that case, the chemical potential becomes

$$\mu = -\frac{e^2 P}{\pi\hbar}\sqrt{2m^*(\mu + E_Z)}. \tag{2.17}$$

We associate an energy scale E_P with the reciprocal capacitance P, given by

$$E_P = \frac{2m^* e^4 P^2}{\pi^2\hbar^2}, \tag{2.18}$$

and study the two limits $E_P \gg E_Z$ and $E_P \ll E_Z$. In the strong screening limit $E_P \gg E_Z$ we find the asymptotic behavior $\mu \approx -E_Z$, corresponding to a constant-density regime. The opposite limit $E_P \ll E_Z$ yields $\mu \approx -\sqrt{E_P E_Z}$, close to a constant chemical potential regime. We computed E_P explicitly for the chemical potential variations as shown in the top panel of Fig. 2.5. For a nanowire without a superconducting lead, we find an energy $E_P \approx 42\,\mathrm{meV} \gg E_Z$, indicating a constant-density regime. Using the classical approximation of a metallic cylinder above a metallic plate, we find an energy of the same order of magnitude. For a nanowire with an attached superconducting lead at $V_{SC} = 0\,\mathrm{V}$, we get $E_P \approx 7\,\mathrm{meV} \sim E_Z$, intermediate between constant density and constant chemical potential. Finally, a superconducting lead at $V_{SC} = 0.2\,\mathrm{V}$ yields $E_P \approx 0.5\,\mathrm{meV} \ll E_Z$, indicating a system close to the constant chemical potential regime.

Since integrating over density-of-states measurements yields δn_0, the inverse self-capacitance $-e\langle\psi_0|P_0|\psi_0\rangle$ can be inferred from experimental data by fitting the density variation curves to the theoretical dependence $\mu(E_Z)$. This allows to experimentally measure the effect of the electrostatic environment, when knowing the remaining Hamiltonian parameters.

We compare the response to Zeeman field in the multi-band case for $N = 3$ and $N = 10$ to the single band behavior in Fig. 2.6. We observe that presence of extra charges further reduces the sensitivity of the chemical potential to the magnetic field. We interpret the non-monotonous behavior of the chemical potential (most pronounced for $N = 10$ in Fig. 2.6, but in principle present for all N) as being due to a combination of the Van Hove singularities in the density of states and screening by charges. For a fixed chemical potential, the upper band, moving up in energy due to the magnetic field, loses more states than the lower band acquires, since it

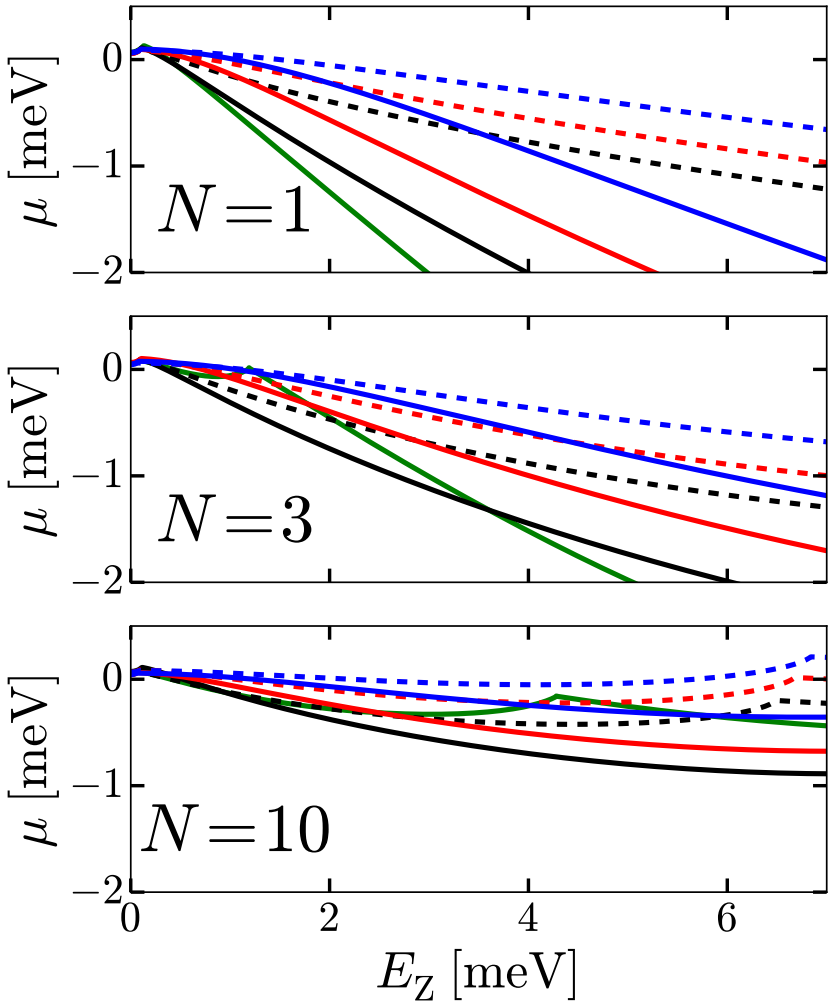

Figure 2.6: Response of μ_N as a function of magnetic field for $N = 1, 3$, and 10, all close to the band bottom. The solid green line corresponds to the case of no screening by a superconductor. Other solid lines correspond to $V_{SC} = 0\,\mathrm{V}$, dashed lines to $V_{SC} = 0.2\,\mathrm{V}$. Black, red and blue indicate spin-orbit lengths of 233, 100, and 60 nm respectively.

approaches the Van Hove singularity in its density of states. To keep the overall density fixed, the chemical potential increases. Once the density in the lower band equals the initial density, the upper band is empty and the chemical potential starts dropping again. In the limit of constant density and a single mode the magnetic field dependence of the chemical potential can be solved analytically, reproducing the non-monotonicity and kinks (see App. 2.7.4). Relating the variation in μ_i to density measurements is experimentally inaccessible for $N > 1$, since corrections to μ_i

depend on the density changes of each individual mode, as expressed in Eq. (2.15).

2.5. IMPACT OF ELECTROSTATICS ON MAJORANA PROPERTIES

2.5.1. SHAPE OF THE MAJORANA PHASE BOUNDARY

The nanowire enters the topological phase when the bulk energy gap closes at a Zeeman energy of $E_Z = \sqrt{\mu^2 + \Delta^2}$. The electrostatic effects affect the shape of the topological phase boundary through the dependence of μ on E_Z. To find the topological phase boundary as a function of both experimentally controllable parameters V_G and E_Z, we perform a full self-consistent simulation at $E_Z = 0$. We then compute corrections to the resulting chemical potential at arbitrary E_Z using Eq. (2.15), and find topological phase boundary $E_Z = \sqrt{\mu^2 + \Delta^2}$ by recursive bisection.

Figure 2.7 shows the resulting phase boundary corresponding to $\Delta = 0.5\,\mathrm{meV}$. The phase boundary has a non-universal shape due to the interplay between electrostatics and magnetic field. In agreement with our previous conclusions, the electrostatic effects are the strongest with absent work function difference $V_{SC} = 0\,\mathrm{V}$ (top panel of Fig. 2.7) when the nanowire is intermediate between constant density and constant chemical potential. [4] Close to the band bottom, the charge screening reduces changes in density, and thus lowers the chemical potential by an amount that is similar to E_Z. Hence, the lower phase boundary (at smaller V_G) has a weaker slope than the upper phase boundary (at larger V_G). Note that in the limit of constant density, the lower phase boundary would be a constant independent of E_Z (see App. 2.7.4).

For a work function difference $V_{SC} = 0.2\,\mathrm{V}$, the system is closer to the constant chemical potential regime. In this regime, μ changes linearly with V_G, yielding a hyperbolic phase boundary with symmetric upper and lower arms and its vertex at $E_Z = \Delta$. When spin-orbit interaction is strong, a transition in the lower arm of the phase boundary from constant chemical potential (hyperbolic phase boundary) to constant density (more horizontal lower arm) occurs, resulting in a 'wiggle' which is most pronounced for $V_{SC} = 0\,\mathrm{V}$ and $l_{SO} = 60\,\mathrm{nm}$. This feature is less pronounced for $V_{SC} = 0.2\,\mathrm{V}$ due to the screening by the superconductor suppressing the Coulomb interactions.

2.5.2. OSCILLATIONS OF MAJORANA COUPLING ENERGY

The wave functions of the two Majorana modes at the endpoints of a finite-length nanowire have a finite overlap that results in a finite nonzero energy splitting ΔE of the lowest Hamiltonian eigenstates [17–21]. This splitting oscillates as a function of the effective Fermi wave vector $k_{F,\mathrm{eff}}$ as $\cos(k_{F,\mathrm{eff}}L)$ [20]. We investigate the dependency of the oscillation frequency, or the oscillation peak spacing on magnetic field and the electrostatic environment.

[4] The presence of a superconductor is essential for Majorana fermions, but inevitably leads to screening. For the geometries of our calculations we thus do not have a situation close to constant density.

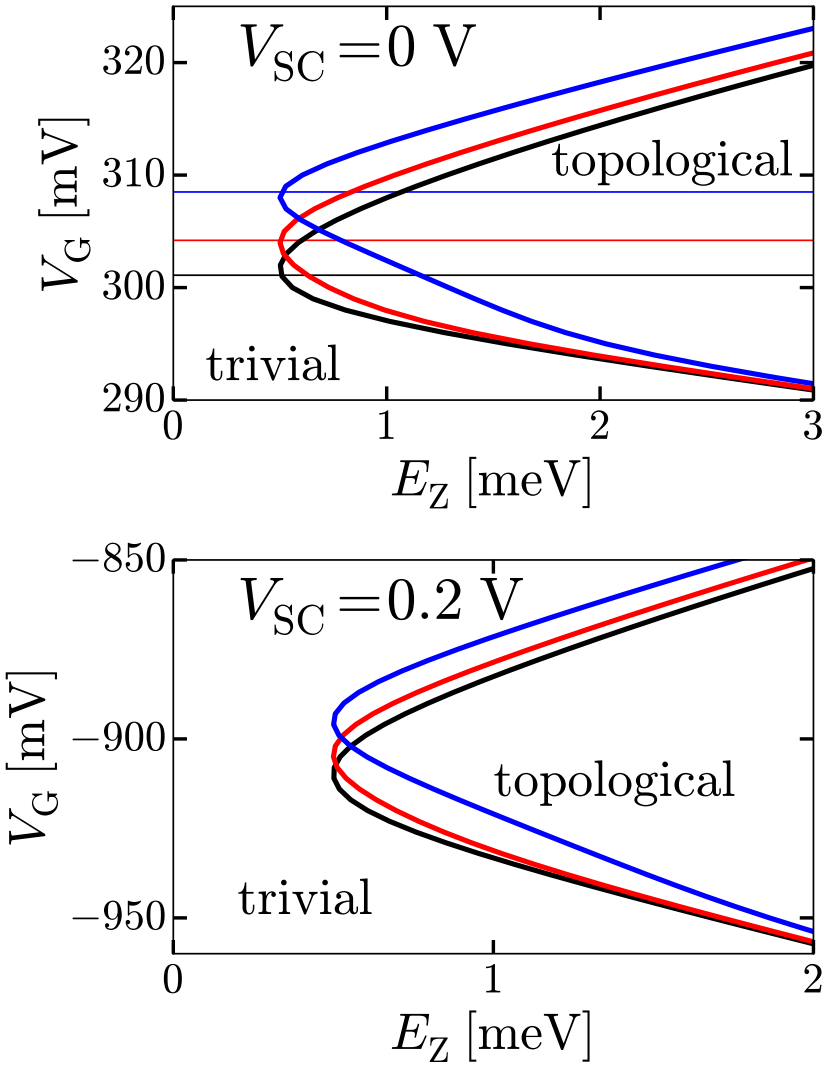

Figure 2.7: Majorana transition boundary for a superconductor at $V_{SC} = 0\,\mathrm{V}$ (upper panel) or a superconductor at $V_{SC} = 0.2\,\mathrm{V}$ (lower panel). The superconducting gap $\Delta = 0.5\,\mathrm{meV}$. The boundaries are obtained for the single-band case. The solid black, red, and blue lines correspond to a spin-orbit length of 233, 100, and $60\,\mathrm{nm}$ respectively. The black, red and blue horizontal lines in the upper plot indicate the gate voltages at which we compute the correspondingly colored Majorana coupling oscillations in the inset of Fig. 2.8.

A peak in the Majorana splitting energy occurs when Majorana wave functions constructively interfere, or when the Fermi momentum equals $q\pi/L$, with q the peak

number and L the nanowire length. The momentum difference between two peaks is

$$k_{\text{F,eff}}(E_{\text{Z},q+1}) - k_{\text{F,eff}}(E_{\text{Z},q}) = \frac{\pi}{L}, \tag{2.19}$$

where $E_{\text{Z},q}$ is the Zeeman energy corresponding to the q-th oscillation peak. In the limit of small peak spacing, we expand $k_{\text{F,eff}}(E_{\text{Z},q+1}) - k_{\text{F,eff}}(E_{\text{Z},q})$ to first order in E_{Z}:

$$\frac{dk_{\text{F}}}{dE_{\text{Z}}}\Delta E_{\text{Z}} = \frac{\pi}{L}, \tag{2.20}$$

yielding the peak spacing

$$\Delta E_{\text{Z, peak}} = \frac{\pi}{L}\left(\frac{dk_{\text{F}}}{dE_{\text{Z}}}\right)^{-1}. \tag{2.21}$$

Since $k_{\text{F,eff}} = k_{\text{F,eff}}(E_{\text{Z}}, \mu(E_{\text{Z}}))$, we substitute

$$\frac{dk_{\text{F}}}{dE_{\text{Z}}} = \frac{\partial k_{\text{F}}}{\partial E_{\text{Z}}} + \frac{\partial k_{\text{F}}}{\partial \mu}\frac{d\mu}{dE_{\text{Z}}}. \tag{2.22}$$

We obtain the values of $\partial k_{\text{F}}/\partial E_{\text{Z}}$ and $\partial k_{\text{F}}/\partial \mu$ from the analytic expression for k_{F}, presented in App. 2.7.3. The value $d\mu/dE_{\text{Z}}$ results from the dependence $\mu(E_{\text{Z}})$ shown in Fig. 2.5.

Figure 2.8 shows the peak spacing as a function of E_{Z} for a nanowire of length $L = 2\,\mu\text{m}$. Stronger screening reduces the peak spacing (i.e. increases the oscillation frequency) by reducing the sensitivity of the chemical potential to the magnetic field, as discussed in Sec. 2.4. In addition, spin-orbit strength has a strong influence on the peak spacing, since for $E_{\text{Z}} \ll E_{\text{SO}}$ the density, and thus $k_{\text{F,eff}}$, stays constant. This results in a lower oscillation frequency and hence a larger peak spacing. Correspondingly, we find that the peak spacing may increase, decrease, or roughly stay constant as a function of the magnetic field.

Similarly to the shape of the Majorana transition boundary, Fig. 2.8 shows that the peak spacing does not follow a universal law, in contrast to earlier predictions [21]. In particular, our findings may explain the zero-bias oscillations measured in Ref. [11], exhibiting a roughly constant peak spacing.

Fig. 2.9 shows Majorana energy oscillations as a function of both gate voltage and magnetic field strength for $V_{\text{SC}} = 0.2\,\text{V}$, with $L = 1000\,\text{nm}$ to increase the Majorana coupling. The diagonal ridges are lines of constant chemical potential. The difference in slope between the ridges of both plots indicates a difference in the equilibrium situation: closer to constant density for weak spin-orbit coupling, closer to constant chemical potential for strong spin-orbit coupling. The bending of the constant chemical potential lines in the lower panel indicates a transition from the latter mechanism to the former mechanism, due to the increase of magnetic field, as explained in Sec. 2.4.

2.6. SUMMARY

We have studied the effects of the electrostatic environment on the field control of Majorana devices and their properties. Screening by charge and by the superconductor strongly reduce the field effect of the gates. Furthermore, screening by the

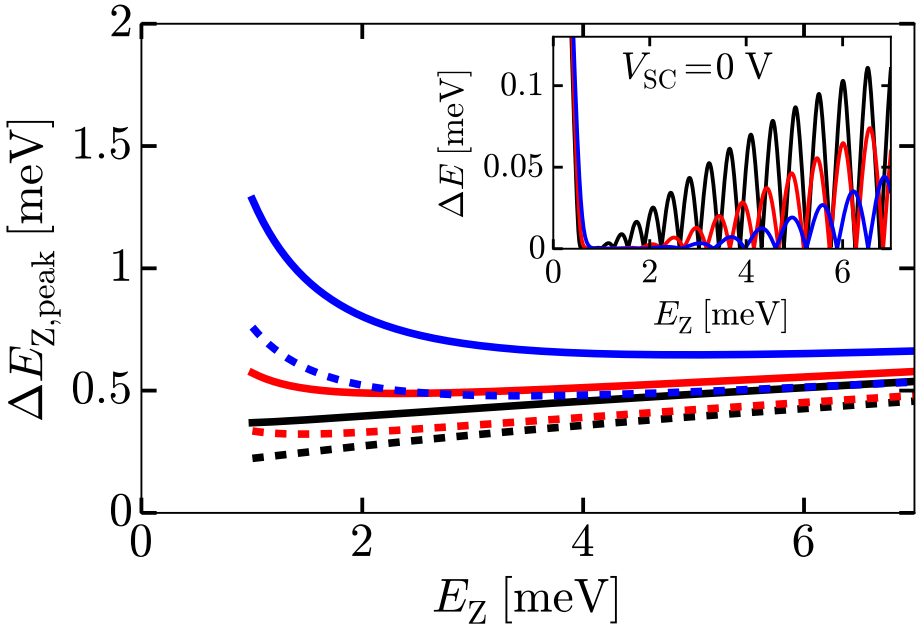

Figure 2.8: Peak spacing of the Majorana energy oscillations in a magnetic field for a nanowire of length $L = 2\,\mu\mathrm{m}$. Solid lines correspond to $V_{SC} = 0\,\mathrm{V}$, dashed lines to $V_{SC} = 0.2\,\mathrm{V}$. Black, red and blue indicate spin-orbit lengths of 233, 100, and 60 nm respectively. Inset: Splitting energy oscillations for $V_{SC} = 0\,\mathrm{V}$. The three horizontal lines in the upper panel of Fig. 2.7 indicate the corresponding gate potential. The energy splittings are found by solving for the lowest energy of the Hamiltonian of Eq. (2.8), using the chemical potentials obtained from the perturbation scheme as described in Sec. 2.4.

superconductor localizes the charge and induces a large internal electric field. When we assume the superconductor to have a zero work function difference with the nanowire, charge localizes at the bottom of the wire, which reduces the induced superconducting gap.

Coulomb interaction causes the chemical potential to respond to an applied magnetic field, while screening by the superconductor and spin-orbit interaction suppress this effect. If a superconductor is attached, the equilibrium regime is no longer close to constant density, but either intermediate between constant density and constant chemical potential for a superconductor with zero work function difference, or close to constant chemical potential for a superconductor with a positive work function difference.

Due to this transition in equilibrium regime for increasing screening and spin-orbit interaction, the shape of the Majorana phase boundary and the oscillations of Majorana splitting energy depend on device parameters rather than following a universal law.

We have shown how to relate the measurement of density variations to the chemical potential response. Since the Majorana signatures directly depend on this

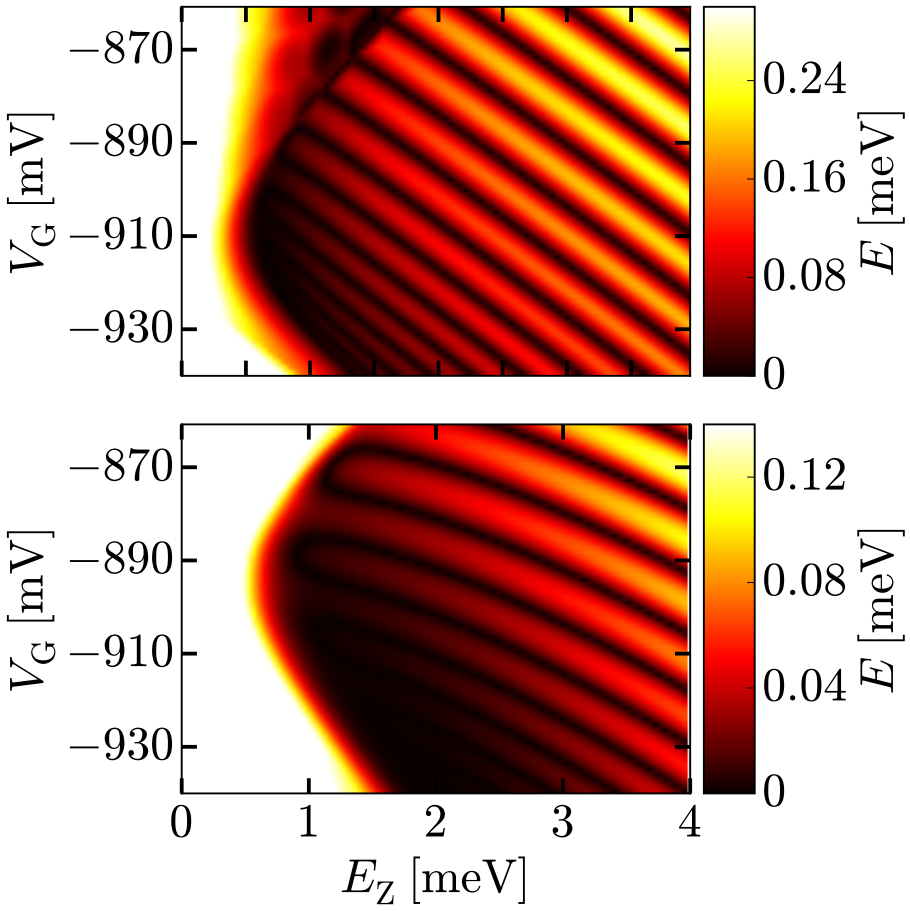

Figure 2.9: Majorana energy oscillations as a function of gate voltage and magnetic field for a superconductor at $V_{SC} = 0.2\,\mathrm{V}$ with weak spin-orbit interaction, $l_{SO} = 233\,\mathrm{nm}$ (upper panel), and strong spin-orbit interaction, $l_{SO} = 60\,\mathrm{nm}$ (lower panel).

response, our work offers a way to compare direct experimental observations of both signatures with theoretical predictions, and to remove the uncertainty caused by the electrostatic environment.

Our Schrödinger-Poison solver, available in the supplementary files for this manuscript, can be used to compute lever arms and capacities for different device dimensions and geometries, providing practical help for the design and control of experimental devices.

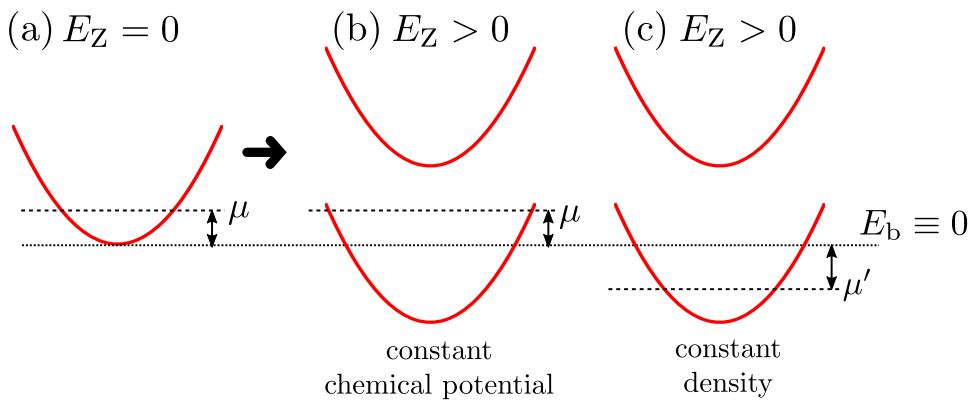

Figure 2.10: Schematic explanation of constant chemical potential and constant density limits discussed in Ref. [20]: (a) In the absence of a magnetic field, a band is filled up to the chemical potential μ. μ is measured with respect to the band edge E_b that serves as a reference energy. For a finite Zeeman splitting E_Z the two spin-bands split by $\pm E_Z$ with respect to E_b. In this case there can be two extreme situations: (b) constant chemical potential – μ stays unchanged (and hence the total electron density changes). (c) constant density – the total electron density stays constant leading to a new chemical potential μ'. (For simplicity, all plots are shown for $\alpha = 0$.)

2.7. APPENDIX

2.7.1. NOMENCLATURE – CONSTANT DENSITY AND CONSTANT CHEMICAL POTENTIAL

In Ref. [20] Das Sarma *et al.* considered Majorana oscillations as a function of magnetic field. The authors considered there two extreme electrostatic situations that they refer to as constant chemical potential and constant density.

In particular, Ref. [20] considers a one-dimensional nanowire BdG Hamiltonian as in Eq. (2.8), with μ_1 being denoted as μ. In this model, the subband energy E_b is fixed and set to 0. The electron density is changed by adjusting μ (shown for the $E_Z = 0$ case in Fig. 2.10(a).

For fixed μ in Eq. (2.8) electron density will change upon changing E_Z. For example, if $E_Z \gg \mu, E_{so}$, electron density will increase monotonically as E_Z is increased (see Fig. 2.10(b). This constant chemical potential situation is realized in the limit of vanishing Coulomb interaction, as then density changes do not influence the electrostatic potential. The same assumption is used in Refs. [19, 21].

Reference [20] also considered the opposite case of infinitely strong Coulomb interaction. In this case the electron density is fixed, and consequently μ must change as E_Z changes. This constant density situation is schematically shown in Fig. 2.10(c).

2.7.2. LEVER ARMS IN AN INAS-AL NANOWIRE

Another promising set of devices for the creation of Majorana zero modes is an epitaxial InAs-Al semiconductor–superconductor nanowire. These systems exhibit a hard superconducting gap and a high interface quality due to the epitaxial growth of the Al superconductor shell [30].

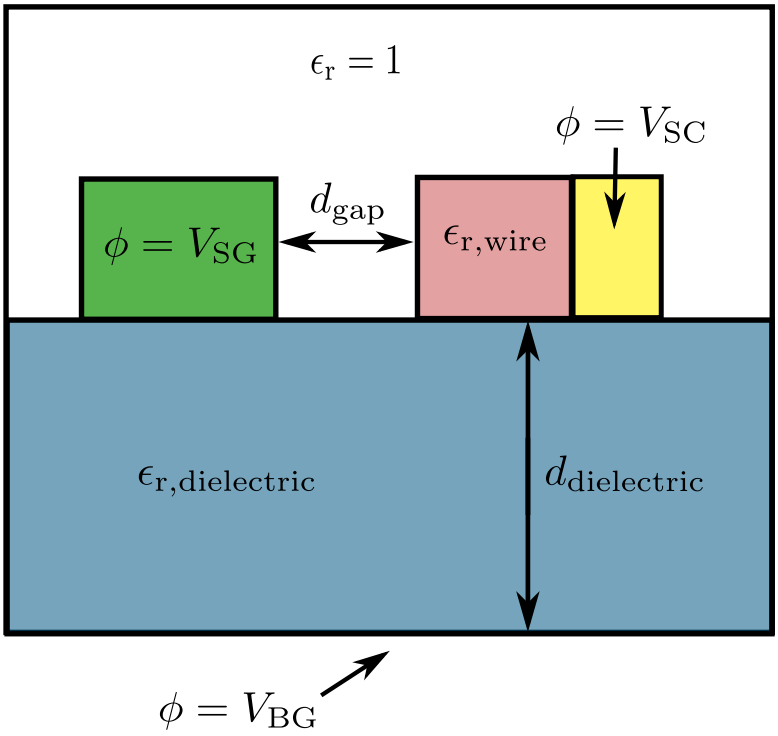

Figure 2.11: Schematic picture of the cross section of an InAs-Al device. It consists of a nanowire with a square cross section on a dielectric layer which covers a global back gate. A superconducting lead covers one side of the wire. A vacuum gap separates the wire from a second gate.

Figure 2.11 shows a cross section of the device. The $\epsilon_r = 14.6$ nanowire (InAs) lies on an $\epsilon_r = 4$ dielectric layer (SiO_2) of thickness $d_{\text{dielectric}} = 200\,\text{nm}$ and is connected on one side to an Al superconducting shell. The device has two gates: a global back-gate with a gate potential V_{BG}, and a side gate with a potential V_{SG}, separated by a vacuum gap of width d_{gap}. We model the superconductor again as a metal with a fixed potential V_{SC}. These three potentials form the boundary conditions of the system.

We estimate the dependence of the lever arm of the side date dE/dV_{SG} on d_{gap} using the self-consistent Schrödinger-Poisson simulations. We set the back gate to $V_{BG} = -3.5\,\text{V}$, and choose the work function difference of the Al shell equal to $0.26\,\text{eV}$, such that one electron mode is present at a side gate voltage of $V_{SG} = -2\,\text{V}$, with $d_{gap} = 145\,\text{nm}$, as was observed in experiments [31]. We use the band gap $0.36\,\text{eV}$ for InAs.

Our results are shown in Fig. 2.12, and allow to translate the gate voltages into the nanowire chemical potential. The work for the InAs-Al device shows that our numerical algorithm is easily adjusted to different device geometries, as long as the nanowire stays translationally invariant.

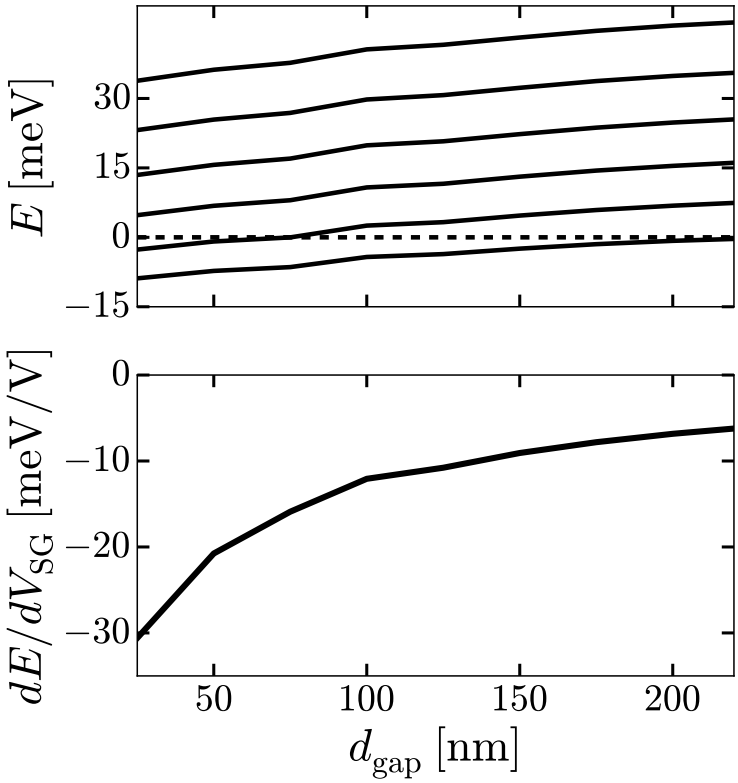

Figure 2.12: Top panel: six lowest energy levels with a fixed gate potential $V_{\mathrm{BG}} = V_{\mathrm{SG}} = 0\,\mathrm{V}$. Bottom panel: lever arm in the InAs-Al device as a function of gate spacing with $V_{\mathrm{BG}} = 0\,\mathrm{V}$.

2.7.3. ELECTRON DENSITY IN A NANOWIRE

Integration over the 1D density of states yields the electron density $n(E, E_{\mathrm{Z}}, \alpha)$, related to the charge density by Eq. (2.3). To derive the density of states, we start from the nanowire Hamiltonian, consisting of the transverse Hamiltonian of Eq. (2.1) and the longitudinal Hamiltonian of Eq. (2.2):

$$\mathcal{H} = \left(-\frac{\hbar^2}{2m^*}\nabla^2 - e\phi(x,y)\right)\sigma_0 - i\alpha\frac{\partial}{\partial z}\sigma_y + E_{\mathrm{Z}}\sigma_z. \tag{2.23}$$

Assuming that the wave function has the form of a plane wave $\propto e^{ikz}$ in the longitudinal direction, and quantized transverse modes ψ_i with corresponding energies E_i in the transverse direction (where i denotes the transverse mode number), the energies of the Hamiltonian are

$$E(k) = E_i + \frac{\hbar^2 k^2}{2m^*} \pm \sqrt{E_{\mathrm{Z}}^2 + \alpha^2 k^2}, \tag{2.24}$$

yielding the dispersions of the upper and the lower spin band. Converting Eq. (2.24) to momentum as a function of energy yields

$$k_{\pm}(E, E_i, E_{\rm Z}, \alpha) = \frac{1}{\sqrt{2}}\sqrt{\alpha^2 + 2(E - E_i) \pm \sqrt{\alpha^4 + 4\alpha^2(E - E_i) + 4E_{\rm Z}^2}}, \quad (2.25)$$

where α, E, $E_{\rm Z}$, and E_i are in units of $\hbar^2/2m^*$. The relation between the density of states $D(E)$ and k is

$$D(E) = \frac{1}{\pi}\frac{dk}{dE}. \quad (2.26)$$

We obtain the density $n(E_i, E_{\rm Z}, \alpha)$ by integrating the density of states up to the Fermi level $E_{\rm F} \equiv 0$. The Zeeman field opens a gap of size $2E_{\rm Z}$ between the upper and the lower spin band. Due to the W-shape of the lower spin band, induced by the spin-orbit interaction, we distinguish three energy regions in integrating up to $E_{\rm F}$. If $-E_i > E_{\rm Z}$, both spin bands are occupied and the integration yields

$$n(E_i, E_{\rm Z}, \alpha) = \frac{1}{\pi}(k_+(E_{\rm F}, E_i, E_{\rm Z}, \alpha) + k_-(E_{\rm F}, E_i, E_{\rm Z}, \alpha)). \quad (2.27)$$

If $-E_{\rm Z} < -E_i < E_{\rm Z}$, only the lower band is occupied, and the dispersion has two crossings with the Fermi level, yielding a density

$$n(E_i, E_{\rm Z}, \alpha) = \frac{1}{\pi}k_+(E_{\rm F}, E_i, E_{\rm Z}, \alpha). \quad (2.28)$$

For a nonzero spin-orbit strength, we have four crossings of the lower spin band with $E_{\rm F}$ if $-E_i < -E_{\rm Z}$ (see Fig. 2.5, bottom panel). Since only the interval $k_- \leq k \leq k_+$ contributes to the density, integration of the density of states yields

$$n(E_i, E_{\rm Z}, \alpha) = \frac{1}{\pi}(k_+(E_{\rm F}, E_i, E_{\rm Z}, \alpha) - k_-(E_{\rm F}, E_i, E_{\rm Z}, \alpha)). \quad (2.29)$$

Equations (2.27), (2.28), and (2.29) provide analytic expressions for the electron density. We use these equations to calculate the charge density of Eq. (2.3).

2.7.4. RESPONSE TO THE ZEEMAN FIELD IN THE CONSTANT DENSITY LIMIT AND FOR SMALL SPIN-ORBIT

The limit of small spin-orbit interaction and constant electron density in the nanowire independent of Zeeman field allows for an analytic solution the magnetic field dependence of the chemical potential, $\mu = \mu(E_{\rm Z})$. In particular, we have from Eqs. (2.27) and (2.29) for $\mu(E_{\rm Z} = 0) = \mu_0 > 0$:

$$\frac{2\sqrt{2m^*}}{\pi\hbar}\sqrt{\mu_0} = \frac{\sqrt{2m^*}}{\pi\hbar}\left(\sqrt{\mu + E_{\rm Z}} + \theta(\mu - E_{\rm Z})\sqrt{\mu - E_{\rm Z}}\right), \quad (2.30)$$

where θ is the Heaviside step function. This is readily solved as

$$\mu = \begin{cases} \mu_0 + E_{\rm Z}^2/(4\mu_0) & \text{for } E_{\rm Z} < 2\mu_0, \\ 4\mu_0 - E_{\rm Z} & \text{for } E_{\rm Z} > 2\mu_0. \end{cases} \quad (2.31)$$

Hence, the chemical potential first increases with increasing E_Z until the upper spin-band is completely depopulated. Then the chemical potential decreases linearly with E_Z. At the cross-over point the dependence of the chemical potential is not smooth but exhibits a kink, also seen for example in the numerical results of Fig. 2.6.

In the constant density limit we can also compute the asymptotes of the topological phase in μ-E_Z-space. For $E_Z \gg \Delta$, the topological phase coincides with the chemical potential range where only one spin subband is occupied. From Eq. (2.31) we find the two asymptotes thus as $\mu = 0$ and $\mu = E_Z/2$. Hence, in the constant density limit, the phase boundary that corresponds to depleting the wire becomes magnetic field independent.

2.7.5. BENCHMARK OF NONLINEAR OPTIMIZATION METHODS

We apply the Anderson mixing scheme to solve the coupled nonlinear Schrödinger-Poisson equation:

$$\begin{cases} \nabla^2\phi(x,y) = -\rho(\psi_i(x,y), E_i)/\epsilon \\ \mathcal{H}[\phi(x,y)]\psi_i(x,y) = E_i\psi_i(x,y) \end{cases} . \tag{2.32}$$

Optimization methods find the root of the functional form of Eq. (2.32), as given in Eq. (2.5). As opposed to other methods, the Anderson method uses the output of the last M rounds as an input to the next iteration step instead of only the output of the last round [29]. The memory of the Anderson method prevents the iteration scheme from oscillations and causes a significant speedup in computation times in comparison to other methods, and in particular the simple under-relaxation method often used in nanowire simulations [32, 33].

As a test system, we take a global back gate device, consisting of a hexagonal InSb nanowire on an $\epsilon_r = 4$ dielectric layer (SiO_2) of thickness $285\,\mathrm{nm}$, without a superconducting lead. Due to the thick dielectric layer in comparison to the Majorana device, this device is more sensitive for charge oscillations (a different number of electron modes in the system between two adjacent iteration steps). This makes the device well-suited for a performance benchmark. We compare the Anderson method to three other nonlinear optimization methods: Broyden's First and Second method [34] and a method implementing a Newton-Krylov solver (BiCG-stab) [35].

Figure 2.13 shows the results. In this plot, we show the cumulative minimum of the error. Plateaus in the plot correspond to regions of error oscillations. The figure shows that the Anderson method generally converges quickly and is not affected by error oscillations. However, the three other methods show oscillatory behavior of the error over a large range of iterations. Both Broyden's methods perform worse than the Anderson method, but generally converge within $\sim 10^3$ iterations. The Newton-Krylov method performs the worst, having a large region of oscillations up to $\sim 10^3 - 10^4$ iterations. Due to its robustness against error oscillations, the Anderson method is the most suited optimization method for the Schrödinger-Poisson problem. For a much thinner dielectric layer, such as the 30 nm layer in the Majorana device, the iteration number is typically $\sim 10^1$ for all four tested optimization methods.

In our approach, we choose not to use a predictor-corrector approach [36, 37] that can also be used together with a more advanced nonlinear solver such as

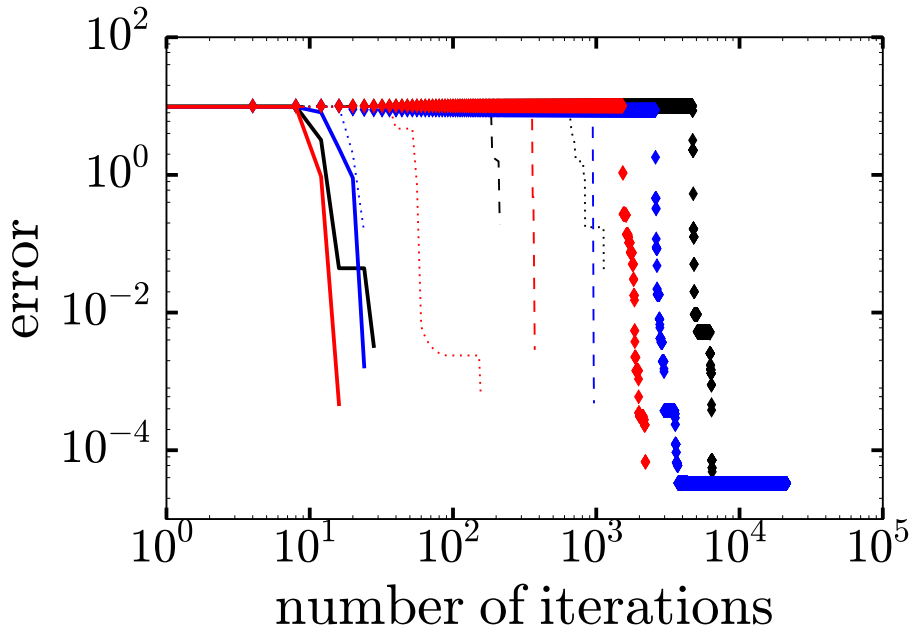

Figure 2.13: Benchmark of the Anderson solver (solid lines) with the First Broyden's method (dashed lines), the Second Broyden's method (dotted lines) and the BiCG-stab Newton-Krylov method (diamond markers). Black, blue and red colors correspond to a gate voltage $V_G = 0.3$, 0.4, and $0.5\,\mathrm{V}$ respectively. We show the cumulative minimum of the error.

the Anderson method [38]. The advantage of the direct approach used here is its simplicity, without a significant compromise in stability and efficiency.

REFERENCES

[1] L. Fu and C. L. Kane, *Superconducting Proximity Effect and Majorana Fermions at the Surface of a Topological Insulator,* Phys. Rev. Lett. **100**, 096407 (2008).

[2] J. Alicea, *New directions in the pursuit of Majorana fermions in solid state systems,* Rep. Prog. Phys. **75**, 076501 (2012).

[3] C. Beenakker, *Search for Majorana Fermions in Superconductors,* Annu. Rev. Con. Mat. Phys. **4**, 113 (2013).

[4] J. Alicea, Y. Oreg, G. Refael, F. von Oppen, and M. P. A. Fisher, *Non-Abelian statistics and topological quantum information processing in 1D wire networks,* Nat. Phys. (2011).

[5] C. Nayak, S. H. Simon, A. Stern, M. Freedman, and S. Das Sarma, *Non-Abelian anyons and topological quantum computation,* Rev. Mod. Phys. **80**, 1083 (2008).

[6] Y. Oreg, G. Refael, and F. von Oppen, *Helical Liquids and Majorana Bound States in Quantum Wires,* Phys. Rev. Lett. **105**, 177002 (2010).

[7] R. M. Lutchyn, J. D. Sau, and S. Das Sarma, *Majorana Fermions and a Topological Phase Transition in Semiconductor-Superconductor Heterostructures,* Phys. Rev. Lett. **105**, 077001 (2010).

[8] V. Mourik, K. Zuo, S. M. Frolov, S. R. Plissard, E. P. A. M. Bakkers, and L. P. Kouwenhoven, *Signatures of Majorana Fermions in Hybrid Superconductor-Semiconductor Nanowire Devices,* Science **336**, 1003 (2012).

[9] A. Das, Y. Ronen, Y. Most, Y. Oreg, M. Heiblum, and H. Shtrikman, *Zero-bias peaks and splitting in an Al-InAs nanowire topological superconductor as a signature of Majorana fermions,* Nat. Phys. **8**, 887 (2012).

[10] M. T. Deng, C. L. Yu, G. Y. Huang, M. Larsson, P. Caroff, and H. Q. Xu, *Anomalous Zero-Bias Conductance Peak in a Nb–InSb Nanowire–Nb Hybrid Device,* Nano Lett. **12**, 6414 (2012).

[11] H. O. H. Churchill, V. Fatemi, K. Grove-Rasmussen, M. T. Deng, P. Caroff, H. Q. Xu, and C. M. Marcus, *Superconductor-nanowire devices from tunneling to the multichannel regime: Zero-bias oscillations and magnetoconductance crossover,* Phys. Rev. B **87**, 241401 (2013).

[12] M. Deng, C. Yu, G. Huang, M. Larsson, P. Caroff, and H. Xu, *Parity independence of the zero-bias conductance peak in a nanowire based topological superconductor-quantum dot hybrid device,* Sci. Rep. **4**, 7621 (2014).

[13] D. Bagrets and A. Altland, *Class D Spectral Peak in Majorana Quantum Wires,* Phys. Rev. Lett. **109**, 227005 (2012).

[14] D. I. Pikulin, J. P. Dahlhaus, M. Wimmer, H. Schomerus, and C. W. J. Beenakker, *A zero-voltage conductance peak from weak antilocalization in a Majorana nanowire,* New J. Phys. **14**, 125011 (2012).

[15] T. Stanescu, S. Tewari, J. Sau, and S. Das Sarma, *To Close or Not to Close: The Fate of the Superconducting Gap across the Topological Quantum Phase Transition in Majorana-Carrying Semiconductor Nanowires,* Phys. Rev. Lett. **109**, 266402 (2012).

[16] B. Fregoso, A. Lobos, and S. Das Sarma, *Electrical detection of topological quantum phase transitions in disordered Majorana nanowires,* Phys. Rev. B **88**, 180507(R) (2013).

[17] M. Cheng, R. Lutchyn, V. Galitski, and S. Das Sarma, *Splitting of Majorana modes due to intervortex tunneling in a $p + ip$ superconductor,* Phys. Rev. Lett. **103**, 107001 (2009).

[18] M. Cheng, R. Lutchyn, V. Galitski, and S. Das Sarma, *Tunneling of anyonic Majorana excitations in topological superconductors,* Phys. Rev. B **82**, 094504 (2010).

[19] E. Prada, P. San-Jose, and R. Aguado, *Transport spectroscopy of NS nanowire junctions with Majorana fermions,* Phys. Rev. B **86**, 180503 (2012).

[20] S. Das Sarma, J. D. Sau, and T. D. Stanescu, *Splitting of the zero-bias conductance peak as smoking gun evidence for the existence of the Majorana mode in a superconductor-semiconductor nanowire,* Phys. Rev. B **86**, 220506 (2012).

[21] D. Rainis, L. Trifunovic, J. Klinovaja, and D. Loss, *Towards a realistic transport modeling in a superconducting nanowire with Majorana fermions,* Phys. Rev. B **87**, 024515 (2013).

[22] D. Haneman, *Photoelectric emission and work functions of InSb, GaAs, Bi2Te3 and germanium,* J. Phys. Chem. Solids **11**, 205 (1959).

[23] R. G. Wilson, *Vacuum Thermionic Work Functions of Polycrystalline Nb, Mo, Ta, W, Re, Os, and Ir,* J. Appl. Phys. **37**, 3170 (1966).

[24] M. Scheid, İnanç Adagideli, J. Nitta, and K. Richter, *Anisotropic universal conductance fluctuations in disordered quantum wires with Rashba and Dresselhaus spin–orbit interaction and an applied in-plane magnetic field,* Semicond. Sci. Tech. **24**, 064005 (2009).

[25] M. Diez, J. P. Dahlhaus, M. Wimmer, and C. W. J. Beenakker, *Andreev reflection from a topological superconductor with chiral symmetry,* Phys. Rev. B **86**, 094501 (2012).

[26] B. Nijholt and A. R. Akhmerov, *Orbital effect of magnetic field on the Majorana phase diagram,* Phys. Rev. B **93**, 235434 (2016).

[27] C. Groth, M. Wimmer, A. Akhmerov, and X. Waintal, *Kwant: a software package for quantum transport,* New J. Phys. **16**, 063065 (2014).

[28] A. Logg, K. Mardal, and G. Wells, *Automated Solution of Differential Equations by the Finite Element Method* (Springer, 2012).

[29] V. Eyert, *A Comparative Study on Methods for Convergence Acceleration of Iterative Vector Sequences,* J. Comp. Phys. **124**, 271 (1996).

[30] W. Chang, S. Albrecht, T. Jespersen, F. Kuemmeth, P. Krogstrup, J. Nygård, and C. Marcus, *Hard gap in epitaxial semiconductor–superconductor nanowires,* Nat. Nanotechnol. **10**, 232 (2015).

[31] M. Deng, private communication (2015).

[32] L. Wang, D. Wang, and P. M. Asbeck, *A numerical Schrödinger–Poisson solver for radially symmetric nanowire core–shell structures,* Solid-State Electron. **50**, 1732 (2006).

[33] S. Chin, V. Ligatchev, S. Rustagi, H. Zhao, G. Samudra, N. Singh, G. Lo, and D.-L. Kwong, *Self-Consistent Schrödinger-Poisson Simulations on Capacitance-Voltage Characteristics of Silicon Nanowire Gate-All-Around MOS Devices with Experimental Comparisons,* IEEE Trans. Electron Dev. **56**, 2312 (2009).

[34] C. Broyden, *A class of methods for solving nonlinear simultaneous equations,* Math. Comp. **19**, 577 (1965).

[35] D. Knoll and D. Keyes, *Jacobian-free Newton–Krylov methods: a survey of approaches and applications,* J. Comp. Phys. **193**, 357 (2004).

[36] A. Trellakis, A. Galick, A. Pacelli, and U. Ravaioli, *Iteration schema for the solution of the two-dimensional Schrödinger-Poisson equations in quantum structures,* J. Appl. Phys. **81**, 7880 (1997), cited By 177.

[37] G. Curatola and G. Iannaccone, *NANOTCAD2D: Two-dimensional code for the simulation of nanoelectronic devices and structures,* Comput. Mater. Sci. **28**, 342 (2003).

[38] H. Wang, G. Wang, S. Chang, and Q. Huang, *Accelerated solution of Poisson-Schrödinger equations in nanoscale devices by Anderson mixing scheme,* Micro Nano Lett. **4**, 122 (2009).

3

Conductance through a helical state in an InSb nanowire

This chapter has been previously published as J. Kammhuber, M. C. Cassidy, F. Pei, M. P. Nowak, A. Vuik, Ö. Gül, D. Car, S. R. Plissard, E. P. A. M Bakkers, M. Wimmer, and L. P. Kouwenhoven, *Conductance through a helical state in an Indium antimonide nanowire*, Nat. Comm. **8**, 478 (2017).

3.1. INTRODUCTION

Spin-orbit interaction (SOI) is a relativistic effect where a charged particle moving in an electric field E with momentum k and velocity $v = k/m_0$, experiences an effective magnetic field $B_{\text{SO}} = (-1/m_0 c)k \times E$ in its rest frame. The magnetic moment of the electron spin, $\mu = eS/m_0$, interacts with this effective magnetic field, resulting in a spin-orbit Hamiltonian $H_{\text{SO}} = -\mu.B_{\text{SO}}$ that couples the spin to the orbital motion and electric field. In crystalline materials, the electric field arises from a symmetry breaking that is either intrinsic to the underlying crystal lattice in which the carriers move, known as the Dresselhaus SOI [1], or an artificially induced asymmetry in the confinement potential due to an applied electric field, or Rashba SOI [2]. Wurtzite and certain zincblende nanowires possess a finite Dresselhaus SOI, and so the SOI is a combination of both the Rashba and Dresselhaus components. For zincblende nanowires grown along the [111] growth direction the crystal lattice is inversion symmetric, and so only a Rashba component to the spin-orbit interaction is thought to remain [3].

Helical states have been shown to emerge in the edge mode of 2D quantum spin hall topological insulators [4, 5], and in quantum wires created in GaAs cleaved edge overgrowth samples [6]. They have also been predicted to exist in carbon nanotubes under a strong applied electric field [7], RKKY systems [8], and in InAs and InSb semiconducting nanowires where they are essential for the formation of Majorana zero modes. Although the signatures of Majoranas have been observed in nanowire-superconductor hybrid devices [9, 10], explicit demonstration of the helical state in these nanowires has remained elusive. The measurement is expected to show a distinct experimental signature of the helical state - a return to $1e^2/h$ conductance at the $2e^2/h$ plateau in increasing magnetic field as different portions of the band dispersion are probed [11–13]. While ballistic transport through nanowire QPCs is now standard [14, 15], numerical simulations have shown that the visibility of this experimental signature critically depends on the exact combination of geometrical and physical device parameters [13].

Here we observe a clear signature of transport through a helical state in a QPC formed in an InSb nanowire when the magnetic field has a component perpendicular to the spin-orbit field. We show that the state evolves under rotation of the external magnetic field, disappearing when the magnetic field is aligned with B_{SO}. By comparing our data to a theoretical model, we extract a spin-orbit energy $E_{\text{SO}} = 6.5\,\text{meV}$, significantly stronger than that measured in InSb nanowires by other techniques.

3.2. NUMERICAL SIMULATIONS OF THE CONDUCTANCE THROUGH A HELICAL STATE

3.2.1. POISSON CALCULATIONS IN A 3D NANOWIRE DEVICE

Observing the helical gap in a semiconducting nanowire crucially depends on the smoothness of the electrostatic potential profile between the two contacts [13]. When the potential profile changes too abruptly, it forms a tunnel barrier which suppresses conductance well below quantized values, thereby masking features of

the helical gap. On the other hand, if the potential varies on a length scale much larger than the characteristic spin-orbit coupling length l_{SO}, transmission through the 'internal state' (the smaller-momentum state of the two right-moving states in the bottom of the lower band) is suppressed. This reduces the first $2e^2/h$ plateau in the conductance to a $1e^2/h$ plateau, thereby concealing again the helical gap.

Because of the crucial role of the electrostatic potential, we perform realistic Poisson calculations to compute the potential $\phi(\vec{r})$ in the nanowire (with $\vec{r} = (x, y, z)$), solving the Poisson equation of the general form

$$\nabla^2 \phi(\vec{r}) = -\frac{\rho(\vec{r})}{\epsilon}, \tag{3.1}$$

with ϵ the dielectric permittivity and ρ the charge density. For the charge density ρ, we apply the Thomas-Fermi approximation [16]

$$\rho(\vec{r}) = \frac{e}{3\pi^2 \epsilon} \left(\frac{2m^* e \phi(\vec{r})}{\hbar^2} \right)^{3/2}, \tag{3.2}$$

where m^* is the effective mass of InSb.
For a given charge density ρ, we solve Eq. (3.1) numerically for the potential using the finite element method (FEM) package FEniCS [17]. We model the two normal contacts as metals with a fixed potential $V_{\mathrm{N}} = 0.22$ V, assuming a small work function difference between the nanowire and the normal contacts. The back gate is modeled as a fixed potential V_{G} along the bottom surface of the dielectric layer. We use the dielectric permittivities for InSb and SiN in the wire and the dielectric layer respectively. The FEM mesh, with its dimensions and boundary conditions, is depicted in Fig. 3.1(a). We apply the Anderson mixing scheme [18] to solve the nonlinear equation formed by Eqs. (3.1) and (3.2) self-consistently. An example of a self-consistent Poisson potential with Thomas-Fermi density is plotted in Fig. 3.1(b).

3.2.2. CONDUCTANCE CALCULATIONS IN A 1D MODEL WITH A PROJECTED POTENTIAL BARRIER

To apply the 3D Poisson potential in a simple 1D nanowire model, we convert the three-dimensional potential $\phi(x, y, z)$ to a one-dimensional effective potential barrier $\hat{\phi}(x)$ by projecting ϕ on the transverse wave functions $\psi(y, z)$ in the nanowire:

$$\hat{\phi}(x) = \langle \psi(y, z) | \phi(x, y, z) | \psi(y, z) \rangle. \tag{3.3}$$

To do this, we compute the eigenenergies of the Hamiltonian of a two-dimensional cross section at a point x_0 along the wire, with a corresponding potential $\phi(x_0, y, z)$. The effective potential barrier is then given by the ground state of the Hamiltonian. The longitudinal variation of the potential barrier is obtained by computing the ground state of the transverse Hamiltonian at many points along the wire. An example of the projected potential is given in Fig. 3.1(c) with the solid-black curve.

Due to rough boundary conditions in the FEM mesh (see the edges of the dielectric layer and the normal contacts in the potential of Fig. 3.1(b), the projected potential

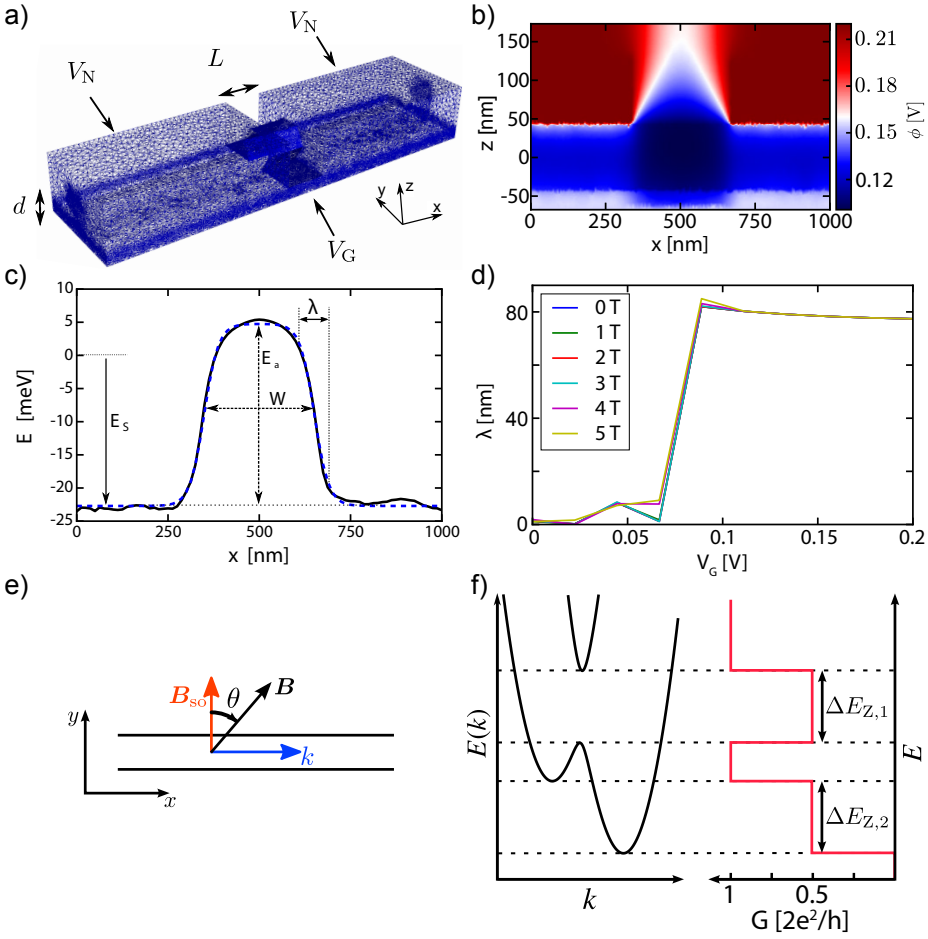

Figure 3.1: (a): Example of a finite element mesh used for 3D Poisson calculations. L denotes the QPC length (spacing between the two contacts), d the thickness of the dielectric layer, which is set to $20\,\mathrm{nm}$. L is set to $325\,\mathrm{nm}$ for the simulations in the main text, and varied from 175 to $425\,\mathrm{nm}$ to show the length dependence of the helical gap feature in Fig. 3.11. The two boundary conditions applied are a potential V_N on the contacts and a potential V_G underneath the dielectric layer. The mesh between the two contacts is left out for visibility purposes. (b): Cross section plot of the 3D Poisson potential for $V_\mathrm{G} = 0.156\,\mathrm{V}$ and $V_\mathrm{N} = 0.22\,\mathrm{V}$. The cross section is taken along the wire axis (x-axis) for fixed $y = 0\,\mathrm{nm}$ in the middle of the wire. The effective QPC length runs from ~ 340 to $\sim 660\,\mathrm{nm}$. The nanowire is situated between $z = -50\,\mathrm{nm}$ and $z = 50\,\mathrm{nm}$. (c): Projected potential $\hat{\phi}(x)$ (black curve) and fitted potential $V(x)$ (blue dashed curve) for $V_\mathrm{G} = 0.156\,\mathrm{V}$, corresponding to the potential of Fig. 3.1(b). Indicated are the fitting parameters E_s, E_a, W and λ of the function Eq. (3.4). (d): The fitting parameter λ as a function of back gate voltage V_G. Different colors denote different magnetic field strengths B. A jump in $\lambda \approx 0$ (abrupt step potential) to $\lambda \approx 80\,\mathrm{nm}$ occurs when charge enters the wire, screening the electric field. (e): Rashba nanowire in an external magnetic field: the one-dimensional nanowire is oriented along the x-axis, and the spin-orbit field B_SO perpendicular, along the y-axis. The external magnetic field B forms an angle θ with respect to B_SO. (f): Schematic picture of the band structure $E(k)$ of a Rashba nanowire in a magnetic field (left panel) and the corresponding quantum point conductance G (right panel).

$\hat{\phi}(x)$ shows some roughness that may cause unwanted scattering events (see black curve in Fig. 3.1(c). To avoid this, we fit $\hat{\phi}(x)$ to a linear combination of hyperbolic tangents, given by

$$V(x) = \frac{E_\mathrm{a}}{2}\left[\tanh\left(\frac{x - x_\mathrm{s} + W/2}{\lambda/2}\right) - \tanh\left(\frac{x - x_\mathrm{s} - W/2}{\lambda/2}\right)\right] + E_\mathrm{s}. \tag{3.4}$$

Here, E_a is the amplitude, W the width and E_s the downshift in energy of the potential barrier, which varies along x on a typical length scale λ, as indicated in Fig. 3.1(c). The horizontal shift of the barrier to the middle of the nanowire is denoted by $x_\mathrm{s} = 500\,\mathrm{nm}$.

The parameter λ expresses the smoothness of the barrier. We find that λ is close to zero when no charge is present in the wire and the boundary conditions result in an abrupt step in the potential between the contacts and the uncovered part of the wire. When charge enters the wire, it screens the electric field, thereby smoothening the potential. For a QPC length of $325\,\mathrm{nm}$ we find in this regime $\lambda \approx 80\,\mathrm{nm}$. The value of λ is reduced for smaller QPC lengths, but saturates to $\lambda \approx 80\,\mathrm{nm}$ for longer QPC lengths. Moreover we find that λ has only a little dependency on the back gate voltage V_G or the applied magnetic field B (Fig. 3.1(d). Taking advantage of the latter and the fact that we are interested in the conductance of the wire in the vicinity of the helical-gap feature – where the screening *is* present – we assume λ constant in V_G and B space for the conductance calculation.

For the conductance calculations we consider transport through a two-mode nanowire described by the Hamiltonian

$$\mathcal{H} = \left[\frac{\hbar^2 k_x^2}{2m^*} + V(x)\right]\sigma_0 + \alpha\sigma_y k_x + \frac{1}{2}g\mu_B B(\sigma_x \sin\theta + \sigma_y \cos\theta), \tag{3.5}$$

where σ denote the Pauli matrices (with σ_0 the identity matrix) and $V(x)$ is fit to the projected potential barrier, as expressed in Eqs. (3.3) and (3.4). Spin-orbit coupling strength is given by $\alpha = \hbar^2/m^* l_\mathrm{SO}$ where l_SO we use as a free parameter. We take the effective mass $m^* = 0.014 m_0$ of InSb and $g = 38$ (unless stated otherwise) as estimated in the main text. Note that for the coordinate system used here, where the wire lies along the x direction and θ is the angle between B_{SO} and the external magnetic field. The Hamiltonian Eq. (3.5) is discretized on a mesh with lattice spacing $\Delta x = 4\,\mathrm{nm}$. Assuming translational invariance of the boundary conditions at the ends of the wire one arrives at the scattering problem that is solved using the Kwant package [19] to obtain the linear-response conductance within the Landauer-Büttiker formalism.

3.3. DEVICE LAYOUT

Figure 3.2(a) shows a schematic image of a typical QPC device. An InSb nanowire is deposited on a degenerately doped silicon wafer covered with a thin ($20\,\mathrm{nm}$) SiN dielectric. The QPC is formed in the nanowire channel in a region defined by the source and drain contacts spaced $\sim 325\,\mathrm{nm}$ apart. The chemical potential μ in the QPC channel, which sets the subband occupation, is controlled by applying a voltage

to the gate V_g. The electric field in the nanowire, E, generated by the backgate and the substrate that the nanowire lies on, both induce a structural inversion asymmetry that results in a finite Rashba spin-orbit field. As the wire is translationally invariant along its length, the spin-orbit field, B_{SO}, is perpendicular to both the electric field and the wire axis. The effective channel length, $L_{QPC} \sim 245\,\mathrm{nm}$, as well as the shape of the onset potential $\lambda \sim 80\,\mathrm{nm}$ are set by electrostatics which are influenced by both the thickness of the dielectric and the amount of electric field screening provided by the metallic contacts to the nanowire, see Fig. 3.2(b). Here we report measurements from one device. Data from an additional device that shows the same effect, as well as control devices of different channel lengths and onset potentials, is provided in the Appendix.

The energy-momentum diagrams in Fig. 3.2(c)–(e) show the dispersion from the 1D nanowire model of Refs. [11] and [12] including both SOI with strength α and Zeeman splitting $E_Z = g\mu_B B$, where g is the g-factor, μ_B the Bohr magneton and B the magnetic field strength. These dispersion relations explain how the helical gap can be detected: Without magnetic field, the SOI causes the first two spin degenerate subbands to be shifted laterally in momentum space by $\pm k_{SO} = m^*\alpha/\hbar^2$ with m^* the effective electron mass, as electrons with opposite spins carry opposite momentum, as shown in Fig. 3.2(c). The corresponding spin-orbit energy is given by $E_{SO} = \hbar^2 k_{SO}^2/2m^*$. However, here Kramers degeneracy is preserved and hence the plateaus in conductance occur at integer values of $G_0 = 2e^2/h$, as for a system without SOI. Applying a magnetic field perpendicular to B_{SO} the spin bands hybridize and a helical gap of size E_Z opens, as shown in Fig. 3.2(d). When the chemical potential μ is tuned by the external gate voltage, it first aligns with the bottom of both bands resulting in conductance at $1 \cdot G_0$ before reducing from $1 \cdot G_0$ to $0.5 \cdot G_0$ when μ is positioned inside the gap. This conductance reduction with a width scaling linearly with increasing Zeeman energy, is a hallmark of transport through a helical state. When the magnetic field is orientated at an angle θ to B_{SO}, the size of the helical gap decreases as it is governed by the component of the magnetic field perpendicular to B_{SO}, as shown in Fig. 3.2(e). Additionally, the two subband bottoms also experience a spin splitting giving rise to an additional Zeeman gap. For a general angle θ, the QPC conductance first rises from 0 to $0.5 \cdot G_0$, then to $1 \cdot G_0$, before dropping to $0.5 \cdot G_0$ again. The helical gap thus takes the form of a re-entrant $0.5 \cdot G_0$ conductance feature. By comparing to a 1D nanowire model, we can extract both the size of the helical gap $E_{helical} \approx E_Z \sin\theta$ and the Zeeman shift $E_{Zeeman} \approx E_Z \cos\theta$ (see Appendix). This angle dependency is a unique feature of SOI and can be used as a decisive test for its presence in the experimental data.

3.4. LINEAR MAGNETIC FIELD

Figure 3.3 shows the differential conductance dI/dV of our device at zero source-drain bias as a function of gate and magnetic field. Here the magnetic field B is offset at a small angle $\theta = 17°$ from B_{SO} in the x-y plane, see Fig. 3.3(a). We determine that our device has this orientation from the angle-dependence of the magnetic field, by clearly resolving the $1 \cdot G_0$ plateau before the re-entrant conductance feature, which is reduced at larger angles (see Appendix). For low magnetic fields, we observe

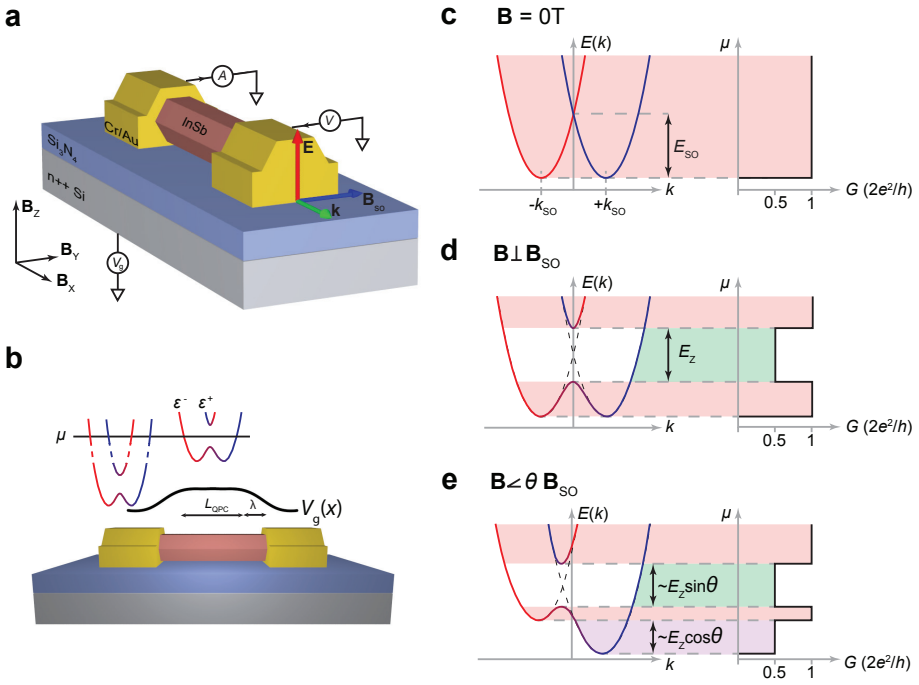

Figure 3.2: The helical gap in a 1D nanowire device. (a): An InSb nanowire device with a Rashba spin-orbit field B_{SO} perpendicular to the wave vector k and the electric field E. A voltage is sourced to one contact, and the resulting conductance measured from the second contact. The chemical potential in the wire, μ, is tuned with a global backgate V_g. (b): The QPC channel of length L is defined by the two contacts. Underneath the nanowire contacts, many subbands are occupied as the contacts screen the gate electric field. In the nanowire channel away from the contacts, the chemical potential in the wire, μ, is tuned with V_g. The onset shape of V_g with a lengthscale λ is set by the dielectric and screening of the electric field from the metallic contacts resulting in an effective QPC length $L_{QPC} = L - 2\lambda$. (c): The energy dispersion of the first two subbands for a system with SOI at external magnetic field $B = 0$. The SOI causes subbands to shift by k_{SO} in momentum space, as electrons with opposite spins carry opposite momentum. When the electrochemical potential μ in the wire is tuned conductance plateaus will occur at integer values of G_0. (d) At finite magnetic field B perpendicular to B_{SO}, the spin polarized bands hybridize opening a helical gap of size E_Z (green). In this region the conductance reduces from $1 \cdot G_0$ to $0.5 \cdot G_0$ when μ is positioned inside the gap. (e): When the magnetic field is orientated at an angle θ to B_{SO}, the size of the helical gap decreases to only include the component of the magnetic field perpendicular to B_{SO}. For all angles the reentrant conductance feature at $0.5 \cdot G_0$ in the $1 \cdot G_0$ plateau will scale linearly with Zeeman energy.

conductance plateaus quantized in steps of $0.5 \cdot G_0$, as typical for a QPC in a spin polarizing B-field with or without SOI. Above $B = 3\,\mathrm{T}$, the $1 \cdot G_0$ plateau shows a conductance dip to $0.5 \cdot G_0$. This reentrant conductance feature evolves continuously as a function of magnetic field, before fully enveloping the $1 \cdot G_0$ plateau for magnetic fields larger than around $5.5\,\mathrm{T}$. Line traces corresponding to the colored arrows in Fig. 3.3(b) are shown in Fig. 3.3(d). The feature is robust at higher temperatures up to 1K, as well across multiple thermal cycles (see Appendix). Using the 1D nanowire model with $\theta = 17°$ we find that the helical gap feature vanishes into a continuous

$0.5 \cdot G_0$ plateau when $E_Z > 2.4E_{SO}$. Using the extracted g-factor $g = 38$ of our device (see Fig. 3.4 and Appendix) we find a lower bound for the spin-orbit energy $E_{SO} = 5.5\,\mathrm{meV}$, corresponding to a spin-orbit length $l_{SO} = 1/k_{SO} \approx 22\,\mathrm{nm}$. For a second device, we extract a similar value $E_{SO} = 5.2\,\mathrm{meV}$. Recently it has been highlighted that the visibility of the helical gap feature depends crucially on the shape of the QPC potential [13]. To verify that our observation is compatible with SOI in this respect, we perform self-consistent simulations of the Poisson equation in the Thomas-Fermi approximation for our device geometry. The resulting electrostatic potential is then mapped to an effective 1D QPC potential for a quantum transport simulation using parameters for InSb (for details, see Appendix). These numerical simulations, shown in Fig. 3.3(c), fit best for $l_{SO} = 20\,\mathrm{nm}$ ($E_{SO} = 6.5\,\mathrm{meV}$) and agree well with the experimental observation, corroborating our interpretation of the re-entrant conductance feature as the helical gap.

Voltage bias spectroscopy, shown in Fig. 3.4(a), confirms that this state evolves as a constant energy feature. By analyzing the voltage bias spectroscopy data at a range of magnetic fields, we directly convert the development of the initial $0.5 \cdot G_0$ plateau, as well as the re-entrant conductance feature to energy (Fig. 3.4(b). From the evolution of the width of the first $0.5 \cdot G_0$ plateau, we can calculate the g-factor of the first subband $g = 38 \pm 1$. This number is consistent with the recent experiments, which reported g factors of $35 - 50$ [20, 21]. Comparing the slopes of the Zeeman gap and the helical gap $E_{\mathrm{helical}}/E_Z \approx \tan\theta$ provides an alternative way to determine the offset angle θ. We find $\theta = 13^\circ \pm 2^\circ$ which is in reasonable agreement with the angle determined by magnetic field rotation.

3.5. ROTATING MAGNETIC FIELD

To confirm that the re-entrant conductance feature agrees with spin-orbit theory, we rotate the magnetic field in the plane of the substrate at a constant magnitude $B = 3.3\,\mathrm{T}$, as shown in Fig. 3.5(a). When the field is rotated towards being parallel to B_{SO}, the conductance dip closes, while when it is rotated away from B_{SO}, the dip increases in width and depth. In contrast, when the magnetic field is rotated the same amount around the y-z plane, which is largely perpendicular to B_{SO}, there is little change in the re-entrant conductance feature, as shown in Fig. 3.5(b). Figure 3.5(c) shows the result of rotating through a larger angle in the x-y plane shows this feature clearly evolves with what is expected for spin-orbit. Our numerical simulations in Fig. 3.5(d) agree well with the observed experimental data. The small difference in the angle evolution between the numerical simulations and experimental data can be attributed to imperfect alignment of the substrate with the x-y plane.

3.6. CONCLUSIONS

The extracted SO energy of $6.5\,\mathrm{meV}$ is significantly larger than that obtained via other techniques, such as weak anti localization (WAL) measurements [22], and quantum dot spectroscopy [21]. This is not entirely unexpected, due to the differing geometry for this device and different conductance regime it is operated in. Quantum dot measurements require strong confinement, and so the Rashba SOI is modified by

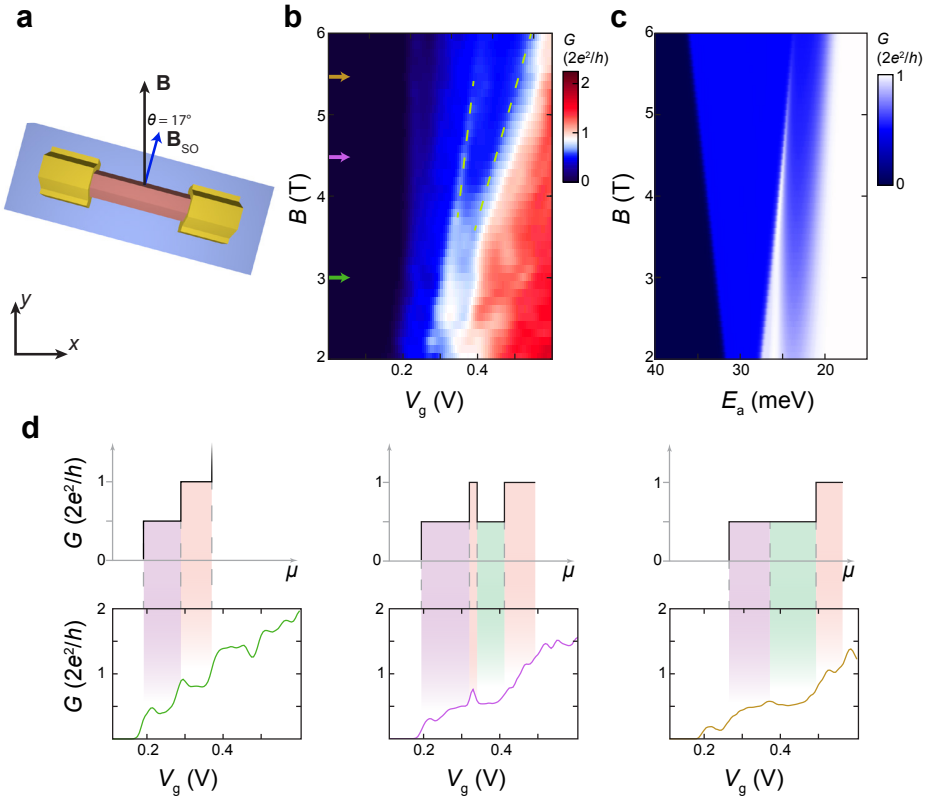

Figure 3.3: Magnetic field dependence of the helical gap. (a): The nanowire lies in the x-y plane at an angle $\theta = 17°$ relative to the external magnetic field. (b): Differential conductance dI/dV at zero source-drain bias as a function of back gate voltage and external magnetic field. At low magnetic fields conductance plateaus at multiples of $0.5 \cdot G_0$ are visible. Above $B = 3\,\mathrm{T}$, a reentrant conductance feature at $0.5 \cdot G_0$ appears in the $1 \cdot G_0$ plateau. The feature evolves linearly with Zeeman energy indicated by dashed green lines. (c): Numerical simulations of the differential conductance as a function of the potential $\mathrm{E_a}$ and external magnetic field for $L = 325\,\mathrm{nm}$, $\theta = 17°$ and $l_{\mathrm{SO}} = 20\,\mathrm{nm}$ (See Appendix for a more detailed description of the model). In the numerical simulations, the conductance plateaus have a different slope compared to the experimental data as the calculations neglect screening by charges in the wire. (d): Line traces of the conductance map in (b). As the helical gap is independent of disorder or interference effects, these and other anomalous conductance features average out in a 2D colorplot improving the visibility of the helical gap in (b) compared to the individual traces in (d).

the local electrostatic gates used to define the quantum dot. Weak anti-localization measurements are performed in an open conductance regime, however they assume transport through a diffusive, rather than a ballistic channel. Neither of these measurements explicitly probe the spin-orbit interaction where exactly one mode is transmitting in the nanowire, the ideal regime for Majoranas, and so the spin-orbit parameters extracted from QPC measurements offer a more accurate measurement of the SOI experienced by the Majorana zero mode. Also, the SOI in a nanowire can be different for every subband, and it is expected that the lowest mode has the

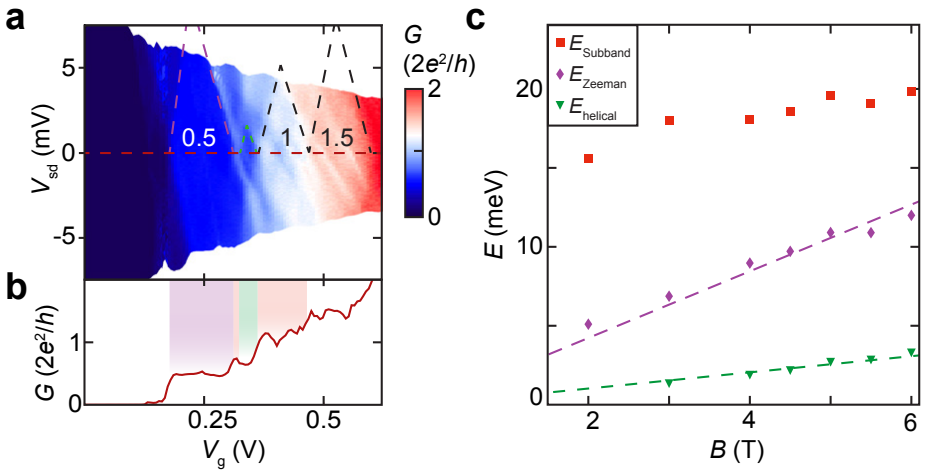

Figure 3.4: Voltage bias spectroscopy of the helical gap. (a): Conductance measurement as a function of QPC gate and source-drain bias voltage at $B = 4\,\mathrm{T}$. The observed helical gap (green) is a stable feature in voltage bias. Dotted lines are drawn as guide to the eye indicating the plateau edges. (b): Evolution of the energy levels extracted from scans similar to (a) at increasing magnetic field. Fits with intercept fixed at zero (dotted lines) give the g-factor of the first subband and the offset angle via $g = 1/(\mu_B \cos\theta) \cdot dE/dB$ and $E_{\mathrm{helical}}/E_{\mathrm{Zeeman}} \approx \tan\theta$. We find $g = 38 \pm 1$ and $\theta = 13° \pm 2°$. Individual scans are included in the Appendix.

strongest spin-orbit due to a smaller confinement energy [3]. Additionally, the finite diameter of the nanowire, together with impurities within the InSb crystal lattice [23] both break the internal symmetry of the crystal lattice and may contribute a non-zero Dresselhaus component to the spin-orbit energy that has not been previously considered. While high quality quantized conductance measurements have been previously achieved in short channel devices [14] ($L \sim 150\,\mathrm{nm}$), the channel lengths required for observing the helical gap are at the experimental limit of observable conductance quantization. As shown in the Appendix, small changes in the QPC channel length, spin-orbit strength or the QPC potential profile are enough to obscure the helical gap, particularly for wires with weaker SOI. We have fabricated and measured a range of QPCs with different length and potential profiles, and only two devices of $L \sim 300\,\mathrm{nm}$ showed unambiguous signatures of a helical gap. Possibly some of the other devices did not show clear signatures because they had weaker SOI.

Several phenomena have been reported to result in anomalous conductance features in a device such as this. Oscillations in conductance due to Fabry-Perot resonances are a common feature in clean QPCs. Typically the first oscillation at the front of each plateau is the strongest and the oscillations monotonically decrease in strength further along each plateau [13, 24]. In our second device, we clearly observe Fabry-Perot conductance oscillations at the beginning of each plateau, however these oscillations are significantly weaker than the subsequent conductance dip. Furthermore we observe Fabry-Perot oscillations at each conductance plateau, while

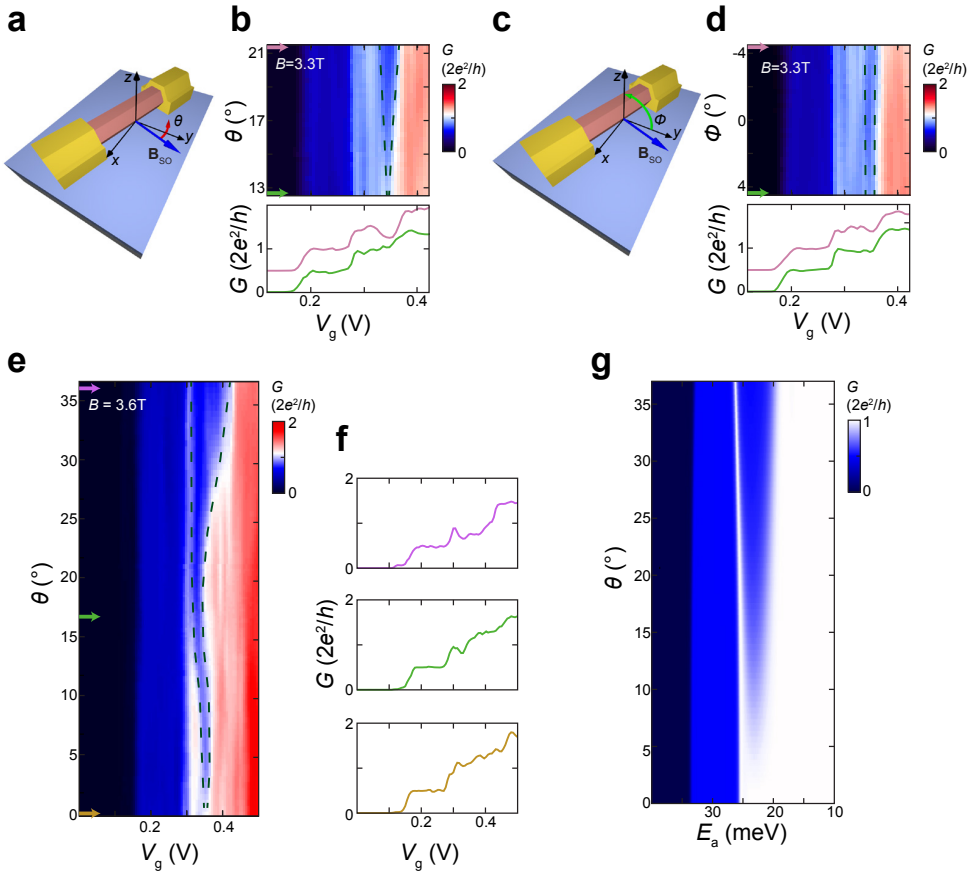

Figure 3.5: Angle dependence of the helical gap. (a) Rotation of the magnetic field at $B = 3.3\,\mathrm{T}$ in the x-y plane parallel to the substrate shows strong angle dependence of the helical gap. The conductance dip closes when B is rotated towards B_{SO} and opens when B is rotated away from B_{SO}. (b) Rotation of the magnetic field at $B = 3.3\,\mathrm{T}$ in the y-z plane, mostly perpendicular to B_{SO}. While the angle range is identical to (a), there is little change in the conductance dip. (c) Rotation of the magnetic field at $B = 3.6\,\mathrm{T}$ in the x-y plane over a large angle range. The conductance dip disappears when B is parallel to B_{SO} which gives the exact offset angle between B_{SO} and B_{Z}, $\theta = 17°$. (d) Numerical simulations of the differential conductance in a magnetic field rotated along θ in the x-y plane with $L = 325\,\mathrm{nm}$ and $l_{\mathrm{SO}} = 20\,\mathrm{nm}$.

the reentrant conductance feature is only present at the $1 \cdot G_0$ plateau. Additionally, the width of the Fabry-Perot oscillations does not change with increasing magnetic field, unlike the observed re-entrant conductance feature. A local quantum dot in the Coulomb or Kondo regimes can lead to conductance suppression, which increases in magnetic field [25]. However both effects should be stronger in the lower conductance region, and exists at zero magnetic field, unlike the feature in our data. Additionally, a Kondo resonance should scale with $V_{\mathrm{sd}} = \pm g\mu_B B/e$ as a

function of external magnetic field, decreasing instead of increasing the width of the region of suppressed conductance. Given the g-factor measured in InSb quantum dots, and its variation with the angle of applied magnetic field $g = 35 - 50$ [21], we can exclude both these effects. Similarly the Fano effect and disorder can also induce a conductance dip, but these effects should not increase linearly with magnetic field. The 0.7 anomaly occurs at the beginning of the plateau, and numerical studies have shown it does not drastically affect the observation of the helical gap [26]. In conclusion, we have observed a return to $1e^2/h$ conductance at the $2e^2/h$ plateau in a QPC in an InSb nanowire. The continuous evolution in increasing magnetic field and the strong angle dependence in magnetic field rotations agree with a SOI related origin of this feature and distinguish it from Fabry-Perot oscillations and other g-factor related phenomena. Additional confirmation is given by numerical simulations of an emerging helical gap in InSb nanowires. The extracted spin-orbit energy of $6.5\,\mathrm{meV}$ is significantly larger than what has been found by other techniques, and more accurately represents the true spin-orbit energy in the first conduction mode. Such a large spin-orbit energy reduces the requirements on nanowire disorder for reaching the topological regime [27], and offers promise for using InSb nanowires for the creation of topologically protected quantum computing devices.

3.7. METHODS

DEVICE FABRICATION

The InSb nanowires were grown using the metalorganic vapor phase epitaxy (MOVPE) process and are grown along the $[111]$ growth direction in a zinc-blende crystal structure [28]. The InSb nanowires were deposited using a deterministic deposition method on a degenerately doped silicon wafer. The wafer covered with $20\,\mathrm{nm}$ of low stress LPCVD SiN which is used as a high quality dielectric. Electrical contacts (Cr/Au, $10\,\mathrm{nm}/110$ nm) defined using ebeam lithography were then evaporated at the ends of the wire. Before evaporation the wire was exposed to an ammonium polysulfide surface treatment and short helium ion etch to remove the surface oxide and to dope the nanowire underneath the contacts [14].

MEASUREMENTS

Measurements are performed in a dilution refrigerator with base temperature $\sim 20\,\mathrm{mK}$ fitted with a 3-axis vector magnet, which allowed for the external magnetic field to be rotated in-situ. The sample is mounted with the substrate in the x-y plane with the wire orientated at a small offset angle $\theta = 17^\circ$ from the x-axis. We measure the differential conductance $G = dI/dV$ using standard lock-in techniques with an excitation voltage of $60\,\mu\mathrm{V}$ and frequency $f = 83\,\mathrm{Hz}$. Additional resistances due to filtering are subtracted to give the true conductance through the device. The helical gap, Zeeman gap, and subband spacing reported in Fig. 3.4(b) were extracted from analysis of the full voltage bias conductance diamonds shown in Fig. 3.4(a) and Fig. 3.9. The subband spacing was extracted by summing the widths of the 0.5 and 1 plateaus, the helical gap and Zeeman gap from their respective conductance diamonds.

NUMERICAL TRANSPORT SIMULATIONS

We use the method of finite differences to discretize the one-dimensional nanowire model of Ref. [12]. In order to obtain a one-dimensional QPC potential, we solve the Poisson equation self-consistently for the full three-dimensional device structure treating the charge density in the nanowire in Thomas-Fermi approximation. To this end, we use a finite element method, using the software FEniCS [17]. The resulting three-dimensional potential is then projected onto the lowest nanowire subband and interpolated using the QPC potential model of Ref. [13]. Transport in the resulting tight-binding model is calculated using the software Kwant [19].

3.8. APPENDIX

3.8.1. ANGLE DEPENDENCE OF THE CONDUCTANCE IN RASHBA NANOWIRES

THEORETICAL MODEL

We consider a one-dimensional nanowire with Rashba spin-orbit interaction (SOI) in an external magnetic field B. The field B is oriented at an angle θ with respect to the effective magnetic field B_{SO} due to Rashba SOI, as shown in Fig. 3.1(e). This setup is described by the Hamiltonian: [12]

$$H = \frac{p^2}{2m^*} + \frac{\alpha}{\hbar} p\sigma_y + \frac{1}{2} E_{\text{Z}} \left(\sin(\theta)\sigma_x + \cos(\theta)\sigma_y\right) . \tag{3.6}$$

In this expression, p is the momentum operator, m^* is the effective mass, α the Rashba SOI-strength, and $\sigma_{x,y}$ the Pauli matrices. The Zeeman energy $E_{\text{Z}} = g\mu_B B$, where g is the g-factor, and μ_{B} the Bohr magneton. In Eq. (3.6) we assumed without loss of generality a magnetic field in the x-y-plane; the band structure however only depends on the relative angle θ of B with B_{SO}.

The Rashba SO-strength α can be related to an effective length scale, the spin-orbit length

$$l_{\text{SO}} = \frac{\hbar^2}{m\alpha} \tag{3.7}$$

and to an energy scale, the spin-orbit energy

$$E_{\text{SO}} = \frac{m\alpha^2}{2\hbar^2} . \tag{3.8}$$

Defining length in units of l_{SO} and energy in units of E_{SO}, it is possible to write the Hamiltonian in a convenient dimensionless form:

$$H = \frac{d^2}{dx^2} + 2\frac{d}{dx}\sigma_y + \frac{1}{2}\frac{E_Z}{E_{\text{so}}}(\sin(\theta)\sigma_x + \cos(\theta)\sigma_y) . \tag{3.9}$$

Proper units will be restored in the final result.

In an translationally invariant nanowire, the wave vector k is a good quantum number and the Rashba Hamiltonian is readily diagonalized as [12]:

$$E_{\pm}(k) = k^2 \pm \frac{1}{2}\sqrt{\left(\frac{E_{\text{Z}}}{E_{\text{so}}}\right)^2 + 16k^2 + 8\frac{E_{\text{Z}}}{E_{\text{so}}}k\cos(\theta)} . \tag{3.10}$$

The resulting band structure for a general angle θ is shown schematically in the left panel of Fig. 3.1f). The band structure can be related to an idealized quantum point contact (QPC) conductance by counting the number of propagating modes at a given energy E (see right panel of Fig. 3.1(f).

In the following we will derive from the band structure: (i) the size of the $1e^2/h$ plateaus in energy (denoted by $\Delta E_{\mathrm{Z},1}$ and $\Delta E_{\mathrm{Z},2}$). This is directly measurable using the finite bias dependence of the QPC conductance (measuring so-called QPC diamonds). (ii) The critical field for which the spin-orbit induced $2e^2/h$ conductance (the size of this plateau is denoted as ΔE_{SO}) vanishes. This allows for an estimate of the spin-orbit strength from the magnetic field dependence in experiment.

SIZE OF ZEEMAN-INDUCED GAPS

In order to compute the size of the different QPC plateaus in energies, we need to compute the value of the minima and maxima of the bands $E_{\pm}(k)$. This can be done exactly using a computer algebra program (we used Mathematica), as it only involves solving for the roots of polynomials up to fourth order. The resulting expressions are however quite cumbersome, and it is more useful to find an approximate expression doing a Taylor approximation. Up to second order in $E_{\mathrm{Z}}/E_{\mathrm{SO}}$ we then find the simple expressions

$$\Delta E_{\mathrm{Z},1} \approx E_{\mathrm{Z}} \sin\theta\,, \tag{3.11}$$

$$\Delta E_{\mathrm{Z},2} \approx E_{\mathrm{Z}} \cos\theta\,. \tag{3.12}$$

CRITICAL MAGNETIC FIELD FOR THE SPIN-ORBIT INDUCED $2e^2/h$-PLATEAU

The spin-orbit induced $2e^2/h$ region persists only up to a critical Zeeman splitting $E_{\mathrm{Z,crit}}$, after which the two $1e^2/h$-plateaus merge into one. In the band structure, this corresponds to a transition from three extrema in $E_{-}(k)$ (two minima, one maximum) to only one minimum. The critical Zeeman splitting where this happens can be solved for exactly using Mathematica:

$$\frac{E_{\mathrm{Z,crit}}}{E_{\mathrm{so}}} = \sqrt{\frac{54\cos(8\theta) + 3M_1^{\frac{2}{3}} + 6\left(3M_1^{\frac{1}{3}} - 4\right)\cos(4\theta) - 2M_1^{\frac{1}{3}} - 30}{M_2^{\frac{1}{3}}}} \tag{3.13}$$

where

$$M_1 = 68 - 86\cos(4\theta) - 36\cos(8\theta) + 54\cos(12\theta) + 512\sqrt{\sin^4(2\theta)\cos^2(2\theta)} \tag{3.14}$$

$$M_2 = 68 - 86\cos(4\theta) - 36\cos(8\theta) + 54\cos(12\theta) + 256\sqrt{\sin^2(2\theta)\sin^2(4\theta)} \tag{3.15}$$

For $\theta = 17^\circ$ this gives $E_{\mathrm{Z,crit}} = 2.386 E_{\mathrm{SO}}$ and for $\theta = 10^\circ$ $E_{\mathrm{Z,crit}} = 2.695 E_{\mathrm{SO}}$. When the value of the nanowire g-factor is extracted from experiment, the critical Zeeman splitting can be translated into a critical magnetic field. The magnetic field up to which the spin-orbit induced $2e^2/h$-plateau is still visible in experiment can then be used to set a *lower bound* on the spin-orbit energy. It is a lower bound, as for a given QPC potential the $2e^2/h$ may not be visible any more despite in principle being present in the band structure. A more detailed transport calculation can be used to improve on this bound.

3.8.2. DEVICE 1 - ADDITIONAL DATA

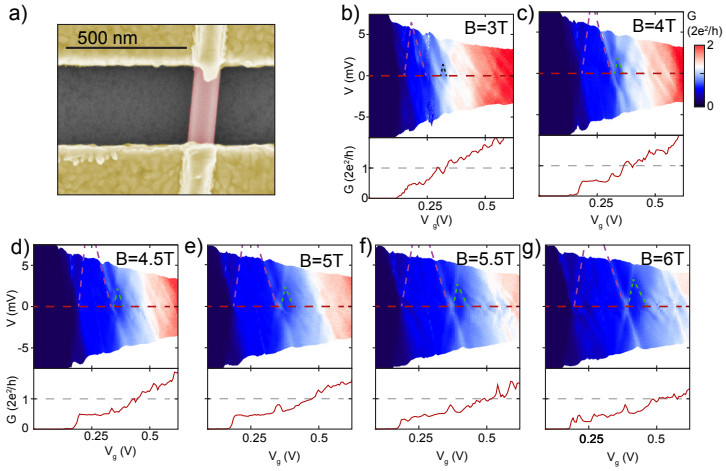

Figure 3.6: Voltage bias spectroscopy. (a): False color SEM image of device 1. The InSb nanowire is shown in red and Cr/Au contacts in yellow. (b)–(g): Conductance measurements as a function of QPC gate voltage V_G and source-drain bias voltage V_{SD} at increasing magnetic field. Dotted lines indicate the helical gap as well as the $0.5 \cdot G_0$ plateau. The helical gap shows as feature stable in V_{SD} and evolves linearly with magnetic field.

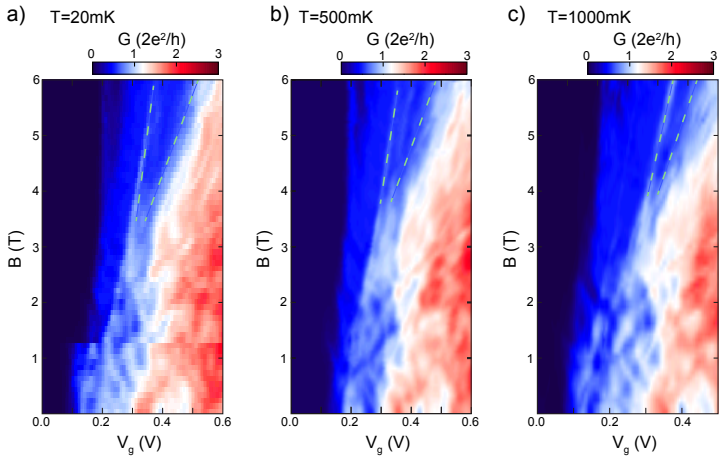

Figure 3.7: Temperature dependence of the helical gap. Measurements of the differential conductance dI/dV ($V_{SD} = 0\,\mathrm{mV}$) as function of magnetic field at (a): T $= 20\,\mathrm{mK}$ (b): T $= 500\,\mathrm{mK}$ (c): T $= 1000\,\mathrm{mK}$. The helical gap (dotted lines) evolves similarly in all three measurements showing that it stays stable at increased temperatures as expected for the energy scale extracted for E_{SO}.

3.8.3. DEVICE 2 - DATA

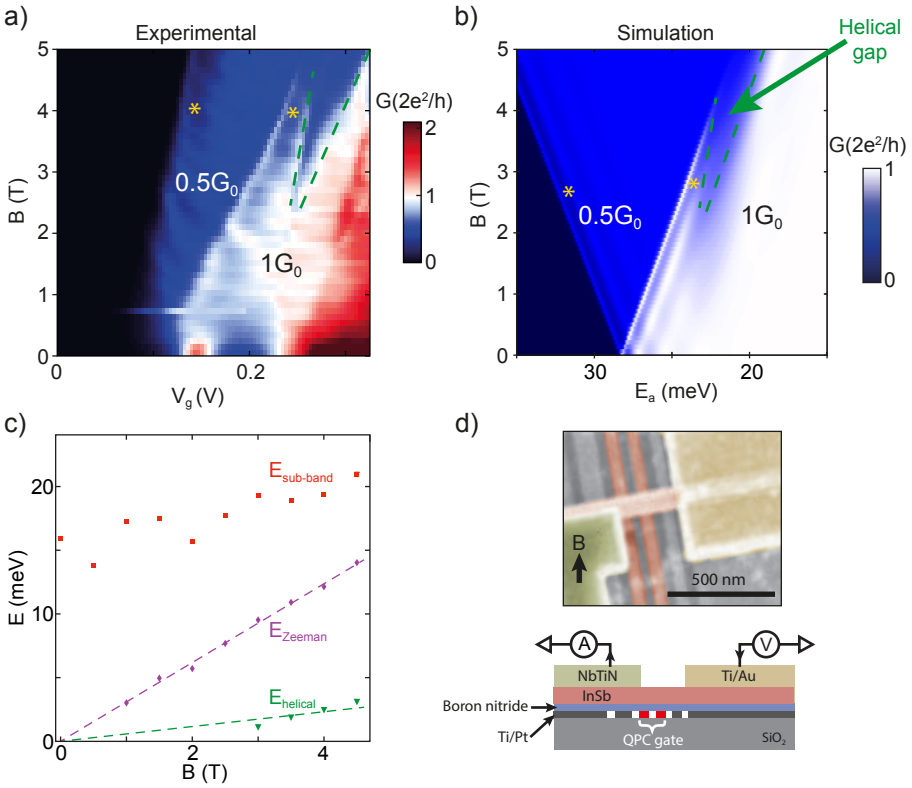

Figure 3.8: Measurements of a second device. (a): Differential conductance dI/dV as function of QPC gate Voltage V_G and magnetic field B. Around $B = 2\,\mathrm{T}$ a gap opens in the $1 \cdot G_0$ plateau and increases linearly with magnetic field. At the onset of the $0.5 \cdot G_0$ and the $1 \cdot G_0$ plateaus Fabry-Perot resonances are visible (yellow asterisk). In contrast to the helical gap the width of the resonances stays constant at changing magnetic field. (b): Numerical simulations of the helical gap with $\theta = 10°$, $g = 53$ and $E_{SO} = 5.6\,\mathrm{meV}$. We use the potential parametrization as for the device discussed in the main text and find a good agreement with the data shown in (a) for $\lambda = 40\,\mathrm{nm}$ and $W = 300\,\mathrm{nm}$. (c): Evolution of the energy levels with magnetic field extracted from the scans shown in Fig. 3.9. Dotted lines show fits with intercept fixed at zero and we find a subband spacing $E_{\mathrm{subband}} = 18 \pm 2\,\mathrm{meV}$ and g-factor $g = 53 \pm 1$. By comparing the slopes of $E_{\mathrm{Zeeman}} \sim E_Z \cos\theta$ and $E_{\mathrm{helical}} \sim E_Z \sin\theta$ we find $\theta = 10° \pm 2°$. (d): Cross section and false color SEM image of device 2. An InSb nanowire (orange) is contacted by one Ti/Au electrode (yellow) and one NbTiN electrode (green). Two bottom gates (red) are combined to form the QPC constriction. The black arrow indicates the orientation of the applied magnetic field. Measurements are taken at $20\,\mathrm{mK}$ with the use of standard lock-in technique ($100\,\mu\mathrm{V}$ excitation at $73\,\mathrm{Hz}$).

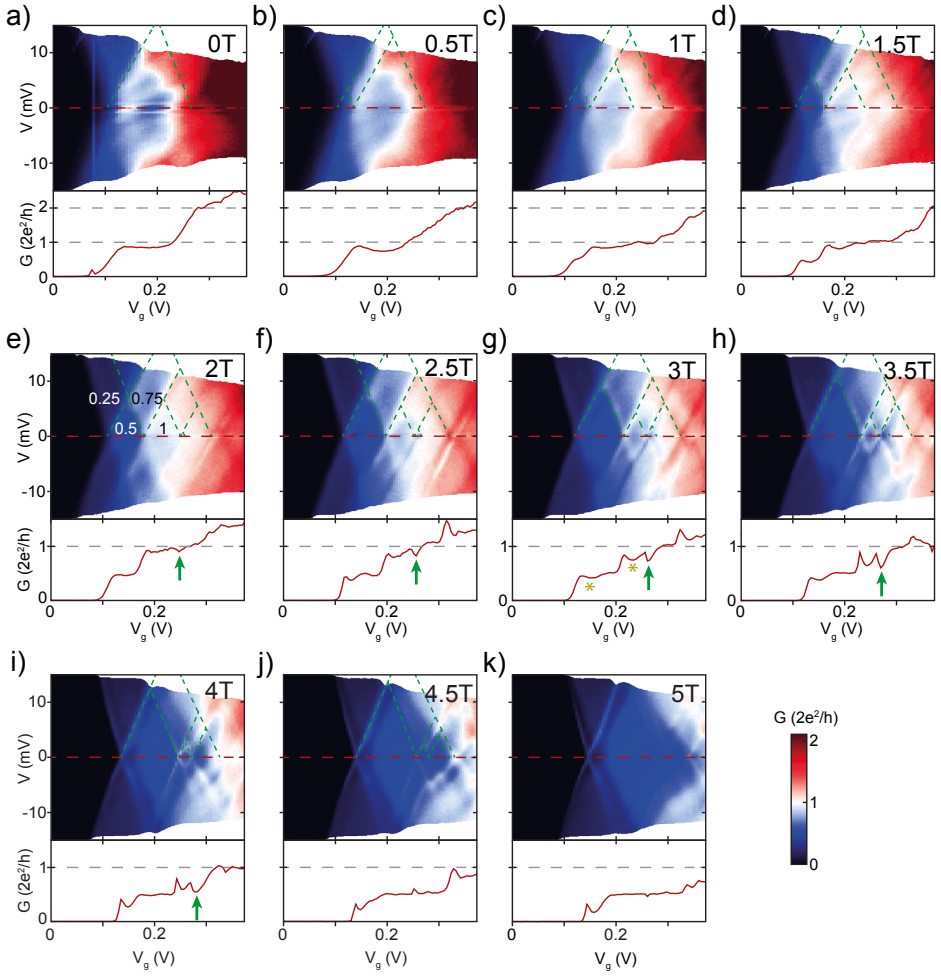

Figure 3.9: Voltage bias spectroscopy of device 2 at increasing magnetic field. (a)–(k): (Top) Differential conductance dI/dV as a function of QPC gate voltage V_G and bias voltage V_{SD}. Conductance plateaus show up as diamond shaped region indicated by dashed green lines and can be used to extract the energy spacings shown in Fig. 3.8(c). Conductance traces in the bottom panels show line cuts taken at $V_{SD} = 0\,\mathrm{mV}$. Green arrows in (e)–(i) indicate the position of the helical dip. Yellow asterisks in (g) indicate conductance dips originating from Fabry-Perot resonances also visible in Fig. 3.8(a). Numbers in (e) denote conductance in units of $2e^2/h$.

3.8.4. CONTROL DEVICES

QPC LENGTH DEPENDENCE

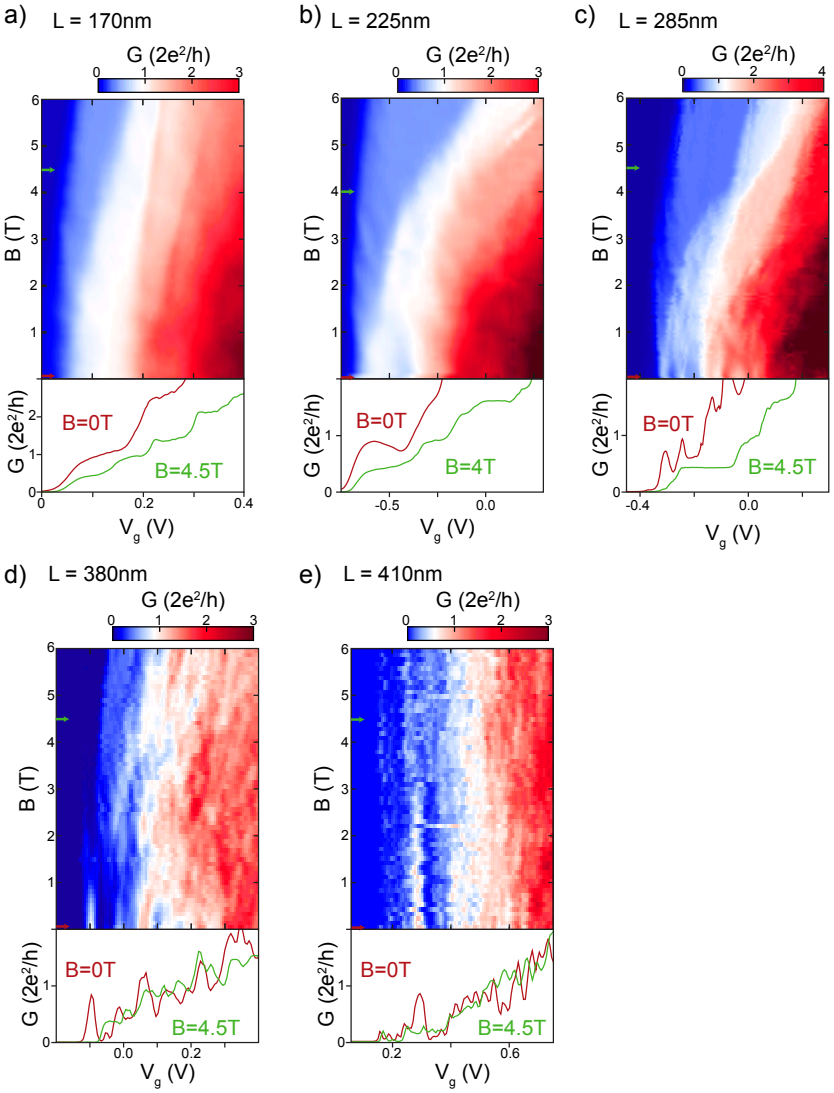

Figure 3.10: Length dependence of nanowire QPCs. Magneto-conductance measurements (at $V_{SD} = 0\,\mathrm{mV}$) of QPCs with increasing length. The contact spacing L is changed in steps of $\sim 50\,\mathrm{nm}$. (a)–(c) are shorter and (d,e) are longer than device 1 ($L = 325\,\mathrm{nm}$). Line traces at $0\,\mathrm{T}$ and finite field are added in the bottom panel. The short channel devices (a, b) show well defined and flat plateaus throughout the full magnetic field range. For intermediate channel lengths, (c), resonances start to appear and modify the conductance at low magnetic fields. Long channel devices, (d, e), are dominated by backscattering and conductance fluctuations dominate for the full magnetic field range.

3.8.5. ADDITIONAL SIMULATIONS

LENGTH DEPENDENCE

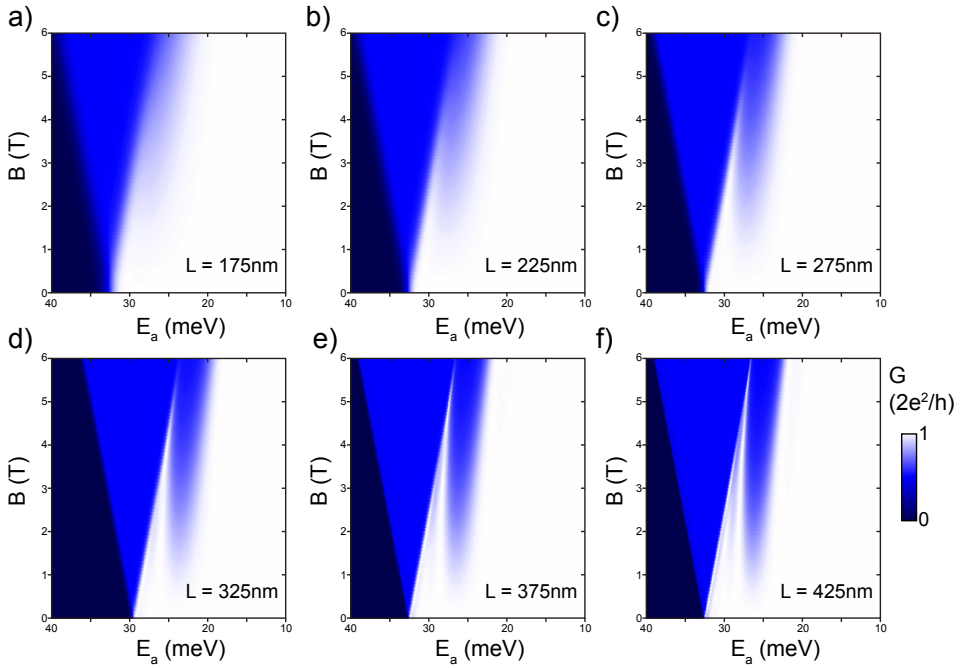

Figure 3.11: Simulations for a QPC of different lengths at fixed angle $\theta = 17°$, $l_{SO} = 20\,\mathrm{nm}$. The contact spacing L is increased in steps of $50\,\mathrm{nm}$ starting from $L = 175\,\mathrm{nm}$ (a), up to $L = 425\,\mathrm{nm}$ (f). The simulations demonstrate the reduced visibility of the helical gap in short devices. At increasing channel length the conductance dip becomes sharper and sets on at lower magnetic fields. A clear re-entrant feature can only be seen in (d)–(f) which are at the limit of experimental capabilities (Fig. 3.10).

ANGLE DEPENDENCE

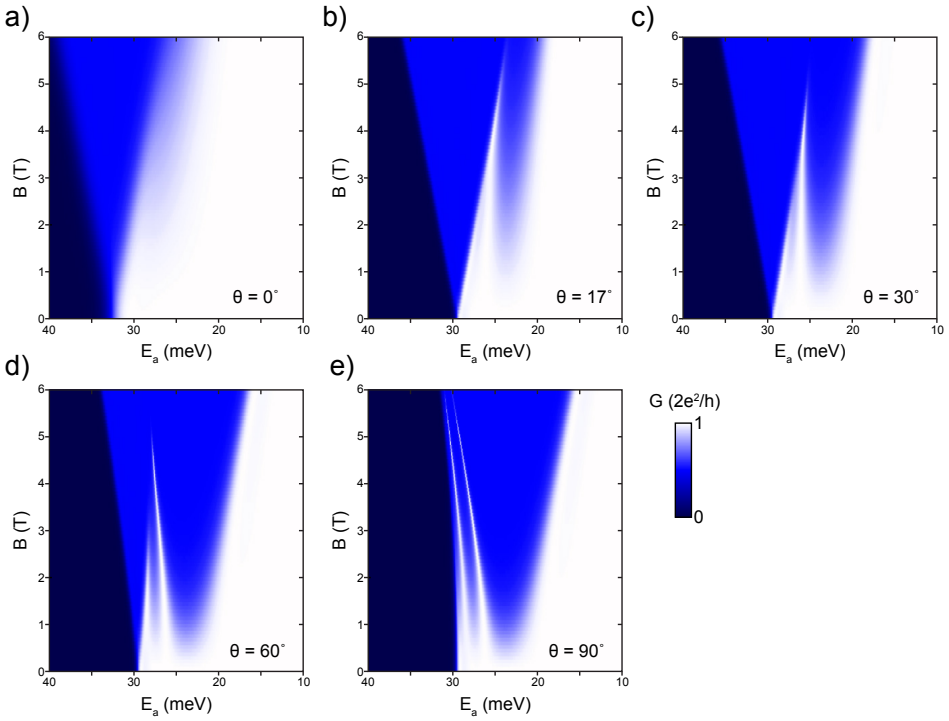

Figure 3.12: Simulations of the angle dependence for a QPC with fixed length $L = 325\,\mathrm{nm}$. θ is the angle between B_{SO} and the applied magnetic field as defined in the main text. (a): For $\theta = 0°$, $B_{\mathrm{ext}} \parallel B_{\mathrm{SO}}$ and the helical gap disappears. (b)–(e): At increasing angles θ the width of the helical gap increases and the width of the initial $0.5 \cdot \mathrm{G}_0$ plateau decreases.

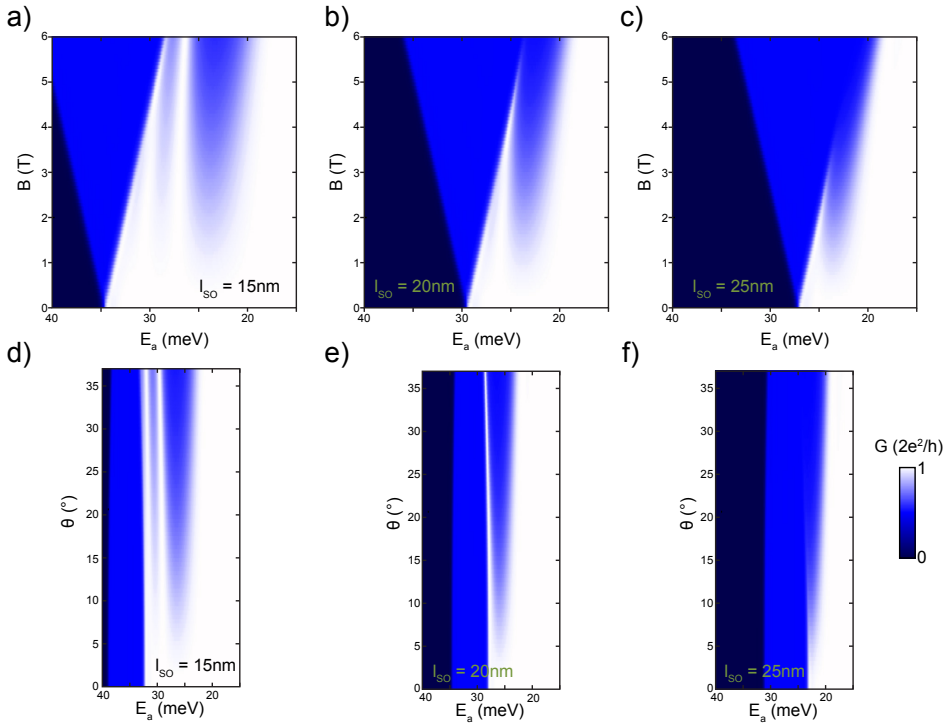

Figure 3.13: Simulations of the magnetoconductance for varying l_{SO}. Variations of $l_{\mathrm{SO}} = 1/k_{\mathrm{SO}}$ strongly influence the visibility of the helical gap in QPC conductance measurements. The simulations for (a)–(c) used identical QPC length $L = 325\,\mathrm{nm}$ and offset angle $\theta = 17°$.

REFERENCES

[1] G. Dresselhaus, *Spin-Orbit Coupling Effects in Zinc Blende Structures,* Phys. Rev. **100**, 580 (1955).

[2] E. Rashba and V. Sheka, *Symmetry of Energy Bands in Crystals of Wurtzite Type II. Symmetry of Bands with Spin-Orbit Interaction Included,* Fiz. Tverd. Tela: Collected Papers **2**, 162–176 (1959).

[3] R. Winkler, S. Papadakis, E. De Poortere, and M. Shayegan, *Spin-Orbit Coupling in Two-Dimensional Electron and Hole Systems*, Vol. 41 (Springer, 2003).

[4] M. König, S. Wiedmann, C. Brüne, A. Roth, H. Buhmann, L. W. Molenkamp, X.-L. Qi, and S.-C. Zhang, *Quantum Spin Hall Insulator State in HgTe Quantum Wells,* Science **318**, 766 (2007), http://science.sciencemag.org/content/318/5851/766.full.pdf .

[5] K. C. Nowack, E. M. Spanton, M. Baenninger, M. König, J. R. Kirtley, B. Kalisky, C. Ames, P. Leubner, C. Brüne, H. Buhmann, *et al.*, *Imaging currents in HgTe quantum wells in the quantum spin Hall regime,* Nature materials **12**, 787 (2013).

[6] C. Quay, T. Hughes, J. Sulpizio, L. Pfeiffer, K. Baldwin, K. West, D. Goldhaber-Gordon, and R. De Picciotto, *Observation of a one-dimensional spin–orbit gap in a quantum wire,* Nature Physics **6**, 336 (2010).

[7] J. Klinovaja, M. J. Schmidt, B. Braunecker, and D. Loss, *Helical modes in carbon nanotubes generated by strong electric fields,* Physical review letters **106**, 156809 (2011).

[8] J. Klinovaja, P. Stano, A. Yazdani, and D. Loss, *Topological superconductivity and Majorana fermions in RKKY systems,* Physical review letters **111**, 186805 (2013).

[9] V. Mourik, K. Zuo, S. M. Frolov, S. R. Plissard, E. P. A. M. Bakkers, and L. P. Kouwenhoven, *Signatures of Majorana Fermions in Hybrid Superconductor-Semiconductor Nanowire Devices,* Science **336**, 1003 (2012).

[10] S. M. Albrecht, A. P. Higginbotham, M. Madsen, F. Kuemmeth, T. S. Jespersen, J. Nygård, P. Krogstrup, and C. M. Marcus, *Exponential protection of zero modes in Majorana islands,* Nature **531**, 206 (2016).

[11] P. Středa and P. Šeba, *Antisymmetric Spin Filtering in One-Dimensional Electron Systems with Uniform Spin-Orbit Coupling,* Phys. Rev. Lett. **90**, 256601 (2003).

[12] Y. V. Pershin, J. A. Nesteroff, and V. Privman, *Effect of spin-orbit interaction and in-plane magnetic field on the conductance of a quasi-one-dimensional system,* Phys. Rev. B **69**, 121306 (2004).

[13] D. Rainis and D. Loss, *Conductance behavior in nanowires with spin-orbit interaction: A numerical study,* Phys. Rev. B **90**, 235415 (2014).

[14] J. Kammhuber, M. C. Cassidy, H. Zhang, Ö. Gül, F. Pei, M. W. de Moor, B. Nijholt, K. Watanabe, T. Taniguchi, D. Car, *et al.*, *Conductance Quantization at zero magnetic field in InSb nanowires,* Nano letters **16**, 3482 (2016).

[15] S. Heedt, W. Prost, J. Schubert, D. Grützmacher, and T. Schäpers, *Ballistic transport and exchange interaction in InAs nanowire quantum point contacts,* Nano letters **16**, 3116 (2016).

[16] N. March, *The Thomas-Fermi approximation in quantum mechanics,* Advances in Physics **6**, 1 (1957).

[17] A. Logg, K. Mardal, and G. Wells, *Automated Solution of Differential Equations by the Finite Element Method* (Springer, 2012).

[18] V. Eyert, *A Comparative Study on Methods for Convergence Acceleration of Iterative Vector Sequences,* J. Comp. Phys. **124**, 271 (1996).

[19] C. Groth, M. Wimmer, A. Akhmerov, and X. Waintal, *Kwant: a software package for quantum transport,* New J. Phys. **16**, 063065 (2014).

[20] I. van Weperen, S. R. Plissard, E. P. A. M. Bakkers, S. M. Frolov, and L. P. Kouwenhoven, *Quantized conductance in an InSb nanowire,* Nano Lett. **13**, 387 (2012).

[21] S. Nadj-Perge, V. Pribiag, J. Van den Berg, K. Zuo, S. Plissard, E. Bakkers, S. Frolov, and L. Kouwenhoven, *Spectroscopy of spin-orbit quantum bits in indium antimonide nanowires,* Physical review letters **108**, 166801 (2012).

[22] I. Van Weperen, B. Tarasinski, D. Eeltink, V. Pribiag, S. Plissard, E. Bakkers, L. Kouwenhoven, and M. Wimmer, *Spin-orbit interaction in InSb nanowires,* Physical Review B **91**, 201413 (2015).

[23] S. Koelling, A. Li, A. Cavalli, S. Assali, D. Car, S. Gazibegovic, E. P. Bakkers, and P. M. Koenraad, *Atom-by-atom analysis of semiconductor nanowires with parts per million sensitivity,* Nano Lett. **17**, 599 (2017).

[24] J. Cayao, E. Prada, P. San-Jose, and R. Aguado, *SNS junctions in nanowires with spin-orbit coupling: Role of confinement and helicity on the subgap spectrum,* Physical Review B **91**, 024514 (2015).

[25] J. Heyder, F. Bauer, E. Schubert, D. Borowsky, D. Schuh, W. Wegscheider, J. von Delft, and S. Ludwig, *Relation between the 0.7 anomaly and the Kondo effect: Geometric crossover between a quantum point contact and a Kondo quantum dot,* Physical Review B **92**, 195401 (2015).

[26] O. Goulko, F. Bauer, J. Heyder, and J. von Delft, *Effect of Spin-Orbit Interactions on the 0.7 Anomaly in Quantum Point Contacts,* Phys. Rev. Lett. **113**, 266402 (2014).

[27] J. D. Sau, S. Tewari, and S. D. Sarma, *Experimental and materials considerations for the topological superconducting state in electron-and hole-doped semiconductors: Searching for non-Abelian Majorana modes in 1D nanowires and 2D heterostructures,* Physical Review B **85**, 064512 (2012).

[28] S. R. Plissard, D. R. Slapak, M. A. Verheijen, M. Hocevar, G. W. G. Immink, I. van Weperen, S. Nadj-Perge, S. M. Frolov, L. P. Kouwenhoven, and E. P. A. M. Bakkers, *From InSb nanowires to nanocubes: Looking for the sweet spot,* Nano Lett. **12**, 1794 (2012).

4

Reproducing topological properties with quasi-Majorana states

This chapter has been previously published as A. Vuik, B. Nijholt, A. R. Akhmerov, M. Wimmer, *Reproducing topological properties with quasi-Majorana states*, arXiv:1806.02801 (2018).

4.1. INTRODUCTION

One-dimensional topological superconductors support Majorana bound states with zero energy at its endpoints [1–4]. Because of their non-Abelian exchange statistics and their topological protection to local sources of error, Majorana states are candidates for fault-tolerant qubits in quantum computing [5, 6]. In addition to their non-Abelian properties, Majorana states have local signatures, namely 4π-periodicity of the supercurrent in a topological Josephson junction [7, 8], and a quantized zero-bias conductance peak in the tunnel spectroscopy of a single topological wire [9–11]. Because of the complexity of a braiding experiment demonstrating the non-Abelian statistics, experimental efforts so far focus on observing the local Majorana signatures [12–14].

An alternative explanation of the experimental observations is Andreev states with near-zero energy that appear in the topologically trivial phase [15–17]. These Andreev states can form at the wire's end, provided the confinement potential is sufficiently smooth [15]. Because smooth confinement potentials are likely to appear due to the separation between metallic gates and nanowires by dielectric layers, these quasi-Majorana states became a focus of recent theoretical research [18–23]. In particular, Ref. [18] shows that in case of smooth confinement potentials, trivial zero-bias conductance peaks are commonly appearing in Majorana devices, Ref. [21] demonstrates that near-zero energy Andreev bound states which are partially separated in space can reproduce quantized zero-bias conductance peaks, and Ref. [23] shows that such partially separated states can reproduce the fractional Josephson effect.

We demonstrate that quasi-Majorana states can be either partially separated or spatially fully overlapping, but in both cases these states have an approximately opposite spin. Because quasi-Majorana states are spin-polarised, the couplings across a smooth tunnel barrier within the WKB approximation are equal to:

$$\begin{aligned} \Gamma_{1,2} &\propto \exp\left[-\tfrac{2}{\hbar}\int_{-w_{1,2}}^{w_{1,2}} |p_{1,2}(x)|dx\right], \\ p_{1,2}(x) &= \sqrt{2m(E-(V_{\text{pot}}(x)\pm E_{\text{Z}}))} \end{aligned} \tag{4.1}$$

with E the energy, V_{pot} the potential energy, E_{Z} the Zeeman energy, and $w_{1,2}$ the spin-dependent width of the tunnel barrier. The ratio of the tunnel probabilities is

$$\Gamma_1/\Gamma_2 = \exp[-2(\gamma_1-\gamma_2)], \tag{4.2}$$

where $\gamma_{1,2} = \int_{-w_{1,2}}^{w_{1,2}} |p_{1,2}(x)|dx$. Therefore, when the tunnel barrier is smooth and Zeeman splitting is sufficiently large, the quasi-Majorana couplings are exponentially different in width of the barrier.

Such an exponential difference of the couplings, combined with the exponentially small coupling between the quasi-Majorana states, makes quasi-Majorana states indistinguishable from topological, spatially separated Majorana states, as we illustrate in Fig. 4.1. Because one of the two quasi-Majorana states is exponentially decoupled from the outside for increasing magnetic field in this regime, any local measurement

will give the same result as for a truly topological system. We verify this phenomenon by analysing tunneling spectroscopy of a quasi-Majorana device, the 4π-periodic Josephson effect [24, 25], and a coupled quantum dot-nanowire system, which has recently been proposed [26, 27] and used [28] to measure Majorana non-locality. Because the exponential suppression of Majorana couplings requires a tunnel barrier, we then analyse the open regime and identify a quantized zero-bias conductance dip instead of a peak as distinctive feature of topological Majoranas.

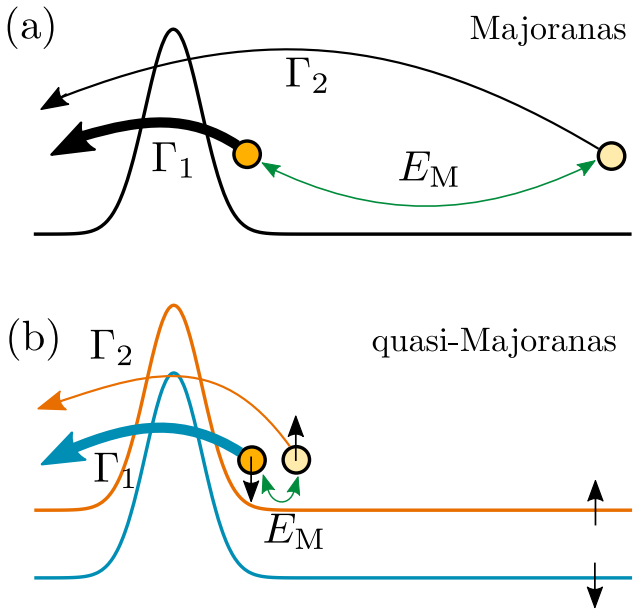

Figure 4.1: Schematic drawing of couplings of (quasi-)Majorana states. (a): Couplings in the topological regime with spinless Majorana states. The spatially separated Majorana states have a coupling energy E_M (green arrow), and couple with coupling strengths Γ_1, Γ_2 across the tunnel barrier The arrow thickness indicates that $\Gamma_1 \gg \Gamma_2$. (b): Couplings in the quasi-Majorana regime with two quasi-Majoranas, located at the tunnel barrier slope and with a suppressed coupling E_M, experience a different effective barrier due to their opposite spin and the finite magnetic field. The spin-down quasi-Majorana state (dark yellow) couples strongly with coupling strength Γ_1 (thick blue arrow, blue effective barrier), the quasi-Majorana state with spin-up (faint yellow) couples weakly with coupling strength Γ_2 (thin orange arrow, orange effective barrier).

Because of the exponentially small coupling between quasi-Majoranas and of one quasi-Majorana across a barrier, a smooth tunnel barrier is an alternative approach to addressing individual Majorana states. As a consequence, braiding schemes can also be realized in a topologically trivial phase with quasi-Majoranas, since braiding effectively requires the coupling to a single (quasi-)Majorana state. Therefore, quasi-Majorana states supply an alternative route towards braiding non-Abelian anyons for quantum computing.

This paper is organized as follows. In Sec. 5.2, we describe our model and a method to compute coupling strengths. In Sec. 4.3, we discuss quasi-Majorana phase diagrams, wave functions, and couplings across a tunnel barrier. Sec. 4.4

describes quasi-Majorana effects on a coupled quantum dot-nanowire device and on a Josephson junction. We investigate an alternative local measurement in Sec. 4.5 and briefly discuss probing a bulk topological phase transition rather than local (quasi-)Majorana modes. To study quasi-Majorana states beyond a simple one-dimensional model, we show in Sec. 4.6 a phase diagram in a 3D nanowire with a smooth potential barrier. In Sec. 4.7, we discuss braiding with quasi-Majoranas. We give a summary and outlook in Sec. 4.8.

4.2. MODEL

4.2.1. HAMILTONIAN

We implement the minimum one-dimensional model, as proposed in Refs. [25, 29], with a Bogoliubov-De Gennes Hamiltonian given by

$$H = \left(\frac{p_x^2}{2m^*} - \mu + V_{\text{pot}}(x) \right) \tau_z - \frac{\alpha}{\hbar} p_x \sigma_y \tau_z + \Delta(x) \tau_x + E_{\text{Z}} \sigma_x, \tag{4.3}$$

with m^* the effective mass, $p_x = -i\hbar\partial_x$ the momentum, μ the chemical potential, V_{pot} the potential, α the spin-orbit interaction (SOI) strength, Δ the superconducting gap and E_{Z} the Zeeman energy due to a parallel magnetic field. The Pauli matrices σ_i and τ_i $(i = x, y, z)$ act in spin and particle-hole space, respectively. The potential V_{pot} and the position dependence of the superconducting gap $\Delta(x)$ vary for different devices, as specified in following subsection. We choose the following parameter values of the Hamiltonian (4.3): $m^* = 0.015 m_{\text{e}}$, corresponding to an InSb nanowire, $\alpha = 50\,\text{meV nm}$, and $\Delta = 0.5\,\text{meV}$, unless specified otherwise.

4.2.2. DEVICES

We implement the Hamiltonian (4.3) in three different devices, schematically shown in Fig. 5.2, that are used to measure local Majorana signatures. The system of Fig. 5.2(a) is a tunnel spectroscopy setup consisting of a proximitized nanowire of length L_{SC} with a chemical potential μ and constant superconducting gap Δ connected on the left to a semi-infinite normal lead via a potential barrier $V_{\text{pot}}(x)$. The potential in this device is given by a Gaussian-shaped barrier, $V_{\text{pot}} = V_{\text{barrier}}$, with

$$V_{\text{barrier}}(x) = V e^{-(x-x_0)^2/2\sigma^2}, \tag{4.4}$$

with V the height, $x_0 = 0$ the center and σ the smoothness of the potential barrier.

Figure 5.2(b) shows the second system, a coupled quantum dot-nanowire device, which has been proposed recently as an additional tool for measuring the non-locality of Majorana states [26, 27]. Compared to the setup of Fig. 5.2(a), we replace the lead by a normal quantum dot ($\Delta = 0$) of length L_{dot}. The effective potential is $V_{\text{pot}} = V_{\text{barrier}} + V_{\text{dot}}$, with V_{barrier} as given in Eq. (4.4) and V_{dot} describing the chemical potential difference between the dot and the nanowire:

$$V_{\text{dot}}(x) = \frac{1}{2}\mu_{\text{dot}} \left(\tanh\left(\frac{x - x_0}{dx} \right) - 1 \right), \tag{4.5}$$

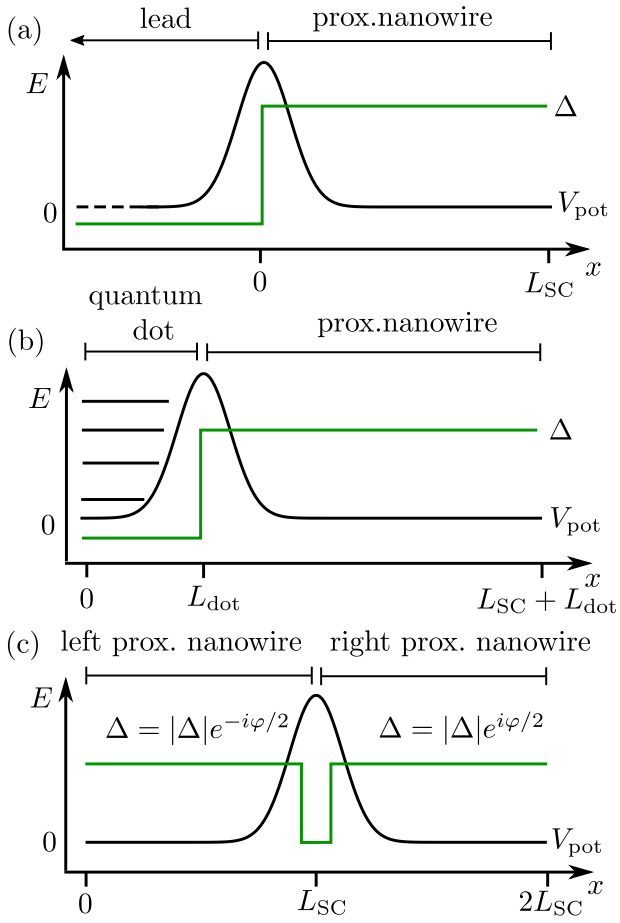

Figure 4.2: Schematic drawings of the three studied devices. The black lines indicate the potential profile $V_{\rm pot}(x)$, the green lines the superconducting gap $\Delta(x)$. (a): Proximitized nanowire of length $L_{\rm SC}$ with constant superconducting gap Δ connected to a semi-infinite normal lead from the left via a potential barrier. (b): Proximitized nanowire of length $L_{\rm SC}$ connected to a normal quantum dot of length $L_{\rm dot}$ on the left via a potential barrier $V_{\rm pot}$. (c): Two finite proximitized nanowires, both of length $L_{\rm SC}$, with a superconducting phase difference φ between them, and separated by a potential barrier $V_{\rm pot}$.

with $\mu_{\rm dot}$ the chemical potential in the quantum dot, $x_0 = L_{\rm dot}$ the interface between dot and nanowire, and dx the length scale over which the chemical potential varies.

Finally, we consider a Josephson junction, consisting of two one-dimensional proximitized nanowires separated by a potential barrier and with a phase difference φ, see Fig. 5.2(c). In this device, $V_{\rm pot} = V_{\rm barrier}$, with the center of the potential barrier between both superconductors ($x_0 = L_{\rm SC}$), and the position-dependent superconducting gap described by

$$\Delta(x) = \begin{cases} |\Delta| e^{-i\varphi/2} & x < L_{\rm SC} \\ |\Delta| e^{i\varphi/2} & x > L_{\rm SC}, \end{cases} \tag{4.6}$$

with a phase difference φ across the junction. In all devices, we fix the nanowire length to $L_{\text{SC}} = 3$ μm. In the coupled quantum dot - nanowire device, we take a quantum dot length of $L_{\text{dot}} = 250$ nm.

We discretize the Hamiltonian (4.3) on an regular one-dimensional grid, and diagonalize this Hamiltonian to obtain wave functions and energy spectra. To compute the differential conductance in the tunneling spectroscopy setup of Fig. 5.2(a) we use the scattering formalism. The scattering matrix, relating incoming and outgoing modes in the normal lead, is

$$S = \begin{bmatrix} S_{\text{ee}} & S_{\text{eh}} \\ S_{\text{he}} & S_{\text{hh}} \end{bmatrix}, \tag{4.7}$$

where $S_{\alpha\beta}$ is the block of the scattering matrix with the scattering amplitudes of incident particles of type β to outgoing particles of type α. The differential conductance is

$$G(E) = \frac{dI}{dV} = \frac{e^2}{h}\left(N_{\text{e}} + T_{\text{he}} - T_{\text{ee}}\right), \tag{4.8}$$

with N_{e} the number of propagating electron modes in the lead and T the transmissions that are related to the scattering matrix by

$$T_{\alpha\beta}(E) = \text{Tr}\left\{\left[S_{\alpha\beta}(E)\right]^{\dagger} S_{\alpha\beta}(E)\right\}. \tag{4.9}$$

We obtain the discretized Hamiltonian and the scattering matrix (4.7) numerically using Kwant [30], see the supplementary material for source code and data [31]. We use adaptive parallel sampling of functions by using the Adaptive package [32].

4.2.3. COUPLINGS FROM MAHAUX-WEIDENMÜLLER FORMULA

We investigate how the low-energy states in the proximitized nanowire couple to the propagating electron modes in the normal lead in the setup of Fig. 5.2(a), since this coupling determines the conductance through the lead-wire interface. To do so, we write the scattering matrix Eq. (4.7) in a different form using a generalized form of the Mahaux-Weidenmüller formula derived in Ref. [33]:

$$S(E) = 1 - 2\pi i W\left(E - H + i\pi W^{\dagger}W\right)^{-1} W^{\dagger}. \tag{4.10}$$

Here, H is the modified Hamiltonian of the scattering region, E is the excitation energy, and W is the matrix containing couplings of the lead modes to the states in the scattering region.

To compute the coupling to the lowest energy eigenstate of the Hamiltonian, $\psi_+(E)$, and its particle-hole symmetric partner $\psi_-(-E) = \mathcal{P}\psi_+(E)$, with $\mathcal{P}$ the particle-hole operator, we introduce a matrix $P = [\psi_+, \psi_-]$. The product WP contains the coupling of the lead modes to the pair of lowest-energy eigenstates of the Hamiltonian H. To calculate the coupling to the Majorana components ψ_1, ψ_2, we write ψ_1, ψ_2 as linear combinations of ψ_+, ψ_-,

$$\begin{bmatrix} \psi_1 \\ \psi_2 \end{bmatrix} = \begin{bmatrix} e^{i\phi} & e^{-i\phi} \\ ie^{i\phi} & -ie^{-i\phi} \end{bmatrix} \begin{bmatrix} \psi_+ \\ \psi_- \end{bmatrix} = U \begin{bmatrix} \psi_+ \\ \psi_- \end{bmatrix} \tag{4.11}$$

for some arbitrary phase ϕ. In this Majorana basis, ψ_1 and ψ_2 satisfy $\psi_1 = \mathcal{P}\psi_1, \psi_2 = \mathcal{P}\psi_2$. The projected coupling matrix $\hat{W}$ in this basis has the form

$$\hat{W} = WPU^\dagger = \begin{bmatrix} t_{1\uparrow} & t_{1\downarrow} & t^*_{1\uparrow} & t^*_{1\downarrow} \\ t_{2\uparrow} & t_{2\downarrow} & t^*_{2\uparrow} & t^*_{2\downarrow} \end{bmatrix}^T, \tag{4.12}$$

where $t_{\gamma\sigma}$ is the coupling of Majorana component $\gamma = 1, 2$ to a lead electron mode with spin $\sigma = \uparrow, \downarrow$, and the complex conjugate $t^*_{\gamma\sigma}$ the coupling to the corresponding lead hole modes. We choose the phase ϕ such that it minimizes the off-diagonal elements $t_{1,\downarrow}, t_{2,\uparrow}$, which results in Majorana components with opposite spin. The computation of the coupling matrix W from the propagating modes in the lead as computed with Kwant [30] is done using the method of Ref. [33].

4.2.4. ANALYTIC CONDUCTANCE EXPRESSIONS IN DIFFERENT COUPLING LIMITS

The anti-alignment of the Majorana spins allows for an analytic expression of the conductance Eq. (4.8). The Hamiltonian in the Majorana basis $\{\psi_1, \psi_2\}$ reads

$$H_{\mathrm{M}} = \begin{bmatrix} 0 & iE_{\mathrm{M}} \\ -iE_{\mathrm{M}} & 0 \end{bmatrix}, \tag{4.13}$$

with E_{M} the coupling energy between ψ_1 and ψ_2. When the spins of the Majorana components are anti-parallel, the projected coupling matrix Eq. (4.12) simplifies to

$$\hat{W} = \begin{bmatrix} t_1 & 0 & t_1^* & 0 \\ 0 & t_2 & 0 & t_2^* \end{bmatrix}^T, \tag{4.14}$$

where $t_1 \equiv t_{1,\uparrow}$ and $t_2 \equiv t_{2,\downarrow}$. For subgap energies, only Andreev reflection processes contribute to conductance, simplifying Eq. (4.8) to

$$G(E) = \frac{2e^2}{h} \mathrm{Tr}\left(\left[S^{eh}\right]^\dagger S^{eh} \right). \tag{4.15}$$

To evaluate this expression, we substitute Eqs. (4.13) and (4.14) into Eq. (4.10) and take out the electron to hole scattering block S^{eh} (see Eq. (4.7)). To further simplify the resulting expression, we define coupling energies $\Gamma_1 = 2\pi t_1^2$ and $\Gamma_2 = 2\pi t_2^2$, [34] and study the regime $\Gamma_1 \gg E_{\mathrm{M}}, \Gamma_2$, which describes one strongly coupled and one weakly coupled low-energy state. This approximation yields

$$G(E) \approx \frac{2e^2}{h} \left(\frac{\Gamma_1^2}{\Gamma_1^2 + E^2} + \frac{\Gamma_2^2 - 2E_{\mathrm{M}}^2\Gamma_2/\Gamma_1}{\Gamma_2^2 + 2E_{\mathrm{M}}^2\Gamma_2/\Gamma_1 + E^2} \right), \tag{4.16}$$

see App. 4.9.1 for a derivation. So, Eq. (4.16) gives the subgap conductance through an NS interface expressed in three energy parameters Γ_1, Γ_2 and E_{M}.

Equation (4.16) is a sum of two (semi-)Lorentzian functions, both with a peak height of $2e^2/h$. In the limit $\Gamma_1 \gg \Gamma_2, E_{\mathrm{M}}$, the first Lorentzian, with a peak width of $\sim \Gamma_1$, is much broader than the second Lorentzian of peak width $\sim \Gamma_2$. The second,

narrower Lorentzian is positive for $\Gamma_2 > 2E_M^2/\Gamma_1$ and negative for $\Gamma_2 < 2E_M^2/\Gamma_1$, and hence respectively increases the conductance around $E = 0$ to $4e^2/h$ or decreases it to 0, depending on the coupling strength of the second low-energy state. This result explains the numerical findings of Ref. [18]. When $\Gamma_2 \ll E_M^2/\Gamma_1$, the curve shape is similar to the single-mode result of Ref. [35]. Temperature broadens the Lorentzian peaks, therefore the second peak is experimentally only observable when $k_B T \lesssim \Gamma_2$. Therefore, in the limit $\Gamma_1 \gg \Gamma_2, E_M$, zero-bias conductance is quantized to $2e^2/h$ provided $k_B T > \Gamma_2$. Upon increasing Γ_2, or decreasing temperature, an additional, narrower zero-bias peak is observable, either positive and increasing the overall conductance to $4e^2/h$ or negative and decreasing it to zero, depending on the sizes of Γ_1, Γ_2 and E_M. When both $\Gamma_{1,2} \lesssim k_B T$, both zero-bias conductance peaks are not observable, resulting in a zero subgap conductance.

4.3. PHASE DIAGRAM, WAVE FUNCTIONS AND COUPLINGS OF QUASI-MAJORANAS

Earlier works have presented Hamiltonian spectra as a function of magnetic field, where for specific parameter choices quasi-Majorana states occur in the trivial regime [15, 19]. To investigate more systematically in which parameter ranges these states occur, we compute a phase diagram as a function of Zeeman energy E_Z and chemical potential μ. To do so, we consider the system Fig. 5.2(a), decoupled from the lead. We compute the energy of the lowest eigenstate of Hamiltonian (4.3) as a function of E_Z and μ, see Fig. 4.3. In all four panels, inside the topological phase (red line), the lowest energy of the Hamiltonian is exponentially small, indicating the existence of a zero-energy state. This zero-energy state only exists in the topological phase for Fig. 4.3(a) and (b), when the potential barrier is steep. For a smooth potential, there is a large area of quasi-Majorana states with zero energy outside the topological phase, with growing area as the SOI weakens, see Fig. 4.3(c) and (d).

Reference [19] investigated Andreev bound states which are separated by a distance comparable or larger than the coherence length of the system, but less than the system length. These partially separated Andreev bound states continuously interpolate between local Andreev bound states and topological Majorana states at the system edges. Reference [36] proposed to trap partially separated Andreev bound states in quantum wells, in order to increase their energy splitting. In addition to these works, we find realistic parameter regimes with quasi-Majorana states consisting of spatially *completely overlapping* Majorana components, that still have an exponentially suppressed near-zero energy. Figure 4.4(a) shows the density of quasi-Majorana states that are partially separated, while Fig. 4.4(b) shows that for a different choice of parameters, the quasi-Majorana components fully overlap. The quasi-Majoranas wave function overlap increases with decreasing SOI strength α and smoothness σ, and increasing barrier height V.

The origin of the decoupling between two quasi-Majorana states lies in the nearly opposite spin, which we show in Fig. 4.4(c) and (d). Because the SOI strength vanishes at the smooth potential slope, the opposite-spin states do not couple [15]. The classical turning points of both quasi-Majorana wave functions are close on the

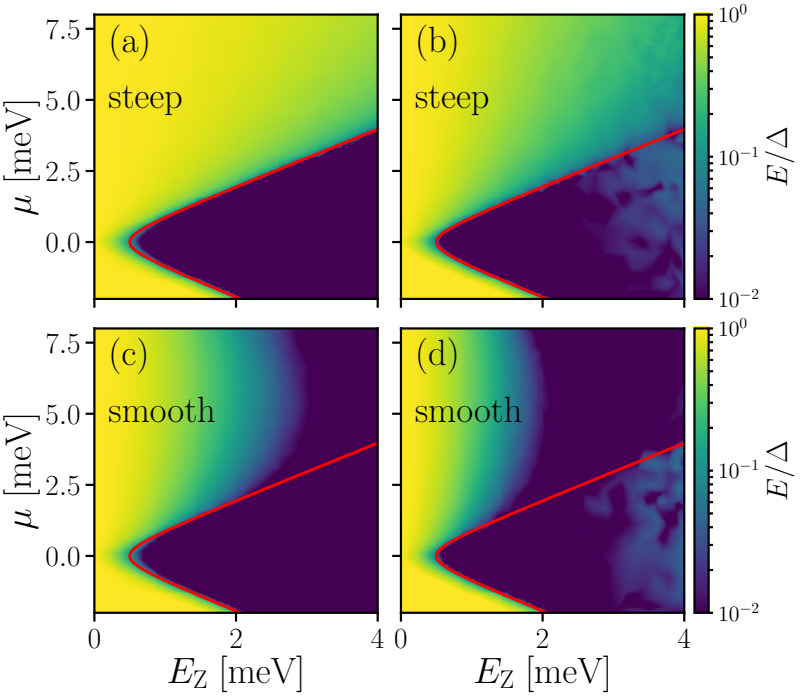

Figure 4.3: Phase diagram as a function of E_Z and μ of the device sketched in Fig. 5.2(a), for (a) $\alpha = 100$ meVnm, $\sigma = 10$ nm, (b) $\alpha = 40$ meVnm, $\sigma = 10$ nm, (c) $\alpha = 100$ meVnm, $\sigma = 200$ nm, and (d) $\alpha = 40$ meVnm, $\sigma = 200$ nm. The red line indicates the topological phase boundary $E_Z = \sqrt{\Delta^2 + \mu^2}$. The color indicates the lowest energy of the Hamiltonian in units of Δ on a logarithmic scale. The potential barrier height is $V = 10$ meV.

length scale of the coherence length for the parameters of the right column of Fig. 4.4, minimizing the spatial separation between both states. Finally, Fig. 4.4(e) and (f) show that both systems go into a topological phase for a further increase of Zeeman energy, with well-separated Majorana bound states at the system's endpoints.

Because quasi-Majorana states are located at the same side of a proximitized nanowire, while topological Majorana states are separated between opposite edges, one might expect local transport measurements to distinguish between both cases. However, this is generally not the case, as shown in Fig. 4.1: the opposite spin of both quasi-Majorana states result in a different effective barrier, which exponentially suppresses one quasi-Majorana coupling, reproducing the coupling regime of topological Majorana states. Figure 4.5(a, c) show the coupling parameters for a steep potential barrier, and Figure 4.5(b, d) for a smooth barrier with quasi-Majorana states. The energy of the lowest Hamiltonian eigenstate E_M is exponentially small for increasing magnetic field only in the topological regime for a steep barrier, see Fig. 4.5(a), but is suppressed well before the topological phase transition for a smooth barrier with quasi-Majorana states, Fig. 4.5(b). Likewise, the couplings across the barrier of the

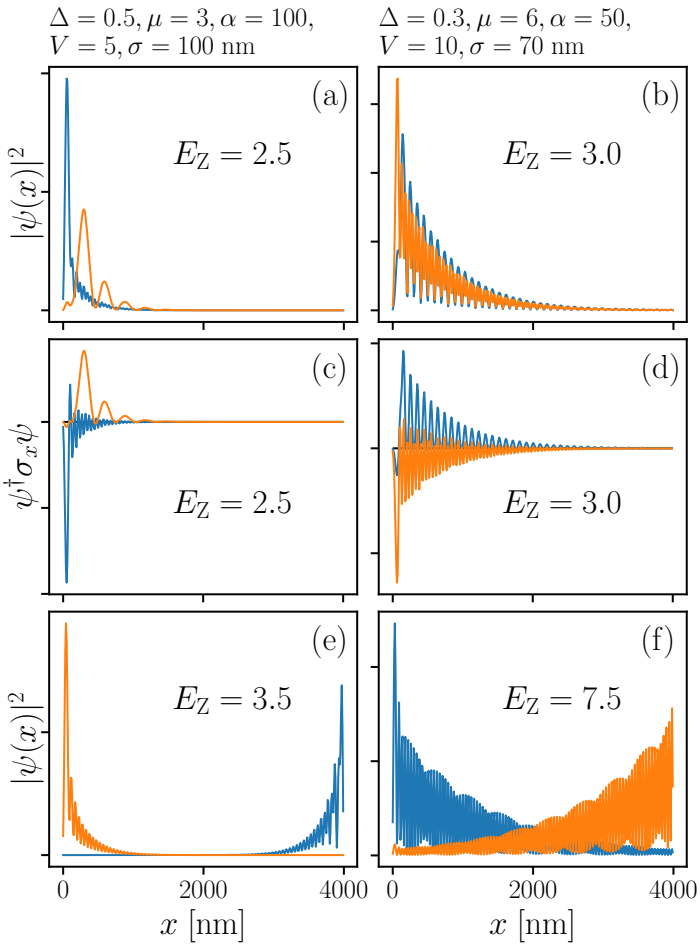

Figure 4.4: Wave functions and spin densities in the device sketched in Fig. 5.2(a) with a smooth potential on the left edge. The left column shows results for parameters such that the Majorana components in the trivial regime are partially separated, the right column for fully overlapping components. (a, b): Probability densities of the Majorana components of the lowest Hamiltonian eigenstate in the quasi-Majorana regime. (c, d): Spin densities of both Majorana components along x. (e, f): Majorana wave functions in the topological regime. Energy scales are given in meV, SOI strenght in meVnm. The nanowire length is set to $L_{\mathrm{SC}} = 4$ μm.

Majorana components of the lowest Hamiltonian eigenstate Γ_1, Γ_2 are exponentially different only in the topological phase for a steep potential barrier, Fig. 4.5(c). However, for a smooth barrier, the couplings are approximately four orders of magnitude different already in the trivial phase, Fig. 4.5(d). Consistently, we find that the exponential suppression of both E_{M} and Γ_2 is stronger in the quasi-Majorana regime than in the topological regime.

The exponential suppression of the coupling between quasi-Majoranas and the

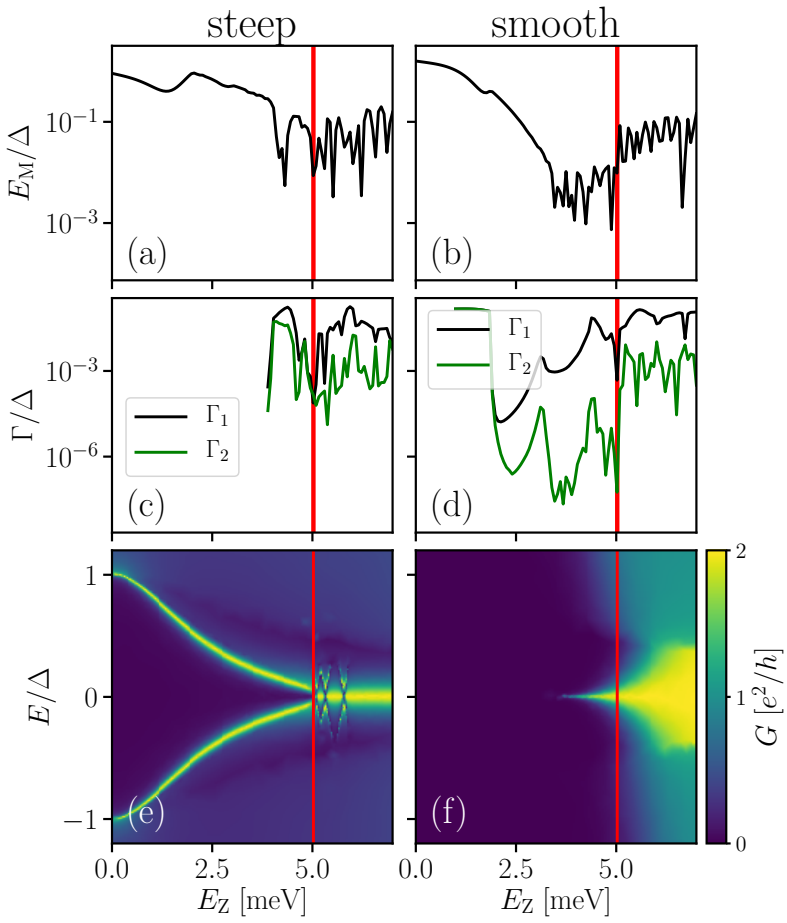

Figure 4.5: Coupling energy and conductance as a function of Zeeman energy E_Z for a steep tunnel barrier ($\sigma = 10$ nm, left column) or for a smooth tunnel barrier ($\sigma = 100$ nm, right column) with quasi-Majorana states. (a,b): Coupling energy between the two lowest states E_M. (c, d): Coupling energy to the probing lead Γ_1, Γ_2 of the two lowest states. We do not include the coupling for small Zeeman energies, since the energy of the lowest state is too large compared to the bulk gap in this regime for the approximation of Sec. 4.2.3 to hold. (e, f): Conductance as a function of bias energy E and Zeeman energy E_Z. In all panels, the red vertical line indicates the topological phase transition. The barrier heights and smoothness are $V = 18$ meV, $\sigma = 10$ nm for the left column and $V = 11.7$ meV, $\sigma = 100$ nm for the right column respectively, and the chemical potential is $\mu = 5$ meV for all panels.

coupling of one of the quasi-Majoranas across a tunnel barrier for increasing magnetic field reproduces the topological coupling regime $\Gamma_2, E_M \ll \Gamma_1$. Hence, the conductance signatures of both the quasi-Majorana regime and the topological Majorana regime are similar. In absence of quasi-Majorana states, a zero-bias conductance peak quantized to $2e^2/h$ only develops after the topological phase transition, Fig. 4.5(e), while in presence of quasi-Majorana states, a quantized zero-bias peak is also present

in the trivial regime, Fig. 4.5(f). This zero-bias peak quantized to $2e^2/h$ coincides with the exponential suppression of the coupling of one of the two zero-bias states, as expected from our analytical formula, Eq. (4.16). Our calculations also show a narrow conductance dip around $E = 0$ due to the coupling of the second (quasi-)Majorana Γ_2 as is consistent with Eq. (4.16), but this is not visible in the color scheme of Fig. 4.5, and experimentally not visible when $\Gamma_2 \lesssim k_B T$. Hence, a quantized $2e^2/h$ zero-bias conductance peak does not distinguish between topological Majorana states and quasi-Majorana states.

4.4. MAJORANA NON-LOCALITY AND TOPOLOGICAL JOSEPHSON EFFECT

References [26, 27] express Majorana non-locality as the ratio between the couplings Γ_1, Γ_2 of the two Majorana states to a probing lead. In Ref. [26], a 'quality factor' $q = 1 - \Gamma_2/\Gamma_1$ is defined, with $q = 0$ denoting two strongly coupled local Majorana states ($\Gamma_1 = \Gamma_2$), and $q = 1$ denoting complete non-locality ($\Gamma_2 = 0$). References [26, 27] propose a coupled quantum dot-nanowire device, see Fig. 5.2(b), to determine the quality factor with a local probe, which has been experimentally implemented in Ref. [28]. The spectum of the hybrid quantum dot-nanowire device shows anti-crossing quantum dot states and a flat zero-energy state as a function of the quantum dot chemical potential in case of well-separated Majorana states, with $E_M, \Gamma_2 \ll \Gamma_1$. When the Majorana states are closer together, the increasing coupling of the second Majorana to the quantum dot results in increasingly asymmetric diamond-like shapes in the lowest energy level across the resonance with the quantum dot states. Hence, the measurement of the energy levels in the hybrid device allows to determine the Majorana non-locality with a local probe.

Reference [22] pointed out that partially separated Andreev bound states can have different couplings to a quantum dot, mimicking the signatures of spatially separated topological Majorana states. We show that quasi-Majorana states systematically have exponentially different couplings to a quantum dot, hence the quasi-Majorana regime generally exhibits a high degree of non-locality. Figure 4.6(a, b) show the spectrum in the topological phase as a function of quantum dot chemical potential μ_{dot} and Zeeman energy E_Z respectively. The quantum dot and the nanowire are separated by a steep barrier, so no quasi-Majorana states appear in the spectrum of Fig. 4.6(b). The non-locality of the Majorana states is expressed in Fig. 4.6(a) by the flat energy level around $E = 0$ of the non-local Majorana state, and spin-dependent anti-crossings of the quantum dot levels coupled to the local Majorana state. A flat energy level around $E = 0$ and strong anti-crossings are absent in Fig. 4.6(c), where the system is topologically trivial and no single Majorana state couples to the quantum dot. However, in the presence of quasi-Majoranas, Fig. 4.6(e, f), these characteristics occur in the trivial phase because of the exponentially different coupling of both quasi-Majorana states to the quantum dot. Therefore, since quasi-Majorana states reproduce the topological coupling regime $E_M, \Gamma_2 \ll \Gamma_1$, we observe that quasi-Majorana states can exhibit a high degree of Majorana non-locality, and consequently give rise to high quality factors, while being highly local in space. This makes

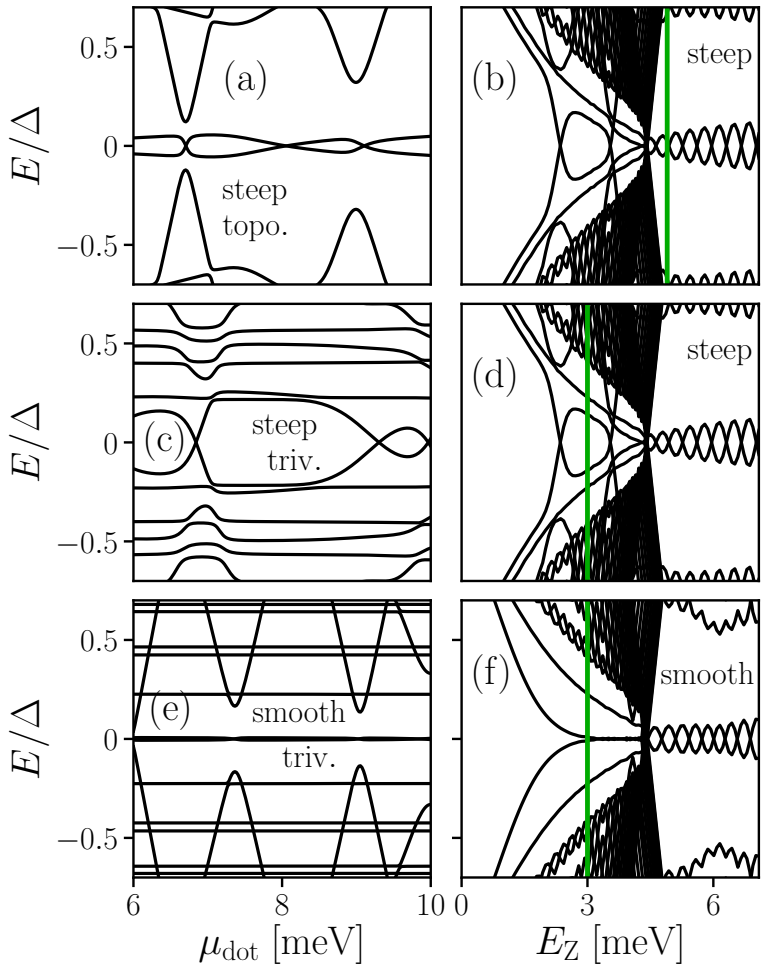

Figure 4.6: Energy levels in a hybrid quantum dot-nanowire device as a function of the chemical potential of the quantum dot μ_{dot} (left column), and as a function of Zeeman energy E_{Z} (right column). Panels (a, b) show the energy levels in the topological phase with a steep barrier ($\sigma = 10$ nm), panels (c, d) in the trivial phase with a steep barrier, and panels (e, f) in the trivial phase with a smooth barrier ($\sigma = 100$ nm) in presence of quasi-Majorana states. The vertical green lines in the right panels indicate the Zeeman energy at which the corresponding left panel is computed. The barrier height and the chemical potential in all panels is $V = 9.5$ meV and $\mu = 4.4$ meV respectively.

Majorana non-locality and the Majorana quality factor as proposed in Refs. [26, 27] unsuitable for distinguishing quasi-Majorana states from topological Majorana states.

Turning to the 4π-periodic Josephson effect in a device sketched in Fig. 5.2(c), we again compare a topological junction to a trivial junction with and without quasi-Majorana states. Figure 4.7(a) shows a 4π-periodicity of the energy levels corresponding to the Majorana states located at the normal barrier, and a flat zero-

energy level corresponding to the Majorana states at the outer edges of the device (with a small splitting due to finite size effects), as is expected theoretically in the topological phase [24, 25]. In the trivial phase, as shown in Fig. 4.7(c), no zero-energy state is present, and energy levels show a 2π-periodicity. When the barrier is smooth, quasi-Majorana states appear in the trivial regime (see Fig. 4.7(f)), reproducing the flat zero-energy levels and 4π-periodic levels that characterize the topological Josephson junction (Fig. 4.7(e)). Quasi-Majorana states reproduce the topological phase winding characteristics because two quasi-Majorana states strongly couple across the barrier, resulting in a 4π-periodic level, and two have an exponentially suppressed coupling, resulting in a flat zero-energy level. Therefore, the measurement of a 4π-periodic Josephson current is not a distinctive signature of topological Majorana states, but can be caused by quasi-Majorana states.

4.5. DISTINCTIVE SIGNATURES OF A TOPOLOGICAL PHASE

Previously discussed measurement setups rely on Majorana modes to determine a topological phase, which makes them inherently sensitive to non-topological local low-energy states. Hence, a better strategy to distinguish a topological from a trivial phase is the measurement of a bulk phase transition rather than the measurement of individual Majorana states, which has been proposed in several earlier works. Reference [37] discusses quantized thermal conductance and electrical shot noise in a proximitized nanowire coupled to two normal leads as signatures of a topological phase transition. Reference [38] proposes the measurement of differences in conductance at one lead connected to a proximitized nanowire when changing the coupling to another lead, while Ref. [39] predicts a sign change of the spin component of bulk bands along the magnetic field as a measure of a topological phase transition. Finally, Ref. [40] proposes the detection of rectifying behavior of the nonlocal conductance G between two spatially separated leads as a function of the bias E, $G(E) \propto E$, as a signature of a bulk phase transition. These proposals all rely on bulk properties, and therefore more reliably detect a topological phase than probing a local Majorana state, which might be mimicked by other localized low-energy states.

We also suggest an alternative approach relying on local conductance measurements that allows to distinguish topological Majorana states from quasi-Majorana states. According to Eq. (4.16), when the coupling of the second low-energy subgap state Γ_2 exceeds $k_\mathrm{B}T$, an experimentally observable zero-bias conductance peak of $4e^2/h$ develops. Hence, our approach does not focus on a quantized conductance peak in the tunneling spectroscopy [41] when Γ_2 is strongly suppressed, but on a conductance measurement in the open regime. We demonstrate the effect of opening the tunnel barrier $V \to 0$ (with V the height of the potential barrier given in Eq. (4.4)) on the conductance with true Majorana states and with quasi-Majorana states in Fig. 4.8. Figure 4.8(a) shows the conductance as a function of bias energy E and barrier height V in the topological phase with spatially separated Majorana states. In the tunneling regime, the conductance shows a zero-bias peak quantized to $2e^2/h$ (see also the light-brown line cut in panel (c)), which broadens to a plateau of $2e^2/h$ height upon opening the barrier (purple line cut). When the barrier height is further reduced, the conductance at finite bias increases due to Andreev doubling,

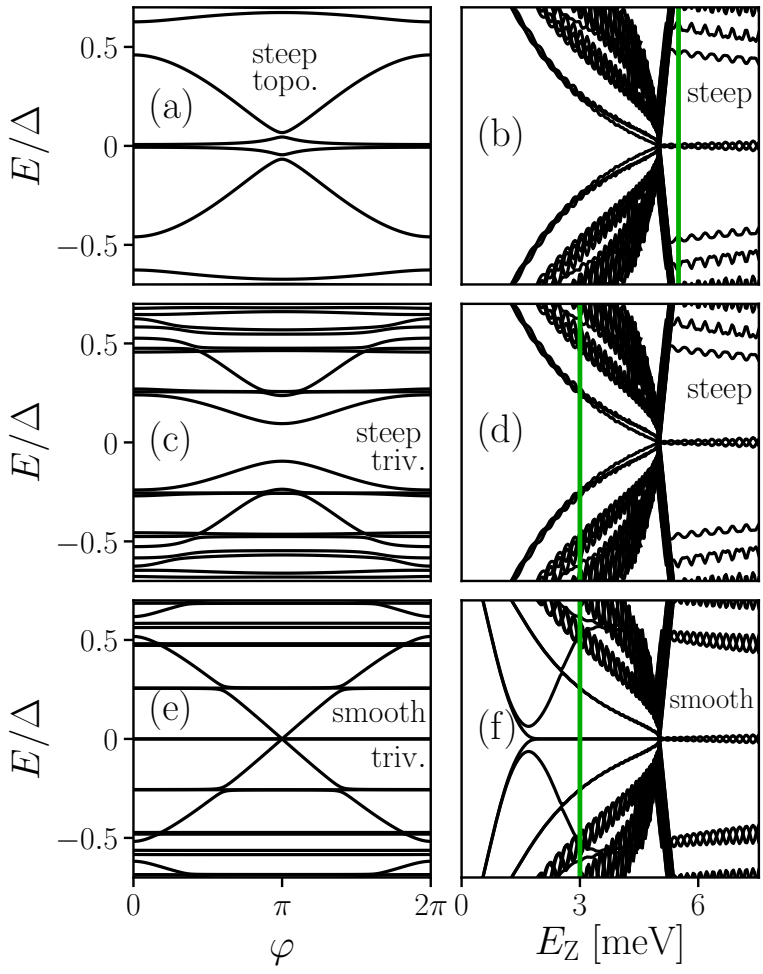

Figure 4.7: Energy levels in a topological Josephson junction as a function of the phase difference across the junction φ (left column), and as a function of Zeeman energy E_{Z} (right column). Panels (a, b) show the energy levels in the topological phase with a steep barrier ($\sigma = 10$ nm), panels (c, d) in the trivial phase with a steep barrier, and panels (e, f) in the trivial phase with a smooth barrier ($\sigma = 100$ nm) in presence of quasi-Majorana states. The vertical green lines in the right panels indicate the Zeeman energy at which the corresponding left panel is computed. The barrier height and the chemical potential in all panels is $V = 7.4$ meV and $\mu = 5$ meV respectively.

but stays fixed to $2e^2/h$ at zero bias due to the presence of a single Majorana state (pink line cut) [11]. Quasi-Majorana states also exhibit a conductance peak of $2e^2/h$ in the tunneling regime and a conductance plateau of $2e^2/h$ in the quasi-open regime as shown in Fig. 4.8(b) and the line cuts in Fig. 4.8(d). However, upon further opening the barrier, both quasi-Majorana states couple to the lead, resulting in a conductance peak of $4e^2/h$ which broadens to a plateau when further reducing V.

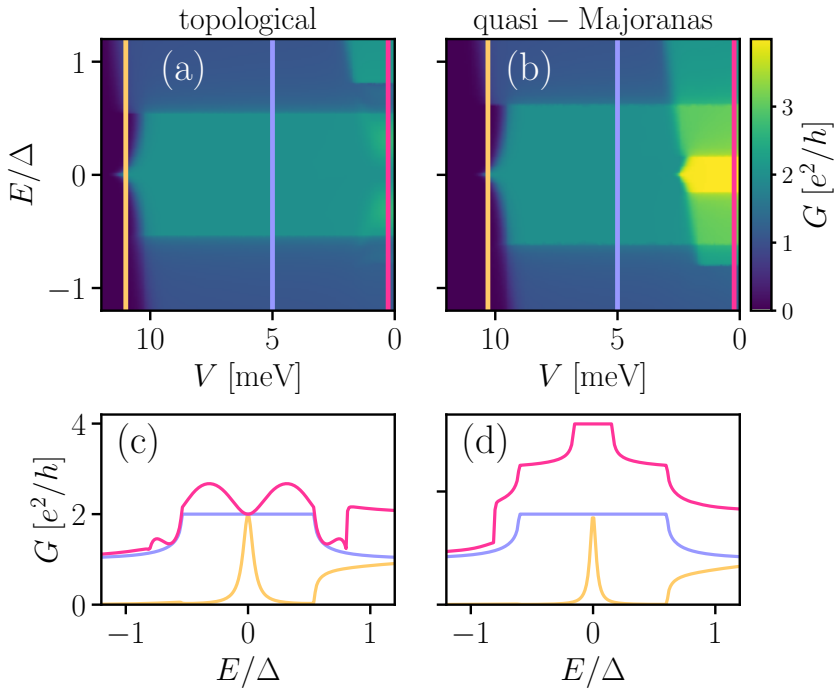

Figure 4.8: (a, b): Conductance as a function of bias energy E and barrier height V for topological Majorana states (left) and for quasi-Majorana states (right). The vertical colored lines point out the values of V at which line cuts, shown in (c, d), are made. The parameter values for this plot are: $V = 7$ meV, $\mu = 4$ meV, and $\sigma = 200$ nm. Panels (a) and (c) are made at $E_Z = 4.4$ meV, in the topological phase, and panels (b) and (d) are made at $E_Z = 3.6$ meV, in the trivial phase.

Therefore, while a zero-bias conductance peak or conductance plateau quantized to $2e^2/h$ does not distinguish quasi-Majorana states from topological Majorana states, a zero-bias *dip* in the conductance in the open regime does.

4.6. QUASI-MAJORANA STATES IN A 3D NANOWIRE

Because quasi-Majorana states so far have been studied in one-dimensional systems [15, 16, 18, 19, 21, 22], it is uncertain how likely quasi-Majoranas are to appear in realistic situations. While currently doing a fully realistic simulation of a three-dimensional device is beyond state of the art, we do a 3D simulation that includes the orbital effect of magnetic field [42, 43], multiple modes mixed by an inhomogeneous potential in the direction perpendicular to the wire axis, and an external superconducting shell proximitizing the nanowire (see App. 4.9.2 for a detailed description of the model).

We show the phase diagram of this 3D device as a function of μ and E_Z in Fig. 4.9. The upper panels, with a steep potential barrier ($\sigma \to 0$), show that the emergence of a zero-energy state coincides with the topological phase, which has

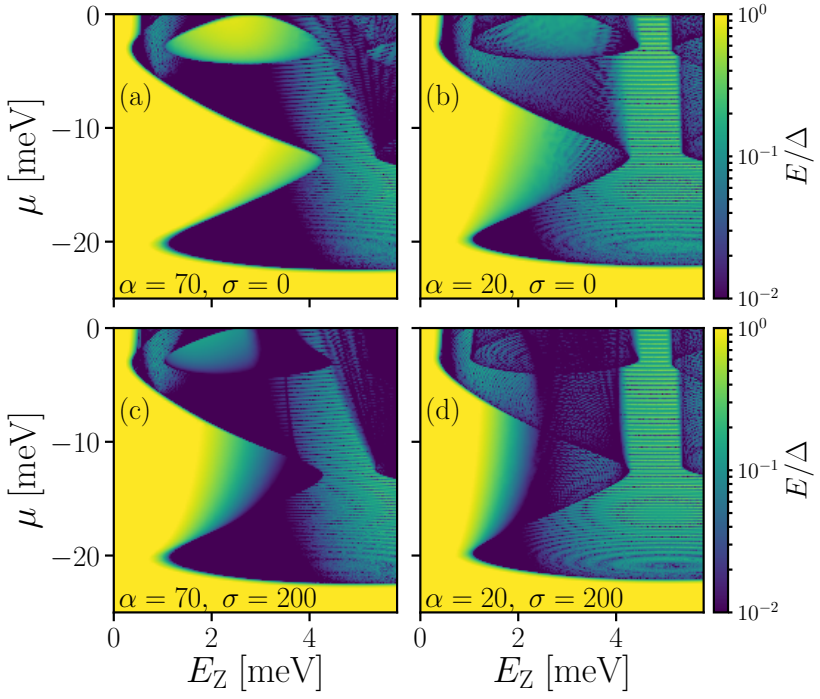

Figure 4.9: Phase diagram as a function of E_Z and μ of the 3D device, with orbital magnetic field and an external superconductor included. The red line indicates the topological phase boundary. The color indicates the lowest energy of the Hamiltonian in units of Δ on a logarithmic scale. Different panels have different parameter values for the SOI strength α (in meVnm) and potential smoothness σ (in nm). The potential barrier height is $V = 25$ meV.

a more complicated shape compared to Fig. 4.3 due to multiple modes and the orbital effect of magnetic field. In Fig. 4.9(b), the gap outside the topological phase is weaker due to a weaker spin-orbit coupling, but no robust trivial zero-energy state emerges. However, Fig. 4.9(c, d) show that for a smooth potential barrier ($\sigma = 200$ nm) a region of zero-energy quasi-Majorana states emerges, especially prominent for weak spin-orbit strength $\alpha = 20$ meVnm, Fig. 4.9(d). Figure 4.9 is qualitatively similar to Fig. 4.3: for a smooth potential, regions of zero-energy quasi-Majoranas emerge, increasing in size for decreasing spin-orbit strength. Thus, we find that quasi-Majorana states are also present in realistic 3D systems with smooth potentials that are close to currently available experimental devices.

4.7. BRAIDING OPERATIONS WITH QUASI-MAJORANA STATES

Braiding schemes that demonstrate and utilize the non-Abelian statistics of Majorana states are subdivided into gate-controlled braiding in T-junctions [44–46], Coulomb-assisted braiding in Josephson junctions [47, 48], or measurement-based braiding in topological nanowires coupled to quantum dots [49–51]. Having quasi-Majorana

states in the topologically trivial phase in these devices still admits braiding. Gate-controlled braiding requires microscopically precise manipulation of electrostatic potentials, and therefore we leave gate-controlled braiding with quasi-Majorana states as a topic for future research. On the other hand, the other two schemes only rely on coupling to individual Majorana states, which is possible in the quasi-Majorana regime, since quasi-Majorana states couple exponentially different across a tunnel barrier. The presence of the second, uncoupled quasi-Majorana state still allows these braiding schemes to work [52]. We show a possible setup for a measurement-based braiding scheme with quasi-Majorana states in Fig. 4.10(a), where only one quasi-Majorana state of each pair couples to the adjacent quantum dot, and for a Coulomb-assisted braiding scheme in Fig. 4.10(b), where only one quasi-Majorana state of each pair couples to one other quasi-Majorana state of the two other nanowires.

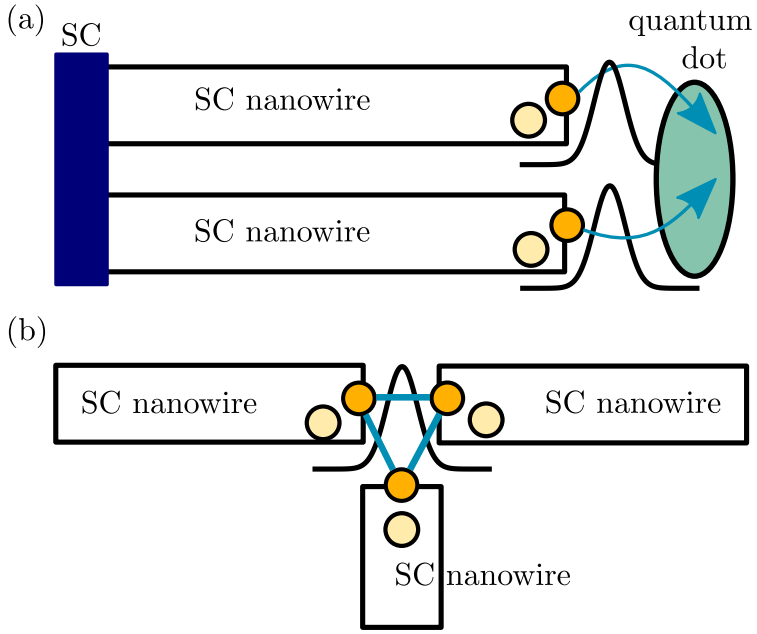

Figure 4.10: (a): Braiding in a measurement-based device of parallel superconducting nanowires coupled to a quantum dot. Only one of each pair of quasi-Majorana states effectively couples across the smooth barrier to the quantum dot (blue arrows). (b): Tri-junction setup for Coulomb-assisted braiding with quasi-Majorana states. From the pairs of quasi-Majoranas in each nanowire, only one couples across the tunnel barrier to the other two quasi-Majoranas (blue lines).

To estimate whether quasi-Majorana states are realistic candidates for braiding, we compare quasi-Majorana energy and length scales to braiding requirements. Coulomb-assisted and measurement-based braiding involves a fermion parity measurement in a transmon [53], where the parity shift is expressed in a resonance frequency shift $\Delta\omega$, which has been estimated in Ref. [51] for realistic parameters as $\Delta\omega \sim 100$ MHz. Hence, the transmon sensitivity must exceed 100 MHz, which

limits the quasi-Majorana energy splitting to $\hbar\Delta\omega \sim 0.1$ μeV. The energy splitting E_{M} for the parameters of Fig. 4.5 does not meet this requirement (see Fig. 4.5(b)), but we find that for increasing barrier smoothness σ and SOI strength α (while keeping the wire length fixed to $L_{\mathrm{SC}} = 3$ μm), the splitting is reduced to a value below the braiding requirement. As an example, for experimentally realistic values of $\sigma = 150$ nm and $\alpha = 100$ meVnm, we find a quasi-Majorana splitting of 0.1 μeV. Additionally, we consistently observe that the coupling energy E_{M} in the quasi-Majorana regime is an order of magnitude smaller than in the topological regime. The smaller quasi-Majorana coupling compared to the topological Majorana coupling is due to the lower magnetic fields in the quasi-Majorana regime, which results in a smaller coupling of quasi-Majorana states to the other end of the wire. The suppression of the coupling of the second quasi-Majorana state to the outside is orders of magnitude smaller, $\Gamma_2 \sim 10^{-3}$ μeV, and again we find this suppression stronger in the quasi-Majorana regime than in the topological regime, see Fig. 4.5(d). Consequently, using quasi-Majorana states may be an attractive approach to demonstrate braiding properties.

4.8. SUMMARY AND OUTLOOK

Experimental setups to measure Majorana states in hybrid semiconductor-superconductor nanowire devices contain electrostatic gates that can generate smooth potential profiles, which give rise to non-topological quasi-Majorana states, that have an exponentially suppressed energy as a function of magnetic field. Additionally, one of the quasi-Majorana states has an exponentially suppressed coupling across the tunnel barrier. This makes quasi-Majoranas mimic all local Majorana signatures, specifically a quantized zero-bias peak conductance in the tunnel spectroscopy, the resonance spectrum in a coupled nanowire - quantum dot device, and 4π-periodicity of the energy levels as a function of phase in a Josephson junction. Therefore, it is impossible to categorise signatures in current Majorana experiments into topological Majorana states or trivial quasi-Majorana states.

A measurement of a bulk phase transition, rather than a measurement of the presence of local (quasi-)Majorana states, can experimentally distinguish non-topological quasi-Majorana states from topological Majorana states. Additionally, we propose to to measure conductance in the open regime, which results in a plateau at $G = 4e^2/h$ around zero bias in the conductance in presence of quasi-Majoranas, and in a conductance dip to $G = 2e^2/h$ at zero bias in presence of topological, spatially separated Majoranas.

While quasi-Majorana states make it harder to unambiguously demonstrate topological Majorana states, they reproduce topological properties such as braiding. Quasi-Majorana states lack true topological protection, and are hence sensitive to magnetic impurities or other short-range disorder mechanisms that break the smoothness of the potential barrier. However, due to the progress in device design, the current experimental devices are likely to be in the ballistic regime required to support robust quasi-Majorana states [54–57]. Also, quasi-Majorana states emerge for smaller magnetic fields, which reduces the coupling to the opposite end of the wire compared to topological Majorana states, resulting in smaller energy splittings.

Furthermore, combined with topological Majorana states, quasi-Majorana states increase the overall phase space in which topological quantum computing can be performed. Therefore, it may be an interesting direction of further research to engineer quasi-Majorana states to study topological properties.

4.9. APPENDIX

4.9.1. ANALYTIC APPROXIMATION FOR THE NS INTERFACE CONDUCTANCE

To arrive at the analytic expression for subgap conductance through an NS interface with two low-energy subgap states in the coupling regime $\Gamma_1 \gg \Gamma_2, E_{\mathrm{M}}$, Eq. (4.16), we start from the Mahaux-Weidenmüller formula for the scattering matrix $S(E)$:

$$S(E) = 1 - 2\pi i W \left(E - H_{\mathrm{M}} + i\pi W^{\dagger} W\right)^{-1} W^{\dagger}. \tag{4.17}$$

As stated in Eqs. (4.13) and (4.14), the low-energy Hamiltonian H_{M} and coupling matrix W of the two lowest-energy states to the normal lead have the form

$$H_{\mathrm{M}} = \begin{bmatrix} 0 & iE_{\mathrm{M}} \\ -iE_{\mathrm{M}} & 0 \end{bmatrix}, W = \begin{bmatrix} t_1 & 0 & t_1^* & 0 \\ 0 & t_2 & 0 & t_2^* \end{bmatrix}, \tag{4.18}$$

with W in the basis $\{\psi_{e,\uparrow}, \psi_{e,\downarrow}, \psi_{h,\uparrow}, \psi_{h,\downarrow}\}$ of propagating electron and hole modes of both spins in the normal lead, and H_{M} in the Majorana basis $\{\psi_1, \psi_2\}$, where ψ_1 and ψ_2 have opposite spin. Substitution of Eq. (4.18) into Eq. (4.17) gives an expression for the scattering matrix $S(E)$ in terms of E_{M} and the coupling energies Γ_1, Γ_2:

$$S(E) = \begin{bmatrix} S^{ee} & S^{eh} \\ S^{he} & S^{hh} \end{bmatrix} = \begin{bmatrix} 1+A & A \\ A & 1+A \end{bmatrix}, \tag{4.19}$$

where

$$A = \frac{1}{Z} \begin{bmatrix} i\Gamma_1(E + i\Gamma_2) & -E_{\mathrm{M}}\sqrt{\Gamma_1\Gamma_2} \\ E_{\mathrm{M}}\sqrt{\Gamma_1\Gamma_2} & i\Gamma_2(E + i\Gamma_1) \end{bmatrix}, \tag{4.20}$$

with

$$Z = E_{\mathrm{M}}^2 - (E + i\Gamma_1)(E + i\Gamma_2), \tag{4.21}$$

and $\Gamma_i = 2\pi t_i^2$ (see also Ref. [34]). Andreev reflection of an incoming electron into an outgoing hole is described by the block of the scattering matrix $S^{eh} = A$. At subgap energies, the Andreev conductance is given by

$$G(E) = \frac{2e^2}{h} \mathrm{Tr}\left(\left[S^{eh}\right]^{\dagger} S^{eh}\right). \tag{4.22}$$

In the limit $\Gamma_1 \gg E_{\mathrm{M}}, \Gamma_2$, Eq. (4.21) is approximated by $Z \approx E_{\mathrm{M}}^2 + \Gamma_1\Gamma_2 - E^2 - iE\Gamma_1$, and hence

$$|Z^2| = \left(E_{\mathrm{M}}^2 - E^2 + \Gamma_1\Gamma_2\right)^2 + E^2\Gamma_1^2 \approx E_{\mathrm{M}}^4 + E^4 + \Gamma_1^2(\Gamma_2^2 + E^2) + 2E_{\mathrm{M}}^2(\Gamma_1\Gamma_2 - E^2). \tag{4.23}$$

We insert this in Eq. (4.20) and work out the trace of Eq. (4.22) using $S^{eh} = A$, which follows from Eq. (4.19). This yields

$$G(E) \approx \frac{2e^2}{h} \frac{2E_{\mathrm{M}}^2\Gamma_1\Gamma_2 + 2\Gamma_1^2\Gamma_2^2 + E^2(\Gamma_1^2+\Gamma_2^2)}{E_{\mathrm{M}}^4 + E^4 + \Gamma_1^2(\Gamma_2^2+E^2) + 2E_{\mathrm{M}}^2(\Gamma_1\Gamma_2 - E^2)}. \tag{4.24}$$

In the limit $\Gamma_1 \gg \Gamma_2, E_{\mathrm{M}}$, square terms in Γ_1 dominate, hence we neglect the other terms in the numerator of Eq. (4.24). This results in a conductance expression for the limit $\Gamma_1 \gg \Gamma_2, E_{\mathrm{M}}$:

$$G(E) \approx \frac{2e^2}{h} \frac{\Gamma_1^2(2\Gamma_2^2+E^2)}{E_{\mathrm{M}}^4 + E^4 + \Gamma_1^2(\Gamma_2^2+E^2) + 2E_{\mathrm{M}}^2(\Gamma_1\Gamma_2 - E^2)}. \tag{4.25}$$

Next, we consider the high- and low-energy regimes separately. In the high-energy limit, $\Gamma_1, E \gg E_{\mathrm{M}}, \Gamma_2$, Eq. (4.25) reduces to

$$G(E) \approx \frac{2e^2}{h} \frac{\Gamma_1^2}{\Gamma_1^2+E^2}. \tag{4.26}$$

Turning to the low-energy limit, $\Gamma_1 \gg E_{\mathrm{M}}, \Gamma_2, E$, we further simplify Eq. (4.23) to $|Z^2| \approx \Gamma_1\Gamma_2\left(\Gamma_1\Gamma_2 + 2E_{\mathrm{M}}^2\right) + E^2\Gamma_1^2$. The correction around zero energy to Eq. (4.25) is given by

$$G(E) - \frac{2e^2}{h} \approx \frac{2e^2}{h} \frac{\Gamma_2^2 - 2E_{\mathrm{M}}^2\Gamma_2/\Gamma_1}{\Gamma_2^2 + E^2 + 2\Gamma_2 E_{\mathrm{M}}^2/\Gamma_1}. \tag{4.27}$$

Summing Eqs. (4.26) and (4.27) gives a simplified expression for the conductance in the limit $\Gamma_1 \gg \Gamma_2, E_{\mathrm{M}}$ at all energies, expressed in two (semi-)Lorentzian functions:

$$G(E) \approx \frac{2e^2}{h}\left(\frac{\Gamma_1^2}{\Gamma_1^2+E^2} + \frac{\Gamma_2^2 - 2E_{\mathrm{M}}^2\Gamma_2/\Gamma_1}{\Gamma_2^2 + 2E_{\mathrm{M}}^2\Gamma_2/\Gamma_1 + E^2}\right). \tag{4.28}$$

This describes a Lorentzian of height $2e^2/h$ and width $\sim \Gamma_1$, with an additional Lorentzian with the same height $2e^2/h$ and a much narrower width $\sim \Gamma_2$ (since $\Gamma_1 \gg \Gamma_2$). This second, narrower Lorentzian is positive when $\Gamma_2 > 2E_{\mathrm{M}}^2/\Gamma_1$ and negative for $\Gamma_2 < 2E_{\mathrm{M}}^2/\Gamma_1$.

4.9.2. THREE-DIMENSIONAL NANOWIRE MODEL

In order to verify that our conclusions still hold in three dimensions, we apply the effective low-energy model [25, 29] of a semiconducting nanowire with spin-orbit coupling and a parallel magnetic field, covered by a superconductor, to a 3D system. We define x as the direction along the wire, y perpendicular to the wire in the plane of the substrate, and z perpendicular to both wire and substrate. The corresponding Hamiltonian reads

$$H_{\mathrm{BdG}} = \left(\frac{\boldsymbol{p}^2}{2m^*} - \mu + V(x,\ z)\right)\tau_z + \alpha\left(p_y\sigma_x - p_x\sigma_y\right)\tau_z + \frac{1}{2}g\mu_{\mathrm{B}}\boldsymbol{B}\cdot\boldsymbol{\sigma} + \Delta\tau_x,$$

Here $\boldsymbol{p} = -i\hbar\nabla + e\boldsymbol{A}\tau_z$ is the canonical momentum, where e is the electron charge, and $\boldsymbol{A} = [B_y z - B_z y,\ 0,\ B_x y]^T$ is the vector potential chosen such that it does

not depend on x, which we include in the tight-binding system using the Peierls substitution [58]. Further, m^* is the effective mass, μ is the chemical potential controlling the number of occupied subbands in the wire, α is the strength of the SOI, g is the Landé g-factor, μ_B is the Bohr magneton, and Δ is the superconducting pairing potential. The Pauli matrices $\boldsymbol{\sigma}$ and $\boldsymbol{\tau}$ act in spin space and electron-hole space respectively. We assume a Gaussian potential $V(x,\ z)$ inside the wire centered around $x = 0$, with different peak heights at the top ($z = R$) and bottom ($z = -R$) of the wire, and linearly interpolated for $-R < z < R$:

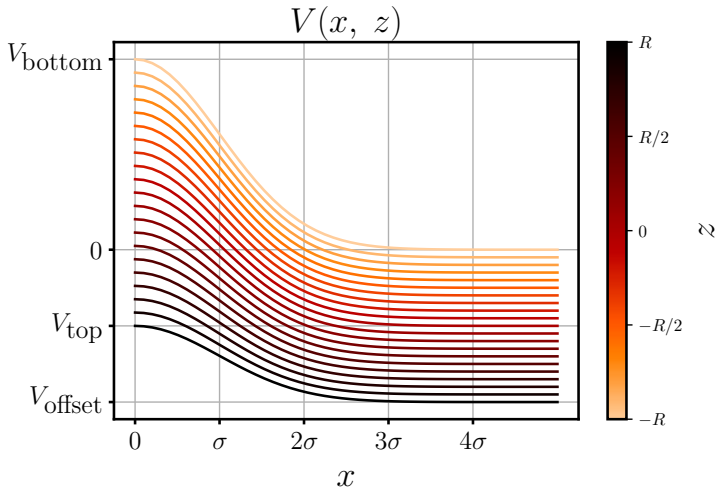

Figure 4.11: Potential shape inside the nanowire as given by Eq. (4.29). The parameter values for the simulations in Fig. 4.9 are $V_{\text{top}} = -30$ meV, $V_{\text{bottom}} = 25$ meV, $V_{\text{offset}} = -50$ meV, and $R = 35$ nm.

$$V(x,\ z) = V_{\text{bottom}} \exp\left(\frac{1}{2}\frac{x^2}{\sigma^2}\right)\left(\frac{R-z}{2R}\right) + V_{\text{offset}}\left(\frac{z+R}{2R}\right) + (V_{\text{top}} - V_{\text{offset}}) \exp\left(\frac{1}{2}\frac{x^2}{\sigma^2}\right)\left(\frac{z+R}{2R}\right), \tag{4.29}$$

where R is the wire radius, V_{bottom} and V_{top} are the heights of the Gaussian peaks at the bottom and top respectively, V_{offset} is the difference in potential between the top and bottom, and σ the width of the peaks. We perform numerical simulations of the Hamiltonian (4.29) on a 3D lattice using Kwant [30]. The source code and the specific parameter values are available in the Supplemental Material [31]. The full set of materials, including the computed raw data and experimental data, is available in Ref. [31].

REFERENCES

[1] A. Yu. Kitaev, *Unpaired Majorana fermions in quantum wires,* Phys.-Usp. **44**, 131 (2001).

[2] J. Alicea, *Majorana fermions in a tunable semiconductor device,* Phys. Rev. B **81**, 125318 (2010).

[3] M. Leijnse and K. Flensberg, *Introduction to topological superconductivity and Majorana fermions,* Semiconductor Science and Technology **27**, 124003 (2012).

[4] C. Beenakker, *Search for Majorana Fermions in Superconductors,* Annu. Rev. Con. Mat. Phys. **4**, 113 (2013).

[5] S. B. Bravyi and A. Yu. Kitaev, *Fermionic Quantum Computation,* Annals of Physics **298**, 210 (2002).

[6] C. Nayak, S. H. Simon, A. Stern, M. Freedman, and S. Das Sarma, *Non-Abelian anyons and topological quantum computation,* Rev. Mod. Phys. **80**, 1083 (2008).

[7] H.-J. Kwon, K. Sengupta, and V. M. Yakovenko, *Fractional ac Josephson effect in p- and d-wave superconductors,* The European Physical Journal B - Condensed Matter and Complex Systems **37**, 349 (2004).

[8] L. Fu and C. L. Kane, *Josephson current and noise at a superconductor/quantum-spin-Hall-insulator/superconductor junction,* Phys. Rev. B **79**, 161408 (2009).

[9] K. T. Law, P. A. Lee, and T. K. Ng, *Majorana Fermion Induced Resonant Andreev Reflection,* Phys. Rev. Lett. **103**, 237001 (2009).

[10] K. Flensberg, *Tunneling characteristics of a chain of Majorana bound states,* Phys. Rev. B **82**, 180516 (2010).

[11] M. Wimmer, A. R. Akhmerov, J. P. Dahlhaus, and C. W. J. Beenakker, *Quantum point contact as a probe of a topological superconductor,* New Journal of Physics **13**, 053016 (2011).

[12] V. Mourik, K. Zuo, S. M. Frolov, S. R. Plissard, E. P. A. M. Bakkers, and L. P. Kouwenhoven, *Signatures of Majorana Fermions in Hybrid Superconductor-Semiconductor Nanowire Devices,* Science **336**, 1003 (2012).

[13] A. Das, Y. Ronen, Y. Most, Y. Oreg, M. Heiblum, and H. Shtrikman, *Zero-bias peaks and splitting in an Al-InAs nanowire topological superconductor as a signature of Majorana fermions,* Nat. Phys. **8**, 887 (2012).

[14] M. T. Deng, C. L. Yu, G. Y. Huang, M. Larsson, P. Caroff, and H. Q. Xu, *Anomalous Zero-Bias Conductance Peak in a Nb–InSb Nanowire–Nb Hybrid Device,* Nano Lett. **12**, 6414 (2012).

[15] G. Kells, D. Meidan, and P. W. Brouwer, *Near-zero-energy end states in topologically trivial spin-orbit coupled superconducting nanowires with a smooth confinement,* Phys. Rev. B **86**, 100503 (2012).

[16] E. Prada, P. San-Jose, and R. Aguado, *Transport spectroscopy of NS nanowire junctions with Majorana fermions,* Phys. Rev. B **86**, 180503 (2012).

[17] C. Fleckenstein, F. Domínguez, N. Traverso Ziani, and B. Trauzettel, *Decaying spectral oscillations in a majorana wire with finite coherence length,* Phys. Rev. B **97**, 155425 (2018).

[18] C.-X. Liu, J. D. Sau, T. D. Stanescu, and S. Das Sarma, *Andreev bound states versus Majorana bound states in quantum dot-nanowire-superconductor hybrid structures: Trivial versus topological zero-bias conductance peaks,* Phys. Rev. B **96**, 075161 (2017).

[19] C. Moore, T. D. Stanescu, and S. Tewari, *Two terminal charge tunneling: Disentangling Majorana zero modes from partially separated Andreev bound states in semiconductor-superconductor heterostructures,* arXiv:1711.06256 (2017).

[20] F. Setiawan, C.-X. Liu, J. D. Sau, and S. Das Sarma, *Electron temperature and tunnel coupling dependence of zero-bias and almost-zero-bias conductance peaks in Majorana nanowires,* Phys. Rev. B **96**, 184520 (2017).

[21] C. Moore, C. Zeng, T. D. Stanescu, and S. Tewari, *Quantized zero bias conductance plateau in semiconductor-superconductor heterostructures without non-Abelian Majorana zero modes,* arXiv:1804.03164 (2018).

[22] C.-X. Liu, J. D. Sau, and S. Das Sarma, *Distinguishing topological Majorana bound states from trivial Andreev bound states: Proposed tests through differential tunneling conductance spectroscopy,* arXiv:1803.05423 (2018).

[23] C.-K. Chiu and S. Das Sarma, *Fractional Josephson Effect with and without Majorana Zero Modes,* arXiv:1806.02224 (2018).

[24] L. Fu and C. L. Kane, *Probing Neutral Majorana Fermion Edge Modes with Charge Transport,* Phys. Rev. Lett. **102**, 216403 (2009).

[25] R. M. Lutchyn, J. D. Sau, and S. Das Sarma, *Majorana Fermions and a Topological Phase Transition in Semiconductor-Superconductor Heterostructures,* Phys. Rev. Lett. **105**, 077001 (2010).

[26] D. J. Clarke, *Experimentally accessible topological quality factor for wires with zero energy modes,* Phys. Rev. B **96**, 201109 (2017).

[27] E. Prada, R. Aguado, and P. San-Jose, *Measuring Majorana nonlocality and spin structure with a quantum dot,* Phys. Rev. B **96**, 085418 (2017).

[28] M. T. Deng, S. Vaitiekénas, E. Prada, P. San-Jose, J. Nygård, P. Krogstrup, R. Aguado, and C. M. Marcus, *Majorana non-locality in hybrid nanowires,* arXiv:1712.03536 (2017).

[29] Y. Oreg, G. Refael, and F. von Oppen, *Helical Liquids and Majorana Bound States in Quantum Wires,* Phys. Rev. Lett. **105**, 177002 (2010).

[30] C. Groth, M. Wimmer, A. Akhmerov, and X. Waintal, *Kwant: a software package for quantum transport,* New J. Phys. **16**, 063065 (2014).

[31] A. Vuik, B. Nijholt, A. R. Akhmerov, and M. Wimmer, *Reproducing topological properties with quasi-majorana states,* (2018), dataset.

[32] B. Nijholt, J. Weston, and A. Akhmerov, *Adaptive, a python package for adaptive parallel sampling of mathematical functions,* (2018), Zenodo.

[33] D. Dresen, *Quantum Transport of Non-Interacting Electrons in 2D Systems of Arbitrary Geometries*, Master's thesis, RWTH Aachen University, Germany (2014).

[34] J. Nilsson, A. R. Akhmerov, and C. W. J. Beenakker, *Splitting of a Cooper Pair by a Pair of Majorana Bound States,* Phys. Rev. Lett. **101**, 120403 (2008).

[35] P. A. Ioselevich and M. V. Feigel'man, *Tunneling conductance due to a discrete spectrum of Andreev states,* New J. Phys. **15**, 055011 (2013).

[36] J. P. T. Stenger, B. D. Woods, S. M. Frolov, and T. D. Stanescu, *Control and detection of Majorana bound states in quantum dot arrays,* arXiv:1805.08119 (2018).

[37] A. R. Akhmerov, J. P. Dahlhaus, F. Hassler, M. Wimmer, and C. W. J. Beenakker, *Quantized Conductance at the Majorana Phase Transition in a Disordered Superconducting Wire,* Phys. Rev. Lett. **106**, 057001 (2011).

[38] B. Fregoso, A. Lobos, and S. Das Sarma, *Electrical detection of topological quantum phase transitions in disordered Majorana nanowires,* Phys. Rev. B **88**, 180507(R) (2013).

[39] P. Szumniak, D. Chevallier, D. Loss, and J. Klinovaja, *Spin and charge signatures of topological superconductivity in Rashba nanowires,* Phys. Rev. B **96**, 041401 (2017).

[40] T. O. Rosdahl, A. Vuik, M. Kjaergaard, and A. R. Akhmerov, *Andreev rectifier: A nonlocal conductance signature of topological phase transitions,* Phys. Rev. B **97**, 045421 (2018).

[41] H. Zhang, C.-X. Liu, S. Gazibegovic, D. Xu, J. A. Logan, G. Wang, N. van Loo, J. D. S. Bommer, M. W. A. de Moor, D. Car, R. L. M. Op het Veld, P. J. van Veldhoven, S. Koelling, M. A. Verheijen, M. Pendharkar, D. J. Pennachio, B. Shojaei, J. S. Lee, C. J. Palmstrøm, E. P. A. M. Bakkers, S. D. Sarma, and L. P. Kouwenhoven, *Quantized Majorana conductance,* Nature **556**, 74–79 (2018).

[42] B. Nijholt and A. R. Akhmerov, *Orbital effect of magnetic field on the Majorana phase diagram,* Phys. Rev. B **93**, 235434 (2016).

[43] O. Dmytruk and J. Klinovaja, *Suppression of the overlap between Majorana fermions by orbital magnetic effects in semiconducting-superconducting nanowires,* Phys. Rev. B **97**, 155409 (2018).

[44] J. Alicea, Y. Oreg, G. Refael, F. von Oppen, and M. P. A. Fisher, *Non-Abelian statistics and topological quantum information processing in 1D wire networks,* Nat. Phys. (2011).

[45] J. D. Sau, D. J. Clarke, and S. Tewari, *Controlling non-Abelian statistics of Majorana fermions in semiconductor nanowires,* Phys. Rev. B **84**, 094505 (2011).

[46] D. Aasen, M. Hell, R. V. Mishmash, A. Higginbotham, J. Danon, M. Leijnse, T. S. Jespersen, J. A. Folk, C. M. Marcus, K. Flensberg, and J. Alicea, *Milestones Toward Majorana-Based Quantum Computing,* Phys. Rev. X **6**, 031016 (2016).

[47] B. van Heck, A. R. Akhmerov, F. Hassler, M. Burrello, and C. W. J. Beenakker, *Coulomb-assisted braiding of Majorana fermions in a Josephson junction array,* New Journal of Physics **14**, 035019 (2012).

[48] T. Hyart, B. van Heck, I. C. Fulga, M. Burrello, A. R. Akhmerov, and C. W. J. Beenakker, *Flux-controlled quantum computation with Majorana fermions,* Phys. Rev. B **88**, 035121 (2013).

[49] P. Bonderson, M. Freedman, and C. Nayak, *Measurement-Only Topological Quantum Computation,* Phys. Rev. Lett. **101**, 010501 (2008).

[50] S. Plugge, A. Rasmussen, R. Egger, and K. Flensberg, *Majorana box qubits,* New Journal of Physics **19**, 012001 (2017).

[51] T. Karzig, C. Knapp, R. M. Lutchyn, P. Bonderson, M. B. Hastings, C. Nayak, J. Alicea, K. Flensberg, S. Plugge, Y. Oreg, C. M. Marcus, and M. H. Freedman, *Scalable designs for quasiparticle-poisoning-protected topological quantum computation with Majorana zero modes,* Phys. Rev. B **95**, 235305 (2017).

[52] I. C. Fulga, B. van Heck, M. Burrello, and T. Hyart, *Effects of disorder on Coulomb-assisted braiding of Majorana zero modes,* Phys. Rev. B **88**, 155435 (2013).

[53] J. Koch, T. M. Yu, J. Gambetta, A. A. Houck, D. I. Schuster, J. Majer, A. Blais, M. H. Devoret, S. M. Girvin, and R. J. Schoelkopf, *Charge-insensitive qubit design derived from the Cooper pair box,* Phys. Rev. A **76**, 042319 (2007).

[54] W. Chang, S. M. Albrecht, T. S. Jespersen, F. Kuemmeth, P. Krogstrup, J. Nygård, and C. M. Marcus, *Hard gap in epitaxial semiconductor–superconductor nanowires,* Nature Nanotechnology **10**, 232 (2015).

[55] H. Zhang, O. Gül, S. Conesa-Boj, M. P. Nowak, M. Wimmer, K. Zuo, V. Mourik, F. K. de Vries, J. van Veen, M. W. A. de Moor, J. D. S. Bommer, D. J. van Woerkom, D. Car, S. R. Plissard, E. P. A. M. Bakkers, M. Quintero-Pérez, M. C. Cassidy, S. Koelling, S. Goswami, K. Watanabe, T. Taniguchi, and L. P. Kouwenhoven, *Ballistic superconductivity in semiconductor nanowires,* Nat. Comm. **8**, 16025 (2017).

[56] S. Gazibegovic, D. Car, H. Zhang, S. C. Balk, J. A. Logan, M. W. A. de Moor, M. C. Cassidy, R. Schmits, D. Xu, G. Wang, P. Krogstrup, R. L. M. Op het Veld, K. Zuo, Y. Vos, J. Shen, D. Bouman, B. Shojaei, D. Pennachio, J. S. Lee, P. J. van Veldhoven, S. Koelling, M. A. Verheijen, L. P. Kouwenhoven, C. J. Palmstrøm,

and E. P. A. M. Bakkers, *Epitaxy of advanced nanowire quantum devices,* Nature **548**, 434 (2017).

[57] O. Gül, H. Zhang, J. D. S. Bommer, M. W. A. de Moor, D. Car, S. R. Plissard, E. P. A. M. Bakkers, A. Geresdi, K. Watanabe, T. Taniguchi, and L. P. Kouwenhoven, *Ballistic Majorana nanowire devices,* Nature Nanotechnology **13**, 192 (2018).

[58] D. R. Hofstadter, *Energy levels and wave functions of Bloch electrons in rational and irrational magnetic fields,* Phys. Rev. B **14**, 2239 (1976).

5

Andreev rectifier: a nonlocal conductance signature of topological phase transitions

This chapter has been previously published as T. Ö. Rosdahl, A. Vuik, M. Kjaergaard, A. R. Akhmerov, *Andreev rectifier: a nonlocal conductance signature of topological phase transitions*, Phys. Rev. B 97, 045421 (2018).

5.1. INTRODUCTION

The superconducting proximity effect occurs when a normal material (metal) is placed in contact with a superconductor. The resulting transfer of superconducting properties to the normal material [1, 2] makes it possible to explore induced superconductivity in a range of materials that are not intrinsically superconducting, for example in ferromagnetic metals [3–5] and in graphene [6–8]. Another recent application of the proximity effect is the creation of the Majorana quasiparticle [9–11], which is a candidate for the realization of topological quantum computation [12], and a focus of research efforts in recent years [13–15].

The proximity effect is due to the Andreev reflection of quasiparticles at the interface with the superconductor [2], which forms correlated electron-hole pairs that induce superconductivity in the normal material. This makes the proximity effect in real systems sensitive to microscopic interface properties, such as coupling strength, charge accumulation and lattice mismatch [16, 17]. Spatial inhomogeneities in the proximitised system, such as charge defects, may furthermore spoil the induced correlations locally. In a typical proximity setup, the superconductor proximitises an extended region of a normal material, as shown in Fig. 5.1. A normal lead attached to one of the ends of the proximitised region probes the response to an applied voltage. When the coupling between the lead and the proximitised region is weak, the lead functions as a tunnel probe of the density of states in the latter. Since induced superconductivity may be inhomogeneous, and Andreev reflection happens locally, such an experiment only probes the region in direct vicinity of the normal lead, and not the overall properties of the proximitised region. For example, if the electrostatic potential is inhomogeneous, it may create accidental low-energy modes that are nearly indistinguishable from Majoranas [18–23].

We show how the *nonlocal* response between two spatially separated normal leads (see Fig. 5.1) may be used to probe both the bulk superconducting gap Δ and the induced gap Δ_{ind}, as well as the induced coherence length ξ. At subgap energies, quasiparticles propagate as evanescent waves with the decay length ξ in the proximitised system. This suppresses the nonlocal response with increasing separation L between the two normal leads [24–26]. Therefore, the length dependence of the nonlocal conductance measures when two ends of a proximitised system are effectively decoupled. When $L/\xi \gtrsim 1$, the nonlocal conductance is only possible in the energy window between the bulk superconducting gap Δ and the induced gap Δ_{ind}. The sensitivity to an induced gap allows one to use nonlocal conductance to distinguish between a induced gap closing and an Andreev level crossing at zero energy. In contrast, a local measurement may produce a similar result in both cases.

Two processes constitute the nonlocal response: direct electron transfer between the normal leads, and the crossed Andreev reflection (CAR) of an electron from one lead into a hole in the second lead [27, 28]. Experimental [29–31] and theoretical [32–37] studies of CAR-dominated signals aim at producing a Cooper pair splitter [38–40], which has potential applications in quantum information processing. We show that applying a Zeeman field in the proximitised system creates wide regions in parameter space where CAR dominates the nonlocal response. Furthermore, we demonstrate how to obtain a CAR dominated signal in the absence of a

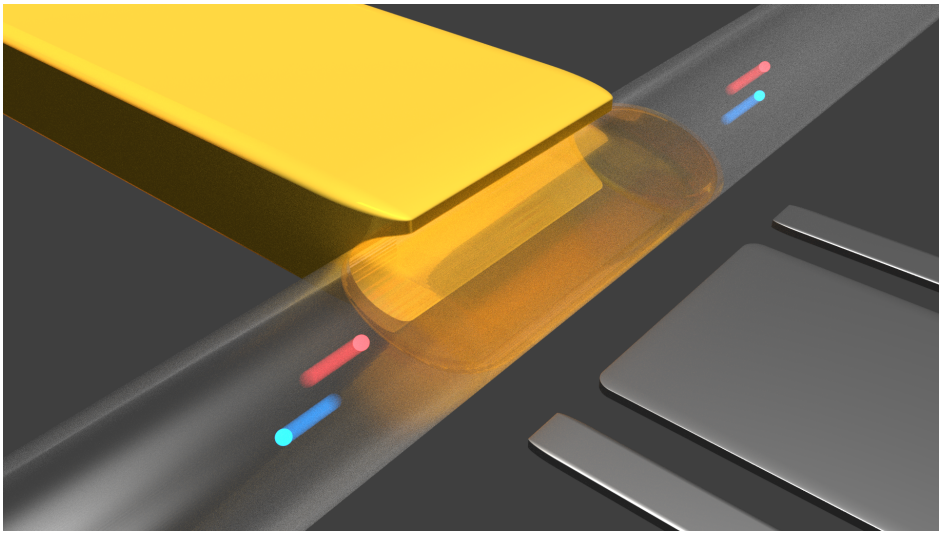

Figure 5.1: A superconductor (yellow) proximitises a semiconducting region (transparent) from the side. Narrow gates control the coupling of the proximitised scattering region with the leads, a wider gate controls the chemical potential. An incoming electron from the left (red dot) either undergoes a local process, i.e. Andreev reflection into a hole (blue outgoing dot to the left) or normal reflection (not shown), or a nonlocal process (outgoing electron or hole to the right).

Zeeman field in the low-doping regime. Finally, we prove that at the topological phase transition and with $L/\xi \gtrsim 1$, the nonlocal conductance is an approximately odd function of bias. This phenomenon only relies on particle-hole symmetry, and hence manifests both in clean and disordered junctions. Therefore, a proximitised system coupled to normal leads acts as a rectifier of the applied voltage bias universally at the topological phase transition.

Our method is based on probing the bulk topological phase transition in Majorana devices, instead of the Majoranas themselves. Several other works propose different methods to probe the bulk instead of the edge states in one-dimensional topological superconductors. Quantized thermal conductance and electrical shot noise measurements are predicted signatures of a bulk topological phase transition [41], and here we present a different route based on straightforward electrical conduction measurements in already available experimental systems. Further work predicts bulk signatures of a topological phase transition in the difference between the local Andreev conductances at each end of the proximitised region [42], or in the spin projection of bulk bands along the magnetic field direction [43]. In addition to probing the bulk topological phase transition, our proposed method allows to probe a number of relevant physical parameters, and can be implemented in ongoing experiments, providing a novel technique to use in the hunt for Majoranas.

This paper is organized as follows. In Sec. 5.2, we give an overview of our model and discuss the relevant energy and length scales. In Sec. 5.3, we study how nonlocal conductance measures superconductor characteristics. We investigate the effects of a

Zeeman field in homogeneous and inhomogeneous systems in Sec. 5.4. In Sec. 5.5 we consider the possible application of the proximitised system as a Cooper pair splitter. We finish with a summary and discussion of our results in Sec. 5.6.

5.2. MODEL AND PHYSICAL PICTURE

We consider a three terminal device sketched in Fig. 5.2, with a normal central region of lateral length L and width W separating two normal leads of width W_{L}. The device has a grounded superconducting lead of width L attached to the central region perpendicularly to the other two leads. This geometry models the proximity effect of a lateral superconductor on a slab of normal material, with normal leads probing the transport properties, and is therefore relevant both for heterostructures based on nanowires and quantum wells.

We model the hybrid system using the Bogoliubov-de Gennes Hamiltonian. For a semiconductor electron band with effective mass m^* and Rashba spin-orbit interaction (SOI) with strength α, it reads

$$H = \left(\frac{p_x^2 + p_y^2}{2m^*} - \mu \right) \tau_z + \Delta(y)\tau_x + \frac{\alpha}{\hbar} \left(p_y \sigma_x - p_x \sigma_y \right) \tau_z + E_{\mathrm{Z}}(y)\sigma_x, \tag{5.1}$$

with $p_{x,y} = -i\hbar\partial_{x,y}$, μ the equilibrium chemical potential and E_{Z} the Zeeman energy due to an in-plane magnetic field parallel to the interface between the central region and the superconductor. We assume a constant s-wave pairing potential that is nonzero only in the superconductor, $\Delta(y) = \Delta\theta(y - W)$ with $\theta(y)$ a step function, and choose Δ to be real since only one superconductor is present. We neglect the g-factor in the superconductor since it is much smaller than in the adjacent semiconductor, such that $E_{\mathrm{Z}}(y) = E_{\mathrm{Z}}\theta(W - y)$, and our conclusions are not affected by this choice. The Pauli matrices σ_i and τ_i act in spin and particle-hole space, respectively. The Hamiltonian acts on the spinor $\Psi = (\psi_{e\uparrow}, \psi_{e\downarrow}, \psi_{h\downarrow}, -\psi_{h\uparrow})$, which represent the electron (e) or hole (h) components of spin up (↑) or down (↓).

The superconductor induces an energy gap Δ_{ind} in the heterostructure. If $L \gg W$, the larger of two energy scales, namely the bulk gap Δ and the Thouless energy E_{Th}, determines the magnitude of Δ_{ind}, with E_{Th} at low μ given by

$$E_{\mathrm{Th}} = \gamma\delta, \quad \delta = \frac{\hbar^2\pi^2}{2m^*(2W)^2}, \tag{5.2}$$

where γ is the transparency of the interface with the superconductor and δ the level spacing. Our emphasis is on short and intermediate junctions, for which $E_{\mathrm{Th}} \gg \Delta$ and $E_{\mathrm{Th}} \lesssim \Delta$, respectively, such that $\Delta_{\mathrm{ind}} \lesssim \Delta$. A brief review of normal-superconductor junctions in different limits and the relevant length and energy scales is given in App. 5.7. We keep μ constant in the entire system, but assume an anisotropic mass [44] in the superconductor with a component parallel to the interface $m_{\parallel} \to \infty$. This approximation results in a transparent interface $\gamma = 1$ at normal incidence and at $E_{\mathrm{Z}} = 0$, and is motivated by recent advances in the fabrication of proximitised systems with a high-quality superconductor-semiconductor interface [45, 46].

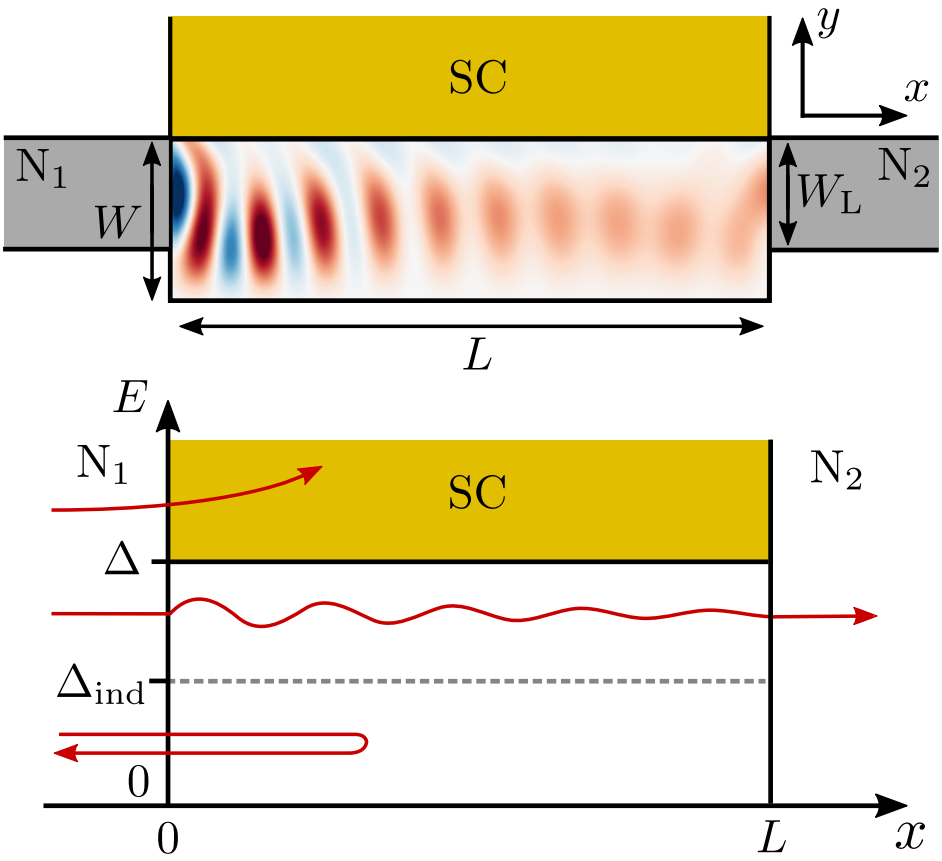

Figure 5.2: Top: schematic drawing of the device. A central region of length L and width W is connected from the sides to two normal leads N_1 (left) and N_2 (right) of width W_L, and from the top to one superconducting lead (SC) of width L. Superimposed is an example of the central region charge density, which oscillates between positive (red) and negative (blue). Bottom: illustrations of possible scattering processes in energy space in the limit $L \gg \xi$. A quasiparticle, with energy below the induced gap, $|E| < \Delta_{\text{ind}}$, is reflected back into the source lead. A quasiparticle at $\Delta_{\text{ind}} < |E| < \Delta$ is transmitted to the right lead, either as an electron (normal transmission) or as a hole (crossed Andreev reflection). At energies exceeding the bulk gap $|E| > \Delta$, the superconducting lead absorbs incoming quasiparticles.

We compute differential conductance using the scattering formalism. The scattering matrix relating all incident and outgoing modes in the normal leads of Fig. 5.2 is

$$S = \begin{bmatrix} S_{11} & S_{12} \\ S_{21} & S_{22} \end{bmatrix}, \quad S_{ij} = \begin{bmatrix} S_{ij}^{ee} & S_{ij}^{eh} \\ S_{ij}^{he} & S_{ij}^{hh} \end{bmatrix}. \tag{5.3}$$

Here, the $S_{ij}^{\alpha\beta}$ is the block of scattering amplitudes of incident particles of type β in lead j to particles of type α in lead i. Since quasiparticles may enter the superconducting lead for $|E| > \Delta$, the scattering matrix (5.3) is unitary only if

$|E| < \Delta$. The zero-temperature differential conductance matrix equals [2, 47]

$$G_{ij}(E) \equiv \frac{\partial I_i}{\partial V_j} = \frac{e^2}{h}\left(T_{ij}^{ee} - T_{ij}^{he} - \delta_{ij} N_i^e\right), \tag{5.4}$$

with I_i the current entering terminal i from the scattering region and V_j the voltage applied to the terminal j, and N_j^e the number of electron modes at energy E in terminal j, and finally the energy-dependent transmissions are

$$T_{ij}^{\alpha\beta} = \mathrm{Tr}\left(\left[S_{ij}^{\alpha\beta}(E)\right]^\dagger S_{ij}^{\alpha\beta}\right). \tag{5.5}$$

The blocks of the conductance matrix involving the superconducting terminal are fixed by the condition that the sum of each row and column of the conductance matrix has to vanish. The finite temperature conductance is a convolution of zero-temperature conductance with a derivative of the Fermi distribution function $f(E) = (1 + \exp(E/k_B T))^{-1}$:

$$G_{ij}(eV_j, T) = -\int_{-\infty}^{\infty} \mathrm{d}E \frac{\mathrm{d}f(E - eV_j, T)}{\mathrm{d}E} G_{ij}(E). \tag{5.6}$$

We discretize the Hamiltonian (5.1) on a square lattice, and use Kwant [48] to numerically obtain the scattering matrix of Eq. (5.3), see the supplementary material for source code [49]. The resulting data is available in Ref. [50]. We obtain ξ numerically by performing an eigendecomposition of the translation operator in the x-direction for a translationally invariant system and computing the decay length of the slowest decaying mode at $E = 0$ [44, 51]. We use the material parameters[1] $m^* = 0.023 m_\mathrm{e}$, $\alpha = 28$ meVnm, and unless otherwise specified $\Delta = 0.2$ meV, typical for an InAs two-dimensional electron gas with an epitaxial Al layer [45]. All transport calculations are done using $T = 30$ mK unless stated otherwise.

5.3. NONLOCAL CONDUCTANCE AS A MEASURE OF SUPERCONDUCTOR PROPERTIES

In the tunnelling regime, the local conductance in a normal lead probes the density of states in the proximitised region, which is commonly used to measure the induced gap in experiment. However, such a measurement only probes the region near the tunnel probe, but fails to give information about the density of states in the bulk of the proximitised region. The tunnelling conductance is thus not a reliable probe of the entire proximitised region if the density of states varies spatially over the proximitised region, for example due to an inhomogeneous geometry. As an illustration, Fig. 5.3 compares the local conductance G_{11} in the tunnelling limit to the nonlocal conductance G_{21} in the open regime for a proximitised system that is inhomogeneous and in a magnetic field. Inhomogeneous systems are further treated in Sec. 5.4. The combination of an inhomogeneous system and broken time-reversal

[1] All parameters are provided per figure in a text file as supplementary material.

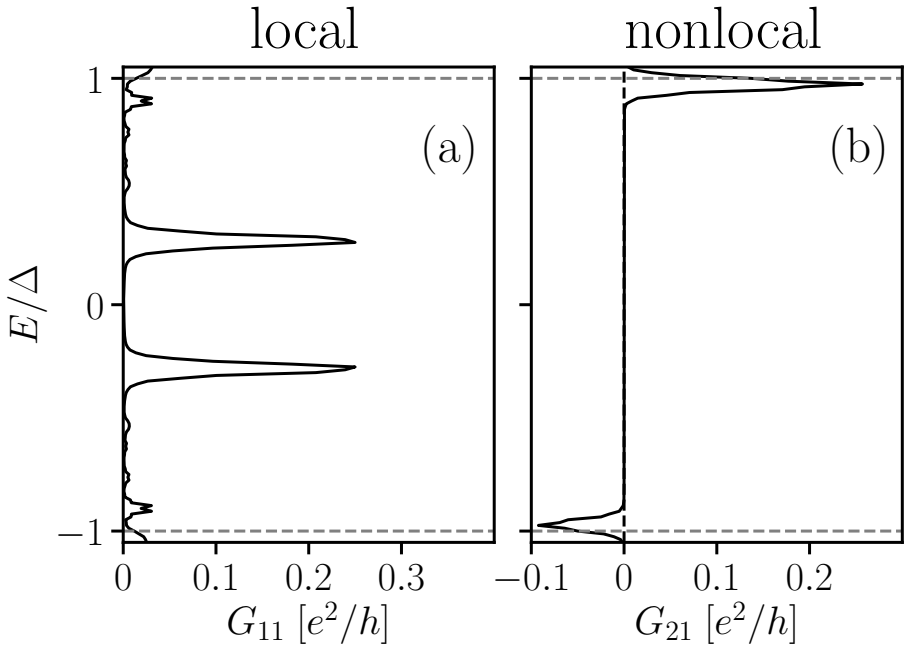

Figure 5.3: Examples of (a) the local conductance in the tunnelling regime and (b) the nonlocal conductance in the open regime, of an inhomogeneous proximitised system with broken time-reversal symmetry. Localized low-energy states are present near the junctions with the normal leads. These manifest as peaks in the tunnelling conductance, indicating $\Delta_{\rm ind} \ll \Delta$. However, $\Delta_{\rm ind} \approx \Delta$ still in the bulk of the proximitised system, with $\Delta_{\rm ind}$ matching the energy at which the nonlocal conductance peaks.

symmetry creates low-energy states localized near the junctions with the normal leads, which appear as peaks in the tunnelling conductance. However, away from the junctions with the normal leads, the proximitised system remains close to fully gapped, the induced gap matching the energies at which the nonlocal conductance becomes finite in Fig. 5.3(b). Therefore, the nonlocal conductance is better than the local tunnelling conductance as a probe for the induced gap in the bulk of the proximitised region. In the following, we describe three ways in which the nonlocal conductance probes induced superconductivity.

First of all, the nonlocal conductance measures the induced decay length ξ in the bulk of the proximitised region between the two normal leads. To understand this, consider a nonlocal process at a subgap energy $|E| < \Delta_{\rm ind}$. An electron injected from a normal lead must propagate as an evanescent wave $\propto e^{-x/\xi + ikx}$ through the gapped central region to the second normal lead, with ξ the decay length. Accordingly, as shown in Fig. 5.4, increasing L suppresses the nonlocal conductance at $E = 0$ exponentially [28, 38]. Therefore, the suppression of the nonlocal conductance with increasing length L at $E = 0$ is a measure of the induced decay length ξ.

Furthermore, the nonlocal conductance measures the bulk gap Δ of the superconductor. Increasing L also suppresses the nonlocal conductance G_{21} for $|E| > \Delta$,

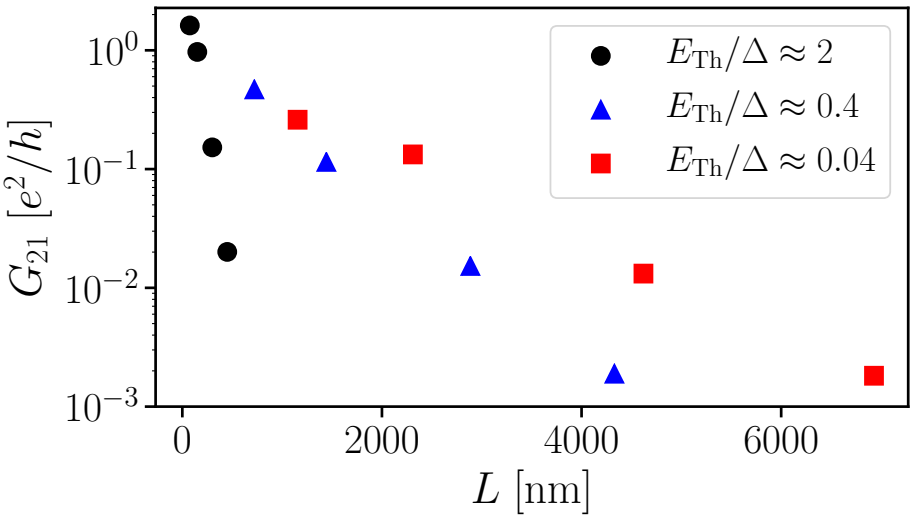

Figure 5.4: Suppression of the nonlocal conductance G_{21} at zero bias $E = 0$ as a function of length for different ratios E_{Th}/Δ. For decreasing ratio E_{Th}/Δ, the induced coherence length ξ increases. This is reflected in the larger absolute length over which the nonlocal conductance is suppressed. Data points are taken from the $E = 0$ values of the nonlocal conductance presented in Fig. 5.5.

as the right column of Fig. 5.5 shows. For energies above the bulk superconducting gap Δ, the superconductor increasingly absorbs quasiparticles when the length is increased, and suppresses the nonlocal conductance to zero when $L \gg \xi$. Hence, the energy above which nonlocal conductance is suppressed at large lengths is a measure of Δ.

In addition, the nonlocal conductance measures the induced superconducting gap Δ_{ind}. When $L \gtrsim \xi$, the nonlocal conductance is suppressed at $E = 0$ but grows in a convex shape with E and peaks around $|E| \approx \Delta_{\mathrm{ind}}$, as shown in the right column of Fig. 5.5. This is due to a divergence in ξ, since the system is no longer gapped. To illustrate the correspondence between the nonlocal conductance and Δ_{ind}, the left column of Fig. 5.5 shows the dispersions of the corresponding proximitised systems that have the normal leads removed and are translationally invariant along the x direction, such that $k = p_x/\hbar$ is conserved. Because the system is not gapped for $|E| > \Delta_{\mathrm{ind}}$, G_{21} is generally nonzero at these energies. Note that aside from occasional dips to negative G_{21}, direct electron transfer dominates the nonlocal response (we investigate this in more detail in Sec. 5.5).

The presence of finite nonlocal conductance in the energy range $\Delta_{\mathrm{ind}} < |E| < \Delta$ depends only on density of states of the proximitised system, and therefore still holds in the presence of disorder. In Fig. 5.6, we show the effects of disorder on the transport signatures of Δ and Δ_{ind} for short and intermediate junctions when $L \gtrsim \xi$. We include onsite disorder in the central region, and vary the elastic mean free path l_{e} from $l_{\mathrm{e}} = L$ to $l_{\mathrm{e}} = 0.1L$ [52]. Even in the presence of disorder, all of the aforementioned qualities are still apparent in the nonlocal conductance (a) and (b),

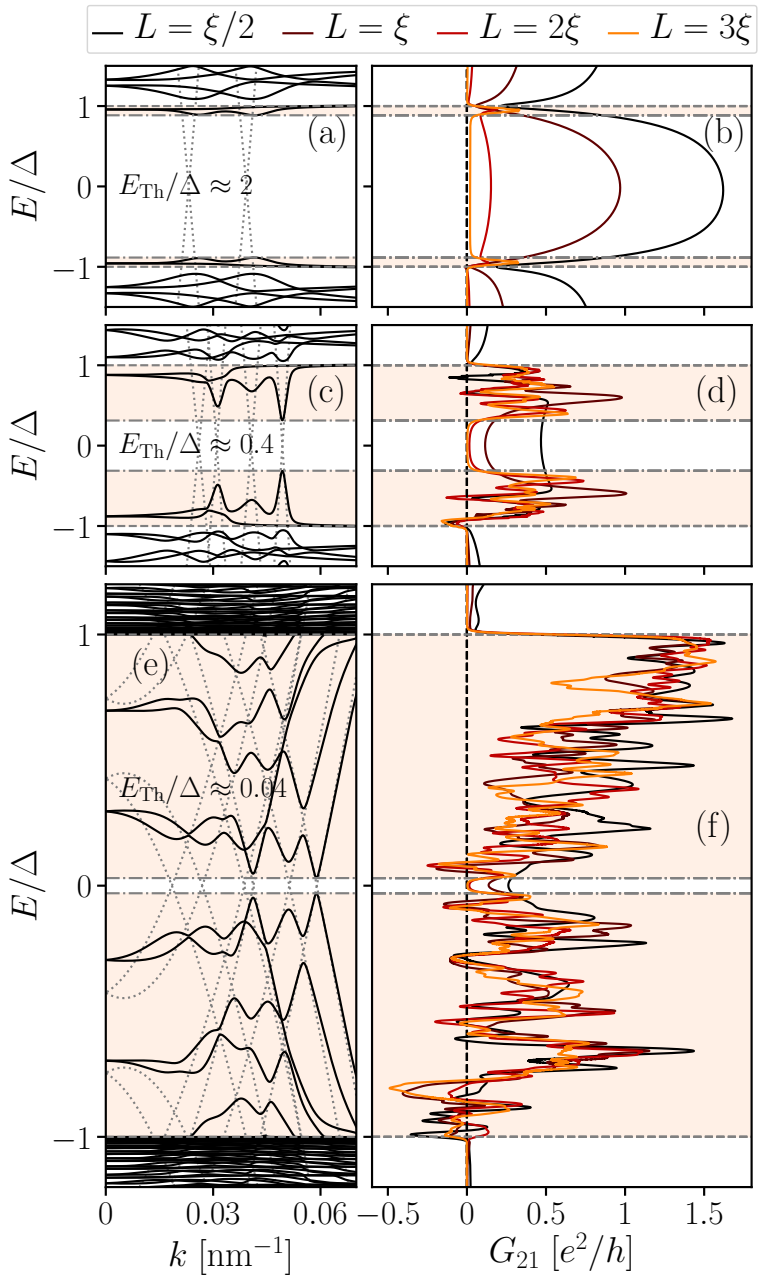

Figure 5.5: (a, c, e) Dispersions of proximitised systems that are translationally invariant along x, and (b, d, f) nonlocal conductance $G_{21}(E)$ of corresponding junctions of finite length. The latter is shown as the separation L between the two normal leads is varied, with brightening colors from black to orange denoting $L = \xi/2,\ \xi,\ 2\xi$ and 3ξ, respectively. The ratio E_{Th}/Δ becomes smaller from top to bottom, such that Δ_{ind} shrinks (dash-dotted lines). For $L \gg \xi$, the nonlocal conductance is suppressed if $|E| < \Delta_{\mathrm{ind}}$, and finite only for $\Delta_{\mathrm{ind}} < |E| < \Delta$ (colored region). The solid lines in the dispersion relations show the dispersion of the normal-superconductor system, while the dotted lines show the electron and hole dispersion of the normal channel only, with the superconductor removed. We have $W = 100$ nm in (a) and (b), $W = 200$ nm in (c), (d), (e) and (f), and $W_L = 100$ nm always in the right column. $\mu = 3$ meV, $\Delta = 0.2$ meV and $T = 30$ mK in the top and middle rows, but $\mu = 4.2$ meV, $\Delta = 2$ meV and $T = 100$ mK in the bottom row. Dispersions are even in k.

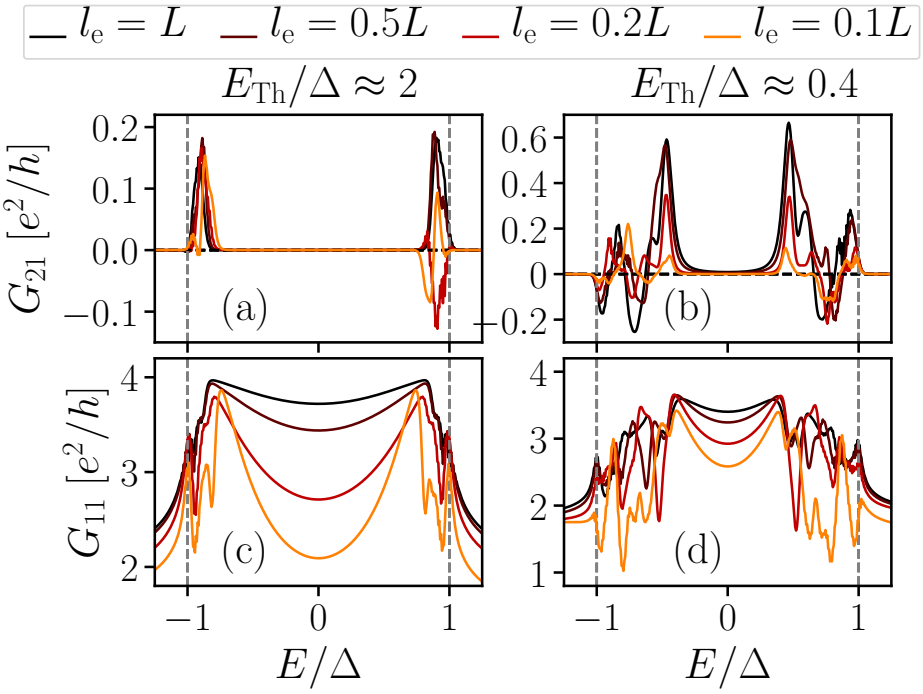

Figure 5.6: Nonlocal (a, b) and local conductance (c, d) G_{21} and G_{11} of short (left column) and intermediate (right column) junctions with $L \gtrsim \xi$, to decouple the two normal leads at $|E| < \Delta_{\text{ind}}$. The mean free path varies between curves, with brightening colors from black to light orange denoting $l_e = L,\ L/2,\ L/5$ and $L/10$ respectively. Even in the presence of disorder, signatures of Δ_{ind} and Δ are visible in the nonlocal conductance. The local conductance is Andreev enchanced at subgap energies, but normal reflection becomes more prominent with increasing disorder. We have $W = 100$ nm and $L = 8\xi$ in (a) and (c), $W = 200$ nm and $L = 2\xi$ in (b) and (d), and $W_L = 100$ nm always, with $\mu = 3$ meV.

namely suppression for $|E| < \Delta_{\text{ind}}$, a finite signal for $\Delta_{\text{ind}} < |E| < \Delta$ and vanishing conductance for $|E| > \Delta$. Therefore, the nonlocal conductance remains a reliable probe of induced superconductivity even in the presence of disorder.

Lastly, in the absence of extended potential inhomogeneities, Δ and Δ_{ind} may also be inferred from the local conductance G_{11} in the open regime. As Figs. 5.6(c) and (d) show, $G_{11} \lesssim 4e^2/h$ in the ballistic case $l_e = L$ for $|E| < \Delta_{\text{ind}}$, which indicates that Andreev reflection is the dominant local process. This is the expected behavior for a normal-superconductor junction with high interface transparency [2, 45], and is consistent with our results. Reducing the mean free path makes normal reflection more likely and hence lowers G_{11}, similar to an ideal normal-superconductor junction with a reduced interface transparency. Here, comparing G_{11} and G_{21} shows that Δ_{ind} and Δ may also be inferred from the local conductance, because it changes smoothly with bias only outside the interval $\Delta_{\text{ind}} < |E| < \Delta$. However, the signatures are clearer in G_{21}, where it is a transition between finite and vanishing conductance that indicates the gaps. Furthermore, the induced gap observed in the local and

nonlocal conductances coincide here only due to the absence of extended potential inhomogeneities. For the case of an inhomogeneous geometry as in Fig. 5.3, only the nonlocal conductance correctly measures Δ_{ind} in the bulk of the proximitised system.

5.4. ANDREEV RECTIFIER AT THE TOPOLOGICAL PHASE TRANSITION

5.4.1. ANDREEV RECTIFICATION AS A MEASURE OF THE TOPOLOGICAL PHASE

In order to study nonlocal conductance at the topological phase transition, we apply an in-plane Zeeman field along the x-direction of the proximitised system. Figure 5.7 shows the nonlocal conductance G_{21} as a function of bias E and Zeeman energy E_{Z}, for short and intermediate junctions in (a) and (b) with $L = 10\xi$ and $L = 3\xi$, respectively, such that the two normal leads are well decoupled, and the nonlocal conductance is exponentially suppressed at subgap energies. Increasing the magnetic field closes the induced gap and the system is driven into a topological phase. The line cuts of Fig. 5.7(c), taken at the critical magnetic field $E_{\mathrm{Z}} = E_{\mathrm{Z}}^c$, show that at the topological phase transition the nonlocal conductance is a linear function of energy, $G_{21}(E) \propto E$ around $E = 0$. At the topological phase transition, the current $I \propto V^2$ with V the voltage bias, and the system functions as a current rectifier due to crossed Andreev reflection.

This Andreev rectifier manifests due to the topology and symmetry of the proximitised system. The system only has particle-hole symmetry and is therefore in class D [53, 54]. Expanding $G_{21}(E, E_{\mathrm{Z}}) = c_0(E_{\mathrm{Z}}) + c_1(E_{\mathrm{Z}})E + O(E^2)$ around $E = 0$, the exponential suppression of G_{21} at subgap energies means that the coefficients c_0 and c_1 are exponentially suppressed at magnetic fields before the topological phase transition. In class D systems, if G_{21} is exponentially suppressed at subgap energies, it is guaranteed to remain exponentially suppressed across the topological phase transition [41, 55]. At the critical magnetic field $E_{\mathrm{Z}} = E_{\mathrm{Z}}^c$, $G_{21}(E = 0, E_{\mathrm{Z}}^c) = c_0(E_{\mathrm{Z}}^c)$ is therefore also exponentially suppressed. However, the system is gapless at the topological phase transition, such that G_{21} is generally finite at any nonzero E, and $c_1(E_{\mathrm{Z}}^c)$ thus not exponentially suppressed. At the topological phase transition, we therefore have $G_{21} \propto E$ in the limit $E \to 0$, where higher order contributions are negligible. Consequently, rectifying behavior in the nonlocal conductance is an indication of a topological phase transition. This makes the nonlocal conductance not only a probe of the bulk properties of induced superconductivity as discussed in Sec. 5.3, but also makes it selectively sensitive to topological phase transitions.

The rectifying behavior $G_{21} \propto E$ at the topological phase transition in Fig. 5.7 is grounded in the symmetry classification of the channel. As a result, we expect it to be robust to the presence of onsite disorder, so long as it does not alter the symmetry class. Figure 5.8 shows G_{21} as a function of E and E_{Z} for systems with the same widths as in Fig. 5.7. In the left column, parameters are chosen identical to those in Fig. 5.7, with the addition of onsite disorder to give an elastic mean free path $l_{\mathrm{e}} = 0.2L$ [52], bringing the systems well into the quasiballistic regime. In the right

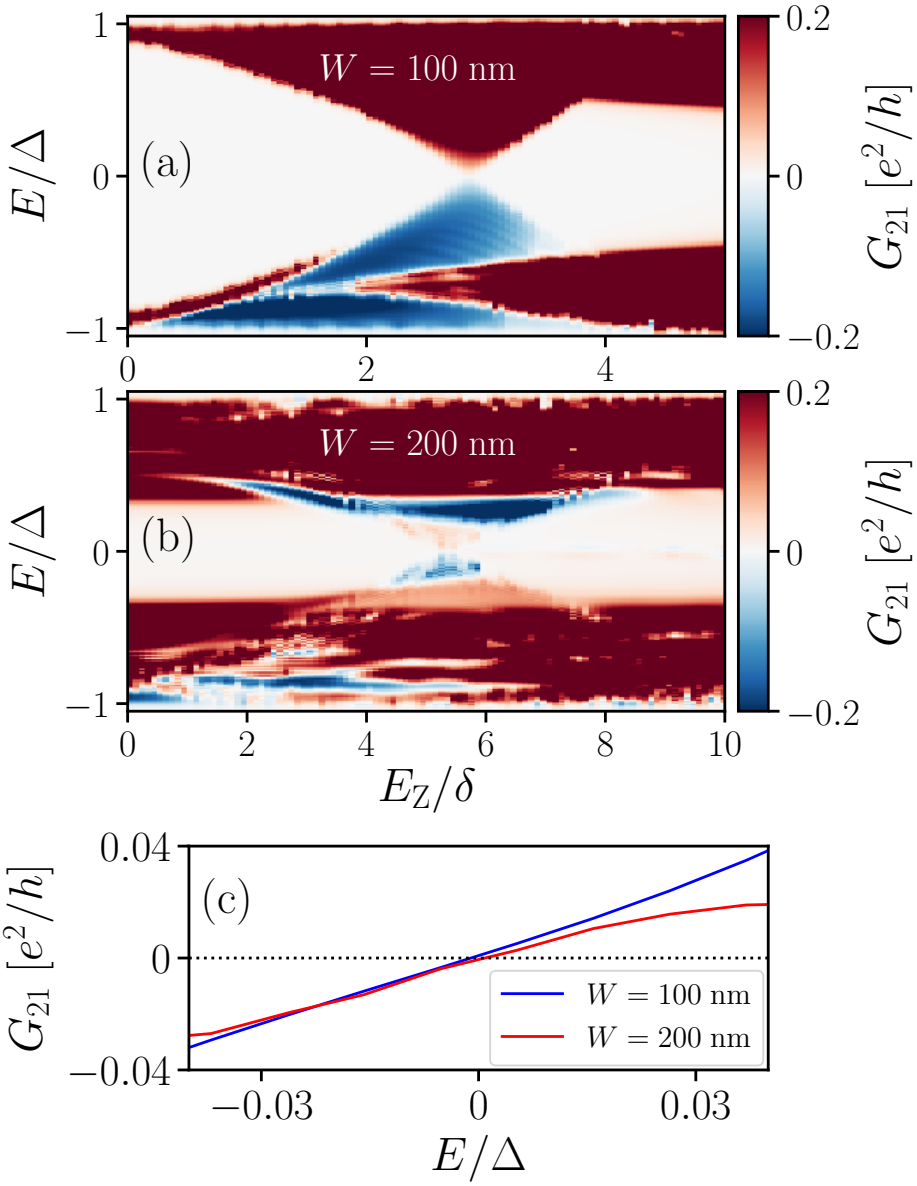

Figure 5.7: (a, b) Nonlocal conductance G_{21} in the single-mode regime as a function of E and E_Z in the absence of disorder. We have $W = 100$ and 200 nm in (a) and (b), respectively. The Zeeman field closes the induced gap and the system undergoes a topological phase transition. At the transition, G_{21} vanishes and changes sign as a function of bias. There are prominent regions where the nonlocal conductance is negative, i.e. where CAR dominates. The color scale is saturated for clarity. (c) Line cuts of G_{21} as a function of bias at the topological phase transition, taken at $E_Z \approx 2.9\delta$ for $W = 100$ nm and $E_Z \approx 5.4\delta$ for $W = 200$ nm, showing that the nonlocal conductance is an approximately odd function of bias.

column of Fig. 5.8, we investigate G_{21} when the central region is in the diffusive limit, with $l_e = 0.2W$. The widths are the same as in the quasiballistic (and clean) case, but μ is increased such that several modes are active. We gate the leads into the single mode regime using quantum point contacts at the junctions with the scattering region. In each case we pick $L \gtrsim \tilde{\xi}$, since in the diffusive limit $\tilde{\xi} = \sqrt{\xi l_e}$ governs the range of the coupling between the two normal terminals at subgap energies [56]. In both quasiballistic and diffusive cases, G_{21} remains an approximately odd function of E around the gap closing, and the proximitised system therefore acts as a rectifier even in the presence of disorder.

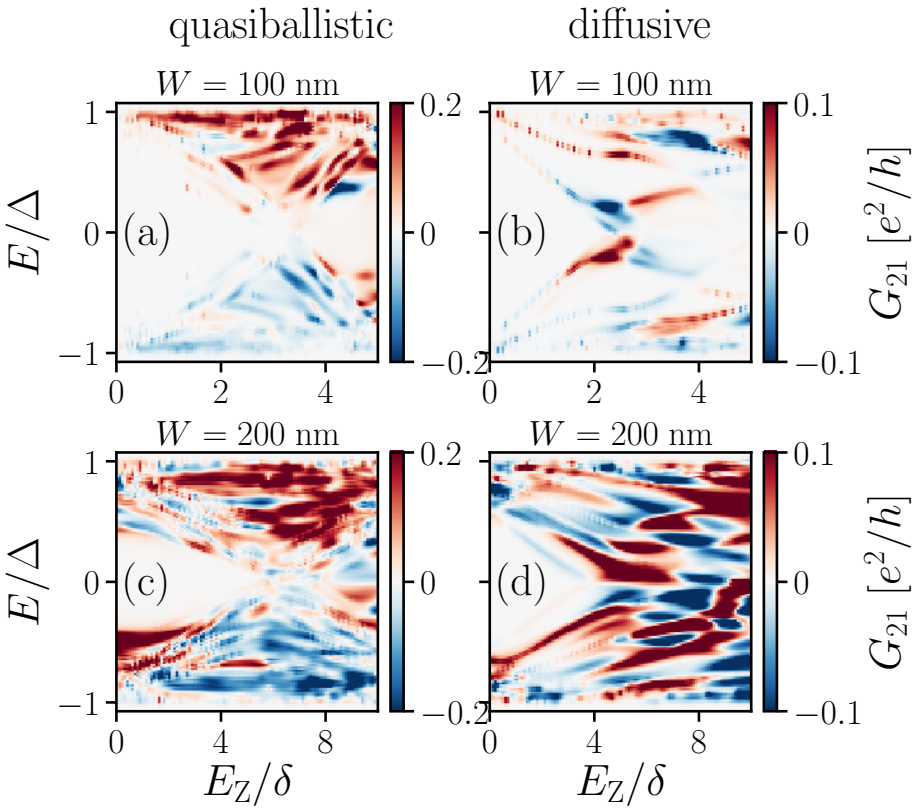

Figure 5.8: The nonlocal conductance G_{21} as a function of E and E_Z for a proximitised system that is quasiballisic (a, c with $\mu = 3$ meV) and diffusive (b, d with $\mu = 16$ meV). For the diffusive junction, the leads are gated into the single-mode regime using quantum point contacts at the junctions with the channel. Top and bottom row present results for $W = 100$ and 200 nm respectively. For the quasiballistic junction, $L/\xi = 8$ and 2 for $W = 100$ nm and 200 nm respectively, and the mean free path is $l_e = 0.2L$ in each case. In the diffusive system, we have $l_e = 0.2W$ and $L/\tilde{\xi} = 5$ and 2 for the widths respectively, where $\tilde{\xi} = \sqrt{l_e \xi}$. The color scale is saturated in both cases for clarity.

5.4.2. DISTINGUISHING THE TOPOLOGICAL PHASE TRANSITION IN SPATIALLY INHOMOGENEOUS DEVICES

Several works [18–23] discuss the emergence of zero-energy modes in the trivial phase of a hybrid semiconductor-superconductor device with an extended, spatially inhomogeneous potential. Local conductance measurements do not distinguish between these modes and well-separated Majorana modes at the endpoints of the proximitised region in the topological phase, since both give rise to zero-bias conductance features.

To study this problem, we include an extended inhomogeneous potential

$$\phi(x,y) = V_0 \exp\left[-\frac{1}{2}\left(\frac{x-x_0}{d_x}\right)^2\right] \exp\left[-\frac{1}{2}\left(\frac{y-y_0}{d_y}\right)^2\right], \tag{5.7}$$

in the setup shown in Fig. 5.2, with V_0 the potential amplitude, x_0 and y_0 the coordinates of the potential center, and d_x and d_y parameters to control the smoothness in x- and y-direction, respectively. We compare conductance for an amplitude $V_0 = -4.5$ mV to conductance in a homogeneous system $V_0 = 0$ V. We calculate the local conductance in the tunneling regime, with tunnel barriers at both wire ends $x = 0$ and $x = L$, and the nonlocal conductance in the open regime, with the system length fixed to $L = 8\xi$ and the width to $W = 100$ nm.

To confirm that such a spatially inhomogeneous system can indeed exhibit trivial zero-energy modes, we calculate the low-energy spectrum of our system when decoupled from the leads, forming a closed superconductor-semiconductor system. The phase transition is computed from the absolute value of the determinant of the reflection matrix in the open system at $E = 0$, with $|\det(r)| = 1$ everywhere for $L \gg \xi$, except at the phase transition, where it drops to zero [57]. Figure 5.9(a) shows the spectrum as a function of E_Z in the homogeneous case ($V_0 = 0$), Fig. 5.9(b) for the inhomogeneous case ($V_0 = -4.5$ mV). While in the first case the closing of the induced superconducting gap coincides with the topological phase transition, in the second case an extended topologically trivial region exists with states around zero energy (yellow region).

Comparing the local conductance with and without an inhomogeneous potential, we find that zero-energy modes appear regardless of whether they are topological or trivial. Panels (c) and (d) of Fig. 5.9 show the local response as a function of bias and Zeeman energy when leads are connected to the central region via tunnel barriers. Since the system is ballistic and long ($L \gg \xi$), the local conductance agrees well with the spectra presented in panels (a) and (b). Accordingly, the local conductance in panel (d) for $V_0 = -4.5$ mV shows zero-energy modes in the topologically trivial regime. Therefore, a gap closing and the emergence of zero-energy modes in the local conductance is not a sufficient sign of a topological phase transition.

On the other hand, nonlocal conductance has a much clearer signature of the topological transition than the local conductance. To demonstrate this, in panels (e) and (f) of Fig. 5.9 we show the nonlocal conductance as a function of bias and Zeeman energy. Both for the homogeneous and the inhomogeneous case, the appearance of nonlocal conductance around $E = 0$ coincides with the change of the

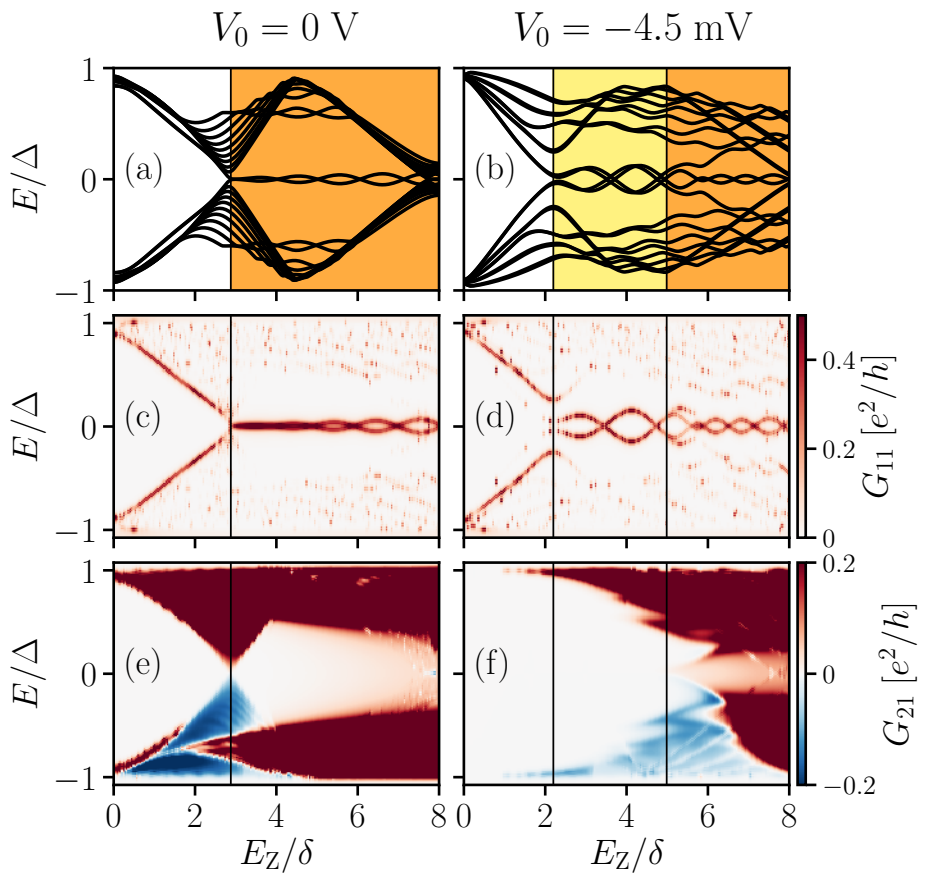

Figure 5.9: Spectrum (a, b), local conductance G_{11} (c, d) and nonlocal conductance G_{21} (e, f) of a system without potential variations (left column) and a system with a long-range Gaussian potential of amplitude $V_0 = -4.5$ mV (right column). The orange region in (a) and (b) denotes the topological phase, yellow the trivial phase with a state around zero energy. G_{11} is calculated in presence of two tunnel barriers at both wire ends, G_{21} in the single mode regime. The color scale is saturated for clarity. For the potential inhomogeneity, we set $V_0 = -4.5$ meV, $x_0 = L/2$, $y_0 = W/2$, $d_x = L/5$ and $d_y = 2W/3$.

topological invariant. In other words, the appearance of finite nonlocal conductance around $E = 0$ implies a global closing of the induced gap. Additionally, the nonlocal conductance shows rectifying behavior around $E = 0$ at the gap closing. These two features of the nonlocal conductance are strong evidence of a topological phase transition. Therefore, due to its insensitivity to spatial inhomogeneities in the potential and the additional feature of Andreev rectification, nonlocal conductance is a more reliable measure of a topological phase transition.

5.5. COOPER PAIR SPLITTER

A negative nonlocal conductance, dominated by CAR, is of fundamental interest, since the proximitised system then functions as a Cooper pair splitter [38–40, 58, 59]. In Sec. 5.3, we observed that the nonlocal conductance in clean systems at zero

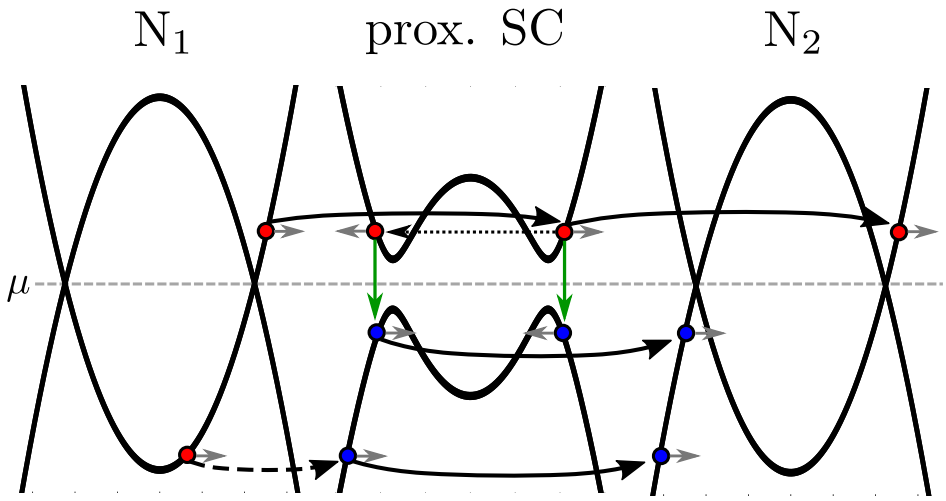

Figure 5.10: Schematic of the quasiparticle transport properties from the normal lead N_1, to the lead N_2 through the proximitised region. Quasiparticles transferring to a neighboring region (solid black arrows) predominantly preserve the quasiparticle type: electron-like (red dots) or hole-like (blue dots). Andreev reflection (green vertical arrows) changes the quasiparticle type, and the direction of propagation (grey arrows). Disorder scattering (black dotted arrow) changes the propagation direction. Finally, if no quasiparticles of the same type are available, quasiparticle transmission between regions may also result in the change of the quasiparticle type (black dashed arrow).

magnetic field is generally positive, and a CAR-dominated signal ($G_{21} < 0$) is rare. The reason for this is shown schematically in Fig. 5.10: an electron entering the proximitised region usually converts into an electron-like quasiparticle. Andreev reflection changes both the quasiparticle charge and velocity, so that the resulting hole-like quasiparticle returns to the source. Therefore under normal circumstances Andreev reflection alone is insufficient to generate a negative nonlocal current.

Despite G_{21} stays predominantly positive in clean systems, in Sec. 5.4 we found that a magnetic field can make the nonlocal conductance negative in large regions of parameter space. We identify these regions with the presence of only hole-like bands in the proximitized region at the relevant energy, as shown in Fig. 5.10. If only hole-like states are present in the proximitized region, the incoming electron may only convert into a right-moving hole-like quasiparticle, which in turn converts predominantly into a hole when exiting the proximitized region. To confirm this argument, we compare the energy ranges where only hole-like quasiparticles are present with the regions of negative G_{21}. Our results are shown in Fig. 5.11, and they exhibit a very good agreement. Since the only required property to get a negative nonlocal conductance is a hole-like dispersion relation, this phenomenon does not require SOI, or even Zeeman field. Indeed, our calculations (not shown here) reveal

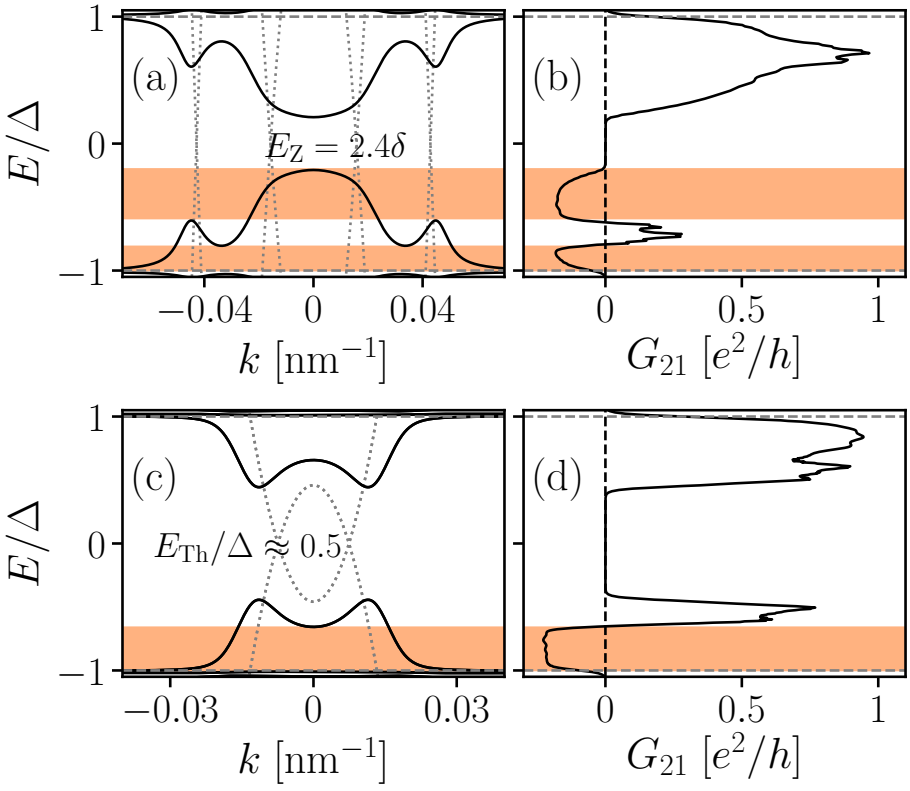

Figure 5.11: Dispersions (left column) and nonlocal conductance with $L \gg \xi$ (right column) of proximitised channels of width $W = 100$ nm (a, b) and $W = 200$ nm (c, d). Dotted lines show the electron and hole dispersions of the channels with the superconductor removed. In both cases, the induced gap is smaller than Δ, due to a Zeeman field in (a), and due to $E_{\mathrm{Th}} \lesssim \Delta$ in (c). There are energy ranges in which only hole-like bands are present, and these correspond to regions of negative G_{21}. Here, (c) is in a low-doping regime $\mu = 0.5$ meV, such that electron modes are absent for $E/\Delta \lesssim -0.5$, producing the hole-like dispersion. As a result, a larger chemical potential $\mu = 0.8$ meV is needed in the normal leads to observe $G_{21} < 0$ at the corresponding energies in (d). In (a) and (b), we have $\mu = 3$ meV.

that it is possible to extend the energy ranges over which CAR dominates by filtering the nonlocal conductance by spin, e.g. by using magnetically-polarized contacts [27].

It is possible to systematically obtain a negative nonlocal conductance in the low-doping regime without using a Zeeman field if $\Delta > \Delta_{\mathrm{ind}}$. This is shown in Fig. 5.11(c) and (d), where we have also neglected SOI for simplicity. By choosing μ comparable to the band offset of the lowest mode in the proximitised channel, at negative energies we obtain an energy range in which the band structure is only hole-like [Fig. 5.11(c)]. However, the small μ implies that no electron modes are active in the normal leads in this energy range. To observe negative nonlocal conductance here, it is therefore necessary to have a larger chemical potential in the normal leads than in the proximitised region, which ensures the presence of propagating electron

modes at the relevant energies. Doing so, we indeed observe a negative nonlocal conductance in the expected energy range of Fig. 5.11(d).

Disorder provides an alternative mechanism to obtain negative nonlocal conductance. Unlike direct electron transfer, which generally conserves the sign of quasiparticle momentum, CAR often requires a sign change of the quasiparticle momentum. Since disorder breaks momentum conservation, the probabilities of CAR and direct electron transfer become comparable once the system length exceeds the mean free path, and CAR thus more prominent than in a clean system. Indeed, as shown in Fig. 5.8, in disordered systems the nonlocal conductance becomes positive or negative with approximately equal probability.

5.6. SUMMARY AND OUTLOOK

The standard experimental tool for probing induced superconductivity in a Majorana device is a tunnelling conductance measurement using an attached normal lead. While this approach detects the density of states, its usefulness is limited because it cannot distinguish the properties in close vicinity of the lead from the properties of the bulk system. We studied how the *nonlocal* conductance between two spatially separated normal leads attached to the proximitised region overcomes this limitation. We find that the nonlocal conductance is selectively sensitive to the bulk properties of a proximity superconductor, and allows to directly measure the induced and the bulk superconducting gaps as well as the induced coherence length of the proximitised region. While we focused on the quasi 1D-systems suitable for the creation of Majorana states, our conclusions are applicable to general proximity superconductors, including 2D materials like graphene covered by a bulk superconductor.

When the probability of CAR is larger than that of electron transmission, the nonlocal conductance turns negative. While this does not happen normally, we identified conditions that allow CAR to dominate. This may happen due to disorder, which breaks the relation between quasiparticle charge, velocity and momentum and makes the nonlocal conductance zero on average. We identified another, systematic way of obtaining dominant CAR by ensuring that the only available states in the proximitised region are hole-like. A special case of this behaviour is the vicinity of the topological phase transition, where the nonlocal conductance becomes proportional to voltage, resulting in a linear relation between the differential conductance and voltage, or in other words a positive nonlocal current regardless of the sign of the voltage. This behavior is specific to topological phase transitions, and we showed how it can be used to distinguish accidental low energy states from Majorana states, resolving a potential shortcoming of Majorana tunneling experiments identified in Refs. [19–23].

Our setup can be used with trivial adjustments to probe the properties of Josephson junctions, proposed as a promising alternative platform for the creation of Majorana states [53, 54]. Further work could investigate interaction effects on the the nonlocal response [60]. An alternative promising avenue of follow-up work is to consider a multiterminal generalization of a nonlocal setup in order to combine local and global sensitivity within the same device. In Fig. 5.12 we show a possible experimental realization of such a multiterminal device, where the effective length can be

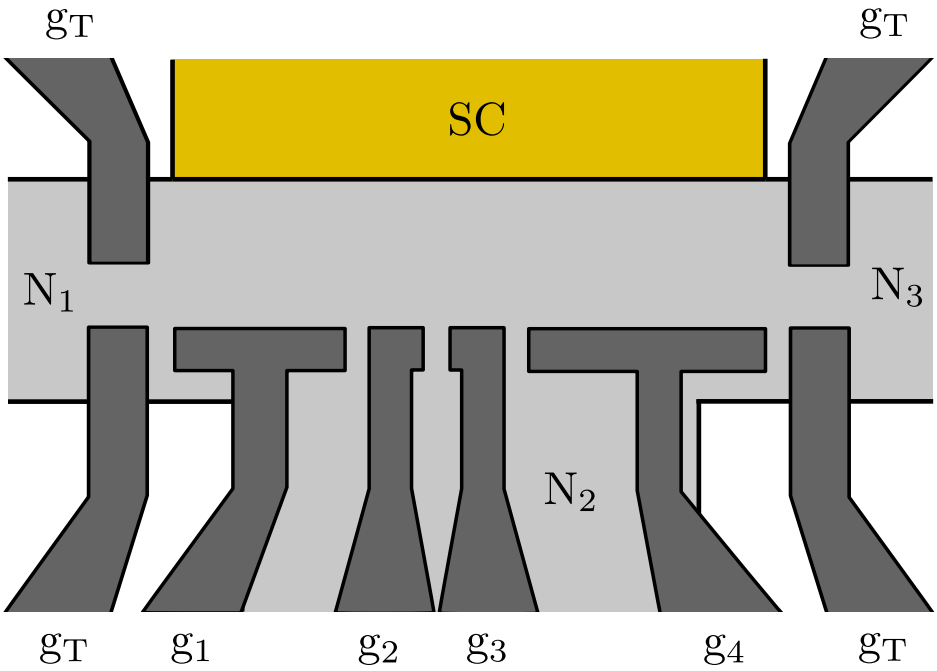

Figure 5.12: A possible experimental realization of a multiterminal proximitized device suited for nonlocal conductance measurements. Electrostatic gates g_i, $i \in \{1, 2, 3, 4\}$, pattern out a quasi-one dimensional region in a two-dimensional electron gas, which is proximitised from the side by a superconductor. Gates g_T create tunnel barriers at the endpoints of the proximised region. Changing the potentials applied to the gates allows for changing the effective device length.

adjusted with gates. Finally, our results regarding control of the CAR dominance can be used to design devices with a large electron-hole conversion efficiency.

5.7. APPENDIX

Short, intermediate and long junction limits for hybrid structures

In this appendix, we briefly discuss the subgap spectral characteristics of normal-superconductor junctions in different limits, using heuristic arguments to highlight the essential physics. For a more rigorous study, we refer the interested reader to e.g. Refs. [61–65]. Consider a quasi-one dimensional channel of length $L \to \infty$ that consists of a junction between a normal part of width W and a superconductor of width $W_{\rm sc} \gg W$. The Hamiltonian is the same as in Eq. (5.1), but with $p_x \to \hbar k$ and as before $\Delta \neq 0$ only in the superconductor. Furthermore, we consider only $E_{\rm Z} = 0$ and neglect SOI ($\alpha = 0$) and disorder for simplicity.

The hybrid structure generally has an energy gap $\Delta_{\rm ind}$, the size of which is determined by two competing energy scales, namely the bulk gap Δ and the Thouless energy $E_{\rm Th} \approx \hbar/\tau$, with τ the quasiparticle dwell time in the normal part of the junction. A short junction has $\Delta \ll E_{\rm Th}$ and a long junction $\Delta \gg E_{\rm Th}$, while $\Delta \gtrsim E_{\rm Th}$

for an intermediate junction. Alternatively, these conditions are expressed in terms of W and the BCS coherence length $\xi_0 = \hbar v_\mathrm{F}/\Delta$, where v_F is the Fermi velocity. For a quasiparticle incident perpendicularly from the normal part to the interface with the superconductor and assuming perfect interface transparency, we have $\tau \propto W/v_\mathrm{F}$ and thus $E_\mathrm{Th} \propto \hbar v_\mathrm{F}/W$. The conditions for short, intermediate and long junctions then become $W \ll \xi_0$, $W \gtrsim \xi_0$ and $W \gg \xi_0$, respectively. In the short junction limit, we have $\Delta_\mathrm{ind} \approx \Delta$, while for long and intermediate junctions $\Delta_\mathrm{ind} \propto E_\mathrm{Th}$.

We now derive a lower bound for E_Th in terms of the level spacing δ in the normal part of the junction. A quasiparticle exiting the superconductor has the dwell time $\tau \propto 2W/\gamma v_\perp(k)$ in the normal part. Here, $v_\perp(k) = \hbar k_\perp(k)/m^*$ and $k_\perp = \sqrt{k_\mathrm{F}^2 - k^2}$ are respectively the velocity and momentum projections perpendicular to the interface with the superconductor at the parallel momentum k, with k_F the Fermi momentum, and $2W$ is the distance the quasiparticle travels before colliding with the superconductor again. The dwell time scales inversely with the transparency γ of the interface between the normal part and the superconductor. In practice, the transparency is determined by interface properties, such as the presence of a barrier or velocity mismatch, which we parametrize with $0 \leq \gamma \leq 1$ for simplicity. We thus obtain $E_\mathrm{Th}(k) \propto \gamma\hbar^2\sqrt{k_\mathrm{F}^2 - k^2}/2m^*W$. Observe that E_Th decreases with k and tends to vanish as $k \to k_\mathrm{F}$ since then $v_\perp \to 0$. However, $v_\perp$ is bounded from below in a finite geometry by the momentum uncertainty associated with the band offset, which corresponds to the velocity $\mathrm{d}v_\perp \approx \hbar\pi/m^*W$ in a square-well approximation. Using $v_\perp = \mathrm{d}v_\perp$ gives the lower bound for the Thouless energy $E_\mathrm{Th} \propto \gamma\hbar^2\pi/2m^*W^2$. The preceding discussion implies that in the absence of magnetic fields, the gap in the spectrum of such a junction decreases with momentum to a minimum $\propto 1/m^*W^2$ at $k = k_\mathrm{F}$ [see left column Fig. 5.13]. Since Δ_ind is the energy of the lowest Andreev bound state in the junction, we define

$$E_\mathrm{Th} = \gamma\delta, \quad \delta = \frac{\hbar^2\pi^2}{2m^*(2W)^2} \tag{5.8}$$

as the Thouless energy of the junction. Observe that we use $2W$ in the denominator, since that is the distance normal to the interface a quasiparticle travels between successive Andreev reflections [44].

The spectral characteristics of a proximitised system strongly depend on which regime the system is in. Figure 5.13 shows the dispersion $\epsilon_n(k)$ and density of states ρ per unit length for junctions in the short, intermediate and long regimes. The density of states is given by

$$\rho(E) = \frac{1}{2\pi\hbar}\sum_n \int \delta\left[E - \epsilon_n(k)\right]\frac{\mathrm{d}E}{|v(E)|} = \frac{1}{2\pi\hbar}\sum_n \left|\frac{\mathrm{d}\epsilon_n(k)}{\mathrm{d}k}\right|^{-1}. \tag{5.9}$$

Here, n is the subband index including spin and we have used $\hbar v = \mathrm{d}E/\mathrm{d}k$ for the velocity v. In the left column, the solid lines give the dispersion of the hybrid structure, while the dotted lines show the electron and hole dispersions of the normal channel only (with $W_\mathrm{sc} = 0$ or $\gamma = 0$). In all cases, $\mu \gg \Delta$, and ρ has been broadened by convolution with a Lorentzian of full width at half maximum $\Gamma \ll \Delta$. For the

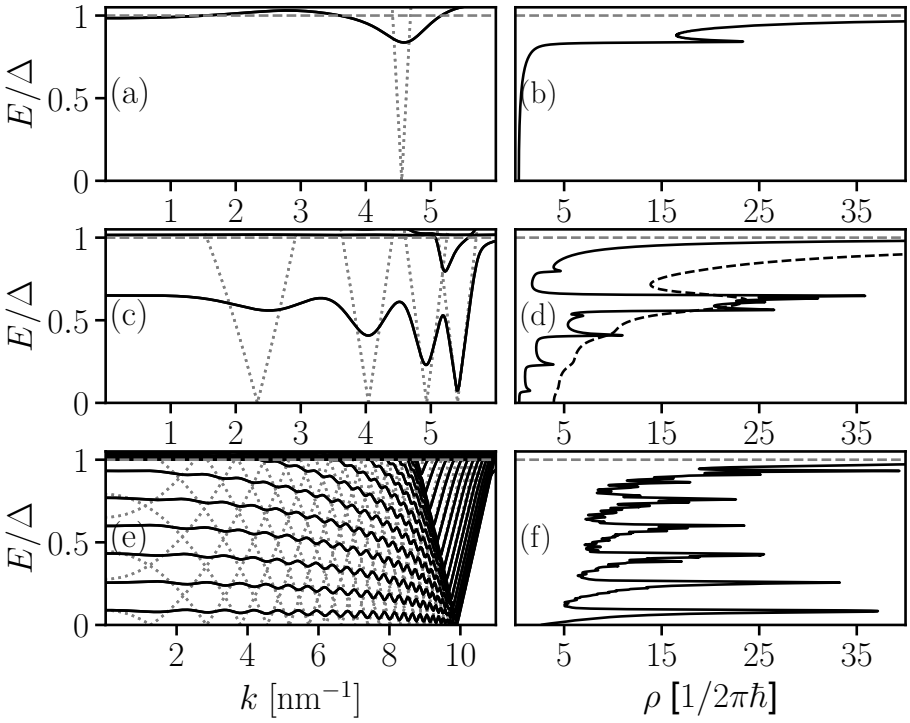

Figure 5.13: Dispersion (left column) and density of states (right column) of a quasi one-dimensional normal-superconductor junction in different regimes: a short junction (top), an intermediate junction (middle) and a long junction (bottom). In the left column, the dotted curves show the electron and hole dispersions of the corresponding normal channel with the superconductor removed. In all cases, a small broadening $\Gamma \ll \Delta$ has been added to the density of states. For the intermediate junction (d), the density of states with larger broadening is also shown (dashed curve). The curves are symmetric under $(k, E) \to (\pm k, \pm E)$.

short junction, we indeed have $\Delta_{\mathrm{ind}} \approx \Delta$, which manifests as an essentially hard superconducting gap for $|E| < \Delta_{\mathrm{ind}}$. We have verified that ρ vanishes identically in this regime with $\Gamma \to 0$. In the intermediate and long regimes, subgap states exist at energies smaller than Δ, which manifests as a nonzero subgap ρ (soft gap). The difference between the two regimes is the number of these states: in an intermediate junction, they are few, but multiple in the long junction limit, as the conditions $\Delta \gtrsim E_{\mathrm{Th}}$ and $\Delta \gg E_{\mathrm{Th}}$ indicate. Observe that in both cases, the subgap bands are flat around $k = 0$ and drop towards a minimum in energy as k increases before rising sharply again [66]. Superimposed on this are intraband oscillations that happen on a smaller energy scale. In principle, oscillations thus manifest in ρ on two energy scales: the larger energy scale is the interband spacing around $k = 0$ ($\propto 1/W^2$), and the smaller the scale of intraband oscillations. Overall, the former has a larger contribution to ρ due to the small curvature in the dispersion. Oscillations on both scales are clearly visible for the intermediate junction. However, increasing Γ further

(dashed curve) washes out the fine structure due to intraband oscillations. As a result, ρ gradually increases towards a maximum, when E aligns with the energy of the subgap state around $k = 0$. On the other hand, in the long junction there are multiple states at subgap energies, and the most prominent feature in ρ is the peaks associated with the flat parts of those bands. The fine structure due to intraband oscillations is superimposed, but masked by the broadening.

REFERENCES

[1] P. G. De Gennes, *Boundary Effects in Superconductors,* Rev. Mod. Phys. **36**, 225 (1964).

[2] G. E. Blonder, M. Tinkham, and T. M. Klapwijk, *Transition from metallic to tunneling regimes in superconducting microconstrictions: Excess current, charge imbalance, and supercurrent conversion,* Phys. Rev. B **25**, 4515 (1982).

[3] T. Tokuyasu, J. A. Sauls, and D. Rainer, *Proximity effect of a ferromagnetic insulator in contact with a superconductor,* Phys. Rev. B **38**, 8823 (1988).

[4] E. A. Demler, G. B. Arnold, and M. R. Beasley, *Superconducting proximity effects in magnetic metals,* Phys. Rev. B **55**, 15174 (1997).

[5] E. C. Gingrich, B. M. Niedzielski, J. A. Glick, Y. Wang, D. L. Miller, R. Loloee, W. P. Pratt Jr, and N. O. Birge, *Controllable 0-[pi] Josephson junctions containing a ferromagnetic spin valve,* Nat Phys **12**, 564 (2016).

[6] M. Titov and C. W. J. Beenakker, *Josephson effect in ballistic graphene,* Phys. Rev. B **74**, 041401 (2006).

[7] H. B. Heersche, P. Jarillo-Herrero, J. B. Oostinga, L. M. K. Vandersypen, and A. F. Morpurgo, *Bipolar supercurrent in graphene,* Nature **446**, 56 (2007).

[8] V. E. Calado, S. Goswami, G. Nanda, M. Diez, A. R. Akhmerov, K. Watanabe, T. Taniguchi, T. M. Klapwijk, and L. M. K. Vandersypen, *Ballistic Josephson junctions in edge-contacted graphene,* Nat. Nano. **10**, 761 (2015).

[9] J. Alicea, *New directions in the pursuit of Majorana fermions in solid state systems,* Rep. Prog. Phys. **75**, 076501 (2012).

[10] M. Leijnse and K. Flensberg, *Introduction to topological superconductivity and Majorana fermions,* Semiconductor Science and Technology **27**, 124003 (2012).

[11] C. Beenakker, *Search for Majorana Fermions in Superconductors,* Annu. Rev. Con. Mat. Phys. **4**, 113 (2013).

[12] S. B. Bravyi and A. Yu. Kitaev, *Fermionic Quantum Computation,* Annals of Physics **298**, 210 (2002).

[13] V. Mourik, K. Zuo, S. M. Frolov, S. R. Plissard, E. P. A. M. Bakkers, and L. P. Kouwenhoven, *Signatures of Majorana Fermions in Hybrid Superconductor-Semiconductor Nanowire Devices,* Science **336**, 1003 (2012).

[14] A. Das, Y. Ronen, Y. Most, Y. Oreg, M. Heiblum, and H. Shtrikman, *Zero-bias peaks and splitting in an Al-InAs nanowire topological superconductor as a signature of Majorana fermions,* Nat. Phys. **8**, 887 (2012).

[15] M. T. Deng, C. L. Yu, G. Y. Huang, M. Larsson, P. Caroff, and H. Q. Xu, *Anomalous Zero-Bias Conductance Peak in a Nb–InSb Nanowire–Nb Hybrid Device,* Nano Lett. **12**, 6414 (2012).

[16] T. M. Klapwijk, *Proximity Effect From an Andreev Perspective,* Journal of Superconductivity **17**, 593 (2004).

[17] S. Guéron, H. Pothier, N. O. Birge, D. Esteve, and M. H. Devoret, *Superconducting Proximity Effect Probed on a Mesoscopic Length Scale,* Phys. Rev. Lett. **77**, 3025 (1996).

[18] D. I. Pikulin and Y. V. Nazarov, *Topological properties of superconducting junctions,* JETP Letters **94**, 693 (2012).

[19] G. Kells, D. Meidan, and P. W. Brouwer, *Near-zero-energy end states in topologically trivial spin-orbit coupled superconducting nanowires with a smooth confinement,* Phys. Rev. B **86**, 100503 (2012).

[20] S. Mi, D. I. Pikulin, M. Marciani, and C. W. J. Beenakker, *X-shaped and Y-shaped Andreev resonance profiles in a superconducting quantum dot,* Journal of Experimental and Theoretical Physics **119**, 1018 (2014).

[21] E. Prada, P. San-Jose, and R. Aguado, *Transport spectroscopy of NS nanowire junctions with Majorana fermions,* Phys. Rev. B **86**, 180503 (2012).

[22] C. Moore, T. D. Stanescu, and S. Tewari, *Majorana bound states in non-homogeneous semiconductor nanowires,* ArXiv e-prints (2016), arXiv:1611.07058 [cond-mat.mes-hall] .

[23] C.-X. Liu, J. D. Sau, T. D. Stanescu, and S. Das Sarma, *Andreev bound states versus Majorana bound states in quantum dot-nanowire-superconductor hybrid structures: Trivial versus topological zero-bias conductance peaks,* Phys. Rev. B **96**, 075161 (2017).

[24] J. M. Byers and M. E. Flatté, *Probing Spatial Correlations with Nanoscale Two-Contact Tunneling,* Phys. Rev. Lett. **74**, 306 (1995).

[25] S. Russo, M. Kroug, T. M. Klapwijk, and A. F. Morpurgo, *Experimental Observation of Bias-Dependent Nonlocal Andreev Reflection,* Phys. Rev. Lett. **95**, 027002 (2005).

[26] R. W. Reinthaler, P. Recher, and E. M. Hankiewicz, *Proposal for an All-Electrical Detection of Crossed Andreev Reflection in Topological Insulators,* Phys. Rev. Lett. **110**, 226802 (2013).

[27] Falci, G., Feinberg, D., and Hekking, F. W. J., *Correlated tunneling into a superconductor in a multiprobe hybrid structure,* Europhys. Lett. **54**, 255 (2001).

[28] R. Mélin and D. Feinberg, *Transport theory of multiterminal hybrid structures,* The European Physical Journal B - Condensed Matter and Complex Systems **26**, 101 (2002).

[29] D. Beckmann, H. B. Weber, and H. v. Löhneysen, *Evidence for Crossed Andreev Reflection in Superconductor-Ferromagnet Hybrid Structures,* Phys. Rev. Lett. **93**, 197003 (2004).

[30] J. Brauer, F. Hübler, M. Smetanin, D. Beckmann, and H. v. Löhneysen, *Nonlocal transport in normal-metal/superconductor hybrid structures: Role of interference and interaction,* Phys. Rev. B **81**, 024515 (2010).

[31] J. Schindele, A. Baumgartner, R. Maurand, M. Weiss, and C. Schönenberger, *Nonlocal spectroscopy of Andreev bound states,* Phys. Rev. B **89**, 045422 (2014).

[32] P. Recher, E. V. Sukhorukov, and D. Loss, *Andreev tunneling, Coulomb blockade, and resonant transport of nonlocal spin-entangled electrons,* Phys. Rev. B **63**, 165314 (2001).

[33] J. P. Morten, A. Brataas, and W. Belzig, *Circuit theory of crossed Andreev reflection,* Phys. Rev. B **74**, 214510 (2006).

[34] H. Haugen, D. Huertas-Hernando, A. Brataas, and X. Waintal, *Crossed Andreev reflection versus electron transfer in three-terminal graphene devices,* Phys. Rev. B **81**, 174523 (2010).

[35] F. Crépin, P. Burset, and B. Trauzettel, *Odd-frequency triplet superconductivity at the helical edge of a topological insulator,* Phys. Rev. B **92**, 100507 (2015).

[36] Y.-T. Zhang, Z. Hou, X. C. Xie, and Q.-F. Sun, *Quantum perfect crossed Andreev reflection in top-gated quantum anomalous Hall insulator–superconductor junctions,* Phys. Rev. B **95**, 245433 (2017).

[37] J. Liu, J. Song, Q.-F. Sun, and X. C. Xie, *Even-odd interference effect in a topological superconducting wire,* Phys. Rev. B **96**, 195307 (2017).

[38] G. Deutscher and D. Feinberg, *Coupling superconducting-ferromagnetic point contacts by Andreev reflections,* Applied Physics Letters **76**, 487 (2000).

[39] L. Hofstetter, S. Csonka, J. Nygard, and C. Schonenberger, *Cooper pair splitter realized in a two-quantum-dot Y-junction,* Nature **461**, 960 (2009).

[40] L. G. Herrmann, F. Portier, P. Roche, A. L. Yeyati, T. Kontos, and C. Strunk, *Carbon Nanotubes as Cooper-Pair Beam Splitters,* Phys. Rev. Lett. **104**, 026801 (2010).

[41] A. R. Akhmerov, J. P. Dahlhaus, F. Hassler, M. Wimmer, and C. W. J. Beenakker, *Quantized Conductance at the Majorana Phase Transition in a Disordered Superconducting Wire,* Phys. Rev. Lett. **106**, 057001 (2011).

[42] B. Fregoso, A. Lobos, and S. Das Sarma, *Electrical detection of topological quantum phase transitions in disordered Majorana nanowires,* Phys. Rev. B **88**, 180507(R) (2013).

[43] P. Szumniak, D. Chevallier, D. Loss, and J. Klinovaja, *Spin and charge signatures of topological superconductivity in Rashba nanowires,* Phys. Rev. B **96**, 041401 (2017).

[44] D. Sticlet, B. Nijholt, and A. Akhmerov, *Robustness of Majorana bound states in the short-junction limit,* Phys. Rev. B **95**, 115421 (2017).

[45] M. Kjaergaard, F. Nichele, H. J. Suominen, M. P. Nowak, M. Wimmer, A. R. Akhmerov, J. A. Folk, K. Flensberg, J. Shabani, C. J. Palmstrøm, and C. M. Marcus, *Quantized conductance doubling and hard gap in a two-dimensional semiconductor–superconductor heterostructure,* Nature Communications **7**, 12841 EP (2016).

[46] H. Zhang, O. Gül, S. Conesa-Boj, M. P. Nowak, M. Wimmer, K. Zuo, V. Mourik, F. K. de Vries, J. van Veen, M. W. A. de Moor, J. D. S. Bommer, D. J. van Woerkom, D. Car, S. R. Plissard, E. P. A. M. Bakkers, M. Quintero-Pérez, M. C. Cassidy, S. Koelling, S. Goswami, K. Watanabe, T. Taniguchi, and L. P. Kouwenhoven, *Ballistic superconductivity in semiconductor nanowires,* Nat. Comm. **8**, 16025 (2017).

[47] M. P. Anantram and S. Datta, *Current fluctuations in mesoscopic systems with Andreev scattering,* Phys. Rev. B **53**, 16390 (1996).

[48] C. Groth, M. Wimmer, A. Akhmerov, and X. Waintal, *Kwant: a software package for quantum transport,* New J. Phys. **16**, 063065 (2014).

[49] See supplementary files available with this manuscript.

[50] T. O. Rosdahl, A. Vuik, M. Kjaergaard, and A. R. Akhmerov, *The Andreev rectifier: a nonlocal conductance signature of topological phase transitions,* (2017).

[51] B. Nijholt and A. R. Akhmerov, *Orbital effect of magnetic field on the Majorana phase diagram,* Phys. Rev. B **93**, 235434 (2016).

[52] T. Ando, *Quantum point contacts in magnetic fields,* Phys. Rev. B **44**, 8017 (1991).

[53] M. Hell, M. Leijnse, and K. Flensberg, *Two-Dimensional Platform for Networks of Majorana Bound States,* Phys. Rev. Lett. **118**, 107701 (2017).

[54] F. Pientka, A. Keselman, E. Berg, A. Yacoby, A. Stern, and B. I. Halperin, *Topological Superconductivity in a Planar Josephson Junction,* Phys. Rev. X **7**, 021032 (2017).

[55] B. J. Wieder, F. Zhang, and C. L. Kane, *Signatures of Majorana fermions in topological insulator Josephson junction devices,* Phys. Rev. B **89**, 075106 (2014).

[56] Feinberg, D., *Andreev scattering and cotunneling between two superconductor-normal metal interfaces: the dirty limit,* Eur. Phys. J. B **36**, 419 (2003).

[57] I. C. Fulga, F. Hassler, A. R. Akhmerov, and C. W. J. Beenakker, *Scattering formula for the topological quantum number of a disordered multimode wire,* Phys. Rev. B **83**, 155429 (2011).

[58] J. J. He, J. Wu, T.-P. Choy, X.-J. Liu, Y. Tanaka, and K. T. Law, *Correlated spin currents generated by resonant-crossed Andreev reflections in topological superconductors,* Nat. Comm. **5**, 3232 EP (2014).

[59] W. Chen, D. N. Shi, and D. Y. Xing, *Long-range Cooper pair splitter with high entanglement production rate,* Sci. Rep. **5**, 7607 EP (2015).

[60] D. Aasen, S.-P. Lee, T. Karzig, and J. Alicea, *Interaction effects in superconductor/quantum spin Hall devices: Universal transport signatures and fractional Coulomb blockade,* Phys. Rev. B **94**, 165113 (2016).

[61] C. W. J. Beenakker, *Three "Universal" Mesoscopic Josephson Effects,* in *Transport Phenomena in Mesoscopic Systems: Proceedings of the 14th Taniguchi Symposium, Shima, Japan, November 10–14, 1991*, edited by H. Fukuyama and T. Ando (Springer Berlin Heidelberg, Berlin, Heidelberg, 1992) pp. 235–253.

[62] A. Volkov, P. Magnée, B. van Wees, and T. Klapwijk, *Proximity and Josephson effects in superconductor-two-dimensional electron gas planar junctions,* Physica C: Superconductivity **242**, 261 (1995).

[63] S. Pilgram, W. Belzig, and C. Bruder, *Excitation spectrum of mesoscopic proximity structures,* Phys. Rev. B **62**, 12462 (2000).

[64] G. Tkachov, *Nonmetallic thermal transport in low-dimensional proximity structures with partially preserved time-reversal symmetry in a magnetic field,* Physica C: Superconductivity **417**, 127 (2005).

[65] C. R. Reeg and D. L. Maslov, *Hard gap in a normal layer coupled to a superconductor,* Phys. Rev. B **94**, 020501 (2016).

[66] M. Titov, A. Ossipov, and C. W. J. Beenakker, *Excitation gap of a graphene channel with superconducting boundaries,* Phys. Rev. B **75**, 045417 (2007).

Curriculum Vitæ

I was born in Capelle aan den IJssel, The Netherlands, on October 4, 1990. I received secondary eduction between 2003 and 2009 at the Comenius College in Capelle aan den IJssel. I began my BSc. studies in Applied Physics at Delft University of Technology in 2009. In 2012, I received my BSc. degree (cum laude), after which I started the Quantum Nanoscience track of the master Applied Physics, obtaining my MSc. degree in 2014. During the final year of my master, I worked as an intern at the Netherlands Forensic Institute, where I quantitatively investigated toolmarks using numerical software. After that, I did my master's research in the Theoretical Physics group under supervision of Dr. Anton Akhmerov and Dr. Michael Wimmer. The results of this research are reported in my master's thesis 'Effects of the electrostatic environment on the properties of Majorana devices'.

This master's thesis formed the basis for my Ph.D. project, that I started in the Theoretical Physics group directly after my graduation in November 2014, employed by the Foundation for Fundamental Research on Matter (FOM) and under supervision of Dr. Anton Akhmerov. Later, after a department reorganisation, I became a member of the Quantum Tinkerer group, directed by Dr. Anton Akhmerov and Dr. Michael Wimmer. In the first two years of my Ph.D. project, I continued investigating electrostatics in Majorana devices, partly in collaboration with experimentalists in the group of Prof. Dr. Ir. Leo Kouwenhoven at QuTech in Delft. In the last two years, the main focus shifted to the study of quasi-Majorana states and nonlocal conductance in Majorana devices.

During my Ph.D. I was a teaching assistant for the Introduction to Quantum Mechanics course and the Solid State Physics course. I presented my research at workshops, schools, and conferences in The Netherlands, Spain, Switzerland, Denmark, Argentina, and the United States.

List of Publications

1. *Reproducing topological properties with quasi-Majorana states.* A. Vuik, B. Nijholt, A. R. Akhmerov, and M. Wimmer, arXiv:1806.02801 (2018).

2. *Andreev rectifier: a nonlocal conductance signature of topological phase transitions.* T. Ö. Rosdahl, A. Vuik, M. Kjaergaard, and A. R. Akhmerov, Physical Review B **97**, 045421 (2018).

3. *Conductance through a helical state in an Indium antimonide nanowire.* J. Kammhuber, M. C. Cassidy, F. Pei, M. P. Nowak, A. Vuik, D. Car, S. R. Plissard, E. P. A. M. Bakkers, M. Wimmer, and L. P. Kouwenhoven, Nature Communications **8**, 478 (2017).

4. *Effects of the electrostatic environment on the Majorana nanowire devices.* A. Vuik, D. Eeltink, A. R. Akhmerov, and M. Wimmer, New Journal of Physics **3**, 033013 (2016).